ABSTRACT

Title of Dissertation: MOLECULAR SPECTROSCOPY OF STAR FORMING REGIONS: COOL AND HOT, CLOSE AND FAR

Jialu Li
Doctor of Philosophy, 2023

Dissertation Directed by: Professor Andrew Harris
Professor Alexander Tielens
Department of Astronomy

Star formation processes originating from dense molecular clouds leave us a molecular universe. How molecules probe the physical conditions at different star-forming stages and how the physical environments control the formation of the chemical inventory becomes a key question to pursue. In the past, the understanding of this problem is impeded by instrumental limitations. With instruments advanced in sensitivity and spatial/spectral resolution, this thesis investigates the molecular environment of different star-forming regions.

Half of this thesis (Chapter 2 and Appendix A) focuses on mapping cold dense molecular gas in an external galaxy, IC 342, at 3 Mpc. The distribution of molecular gas was efficiently mapped with a set of density-sensitive tracers with *Argus*. *Argus* is the first array receiver functioning at 3 mm on the 100 m Green Bank Telescope (GBT) and provides a resolution of 6″–10″. As this study was conducted in the early era of *Argus*' deployment, valuable information on the instrument's behavior is learned. The resolved molecular maps characterize the fundamental

physical properties of the clouds including the volume density and the excitation conditions. Comparisons with results from radiative transfer modeling with RADEX help to decrypt this information. The high spatial resolution of *Argus* also provides an opportunity in inspecting a scale-scatter breakdown of the gas density-star formation correlation in nearby galaxies and in investigating the influence of a finer spatial resolution on the correlation.

The other half of the thesis (Chapters 3 and 4) studies the hot core, an embedded phase during massive star formation, of a proto-binary system W3 IRS 5 at 2.2 kpc. Rovibrational transitions of gaseous H_2O, CO, and isotopologues of CO were detected with mid-IR absorption spectroscopy. The high spectral resolution (R ~50,000–80,000) not only separates each transition individually but also decomposes different kinematic components residing in the system with a velocity resolution of a few km s^{-1}. Physical substructures such as the foreground cloud, high-speed “bullet”, and hot clumps in the disk surface are identified. Characterization of the physical substructures is conducted via the rotation diagram analysis and curve-of-growth analyses. The curve-of-growth analyses, under either a foreground slab model or a disk model, take account of the optical depth effects and correct the derived column densities by up to two orders of magnitude. The disk model specifically suggests a disk scenario with vertically-decreasing temperature from mid-plane, which is intrinsically different from externally illuminated disks in the low-mass protostellar systems that have hot surfaces. Connections between physical substructures and chemical substructures were also established. Investigations on chemical abundances along the line of sight reveal the elemental carbon and oxygen depletion problem.

MOLECULAR SPECTROSCOPY OF STAR FORMING REGIONS: COOL AND HOT, CLOSE AND FAR

by

Jialu Li

Dissertation submitted to the Faculty of the Graduate School of the
University of Maryland, College Park in partial fulfillment
of the requirements for the degree of
Doctor of Philosophy
2023

Advisory Committee:
Professor Andrew Harris, Chair/Advisor
Professor Alexander Tielens, Co-Advisor
Dr. Adwin Boogert, External Examiner
Professor Alberto Bolatto
Professor John Fourkas, Dean's Representative
Professor Stuart Vogel

Preface

The research presented in this thesis has been either previously published or at advanced stages for submission.

Chapter 2 is presented with minimal changes and is going to be submitted to the Astrophysical Journal (ApJ) as "Argus/GBT Observations of Molecular Gas in the Inner Regions of IC 342". The authors are Jialu Li, Andrew I. Harris, Erik Rosolowsky, Amanda A. Kepley, David Frayer, Alberto D. Bolatto, Adam K. Leroy, Jennifer Donovan Meyer, Sarah Church, Joshua Ott Gundersen, Kieran Cleary, and other DEGAS team members.

Chapter 3 is presented with minimal changes since publication in ApJ as "High-Resolution M-band Spectroscopy of CO towards the Massive Young Stellar Binary W3 IRS5" (Li et al., 2022). The authors are Jialu Li, Adwin Boogert, Andrew G. Barr, and Alexander G. G. M. Tielens.

Chapter 4 is presented with minimal changes and has been submited to ApJ as "High-resolution SOFIA/EXES Spectroscopy of Water Absorption Lines in the Massive Young Binary W3 IRS 5". The authors are Jialu Li, Adwin Boogert, Andrew G. Barr, Curtis DeWitt, Maisie Rashman, David Neufeld, Nick Indriolo, Yvonne Pendleton, Edward Montiel, Matt Richter, J. E. Chiar, and Alexander G. G. M. Tielens.

Dedication

To my parents.

Acknowledgments

I regard this thesis as not a compilation of works in the past few years but a journey with a form of “curve-of-growth”. I owe great thanks to all who have accompanied, helped, and guided me into the happy one who is typing now.

I am most grateful to my PhD advisors, Andy Harris and Xander Tielens, without whom this thesis would not have been possible. Andy has been a model of a scientist to me since his first class of instrumentation, and I have always been so curious about the pile of notebooks in his office. I still find it very amusing that when we sat down together and finished deriving some formula, Andy closed his notebook and said, “Jialu, you should be able to derive it by yourself now.” – usually, other graduate students can directly get a copy of the note. I appreciate the most about Andy’s “so what?” question through the years, as this question, repeatedly asked me to think more clearly and express more precisely. This is a challenging task for me, not only from a perspective of language but also from my weakness in defining problems. Andy, thank you for your patience and encouragement along the way; I will take this question as a lifelong companion to become a better researcher.

Xander has been just so good. The dimension of knowledge I learned from you spans from research to life. I always regard our weekly meeting with Adwin as an exhilarating walk. I appreciate it so much that you always “guard the border” when I get distracted or even lost out of curiosity or because I forget my goals. Thanks to you, becoming a happy astronomer who can make contributions even after forty years is now a well-defined question to me.

I also thank Adwin Boogert, Andrew Barr, and Curtis DeWitt for being close collaborators. I appreciate the great discussions with you and the good comments from you. Xander said it's important to work with fun people, and I definitely enjoyed our experience working together. I look forward to working on more exciting projects with you in the future.

I appreciate the rest collaborators I have worked with in different research groups. David Frayer in the GBO is always reliable. Amanda Kepley, Adam Leroy, and Erik Rosolowsky have been helpful for the *Argus* paper over the years. The observation group of the DiSCo survey led by Che-Yu Chen is the most efficient one I have ever seen, and I enjoy the teamwork with Rachel Friesen and Anika Schmiedeke very much. I also want to thank David Neufeld, Nick Indriolo, Yvonne Pendleton, Edward Montiel, and Maisie Rashman in the EXES Hot Core Survey group for improving the water paper with careful thoughts. I would like to thank Karen O'Neil in the GBO for the approval of the DDT request of the IC 342 study. I appreciate the operator teams in the GBT, IRTF, and SOFIA for their help in all the observations relevant to my studies. I thank the anonymous referees for providing helpful suggestions to improve the quality of my paper drafts.

I want to thank the weekly group meetings where Alberto Bolatto, Peter Teuben, Stuart Vogel, Rebecca Levy, Laura Lenkić, Liz Tarantino, Vicente Villanueva, Carrie Volpert, and Serena Cronin, the group of people working on galaxies, listen to my short reports patiently. I believe those stories were very confusing in the first couple of years. I specifically appreciate Alberto for his interesting thoughts, insightful questions, and great suggestions on how to tell a story in a better way.

I appreciate Yefei Yuan, Helmut Dannerbauer, Dimitra Rigopoulou, and Yu Gao for their guidance and supports in my early stage of astronomy researches when I was an undergraduate student. I want to thank Cole Miller, Drake Deming, Derek Richardson, Massimo Ricotti, Doug Hamilton, and Richard Mushotzky for their wonderful classes in the first two years of graduate school. Until today, I often find that I get a new understanding of those class materials.

I am also grateful to all the staff in the astronomy department, including but not limited to Olivia Dent, Barbara Hansborough, Susan Lehr, Lauren Miles, Mona Susanto, Dorinda Kimbrell, Eric McKenzie, Adrienne Newman, and Mary Ann Phillips, for running the administrative things so smooth for us. I want to thank all the other researchers, Marc, Tracy, Kevin, Mark, and graduate students, Drew, Tiara, Qian, Dana, Zeeve, Pradip, Amy, Ginny, Sara, Robyn, Kyle, Carrie, Chongchong, Tomás, Milena, Charlotte, Alex, Ramsey, Erica, and many others that I met over the years.

I am grateful to my friends, Thomas Rimlinger, Weizhe Liu, Peizhi Du, Yu Shi, and Yao Wang from the department of astronomy and others, for their companionship with laughs. Thomas has been more than a great officemate but a good friend who is always concerned about my well beings. I always appreciate your warm hosting with Bernadette. Weizhe has been the best sparring partner all these years, and I am glad that Peizhi usually stands by my side. I appreciate the time with you two and Yu to look for food which may not always be good. Thanks to my roommate Yao, expecting great cooking at home is something more guaranteed.

I want to thank friends I have known long before graduate school. Wenjun Zhao and Ruoshui Wang, you two accompanied me through all big and small bumps with love and have always supported me unconditionally. We were not born to be a family, but you are the dearest sisters in my heart. I also want to thank Can Cui, Ziwei Zhao, Ruochen Wu, Jingyuan Chen, Zhaoyu Wang. My friendship with Shanrong Wang, Mengdie Fan, and Jingyi Liu lasts more than half of my life. I appreciate all of you who are always there when I need help.

A special thanks to my husband Jiali Lu, who should have a position in the previous paragraph. It was quite an amazing moment when I put all the pieces of our memories together and, without any doubts, realized that I should share my future journey with you.

Finally, I thank my parents, Leping Bao and Jianwei Li. You are the most interesting parents in the world, and I love you very, very much.

Table of Contents

List of Tables

List of Figures

List of Abbreviations

ALMA	Atacama Large Millimeter/submillimeter Array
BIMA	Berkeley Illinois Maryland Association
BIMA-SONG	The BIMA Survey of Nearby Galaxies
COM	Complex Organic Molecule
CRIRES	Cryogenic Infrared Echelle Spectrograph
CSA	Canadian Space Agency
DEGAS	Dense Extragalactic GBT+Argus Survey
DSHARP	The Disk Substructures at High Angular Resolution Project
ESA	European Space Agency
EXES	Echelon-Cross-Echelle Spectrograph
FWHM	Full Width at Half Maximum
GBT	the 100 m Robert C. Byrd Green Bank Radio Telescope
HCHII	Hypercompact-HII Region
HMC	Hot Molecular Core
HMPO	High-Mass Protostellar Object
HMSC	High-Mass Starless Core
IRDC	Infrared Dark Cloud
IRTF	The Infrared Telescope Facility
ISM	Interstellar Medium
JCMT	James Clerk Maxwell Telescope
JWST	James Webb Space Telescope
LAMBDA	Leiden Atomic and Molecular Database
LIGs	Luminous Infrared Galaxies
LTE	Local Thermodynamic Equilibrium

MIR	Mid-Infrared
MMIC	Millimeter-wave Integrated Circuit
NASA	The National Aeronautics and Space Administration
NIR	Near-Infrared
NIRCAM	Near Infrared Camera
NRAO	National Radio Astronomy Observatory
OTF	On-The-Fly
PdBI	Plateau de Bure Interferometer
PDR	Photodissociation Region
PSG	Planetary Spectrum Generator
SOFIA	Stratospheric Observatory for Infrared Astronomy
STScI	Space Telescope Science Institute
UCHII	Ultracompact-HII Region
UDO	the Unidentified Depleted Oxygen
ULIRGs	Ultraluminous Infrared Galaxies
UV	Ultraviolet
VLT	the Very Large Telescope
ZAMS	Zero Age Main Sequence

Chapter 1: Introduction

Simple elements, including C, N, O, and H, come together to form life on the Earth. In the prebiotic era, these elements were locked up in volatiles such as H_2O, NH_3, CH_4, CO, CO_2, H_2CO, and CH_3OH. These species were delivered to the Earth in molecular form via a variety of physical processes, including the assemblage of rocky planets from asteroidal bodies (Johansen et al., 2014; Raymond et al., 2014), accretion of pebbles drifting in from the outer solar system (Lambrechts & Johansen, 2012; Ormel & Klahr, 2010), and delivery by comets during the late heavy bombardment (Chyba et al., 1990). Therefore, the organic inventory of the Earth reflects the chemical heritage from a wide range of conditions in the solar system.

Such a chemical heritage can be further traced back to star formation processes originating from dense molecular clouds (Figure 1.1), although as far as we know, not all star-forming systems are fortunate enough to end up with an Earth. As physical and chemical evolutions proceed hand in hand during star formation, understanding the interplay between these evoltions becomes a key question of astrophysics and astrochemistry: How do the molecules probe the physical conditions at different star-forming stages and help to understand the temporal evolutionary scenario, and how do the physical environments control the formation of the organic inventory?

Progress in answering the question above is driven by new observational data. On the

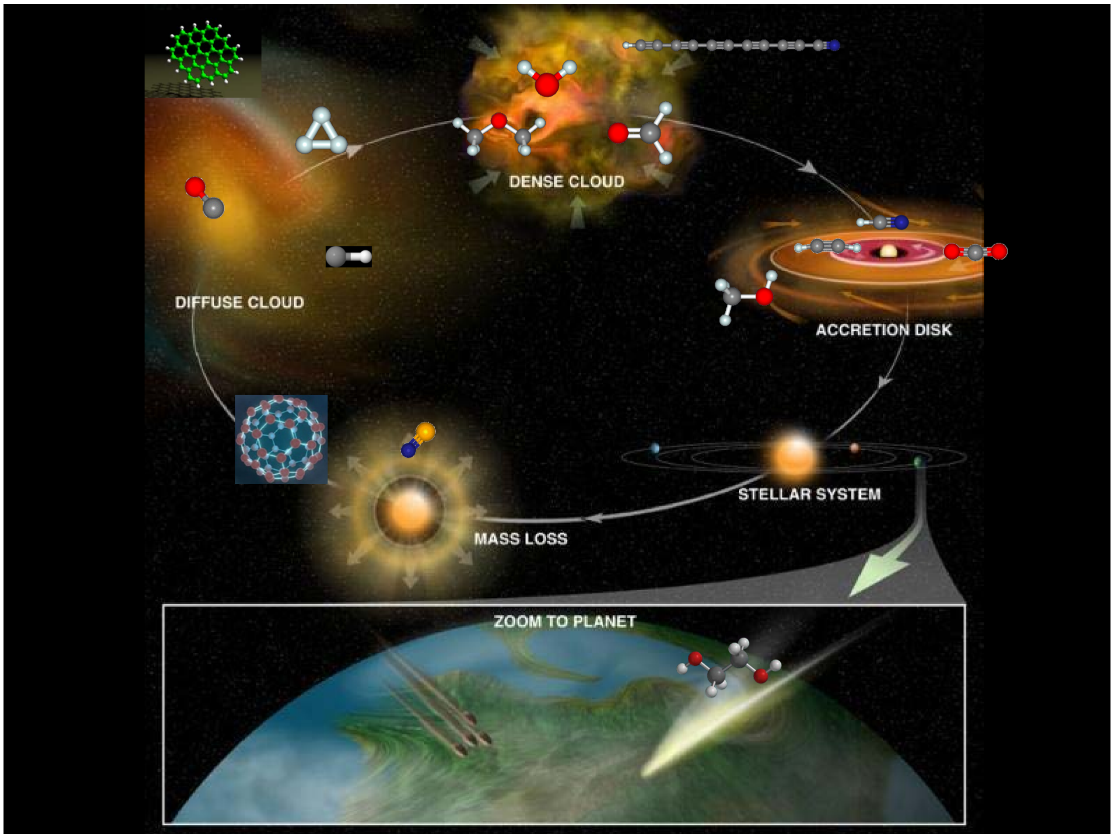

Figure 1.1: Lifecycle of gas and dust in interstellar space. Characteristic molecules at each of the star- and planet formation and stellar death stages are indicated. Figure adapted from van Dishoeck (2018). Image by Bill Saxton (NRAO/AUI/NSF) and molecule pictures from the Astrochymist.

one hand, although Sir Arthur Eddington pointed out some 100 years ago that "it is difficult to admit the existence of molecules in interstellar space because when once a molecule becomes dissociated there seems no chance of the atoms joining up again" (Eddington, 1926), as of late May 2022, about 270 molecules[1] (ignoring the isotopologues) have been identified in the interstellar medium (ISM). On the other hand, our view has also expanded to a variety of physical scales with a deeper understanding. On galactic scales, the distribution of molecular gas was extensively observed through measurements of the CO J =1–0 transition, with which debates on the large-scale distribution of H_2 in the Galaxy and molecular cloud lifetimes are

[1] https://cdms.astro.uni-koeln.de/classic/molecules

resolved (Heyer & Dame, 2015). Of the large-scale molecular gas, the closer and denser cold dark clouds are characterized as filamentary supersonic structures (tens to hundreds of parsec) and starless subsonic cores ($\sim$0.1 pc) by millimeter/submillimeter lines from species such as CO, CS, and N_2H^+ (Bergin & Tafalla, 2007). As the scale decreases to the size of a singular forming star, nowadays, the Atacama Large Millimeter/submillimeter Array (ALMA) is able to resolve substructures of protoplanetary disks in the CO J =2–1 transition with a spatial resolution as small as 5 au (e.g. the DSHARP survey, Andrews et al., 2018).

This thesis focuses on characterizing molecular clouds from galactic (kpc) scales down to proto-stellar (thousands of au) scales. Specifically, we study in Chapter 2 cold, dense molecular clouds that are resolved to hundreds of parsec in an external galaxy. The breakdown of degenerated physical conditions of dense molecular clouds at high spatial resolution is explored. We use high-spectral resolution spectroscopy to investigate in Chapters 3 and 4 the hot cores of several thousands of au dimensions in a massive protostellar system. Highly embedded cloud structures are decomposed with a velocity resolution of a few km s^{-1}. Multiple physical substructures, such as foreground shells, outflows, and the disks therein, were identified, and their connections with different chemical substructures were established.

The aim of this introductory chapter is to frame the current knowledge of star formation processes and the basics of molecular spectroscopy for the reader (§ 1.1 and § 1.2). Readers who feel familiar with the contexts may directly refer to § 1.1.3 and § 1.2.3, as these sections address the main scientific questions asked by this thesis and emphasize specific concerns in analyzing these questions. § 1.3 introduces the main observational instruments used in this thesis, and § 1.4 lists, with details, the contents of the remaining chapters.

1.1 Star Formation

1.1.1 Physical Scenario

The birth of a star, or, more specifically, the mass of a star at its birth, determines much of how the star lives through its life. Low-mass stars ($M \lesssim M_\odot$) are much more numerous, lock up most of the stellar mass in the Galaxy, and live long and rather peacefully. High-mass ($M > 8M_\odot$) stars, while only making up less than 1% of the stellar population in the Milky Way, consume fuel quickly, and strongly reshape the surrounding environment through their intense ultraviolet (UV) radiation, energetic stellar winds, and violent explosions in the end. The cumulative effects of this feedback regulate the immediate interstellar medium (ISM), and ultimately govern the evolution of the host galaxies of the massive stars (Kennicutt, 2005).

1.1.1.1 Star-Forming Environment: Molecular Clouds

For either low- or high-mass stars, it is generally accepted that their formation starts from the gravitational collapse of gas (Shu, 1977) inside cold, dense molecular clouds (Bergin & Tafalla, 2007; Heyer & Dame, 2015), which are presented under *Spitzer*'s view in Figure 1.2. Molecular clouds are cold (10–30 K), self-gravitating objects in which molecular material H_2 is the dominant constituent. Molecular clouds show complex, filamentary structures that are partly hierarchical, and the gravity of molecular clouds is counterbalanced by thermal pressure, magnetic fields, and turbulence. The cloud size spans across 2–20 pc, the mean density (of H_2) is from 10^2–10^3 cm^{-3}, and the mass ranges from 10^2–10^6 $M_\odot$ (Bergin & Tafalla, 2007; Klessen, 2011).

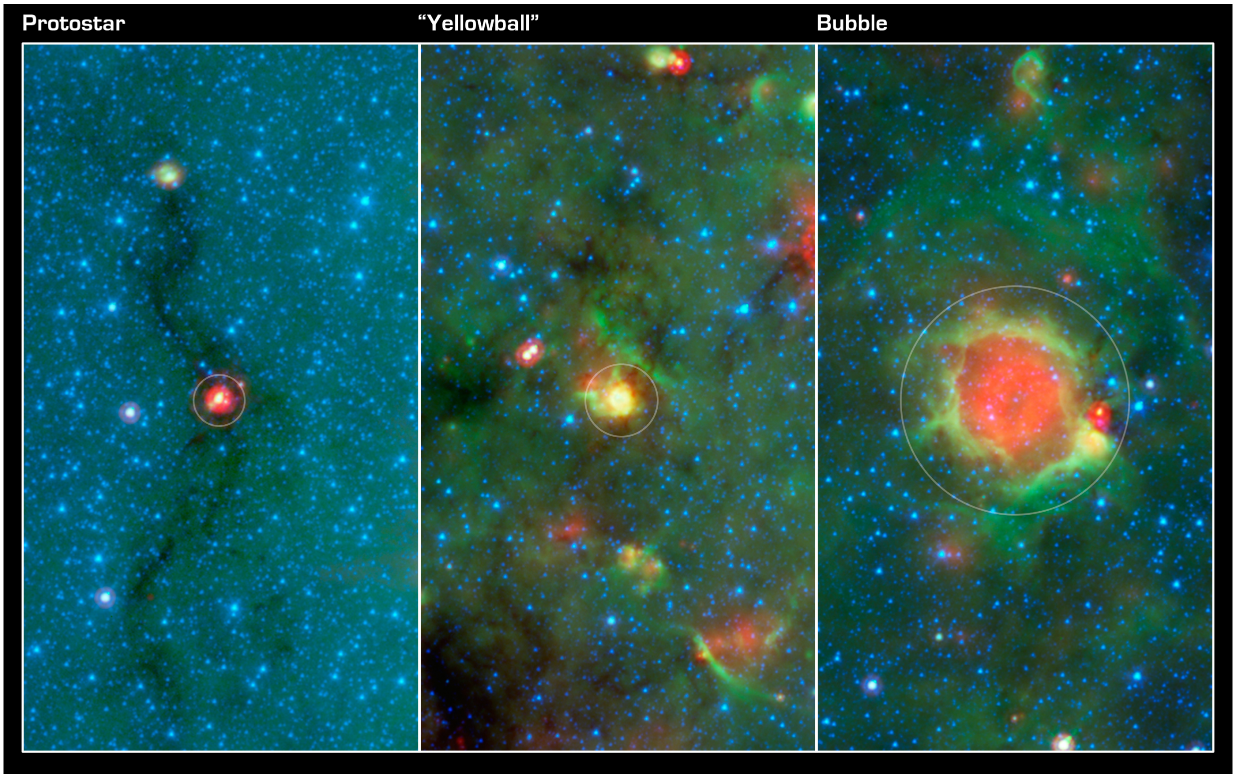

Figure 1.2: This series of images show three evolutionary phases of massive star formation, as pictured in infrared images from NASA's Spitzer Space Telescope. The stars start out in thick cocoons of dust (left), evolve into hotter features dubbed "yellowballs" (center), and finally blow out cavities in the surrounding dust and gas, resulting in green-rimmed bubbles with red centers (right). In this image, infrared light of 3.6 microns is blue; 8-micron light is green; and 24-micron light is red. Credits: NASA/JPL-Caltech.

Stars form by the gravitational collapse of dense molecular gas under the density fluctuation generated by supersonic turbulence. As gas clumps become gravitationally unstable, the central density of the cloud clumps increases significantly and gives birth to a protostar (McKee & Ostriker, 2007). Because the cloud always has some initial angular momentum, the infalling gas ends up in a rotating disk through which mass continues to be transported to the central object, the protostar. Bipolar jets and outflows are usually associated with disks, and push an opening space and generate shocks through the surrounding environment and remove excess angular momentum from the disk. When the central temperature and pressure are sufficient to

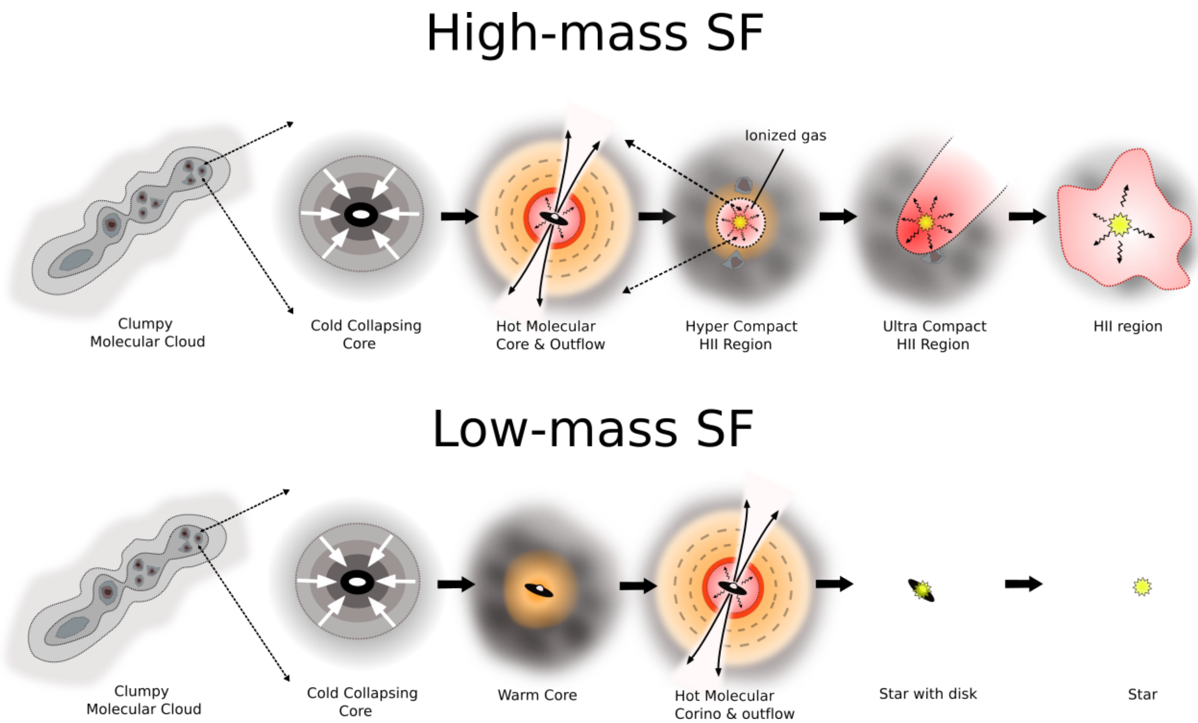

Figure 1.3: Evolutionary sequence for high-mass and low-mass stars. Credits: Cormac Purcell. The original figure is adapted from the personal website of Adam Ginsberg.

start fusion at the star's core, the star reaches the Zero Age Main Sequence (McKee & Ostriker, 2007).

High-mass stars ignite hydrogen fusion before the collapse has ceased, and low-mass stars ignite after the collapse has ceased. For massive protostellar objects, the Kelvin-Helmholtz timescale, which represents the timescale on which a quasi-hydrostatic core contracts toward hydrogen-burning densities and temperatures, is much shorter than the timescale of accretion (McKee & Ostriker, 2007). The strong radiative forces that massive stars exert on gas and dust may dramatically influence the accretion rate and the follow-up evolutionary stages (Figure 1.3). The formation process of massive stars is therefore not a simply scaled-up version of low-mass star formation (Beuther et al., 2007; McKee & Tan, 2003).

1.1.1.2 Low-Mass Star Formation

The formation process of low-mass stars is quite well established both observationally and theoretically (see Luhman, 2012; McKee & Ostriker, 2007; Shu et al., 1987, and references therein). As illustrated by Figure 1.3, three major phases are involved (Shu, 1977; Shu et al., 1987). In the *pre-stellar phase* ($\sim 5 \times 10^6$ yr), the core contracts quasi-statically and isothermally. Energy is released in the form of radiation. Magnetic fields and turbulence provide important support against the gravitational collapse process. As the collapse proceeds, the central object contracts adiabatically, and eventually heats up. In this *protostellar phase* ($\sim 10^5$ yr), a young protostar, which is referred to as a *T-Tauri object*, begins to form, and the disk structure develops. As the star continues to gravitationally contract at this *pre-main sequence* stage, the core continues to heat up. Accretion stops well before hydrogen burning starts. At the same time, a Keplerian disk encircling the protostar is visible, because much of the matter is blown away. This disk lasts for $\sim 10^{6-7}$ yr, and is also referred to as a *proto-planetary disk*, because it is the future formation site of planets (Williams & Cieza, 2011). This nascent system will continue to evolve for $\sim 10^8$ yr under collisions between the planetesimals and planets.

1.1.1.3 High-Mass Star Formation

Understanding the formation processes of massive stars faces obstacles from the perspective of observation. Massive stars are rare, and those at their early formation stages are even rarer, so these stars are usually distant from the observers. In their early stages, massive stars are deeply embedded, and therefore are invisible at optical and near-infrared wavelengths. Massive stars are seldom found to form in isolation (see Figure 1.3), so the highly clustered environment only obscures their formation and evolution processes further.

There also exist theoretical difficulties for high-mass star formation. Massive stars arrive on the ZAMS before the accretion ends, so the outward directed force associated with radiation pressure has to be less than the gravitational force pulling material in (Wolfire & Cassinelli, 1987); viz.,

$$\frac{\kappa L}{4\pi r^2 c} < \frac{GM_*}{r^2}, \text{ or } \kappa < \kappa_{\rm crit} = 130 \left[\frac{M_*}{10M_\odot}\right]\left[\frac{L_*}{1000L_\odot}\right]^{-1} \text{cm}^2\text{g}^{-1}, \tag{1.1}$$

in which κ is the opacity, L is the star luminosity, r is the radius, and M_* is the stellar mass. For a massive star of $10M_\odot$ and $10^4 L_\odot$, $\kappa_{\rm crit} \sim 10$ cm^{2}g^{-1}. This is much smaller than the typical opacity value of dusty ISM ($\kappa \sim 100$ cm^{2}g^{-1}), and is referred to as the *radiation pressure problem*.

Several approaches have been established to reconcile the radiation problem. The generation of radiatively driven bubbles and disc-mediated accretion (Krumholz et al., 2009; Rosen & Krumholz, 2020) in *monolithic collapse models* (Krumholz et al., 2005; McKee & Tan, 2003) have been developed as a way to overcome the radiation pressure barrier. *The coalescence scenario* (Bally & Zinnecker, 2005; Bonnell et al., 1998) in high-stellar-density environments avoids the radiation-pressure issues. *The competitive accretion model* (Bonnell et al., 2004; Bonnell & Bate, 2006) suggests that the forming stars accrete material that is not gravitationally bound to the stellar seed. Each of these different scenarios has implications for cluster formation and binary formation involving disks.

For high-mass, star-forming cores, the current proposed theoretical evolutionary sequence is high-mass, starless cores (HMSCs) $\rightarrow$ high-mass cores harboring accreting low/intermediate-mass protostar(s) destined to become a high-mass star(s) $\rightarrow$ high-mass protostellar objects (HM-

POs) $\rightarrow$ final stars (Beuther et al., 2007). Observationally, the embedded phases of massive protostellar objects are subdivided into infrared dark clouds (IRDC; starless core), hot molecular cores (HMCs; proto-stellar object), hypercompact- and ultracompact-HII regions (HCHIIs and UCHIIs), and compact and classical HII regions (Beuther et al., 2007). In the last two stages, final stars have already been formed. As the formation and evolution proceed, the central object warms and ionizes the environment, and drives a rich chemistry. Complex physical activities are involved in the evolution as well, such as accretion disks, outflows, shocks, disk winds, and these can leave their imprint on the chemical inventory (Cesaroni et al., 2007; Zinnecker & Yorke, 2007).

1.1.2 Chemical Scenario

Although the stellar atmosphere produces and expels molecules and dust particles, most of the unshielded molecules other than the largest are decomposed to atoms by harsh UV radiation within $\sim$100 years (van Dishoeck, 1988). The existence of molecules thus indicates that the chemistry that forms the molecules is local in nature (Herbst & van Dishoeck, 2009).

The increasing chemical complexity of molecules proceeds with the formation process (see Figure 1.4) of either low- or high-mass stars (see Caselli & Ceccarelli, 2012; Herbst & van Dishoeck, 2009; Jørgensen et al., 2020, and references therein):

Pre-stellar phase: In this cold ($\sim$10 K) and dense ($> 10^6$ cm^{-3}) environment, gas-phase chemistry – dominated by ion-neutral reactions – and grain-surface chemistry occurring on the surface of dust grains take the leading role. The gas-phase atoms and molecules freeze out onto the dust grains and form thick icy mantles. The mobile H atoms on the grain surface hydrogenate atoms and CO to form hydrogenated molecules such as water (H_2O), formaldehyde (H_2CO), and methanol (CH_3OH) (Caselli & Ceccarelli, 2012). The other process in this phase is the photolysis of icy mantles, which produces radicals.

Protostellar phase: In this phase, the inner envelope of the protostellar and ice mantles are warmed. Radicals produced in the previous stage may diffuse (Herbst & van Dishoeck, 2009). Sublimation of ice mantles also starts when the temperature is high enough – only 20 K for volatile species such as CO, but $\sim$100 K for more strongly bonded ice species such as H_2O. This stage with ice sublimation is generally better known as *hot core* or *hot corino* – one named for high-mass systems, and the other for low-mass systems. Rich gas-phase ion–molecule chemistry ensues after sublimation. For example, molecules formed on the dust surface in the last period, such as methanol (CH_3OH), sublime and form more complex species, such as $HCOOCH_3$ (Charnley & Rodgers, 2005). Shocks are another source of rich chemical reactions. As accretion goes on, outflows interact with the surrounding environments and create shocks at the interface. In the shocks, dust grains are sputtered and vaporized. Neutral–neutral gas-phase reactions take over, and produce complex molecules (Caselli & Ceccarelli, 2012).

Hot cores and hot corinos attract attention because they are among the richest molecular environments, including the complex organic molecules (COMs), in space (Herbst & van Dishoeck, 2009). Hot cores were first found in the massive protostellar system in the Orion molecular clouds (OMC-1, Blake et al., 1987) based on the jump in molecular abundances. It was some 15 years later that similar structures were confirmed to exist in low-mass protostellar systems (Cazaux et al., 2003) under mechanisms that rich COMs form under gas-phase reactions after the evaporation of ice. However, COMs in hot corinos and hot cores differ in the chem-

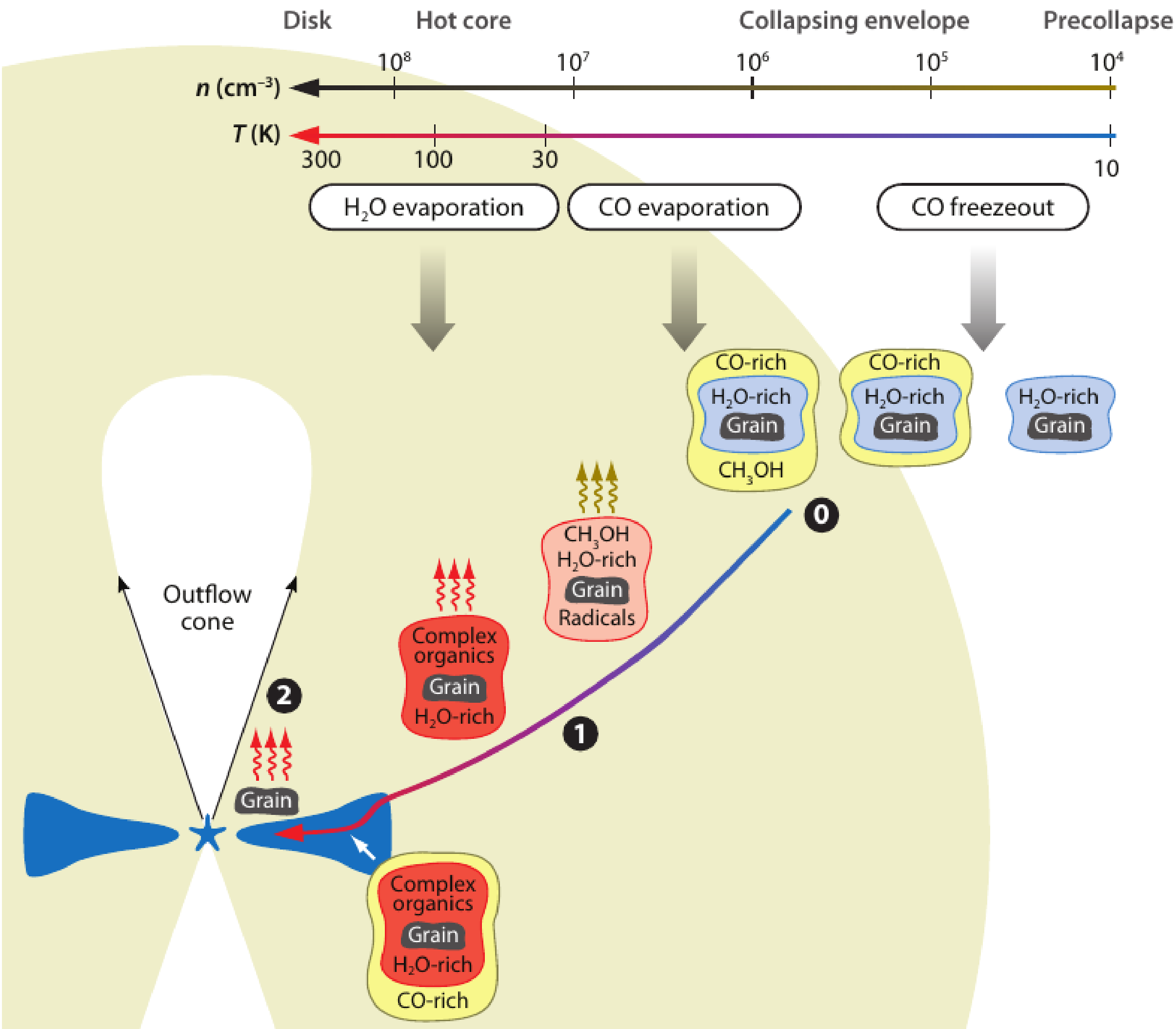

Figure 1.4: The evolution of material from the prestellar core stage through the collapsing envelope (size ∼0.05 pc or 10^4 AU) into a protoplanetary disk. The formation of zeroth- and first-generation organic molecules in the ices is indicated with 0 and 1, and the second-generation molecules in the hot-core/corino region when the envelope temperature reaches 100 K, and even strongly bound ices start to evaporate, are designated 2. The grains are typically 0.1 μm in diameter and are not drawn to scale. The temperature and density scale refer to the envelope, not to the disk. All ices evaporate inside the (species-dependent) sublimation radius. Figure and descriptions are adapted from Herbst & van Dishoeck (2009).

ical composition. When normalized to methanol or formaldehyde, hot corinos have typically one order of magnitude more abundant COMs (such as $HCOOCH_3$ or CH_3OCH_3) than do hot cores (e.g., Bottinelli et al., 2007; Öberg et al., 2011). The temperature, cosmic-ray ionization rate, radiation field, the timescale of evolution, and the past pre-stellar history may all influence the rates at which molecules are created or destroyed (Caselli & Ceccarelli, 2012).

After the protostellar stage, protoplanetary disks in low-mass systems are formed when dust grains coagulate to planetesimals to form future planets, comets, and asteroids. For massive stars, the ultracompact HII regions ionize the surrounding gas and reduce the chemical complexity (Caselli & Ceccarelli, 2012).

1.1.3 Main Questions the Thesis Focuses On

The above summary might read as if the star formation processes in molecular clouds are quite well understood. However, this is by far not the case. Many degeneracy problems exist due to the instrumental limitation from sensitivity and spatial/spectral resolution, and instruments are designed and advanced accordingly to better understand those problems. This thesis tries to address a few of these questions.

1.1.3.1 Dense Molecular Gas in External Galaxies

One question is about the role molecular gas density played in star formation in galaxies. Modern theories (e.g., Federrath & Klessen, 2013; Krumholz & McKee, 2005), as well as observations of local molecular clouds, support the ability of gas to form stars from density variations (e.g., Lada et al., 2010, 2012). However, the quantitative link between gas density and star formation is not established yet in galaxies, as compared to in local molecular clouds in the Milky Way. Dense, star-forming structures are too small to directly image in other galaxies, and molecular tracers in these dense regions, such as HCN and HCO^+, are too faint to observe. For

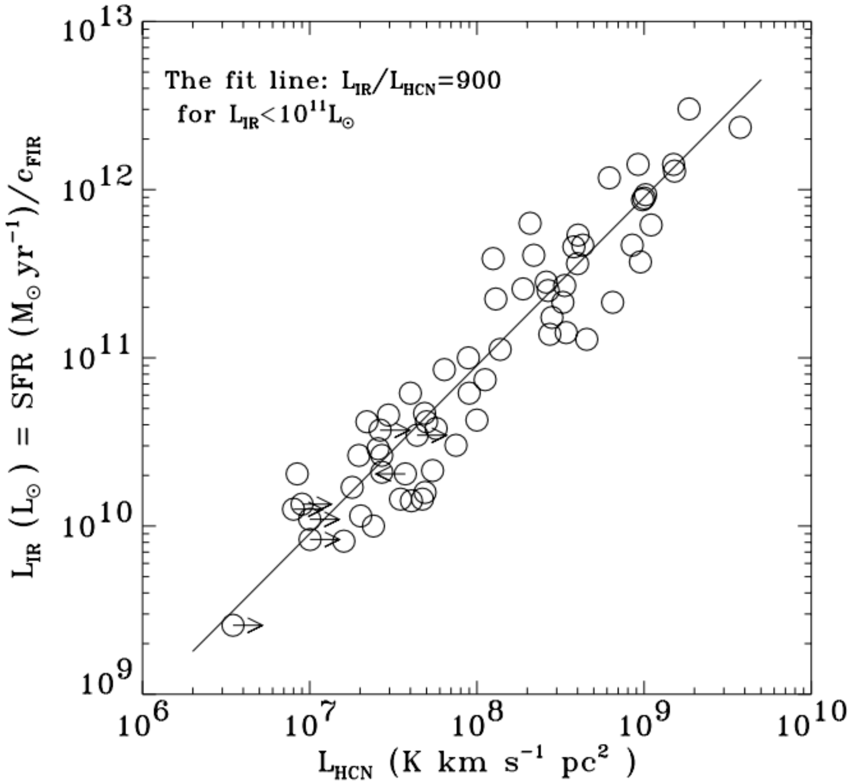

Figure 1.5: The global $L_{\mathrm{IR}} - L_{\mathrm{HCN}}$ correlation in 65 galaxies (adapted from Figure 2a, Gao & Solomon, 2004b). This tight linear correlation in the log-log space is valid over 3 orders of magnitude, has a correlation coefficient R=0.94, and an almost constant average ratio $L_{\mathrm{IR}}/L_{\mathrm{HCN}} = 900 L_\odot$ (K km s^{-1}pc^2)$^{-1}$. The direct consequence of the linear IR-HCN correlation is that the global star formation rate is linearly proportional to the mass of dense molecular gas in normal spiral galaxies, LIRGs, and ULIRGs.

external galaxies, past work was limited to single-point observations on the external galactic centers with a large beam (e.g., Gao & Solomon, 2004a,b; Jiménez-Donaire et al., 2017, 2019). From the unresolved measurements of the dense gas tracer HCN, it was concluded by Gao & Solomon (2004a,b) that the global star formation rate is linearly proportional to the mass of dense molecular gas in normal spiral galaxies, LIRGs, and ULIRGs, and the global star formation efficiency depends on the fraction of the molecular gas in a dense phase (Figure 1.5).

Spatially resolved maps of dense molecular rotational lines are necessary for testing the conclusions above. First, the interpretation of the observed molecular lines results in the degeneracy of some basic physical properties, including even the volume density (see § 1.2.3). Second, on a galactic scale, a scale-dependent scatter has been observed for CO, which is a proxy for less dense molecular gas, in the relation between the molecular gas surface density and the SFR on a galactic scale (e.g., Kruijssen & Longmore, 2014; Schruba et al., 2010). Such a relationship breaks down at some scale due to incomplete sampling of star-forming regions, and such a scenario is naturally suspected for the HCN-IR relationship. With the new multi-pixel receiver *Argus* on the GBT (§ 1.3.1), it is now feasible to study dense molecular gas in external galaxies with spatially resolved molecular line maps of a set of density tracers. This thesis (Chapter 2) studies the properties of dense molecular gas in detail, and inspects the scale-scatter breakdown between HCN-IR in one of the closet HCN-bright galaxies, IC 342.

1.1.3.2 Decomposing Substructures in a Massive Protostellar System

The other question arises from the embedded nature of massive protostellar systems at the hot core stage. As hot cores are among the richest molecular environments in space, it requires taking an "infrared shot" (not an X-ray one!) with a high spectral resolution to unravel and characterize the complex physical and chemical substructures. Decomposing physical substructures and establishing their links with chemical evolution will contribute to a clearer understanding of the massive star formation process in this obscured phase, in contrast to the better-understood low-mass protostellar phase. This question in particular drives the work in Chapters 3 and 4 of this thesis.

A specific question of interest to the massive protostellar system is whether there exists an accretion disk similar to those in low-mass star formation systems. In recent years, a disk-mediated accretion scenario has been gradually established both theoretically (e.g., Bonnell & Bate, 2006; McKee & Tan, 2003) and observationally with sub-mm/mm observations (e.g., Ilee et al., 2016; Johnston et al., 2015, 2020), although the role and properties of an accretion disk remain uncertain. Although disk structures have not yet been imaged directly in W3 IRS 5, the massive protostellar (more specifically, a proto-binary) system studied in this thesis, the disk(s) is one of the possible origins of the mid-IR dust continuum against which the absorption lines lay. This would be an interesting scenario if disks do exist: In contrast to the scenario that *emission lines* originating from the disks associated with the lower mass systems, T-Tauri or Herbig AeBe stars, which are considered to be externally illuminated and have a hotter surface layer, the *absorption lines* in hot cores of massive stars indicate disks with an inversion of the temperature structure on height. If disks in massive protostellar systems are hotter in the mid-plane than on the surface, what mechanisms regulate such an energy balance? And what is the implication of the different evolutionary scenarios of low-mass and massive systems? How do such disks influence the follow-up organic chemical inventory? Although this thesis does not answer all of the questions above, we present in Chapters 3 and 4 how a disk model is feasible in interpreting the observational data. The outlook part in Chapter 5 briefly describes how the questions above may be further addressed.

1.2 Molecular Spectroscopy

Molecules in space interact with the electromagnetic radiation field through absorption, emission, and scattering. The absorption or emission of a molecular species as a function of the wavelength leaves unique spectroscopic signatures whose strength depends on the local phys-

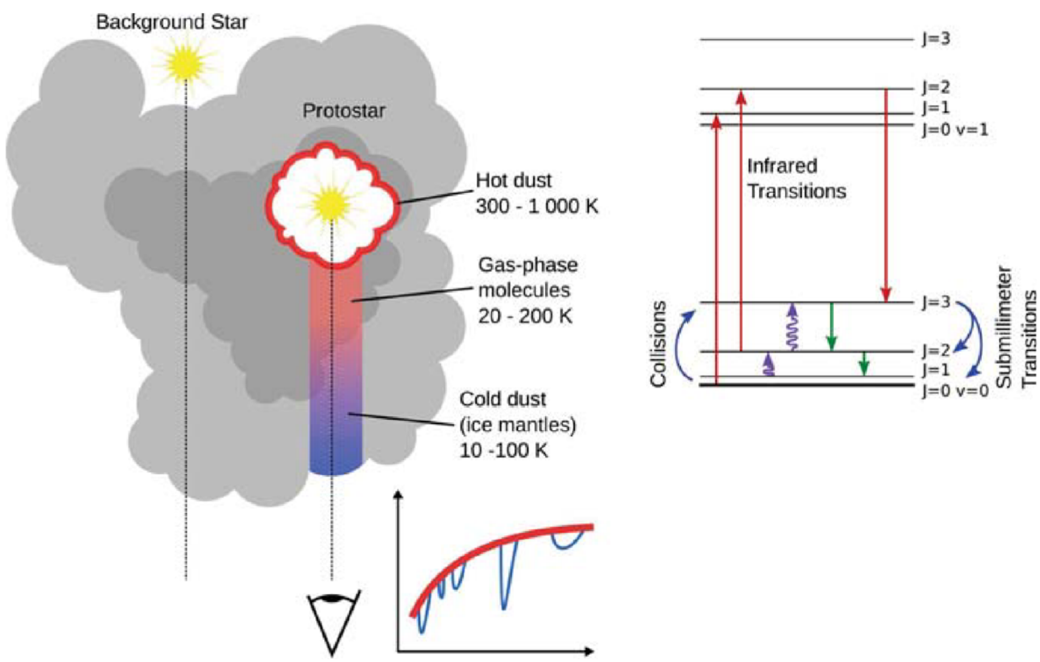

Figure 1.6: Schematic energy level diagram cartoon illustrating rotational and rovibrational absorption observations toward an embedded protostar or a background star. Figure adapted from van Dishoeck et al. (2013).

ical conditions. Hence, molecular spectroscopy is a powerful tool for identifying a species and determining the physical conditions of the absorbing/emitting gas. § 1.2.1 introduces spectroscopic features of gaseous CO and H_2O at mm- and MIR-wavelengths used in this thesis. The exact line profile set the spectra, including the line intensity and the line shape, reflect the actual interaction between the photons and the molecular gas. Molecular spectroscopy therefore can also be used to *quantify* the amount of the molecules, the temperature of the environment, the density of the gas, etc, (see Figure 1.6). § 1.2.2 summarizes, in a crude way, how such information can be decrypted.

1.2.1 Molecular Spectra in the Regime of Infrared/Radio

Molecules can rotate and vibrate. Because the nuclei are much more massive than the electron by $\sim 10^4$–10^5, electrons move fast while the inter-nuclear distance slowly varies. The rotation and vibration of the nuclei can therefore be treated separately from the electronic motion.

1.2.1.1 Pure Rotational Spectra of CO

For the rotation of the nuclei, a diatomic molecule like CO that can be approximated as a linear rigid rotor. Transitions among the rotational states give rise to the *pure rotational spectrum*. The energy levels are

$$E_J = hcB_eJ(J+1) \tag{1.2}$$

with B_e the rotational constant and J the rotational quantum number. The rotation constant is equal to

$$B_e = \frac{h}{8\pi^2 cI}, \tag{1.3}$$

with I the moment of inertia.

Because direct radiative rotational transitions are allowed for $\Delta J = \pm 1$,

$$[(E(J+2) - E(J+1)] - [E(J+1) - E(J)] = 2hcB_e. \tag{1.4}$$

This equation implies that the lines are evenly spaced in frequency space (to first order). Centrifugal distraction term $-D_eJ^2(J+1)^2$ that can be added to equation 1.4, increases the moment of inertia, and leads to a non-constant separation. Taking CO as an example, the frequency of transitions of $J+1$ to J is 115.3, 230.8, 346.0, 461.5 GHz for J from 0 to 3. The actual separations of the lines are corrected by a small number.

1.2.1.2 Vibration-Rotation Spectra of CO

We picture the molecular bond as a harmonic oscillator and a rigid rotor for vibration in a diatomic molecule. In the gas phase, a *rovibrational spectrum* is generated when both the vibrational and the rotational state change together (ΔJ is still ± 1). The energy of different levels is approximately the sum of the vibrational and rotational energy, which is given by

$$E_{\nu,J} = hc\omega_e(\nu + \frac{1}{2}) + hcB_e J(J+1), \tag{1.5}$$

in which ν and J are the vibrational and rotational quantum number, ω_e the harmonic wavenumber, and B_e the rotational constant (eqn 1.3).

Again, for a diatomic molecule like CO, the selection rule for the rovibrational spectrum is $\Delta\nu = \pm 1, \Delta J = \pm 1$. Figure 1.7 shows the ν=1−0 rovibrational transitions of a diatomic molecule, and Figure 1.8 shows an example of CO transitions observed toward the protostar Reipurth 50 at 4.7 μm. It is easily recognized that there are two branches, rather than one for pure rotational transitions. The branch on the higher frequency side is called the “R-branch” ($\Delta J = +1$), and the one on the lower side is the “P-branch” ($\Delta J = -1$). In principle, the constant separation is $2hcB_e$, as is derived in equation 1.4, and the centrifugal stretching brings in small offsets in the frequency. The larger spacing in the P-branch shown in Figure 1.7 is due to the increment of the moment of inertia in a higher vibrational state.

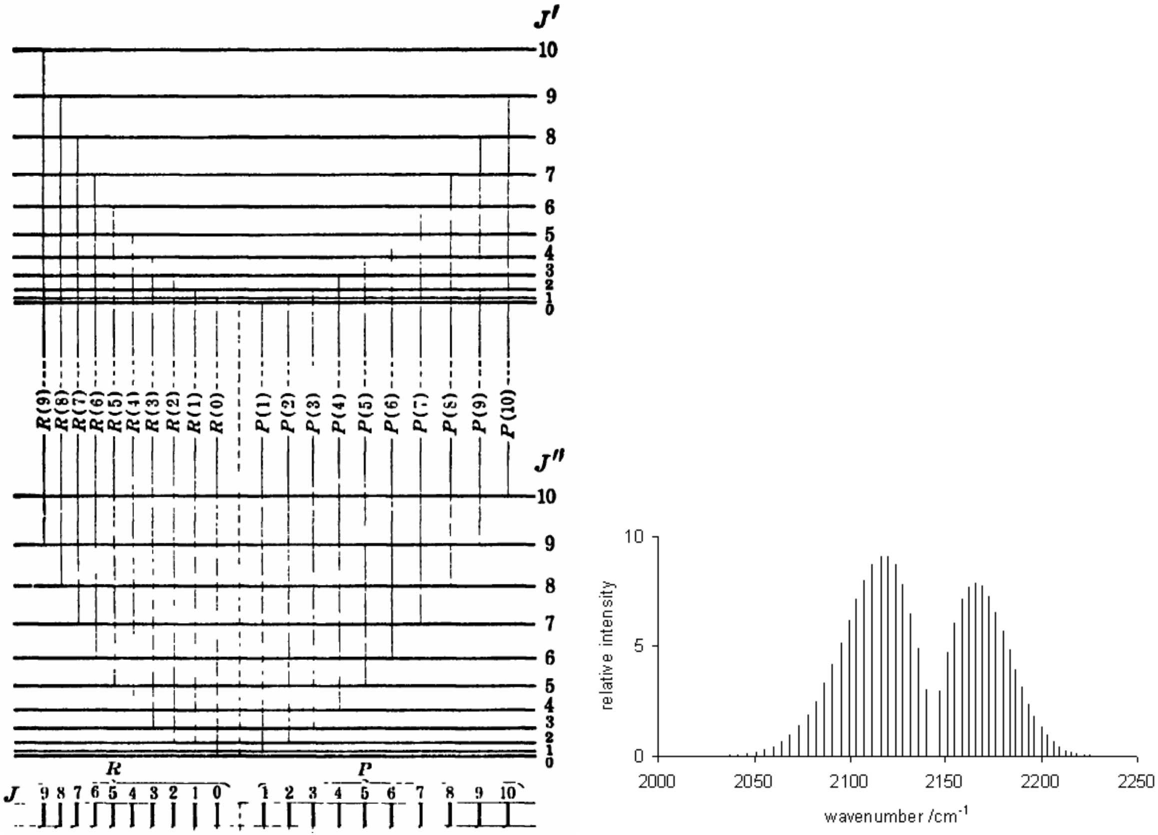

Figure 1.7: Rovibrational transitions of a diatomic molecule (left) and a simulated rovibrational line spectrum of CO. The P-branch is to the left of the gap near 2140 cm^{-1}, and the R-branch is on the right. Figures adapted from Herzberg (1950) and Banwell & McCash (1994).

1.2.1.3 Vibration-Rotation Spectra of H_2O

A nonlinear molecule containing N atoms will have $3N - 6$ normal vibrational modes. Water has three vibrational modes: the ν_1 symmetric stretch centered at 2.7 μm, the ν_2 bending mode at 6.2 μm, and the ν_3 asymmetric stretch at 2.65 μm (van Dishoeck et al., 2013). For an asymmetric top molecule like H_2O, the energy levels are characterized by quantum numbers J_{K_a,K_c}, where J is the total rotational quantum number, and K_a and K_c refer to the corresponding prolate and oblate symmetric tops[2]. From the symmetry, the selection rules are

[2] The moments of inertia are defined by convention with $I_c \geq I_b \geq I_a$. For the prolate case, $I_b \simeq I_c \neq I_a$. For the oblate case, $I_b \simeq I_a \neq I_c$

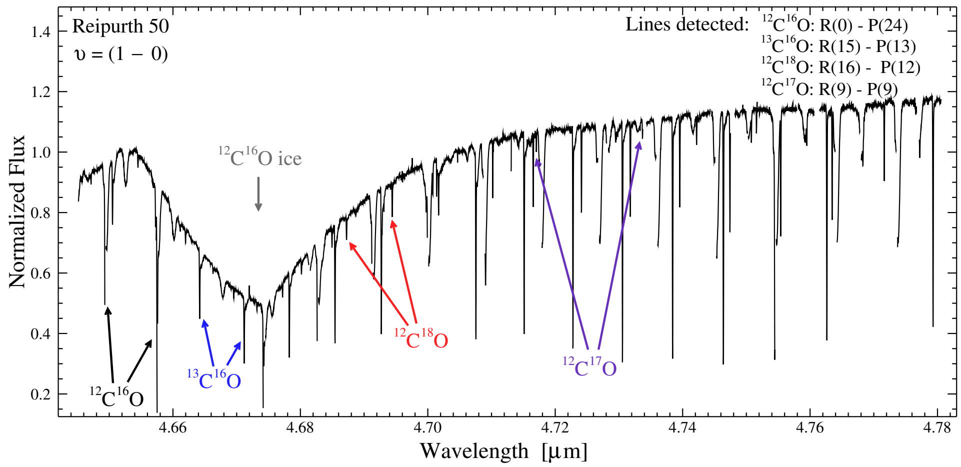

Figure 1.8: Example of rovibrational transitions of CO and its isotopologues observed with the Cryogenic Infrared Echelle Spectrograph (CRIRES) at the Very Large Telescope (VLT) toward the protostar Reipurth 50. The broad absorption feature of CO in the solid phase is shown at $\sim$4.674 μm. Figure adapted from Smith et al. (2009).

$\Delta J = 0, \pm1, \Delta K_a = \pm1, \pm3, ...$ and $\Delta K_b = \pm1, \pm3, ...$ Therefore, transitions between K-ladders are not allowed. H_2O energy levels are grouped into ortho and para states, characterized by parallel and antiparallel nuclear spins. In the ortho states, $K_a + K_c$=odd; in the para states, $K_a + K_c$=even.

1.2.2 Interpreting Molecular Lines

1.2.2.1 Radiative Transfer and the Source Function

To interpret the observed molecular spectra, either emission or absorption, requires understanding the interaction of molecules with the radiation field. Such a process involves the redistribution of energy, and is therefore named *radiative transfer.* The radiation field can have an external origin (e.g. the CMB or emission from a background source), or can be generated from local materials (e.g. thermal continuum emitted by the dust). A simple model for a homogeneous slab describing the radiative transfer results in

$$I_\nu = I_\nu(0)e^{-\tau_\nu} + S_\nu(1 - e^{-\tau_\nu}), \tag{1.6}$$

where $I_\nu(0)$ is the injected specific intensity, τ_ν the optical depth contributed by the slab, and S_ν the source function. All the variables are frequency-dependent. The definition of the source function takes a few more words.

The *source function* S_ν reflects the interaction between the gas and the radiation. If only absorption and emission are involved, the photon energy is coupled to the gas via collision. Both the gas and the radiation field are quickly pushed toward thermodynamic equilibrium. In this case, the source function is solely defined by the emissivity j_ν, the (absorption) opacity coefficient κ_ν, and the density ρ. In contrast, if only scattering is involved, the resulting emission intensity depends on the local radiation field rather than on the thermal properties of the gas.

In general, when absorption and scattering coexist, an absorption fraction ϵ is defined as

$$\epsilon_\nu \equiv \frac{\kappa_{abs}}{\kappa_{abs} + \kappa_{sc}}, \tag{1.7}$$

where κ_{abs} and κ_{sc} are the opacity coefficients for absorption and scattering. With the absorption fraction defined as above, the general form of the source function is

$$S_\nu = \epsilon_\nu B_\nu + (1 - \epsilon_\nu)J_\nu, \tag{1.8}$$

with B_ν the local Planck function and J_ν the angle-average of I_ν at frequency ν.

Equation 1.6 therefore describes an ideal case, as it is almost impossible to have a constant source function along the path where light travels. Decrypting the physical conditions we care about, such as the amount of the molecules or the temperature of the gas from the emergent flux I_ν, or essentially S_ν, is, therefore, a tricky problem. Luckily, to some degree, specific assumptions and methods help to simplify the problem.

1.2.2.2 Level Population and the Excitation Temperature

Consider equations 1.7 and 1.8 from a microscopic view. All involved items are dependent on the level population, i.e. the distribution of molecules over different energy levels. For the bound–bound transitions that produce different molecular lines, the associated line processes are characterized by the Einstein coefficients (A_{ij}, B_{ij}) and the collisional coefficients (C_{ij}). The C_{ij}'s are given by the collisional rate coefficients times the density of collisional partners. Take a two-level system as an example, the equations of *statistical equilibrium* that determines the level populations are:

$$\begin{aligned}\frac{dn_l}{dt} &= -n_l(B_{lu}\bar{J} + C_{lu}) + n_u(A_{ul} + B_{ul}\bar{J} + C_{ul}) \\ \frac{dn_u}{dt} &= n_l(B_{lu}\bar{J} + C_{lu}) - n_u(A_{ul} + B_{ul}\bar{J} + C_{ul})\end{aligned} \tag{1.9}$$

where "l" and "u" denote the lower and the higher level. Equation 1.9 reflects how absorption, emission, and scattering are connected: molecules at the lower level are excited to the higher level by radiative ($n_l B_{lu}\bar{J}$) and collisional ($n_l C_{lu}$) processes; From the high to the low level, there is spontaneous emission ($n_u A_{ul}$), stimulated emission ($n_u B_{ul}\bar{J}$), and collisional de-excitation ($n_u C_{ul}$). $\bar{J}$ is J_ν integrated over the line profile $\phi(\nu)$, and n_i is the (volume) number density.

In thermodynamic equilibrium, the level populations are given by the Boltzmann equation, which for a two-level system reads,

$$\frac{n_2}{n_1} = \frac{g_2}{g_1} e^{-\frac{E_{21}}{k_B T}}, \tag{1.10}$$

with T the kinetic temperature of the gas and E_{21} the energy separation of the two levels. However, the thermodynamic equilibrium is not always satisfied in astronomical conditions, and an arbitrarily defined parameter, which is called the *excitation temperature*, replaces the kinetic temperature T in equation 1.10 to quantify the level population. The parameter T_{ex} has no physical meaning from the perspective of the concept of "temperature". Except in dense regions that the gas is fully thermalized, so that $S_\nu = B_\nu(T_{\text{ex}}) = B_\nu(T_{\text{kin}})$, T_{ex} may deviate from the kinetic temperature significantly.

If all level populations are known, populations can be plotted in a rotation diagram with ln(N_l/g_l) versus E_l/k_B via the equation

$$\frac{N_l}{g_l} = \frac{N_{\text{tot}}}{Q(T_{\text{ex}})} \exp\left(-\frac{E_l}{k_B T_{\text{ex}}}\right), \tag{1.11}$$

in which Q is the partition function. This formula, of course, is similar to equation 1.10, although column densities are used here. The inverse of the slope represents the excitation temperature. I present below how the level population may be solved in different cases.

1.2.2.3 Optically Thin Case

In the optically thin case, $\bar{J}_\nu$ coupled in equation 1.8 is unimportant because photons escape easily, and therefore $S_\nu = B_\nu(T_{\text{ex}})$. The optical depth is easily solved from equation 1.6, and is associated with the level population directly via the definition,

$$\tau_\nu = \int \alpha_\nu ds = \frac{1}{4\pi}\int (n_l B_{lu} - n_u B_{ul})\phi(\nu) h\nu ds, \tag{1.12}$$

where $\alpha_\nu = \kappa_\nu \rho$, and $\phi(\nu)$ is the line profile in frequency space. Note that no opacity contributed by scattering is included in this equation.

All data points on the rotation diagram will fall on a straight line with the inverse of the slope being $T_{\rm ex}$. It is notable that the equation is valid purely due to the arbitrary definition of $T_{\rm ex}$, and $B_\nu(T_{\rm ex}) \neq B_\nu(T_{\rm kin})$ unless the gas is thermalized.

1.2.2.4 Optically Thick Case

Compared to the optically thin case, in which photons escape freely, the optically thick case allows the photons to *leak* or *escape* as a function of the (peak) optical depth of the line. At great optical depth, the high-density regions are driven toward LTE with $S_\nu = B_\nu(T_{\rm kin})$, and no scattering seems to function here. But photons escape from absorption at the surface of the gas. It is worthwhile to note that although the word "escape" seems to apply to an emission line, this concept should also work for an absorption line, because the concept essentially describes the deviation of the radiation field intensity $J_\nu(\tau_\nu)$ from the Planck function $B_\nu(\tau_\nu)$.

Equation 1.6 shows that for either the attenuated incident intensity I_ν or the source function S_ν that contributes to the emission, the modification by $e^{-\tau}$ or $(1-e^{-\tau})$ ends up with saturation as τ increases. Such saturation results in a flat-topped line shape. A more precise way to describe the change of line profiles as a function of the optical depth is called the *curve of growth*.

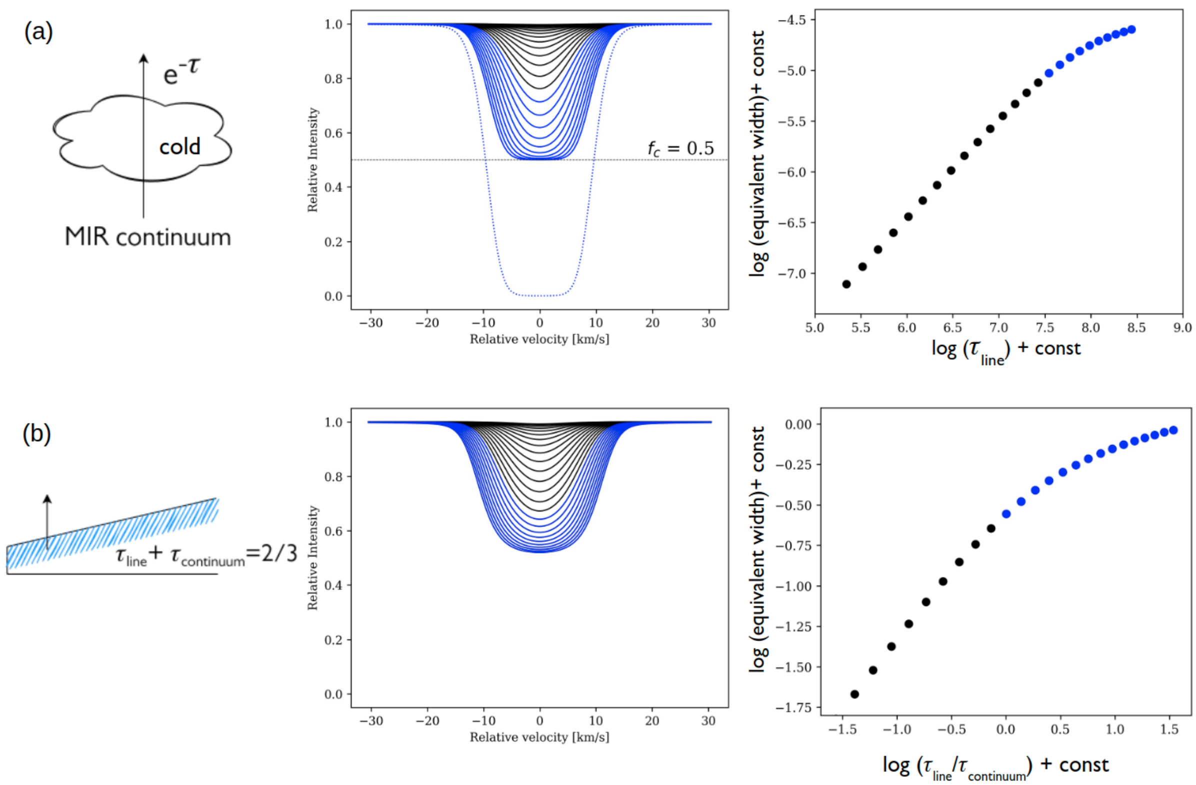

Figure 1.9: Development of absorption lines with an increasing number of atoms along the line center in (a) a slab model where a cold cloud is in front of the warmer background continuum, and the parameter f_c is the partial coverage that dilutes the relative line depth. Panels in (b) illustrate a disk scenario that is hotter in the mid-plane than on the surface. In the disk model, the opacities from both the lines and the continuum should be considered. In the middle panels, the y-axis presents the residual line flux and the x-axis is converted from the frequency space to the velocity space. According to the development of the lines, the equivalent width versus the optical depth in log-log space consists of the curve of growth which illustrates the linear growth region (black) and the logarithmic part (blue).

Take *absorption* lines as an example (see upper panels in Figure 1.9), and assume that there is no continuum opacity. In the curve-of-growth analysis, the line profile is quantified via its equivalent width W. When the line center is still optically thin, the equivalent width scales *linearly* with the number of absorbers, and the line is dominated by the Doppler core. As the optical depth grows, the Doppler core becomes saturated. Adding more absorbers hardly increases the line depth but increases the width, and leads to a slow increment of the equivalent width with $W \sim \sqrt{\log \tau_p}$. This is the *logarithmic* part of the curve of growth. Continuing to increase the number of absorbers will lead to optically thick Lorentzian wings in the end, with $W \sim \sqrt{\tau_p}$. This is the *square root* part of the curve of growth.

Returning to the “escape” word used above, the *escape probability* method is commonly seen in the analysis of *emission* lines. The escape probability β describes the chance that a newly created photon escapes the gas/cloud and removes the coupling of $\bar{J}$ to the population level in equation 1.9 by $\bar{J} = S(1-\beta)$. The computer program RADEX[3] (applied in Chapter 2) uses this method to iteratively solve the level populations and the radiation until a consistent solution is found.

Because absorption and emission are interchangeable, the escape probability is essentially related to the curve of growth (Ch 4.1.6 Tielens, 2021). For $\tau\phi(x)$ of an emission line as a function of the scaled frequency x, mathematically, β equals the wing area, $\int_{x_1}^{\infty} \phi(x)dx$, where x_1 denotes a line-edge frequency with $\tau(x_1)$ = 1. This form of β represents that photons not only escape spatially but also follow a redistribution of the frequency. Similar to the curve of growth in absorption lines, $x_1 \propto N$, $\sqrt{\log N}$, $\sqrt{N}$ as the peak optical line increases: the linear, logarithmic, and the square root parts reappear.

1.2.3 Analysis Specialized for This Thesis

Chapter 2 aims to map the distribution of molecular gas in a galactic nucleus with a set of density-sensitive tracers, to understand the relationship between gas density and star-forming processes. Two points are worthwhile emphasizing when pursuing the goal.

First, why do different molecular transitions have different sensitivity to different (volume

[3]A computer program for performing statistical equilibrium calculations: https://home.strw.leidenuniv.nl/ moldata/radex.html

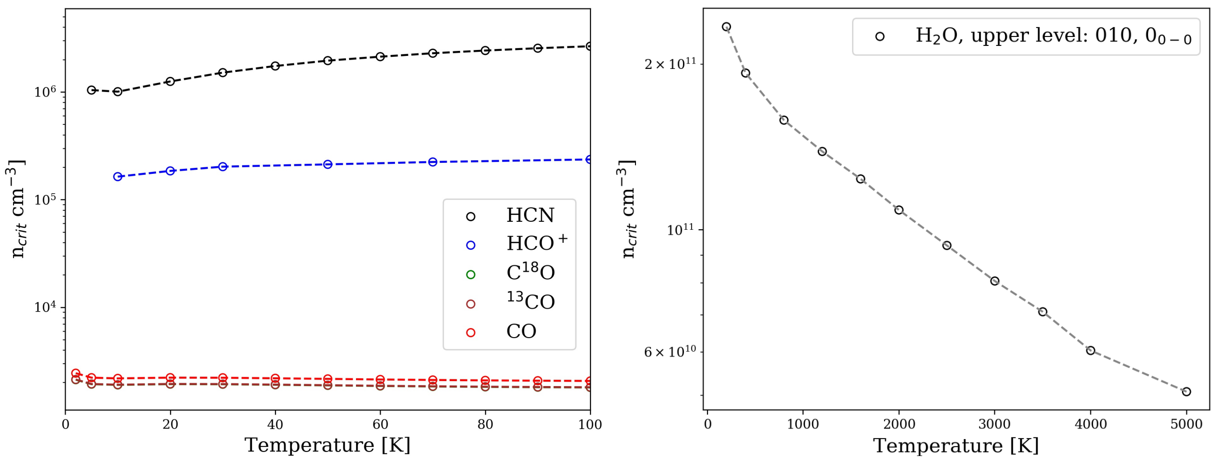

Figure 1.10: Critical densities of (left) the (1–0) transitions of a set of commonly used lines in probing the molecular gas under different temperatures and (right) water rovibrational transitions whose upper level is the ground level of the ν_2=1 state. The Einstein A coefficients and the collisional coefficient rates are adopted from LAMBDA (Leiden Atomic and Molecular Database).

or particle) densities? The *critical density* is often referred to in discussing this problem, and this concept is essentially defined based on the comparison between the time scale for collisions ($1/C_{ij}$) into a level and that for spontaneous decay ($1/A_{ij}$) of that level. As shown in Figure 1.10, different molecular transitions have different critical densities, and those with higher dipole moments (or higher oscillator strengths) tend to have larger critical densities ($A_{ij} \propto \nu^3\mu^2$; ν is the frequency and μ is the dipole moment[4]). A set of molecular transitions with different critical densities is therefore thought to serve as a set of "rulers" in probing the highly structured molecular gas with significantly varying densities.

The second point, is whether the brightness of the density-sensitive lines reflects the densities accordingly. Although it is reasonable and natural to expect that molecular transitions with different critical densities "dye" regions exclusively based on the gas density, the brightness of the lines depends not only on the volume/particle density of the region, but, more in-

[4]or $A_{ij} \propto \nu^3 f$, with the oscillator strength $f \propto |\mu|^2$.

trinsically, on the amount (the column density) and the temperature of the gas. One needs to be careful in interpreting the line brightness: does a bright dense cloud catch our eyeballs on a map of some dense gas tracers because there are many molecules, or because it is hot? Moreover, high column density may result in high opacity, which not only lowers the effective critical density, but also prevents us from knowing the actual conditions inside the clouds. This is the so-called "*radiative trapping*" effect. Therefore, one should use proper methods, as introduced in § 1.2.2, to carefully infer the physical conditions from the molecular lines.

Chapters 3 and 4 aim to use MIR rovibrational absorption lines to characterize the highly embedded, massive, protostellar hot-core phase. Rotation diagram analysis is usually the most straightforward, and therefore commonly used, tool in analyzing a set of rovibrational lines, although line-blending problems or high opacities may result in the ambiguity of the physical conditions in question. With the high spectral resolution available for investigations in this thesis, individual physical/chemical substructures with different temperatures and column densities may be decomposed. Optical depth effects are corrected by the curve-of-growth analysis. A homogeneous foreground slab model, as well as a disk model with a hotter mid-plane than surface, are considered to conduct the curve-of-growth analysis.

MIR absorption spectroscopy is a unique and specialized tool for studying the embedded hot-core phase, and is worth a few more words. Infrared rovibrational transitions in this case only probe pencil-beam regions where a bright background source can be used as a "continuum" source. Although the pencil-beam gives high spatial resolution, it does not allow for full sampling across large areas. One other advantage of the IR is that many transitions are probed simultaneously along the same sight line, greatly simplifying excitation analysis, and hence the derivation of physical conditions. Moreover, the full set of individually resolved rovibrational lines can be covered in a narrow bandwidth, and the multiple frequency settings are not required in contrast with the case for submillimeter observations. Finally, molecules without permanent dipole moments, such as C_2H_2 and CH_4, which are among the most abundant carbon-bearing molecules, can not be observed in pure rotational spectroscopy.

1.3 Telescopes

This thesis utilizes pure-rotational and rovibrational transitions to study molecular gases at different energy regimes, ranging from cold giant molecular clouds, warm foreground clouds in front of proto-stellar systems, and hot molecular gas that is possibly located in the disks surrounding the massive protostars. Telescopes used accordingly at radio (§ 1.3.1) and infrared (§ 1.3.2) wavelengths, together with instruments, are introduced in this section.

1.3.1 Argus/GBT at 3 mm

Argus, at the 100 m Robert C. Byrd Green Bank Radio Telescope (GBT, see Figure 1.11), is a 16-pixel spectroscopic focal plane array that enables fast imaging (Figure 1.12). Historically, spectroscopic imaging has generally been implemented either over small areas of the sky at high angular resolution with interferometers, or over large areas at moderate to low angular resolution with single dishes. *Argus* satisfies the requirements of (1) measuring low surface brightness emission over a large scale on the sky with (2) a high spatial resolution, which is $\sim 7''$ at 100 GHz for the 100 m GBT (thanks to λ/D!).

Figure 1.11: The 100 m Robert C. Byrd Green Bank Radio Telescope (GBT) has a collecting area of 9,300 m^2 which focuses the radio waves falling on it onto sensitive receivers at the top of the boom attached to the side. Credits: NRAO/AUI.

The Rayleigh-Jeans sensitivity for a spectral line is:

$$\Delta T_{\rm min} \propto \frac{T_{\rm sys}}{\sqrt{\Delta\nu\tau}}, \tag{1.13}$$

where $T_{\rm sys}$ is the system noise temperature of a receiver (the atmosphere and telescope losses also matter), $\Delta\nu$ is the spectral resolution, and τ is the integration time for the observation. *Argus* uses recent advancements in Monolithic Millimeter-wave Integrated Circuit (MMIC) technology to build such a large-format focal plane array with low system temperatures ($<$ 53 K per pixel, Sieth et al., 2014). The large numbers of pixel of *Argus* increases the effective integration time. Its large (16) number of pixels, $n_{\rm pix}$, and low system temperatures allow for rapid

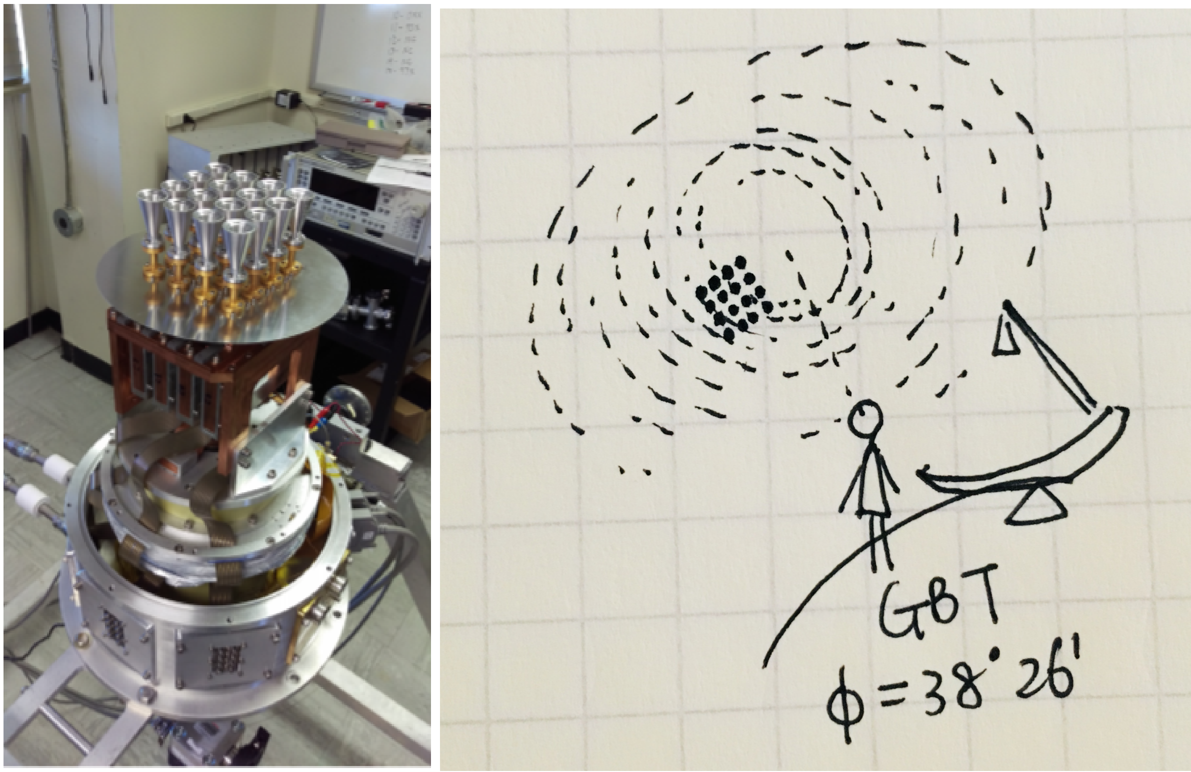

Figure 1.12: *Left*: The 16-pixel spectroscopic focal plane array, *Argus*, to be deployed on the GBT. *Right*: Footprint of the 16 pixels of *Argus* on the sky.

astronomical imaging.

The distance in between each neighboring *Argus* beam projected on the sky is 30.4″. *Argus* uses the OTF (On-The-Fly) mapping strategy (Haslam et al., 1970; Mangum et al., 2007) to produce a complete image. The telescope is driven smoothly and rapidly across a region of the sky. At the same time, spectroscopic data and antenna position information are recorded continuously. The entire field is covered quickly. This process reduces the overhead significantly, and minimizes changes in the atmosphere and the system.

Because the GBT is an altitude-azimuth-mounted telescope, without an optical de-rotator, the multi-beam pattern of the *Argus* on the sky rotates while data are collected. The change of the parallactic angle in a typical 30–45 minute observation session can be large enough to cause noticeable distortion, and even gaps, in the final map. It is therefore important to consider the coordination of the target and the observation time when designing the observational plan.

The deployment of *Argus* expands the operation range of the GBT to the 3 mm band. Compared to observations at lower frequencies, a lower surface RMS level is required to guarantee adequate telescope efficiency (Ruze, 1966). GBT can realize a surface RMS of $\sim$200 μm in good weather, with a semi-active surface that could be used to remove gravitational and thermal distortions in real time. Together with the 100 m aperture, the $\sim 10''$ resolution of GBT overlaps with the angular scales from interferometric arrays such as CARMA, PdBI, and ALMA, which have superior angular resolution but cannot resolve extended emission. The GBT+*Argus* combination is ideal for resolving cold cores within local star-forming regions, tracing the dynamics of molecular filaments, and for mapping giant molecular clouds in nearby galaxies.

1.3.2 iSHELL/IRTF and EXES/SOFIA at MIR

Strong absorption of greenhouse gases in the Earth's atmosphere, including water vapor H_2O, CO_2, O_3, CH_4, and N_2O, covers a substantial part of the spectrum starting roughly at 5 μm (Figure 1.13). For ground-based telescopes, rovibrational transitions that fall in the NIR to MIR are observable in the L (3.5 μm), M (4.7 μm), and N (8–13 μm) bands. In this thesis, the rovibrational transitions of CO and its isotopologues were observed in the M band by iSHELL at the ground NASA Infrared Telescope Facility (NASA-IRTF). iSHELL is a cross-dispersed echelle spectrograph and imager working from 1.06–5.3 μm (Rayner et al., 2022), and it uses a silicon immersion grating to achieve high spectral resolution (up to about R=80,000) in a relatively compact instrument.

An airborne observatory is needed to get to high altitudes higher so no water stops other

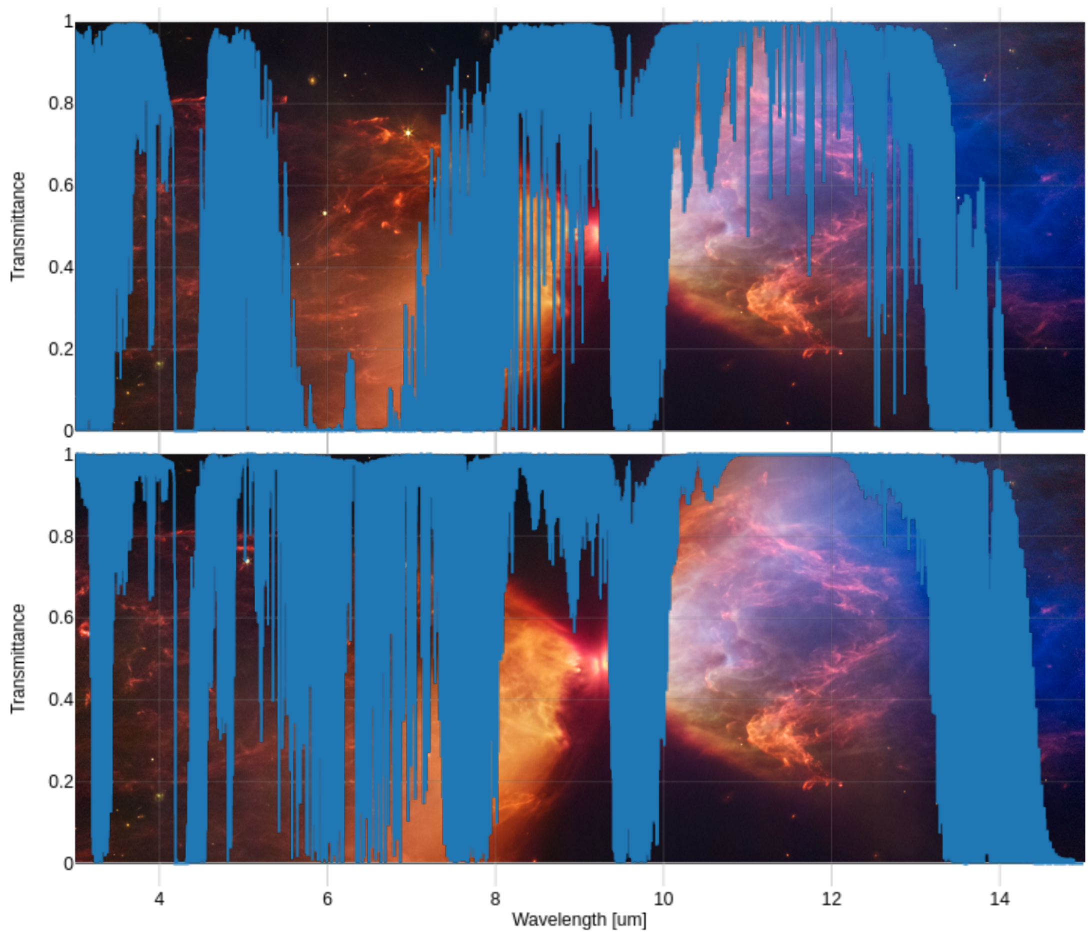

Figure 1.13: Earth's atmospheric transmission from 3–15 μm at the altitude of the IRTF on Maunakea (upper panel) and SOFIA (lower panel) on top of a *JWST* NIRCAM image of L1527 and Protostar. The altitudes are 4,200 m and 14,000 m and the water vapors are 1.5 mm and 1.2 μm, respectively. The transmission is calculated by the Planetary Spectrum Generator (PSG, Villanueva et al., 2018). Credits of the *JWST* image: NASA, ESA, CSA, and STScI.

MIR regimes. SOFIA (Stratospheric Observatory for Infrared Astronomy, Young et al., 2012) is a 2.5 m telescope deployed on a modified Boeing 747SP widebody aircraft. The aircraft was modified to include a large door that can be opened in the flight to allow the telescope to view to the sky (Figure 1.14). During its commission, SOFIA flies above 41,000 ft to rise above almost all of the water vapor in the Earth's atmosphere.

The Echelon-cross-Echelle Spectrograph (EXES, Richter et al., 2018) on the SOFIA operates in the 4.5–28.3 μm wavelength region. In this thesis, the high spectral resolution ($R \approx$ 50,000-

Figure 1.14: SOFIA, a modified Boeing 747SP aircraft, soars over the snow-covered Sierra Nevada mountains with its telescope door open during a test flight. Credits: NASA/Jim Ross.

−100,000) configuration was used to provide a velocity resolution of a few km s^{-1} to decompose different kinetic components in the massive proto-stellar systems. In EXES, high resolution is provided by an echelon grating and an echelle grating to cross-disperse the spectrum (Richter et al., 2018). Generally, the resolution will be higher at shorter wavelengths.

In EXES science observation, the EXES temperature-controlled blackbody source is observed to construct a flat field. This process corrects response variations and provides flux calibration. Wavelength calibration with EXES is performed by applying the grating equation to atmospheric lines observed in the source spectra. The telescope 'nods' to a new position to remove the sky background. For all observations conducted under the high-resolution mode used in this thesis, a nod-off-slit mode is used. The telescope is moved such that the object is not on the slit.

1.4 Thesis Chapters

This thesis uses high spatial/spectral resolution molecular spectroscopy, which benefits from recent advances in instrumentation, to study the physical properties of molecular gas over different spatial and energy scales that are related to star-formation processes. This thesis consists of studies of (1) millimeter spectroscopic imaging of pure rotational transitions of CO and its isotopologues, HCN, and HCO^+ from cold molecular clouds with a resolution of hundreds of parsec in an external galaxy at 3 Mpc, and (2) high spectral resolution ($R \sim 50,000$) mid-IR spectroscopy of rovibrational transitions from hot cores with sizes of several hundred to a 1000 AUs that surround the massive proto-binary system at 2.2 kpc.

Chapter 2 presents GBT's first ^{12}CO (1-0) map of an external galaxy, IC 342, taken at 3 mm. The sky coverage of the multi-beam *Argus* on a large area was investigated before the observation was proposed. Pointing errors due to strong wind were accounted for during the construction of the map. Details of this process are introduced in Appendix A. Other density tracers, such as HCN and HCO^+, were also mapped under the Dense Extragalactic GBT+Argus Survey (DEGAS). The small beam of *Argus* provides a unique opportunity to study the breakdown of the HCN-IR correlation at high spatial resolution. The spatially resolved HCN-to-HCO^+ intensity ratio was surprisingly a constant value of 1.2$\pm$0.2 across the whole 1 kpc galactic bar, suggesting that HCN and HCO^+ are thermalized with intermediate optical depth. The HCN-to-

HCO^+ intensity ratio in IC 342 is concluded to be more sensitive to the abundance ratio of the two molecules, rather than to the particle density.

Chapter 3 uses high spectral resolution MIR absorption spectroscopy of CO and its isotopologues by iSHELL/IRTF at 4.7 μm to study the massive proto-stellar system W3 IRS 5. Different physical components inside this deeply embedded system were decomposed providing velocity information. Absorption spectroscopy also provides pencil-beam spatial resolution that is limited by the size of the background MIR continuum emitter. With the narrow slit width of iSHELL/IRTF, both components in the proto-binary are spatially resolved. Physical structures are identified, such as the cold envelope, the foreground high-speed "bullets," and hot gas clumps that are likely located at the disks. Rotation diagram analysis and curve-of-growth analysis were used to understand the rovibrational transitions and the structure of source. All physical substructures were characterized by the temperatures and column densities via the cross-validation of multiple sets of rovibrational lines of different molecular species.

Chapter 4 studies H_2O rovibrational absorption spectra toward W3 IRS 5 from 5 to 8 μm with the EXES/SOFIA. Although EXES has a comparable high spectral resolution to iSHELL, the beam of SOFIA does not spatially resolve the two protostars. We thus take advantage of the kinetic structures understood via CO studies to elucidate the H_2O components. As different physical substructures are established via the distance to the protostars, temperature, density, and molecular abundance, a chemical substructure is also revealed. Interpretations of the inventory of elements may once again call upon the "oxygen and carbon crisis".

Chapter 2: Argus/GBT Observations of Molecular Gas in the Inner Regions of IC 342

2.1 Chapter preface

Chapter 2 is presented with minimal changes and is going to be submitted to the Astrophysical Journal (ApJ) under the title of this chapter. The authors are Jialu Li, Andrew I. Harris, Erik Rosolowsky, Amanda A. Kepley, David Frayer, Alberto D. Bolatto, Adam K. Leroy, Jennifer Donovan Meyer, Sarah Church, Joshua Ott Gundersen, Kieran Cleary, and other DEGAS team members.

2.2 Introduction

Understanding the distribution, physical conditions, and dynamics of molecular gas is essential to understanding star formation. Studies of individual regions in our galaxy have shown that stars form in dense molecular clouds (e.g., see Heiderman et al., 2010; Lada & Lada, 2003; Lada et al., 2010), whereas resolved observations of external galaxies provide global information related to star formation efficiencies within nuclei, spiral arms, and other regions (e.g., see Bigiel et al., 2008; Elmegreen, 2002; Kennicutt, 1998; Silk, 1997). In all cases, probing the complexity and scale of star formation regions requires a large spatial dynamic range to follow core formation and collapse to circumstellar scales.

Rotational transitions of molecules such as ^{12}CO, ^{13}CO, C^{18}O, HCN, and HCO^{+}, are common tools for probing cold molecular clouds in external galaxies because of their relatively high abundance and the excitation energies from a few to several tens of K. Specifically, the J=1–0 lines of ^{12}CO, ^{13}CO, and C^{18}O trace gas with densities above $\sim 10^2$–10^3 cm^{-2}. Although this density range captures the bulk of the molecular gas, it does not capture the denser gas associated with star formation. HCN and HCO^{+} have higher dipole moments (2.98 and 3.92 D) than do for ^{12}CO(0.11 D); the ground state transitions of the former species trace denser gas ($\sim 10^4$–10^5 cm^{-2}) that are more directly correlated with star formation (Gao & Solomon, 2004a,b). Because of the different critical densities, this set of molecular lines can establish the quantitative link between gas density and star formation across a variety of environments (e.g. the PHANGS/CO survey, Leroy et al. 2021; the EMPIRE/HCN survey, Jiménez-Donaire et al. 2019; the DEGAS survey, Kepley et al., in prep).

Single transitions cannot be easily used to quantify the exact gas density or temperature. The interpretation of the line intensity involves a high degree of degeneracy, including the observational spatial resolution, the optical depth effects, the actual excitation condition, etc. As spatially resolved observations become more accessible, multi-transition ratios, on the other hand, may further break such a degeneracy by comparing the observations and theoretical predictions within specific parameter space due to the different excitation properties among different species (e.g., Leroy et al., 2017; Meijerink et al., 2007; Viti, 2017).

Among the transition ratios of different species, the intensity ratio of HCN(1–0)-to-HCO^{+}(1–0), here denoted as $\mathcal{R} \equiv I(\mathrm{HCN})/I(\mathrm{HCO}^+)$, is of specific interest in this Chapter. The critical density of HCO^{+}(1–0) is lower by 5–20 times than that of HCN(1–0) at temperatures of 20–100

K, because of their different collisional de-excitation rate coefficients. The intensity ratio $\mathcal{R}$ is a potentially valuable probe of the physical conditions of molecular gases in external galaxies, because the correlation between the infrared luminosity L_{IR} and $\mathcal{R}$ was established by single-beam observations (Graciá-Carpio et al., 2006). This correlation is further expected to suggest the importance of AGN in galaxies with higher infrared luminosities (Imanishi et al., 2006, 2007), although recent studies with the 30-m IRAM survey (Privon et al., 2015, 2020) conclude that globally enhanced HCN emission relative to HCO^+ is not correlated with the presence of an AGN.

In this Chapter we report observations of the ground-state transitions of ^{12}CO, ^{13}CO, $C^{18}O$, HCN, and HCO^+ from IC 342 (distance of 3.3 Mpc, Saha et al., 2002). These are part of the DEGAS (Extragalactic GBT[1]+ARGUS Gas Density Survey; Kepley et al., in prep). DEGAS uses the Argus focal plane array spectroscopic imager (Sieth et al., 2014) and the spatial resolution (6–8″) provided by the 100-m aperture of the GBT to conduct efficient multi-line spectral mapping from 86–115 GHz over large areas in 17 external galaxies (Kepley et al., in prep). We summarize our observations and data reduction in Section 2.3. In Section 2.4, we describe the distribution of molecular material across the nucleus and inner spiral arms in ^{12}CO, and along the nuclear bar of IC 342 in all five molecular species. In Section 2.5, we discuss the implication of the constant HCN to HCO^+ intensity ratio observed across the entire 1 kpc bar of IC 342, and specifically analyze the breakdown of the L_{IR}–L_{HCN} correlation of IC 342 at high spatial resolution. Section 2.6 is a summary overview, and in the Appendix, we provide some detailed information connected with our analysis.

[1]The Green Bank Observatory is a facility of the National Science Foundation operated under cooperative agreement by Associated Universities, Inc.

Table 2.1: Summary of Observations

	^{12}CO(1–0)	^{13}CO(1–0)/C^{18}O(1–0)	HCN(1–0)/HCO^{+}(1–0)
Observation date	17-Sep-29	17-Oct-18/19, 17-Nov-21	17-Oct-25/27, 17-Nov-14
Observation ID	GBT17B-412-01/02	GBT17B-151-01/08	GBT17B-151-02/03/05
Mapping area	$3.5' \times 5'$	$2.5' \times 2.5'$	$2.5' \times 2.5'$
On-source integration (hrs)	6.17	1.33	11.52
Total integration (hrs)	10.08	2.38	20.67
Frequency Setup (GHz)	115.271	109.982	88.903
Beam Size ($''$)	6.33	6.63	8.21
Beam Size (pc beam^{-1})	101	106	131
Velocity resolution (km s^{-1})	3.8	4.0	4.9
Main beam efficiency	28.3%	44.5%	52.5%
Scan Rate ($''$ s^{-1})	1.71	1.67	1.67

2.3 Observations and Data Reduction

We used the Argus 16-pixel spectroscopic focal plane array on the 100-m diameter Robert C. Byrd Telescope of the Green Bank Observatory to conduct observations of IC 342 from 2017 September to 2017 November. A summary of observational parameters is given in Table 2.1 for the five molecular species we imaged. The on-source time for all species in total was 19 h of about 33 h including overheads (see Table 2.1). The telescope slewed across a region of the sky in a raster pattern to make OTF (On-The-Fly) maps (Haslam et al., 1970; Mangum et al., 2007), with the data and the antenna position recorded every 0.5 s. Pointing and focus were calibrated every 30–40 min with the source 0359+5057. The backend, VEGAS, was configured in mode 1 with a single spectral window with a bandwidth of 1500 MHz (1250 MHz effective) and a spectral resolution of 1465 kHz. ^{13}CO(1–0) and C^{18}O(1–0) were observed simultaneously in a spectral window centered at 109.99176 GHz, and HCN(1–0) and HCO^{+}(1–0) were observed simultaneously in a spectral window centered at 88.91123 GHz. Observations were mostly conducted under windless conditions ($v_{\rm rms} < 1$ m s^{-1}). For ^{12}CO, however, for half of the observing time, $v_{\rm rms}$ was greater than $5\,{\rm m\,s^{-1}}$, which caused pointing deviations as high as ~ 1 beam ($\sim 6''$ at 115 GHz). We established pointing corrections by cross-correlating each 40 min individual observing session with ^{12}CO maps observed under low wind speed.

We calibrated and post-processed data with the python packages `gbtpipe`[2] and `degas`[3]. Initially, Argus data are on T_a^* scale after chopper-wheel calibration (Kutner, & Ulich, 1981). We obtained atmospheric temperature and opacity information from the GBT weather database and then corrected for atmospheric attenuation, resistive losses, rearward spillover, and scattering. Our final brightness temperature scales are in $T_{\rm MB}$, to better represent the intensity in the main beam. For that, we used conversion factors between T_a^* and $T_{\rm MB}$ of $\eta_{\rm MB}$ of 28.3% for ^{12}CO, 44.5% for ^{13}CO and C^{18}O, and 52.5% for HCN and HCO$^+$ (see GBT Memo #302, Frayer et al., 2019). Next, problematic spectra were automatically detected and dropped. We then removed low-order polynomial baselines and interpolated to a regular grid in data cubes. We used the ^{12}CO map as a spatial and velocity space mask to constrain the emission regions for the other molecules. We integrated data cubes from -100 to 150 ${\rm km\,s^{-1}}$ to make moment maps using functions from the `SpectralCube` package.

2.4 Results

2.4.1 Spatial Distribution of the Molecular Gas

We present the moment 0 (integrated intensity) and the moment 1 (intensity-weighted mean velocity) maps of ^{12}CO(1–0) from the inner disk region of IC 342 over a $3.5'\times5'$ region in Figure 2.1. The ^{12}CO moment 0 is overlaid in contours on the *Herschel* PACS 70 μm map for a

[2] Publicly available at https://github.com/GBTSpectroscopy/gbtpipe
[3] Publicly available at https://github.com/GBTSpectroscopy/degas

comparison with the distribution of dust heated by young stars. We plot the integrated intensity images of the $\sim 1.4'$ (1.3 kpc) long bar region in Figure 2.2 for all five molecular species. For a better signal-to-noise ratio, all images other than ^{12}CO are spatially smoothed to an output resolution 1.3 times lower than the input resolution, following the procedure of the DEGAS survey (Kepley et al., in prep).

We find spatial distributions of molecular gas that closely match past observations (Downes et al., 1992; Hirota et al., 2010; Kuno et al., 2007; Meier et al., 2000; Meier & Turner, 2001; Turner & Hurt, 1992). The large scale ^{12}CO(1–0) image reveals a morphology with two asymmetrical arms extending from the ends of a nuclear bar, oriented roughly from north to south. ^{12}CO emission peaks at $\sim 0.2'$ (191 pc) north of the nuclear center, whereas the peak brightness and the integrated intensities of the other four species all peak at the nuclear center and decrease towards the bar ends (Figures 2.2 and 2.3). Among these species, the morphology of ^{13}CO most resembles that of ^{12}CO, with a rather elongated structure and two tentacle-like substructures to the north. C^{18}O, HCN, and HCO^{+} have more concentrated structures. The morphology of HCN and HCO^{+} emission is essentially identical (see Figure 2.2).

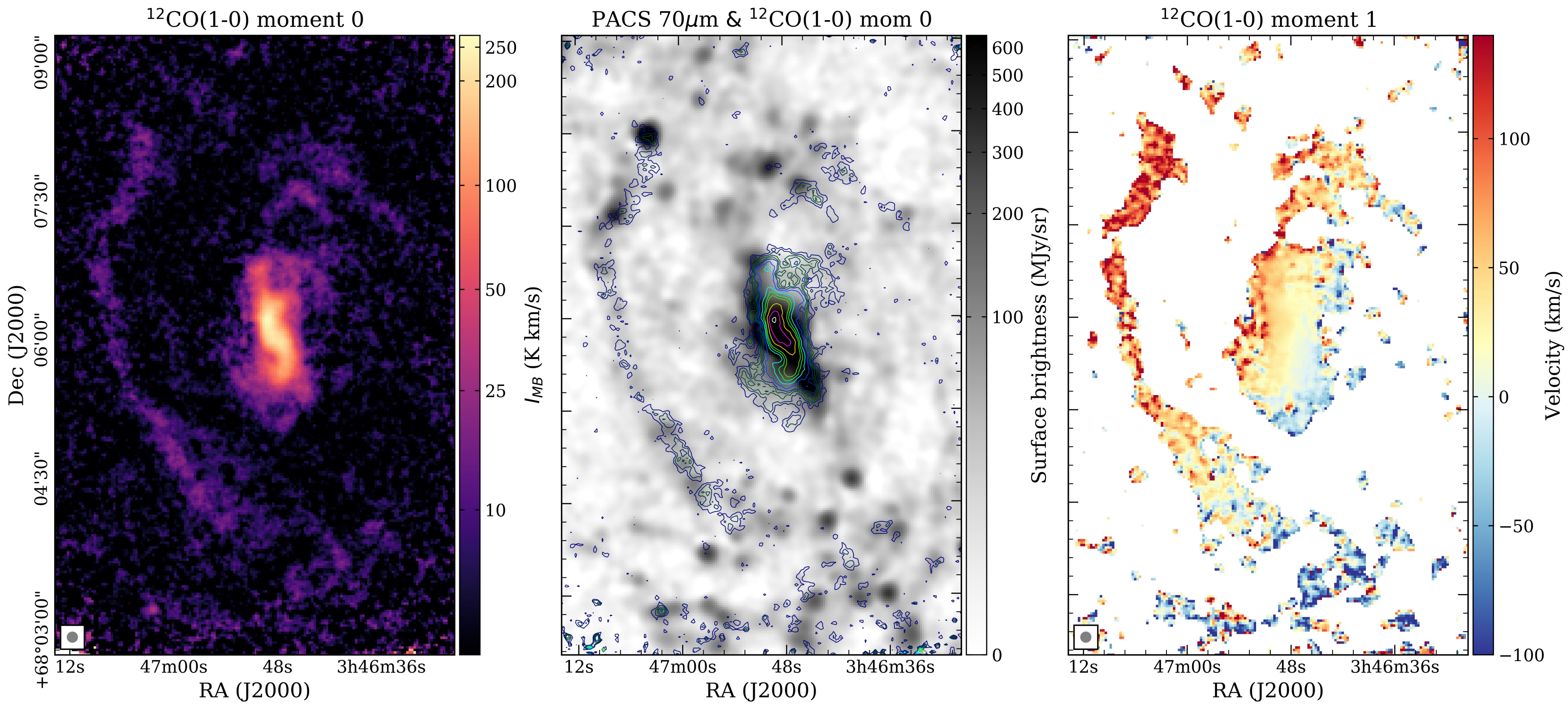

Figure 2.1: The left panel shows the GBT/Argus ^{12}CO (1−0) moment 0 image with an arcsinh intensity stretch. The 6.33″ beam is in the box at the lower left of the plot. The 1σ level of the integrated intensity is 2.8 K km s^{-1}. The middle panel shows the ^{12}CO (1−0) moment 0 contours overlaid on the *Herschel* PACS 70 μm image (Kennicutt et al., 2011), indicating correspondence between the molecular gas distribution and the star formation locations. The contour levels of ^{12}CO are 10, 15, 20, 25, 30, 40, 60, 80, 100, 150, 200, 250 K km s^{-1}. The right panel shows the temperature-weighted mean velocity as the ^{12}CO (1−0) moment 1 image.

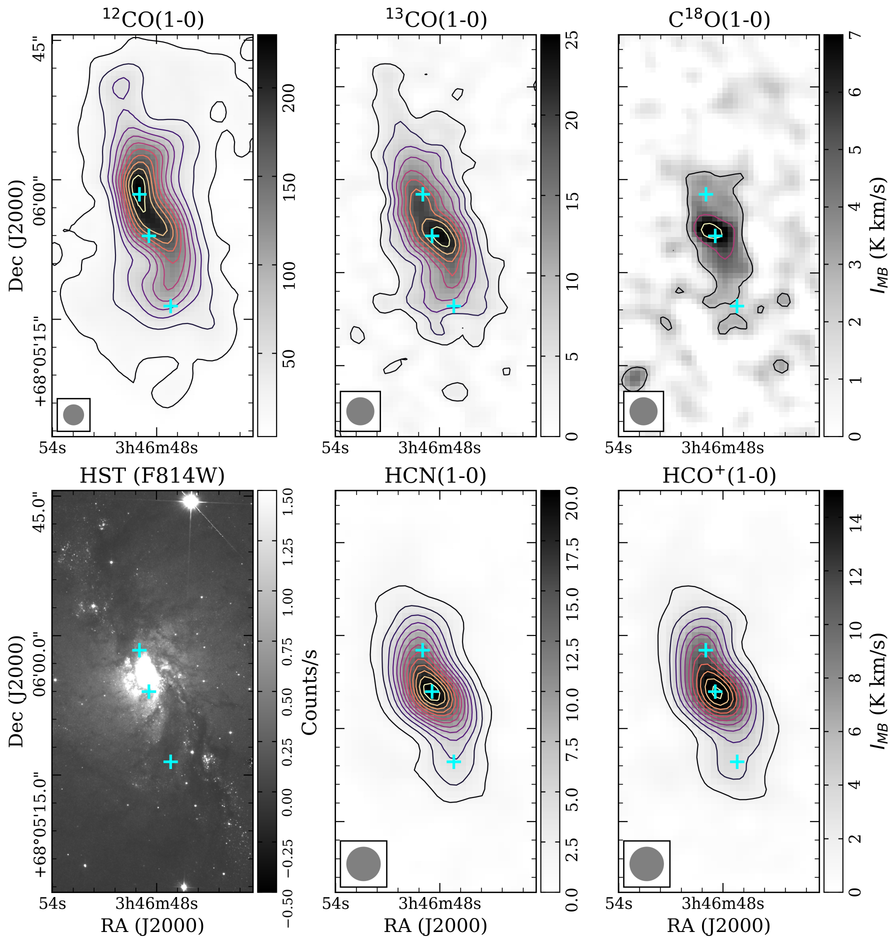

Figure 2.2: *HST* (F814W) map (*lower left*) and the integrated intensity maps of ^{12}CO, ^{13}CO, C^{18}O, HCN, HCO$^+$(1–0) in the central bar region in beam sizes of 8.2″, 8.6″, 8.6″, 10.7″, and 10.7″. For the panels in order of top left to bottom right, contour levels start from 10σ, 1σ, 1σ, 3σ, 3σ and are in steps of 20σ, 1σ, 1σ, 3σ, 3σ. The correspondent 1σ levels are 1, 2.5, 2.5, 0.5, and 0.5 K km s^{-1} for all the five species. The beam resolutions are increased by 1.3 times for consistency with the DEGAS survey for better SNRs. Spectra from the three cyan crosses within a 10.7″ beam are plotted in Figure 2.3 for a comparison of the line properties.

We compare the integrated intensities measured by GBT/Argus to those observed by other single-dish observations. For ^{12}CO, the peak values of the integrated intensities on the image observed by the GBT/Argus and the 45-m telescope (15″, Kuno et al., 2007) are 257 and 180 K km s^{-1}. For ^{13}CO, the values are 24 and 22 K km s^{-1} (20.4″, Hirota et al., 2010). For HCN and HCO$^+$, we compare the Argus data with the 30-m telescope (∼26″, Nguyen-Q-Rieu et al., 1992). The values for HCN are 21 K km s^{-1} and 19.1 K km s^{-1}, separately. The values for HCO$^+$

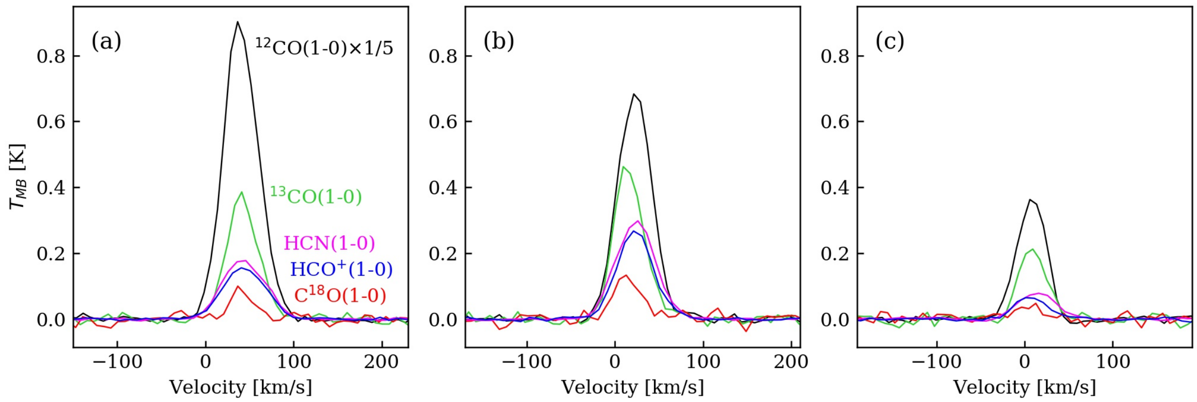

Figure 2.3: Spectra of ^{12}CO(1−0) (scaled by 1/5), ^{13}CO(1−0), C^{18}O(1−0), HCN(1−0), and HCO^{+}(1−0) from the three 10.7″ beams whose centers are marked as cyan crosses in Figure 2.2 (from top to bottom), representing that the line as well as the velocity-integrated intensity of all species other than ^{12}CO peak at the nuclear center and decrease towards the bar ends. Shifts of the centers of the emission lines indicate the kinematic rotation of the molecular bar.

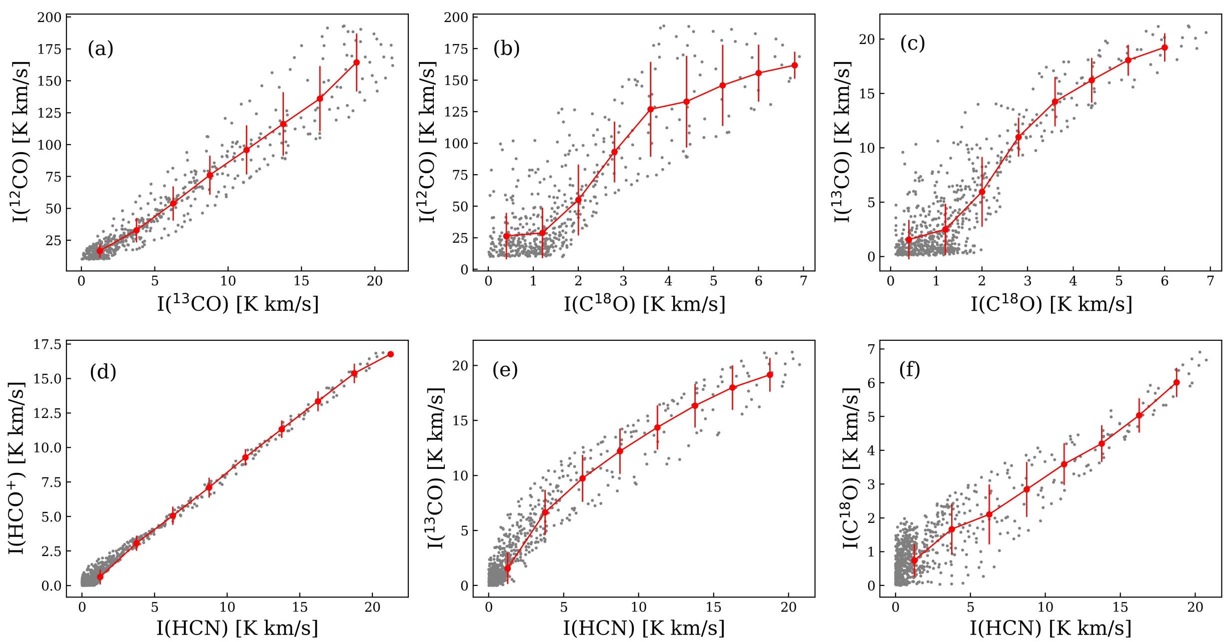

Figure 2.4: A comparison of the integrated intensities of (a) ^{12}CO/^{13}CO, (b) ^{12}CO/C^{18}O, (c) ^{13}CO/C^{18}O, (d) HCO^{+}/HCN, (e) ^{13}CO/HCN, and (f) C^{18}O/HCN from individual image pixels from a $0.9' \times 1.7'$ region that covers the galactic bar. Maps of all the five molecules are convolved to the same resolution of 10.7″.

are 17 and 9.8 K km s^{-1}. Although the peak HCO^{+} integrated intensity measured by Argus is about twice that measured by the 30-m telescope, we stress that the results of Argus have good coherence and an excellent relative calibration. With Argus, HCN and HCO^+ were observed simultaneously, reduced with the same procedure, and compared at the same spatial resolution.

To compare the distribution of molecular gas to dust-reprocessed UV radiation from young stars, we overlaid the contours of the integrated intensity of CO on a *Herschel* 70 μm image (Kennicutt et al., 2011) in Figure 2.1. Overall, within the inner disk region of IC 342, the brightest ^{12}CO emission follows the infrared emission. In the southern and the northern arms, however, the peaks of the ^{12}CO intensity do not coincide with peaks of the infrared emission. A similar spatial offset is also shown in the nuclear bar region, as most ^{12}CO emission is located at the concave side of the "S-shaped" infrared bar.

The spatial offset seen between ^{12}CO (and/or ^{13}CO) and 70 μm emission in the bar region is consistent with the spatial offset seen between ^{13}CO and Hα emission (5–10$''$, Turner & Hurt, 1992). Whereas Hα emission traces young stars, this line also suffers from extinction. The consistency between IR and Hα emission, therefore, implies that young stars emitting in Hα are not entirely hidden in the dust. HST archival images (PID 5446, 6367) also confirm that in the bar region, young stars emit through mixed filamentary dusty structures (see Figure 2.2). Therefore, the angular offset between the ^{12}CO/^{13}CO emission region and the star formation sites appears to be due to physical separation, rather than to variable dust extinction.

2.4.2 Line Intensity Ratios of Different Molecular Species in the Nuclear Bar

We compare the intensities of the lines of the five molecular species to understand their ability to probe different physical conditions in the nuclear bar region of IC 342. To quantify the differences shown in molecular emission distributions, we convolved all images to 10.7$''$ (the resolution of the HCN and HCO^+ maps; see § 2.4.1) resolution, and plotted the pixel-by-pixel integrated intensities between different species in a scatter plot (Figure 2.4).

The interpretation of the physical conditions of the line ratios is considered from two aspects, the optical depth, and the excitation condition. As all five species have similar line widths (see Figure 2.3), the integrated intensity ratio is mainly determined by the peak temperature of the line spectra, for which

$$T_R = J(T_{\text{ex}}) \left(1 - e^{-\tau}\right) f_c, \tag{2.1}$$

where T_{ex} is the excitation temperature, $J(T_{\text{ex}})$ is the Rayleigh-Jeans-corrected excitation temperature, τ is the line optical depth, and f_c is the filling factor. When there is no partial coverage ($f_c = 1$), $J(T_{\text{ex}})$ approaches T_{ex} if the lines are fully thermally excited, i.e., the volume density is higher than n_{crit} and the J=1–0 transition is collisionally de-excited. If both lines are thermalized, the line intensity ratio equals the ratio of $(1 - e^{-\tau})$. Specifically, if the lines are optically thin, we can interpret the line intensity ratio as the abundance ratio. Otherwise, if the lines are optically thick, the line intensity ratio would be closer to the ratio of T_{ex}.

^{12}CO vs. ^{13}CO: Figure 2.4a shows that $I(^{12}\text{CO})$ and $I(^{13}\text{CO})$ have a linear correlation. $I(^{12}\text{CO})/I(^{13}\text{CO})$ = 10.4 $\pm$ 2.2, distinct from the ratio of 4 to 12 measured at $\sim 4.5''$ resolution by the Owens Valley Radio Observatory Millimeter Interferometer (Meier & Turner, 2001). This result suggests that the single-dish and interferometer are capturing emission on different scales; our maps trace the extended molecular gas rather than the smaller-scale molecular features emphasized by an interferometer. This ratio indicates that both lines have intermediate optical depths, because the ratio is larger than one and is smaller than a typical abundance ratio in the Galactic center (24$\pm$7, Halfen et al., 2017).

^{12}**CO,** ^{13}**CO vs. C^{18}O:** Intensities I(^{12}CO) and/or I(^{13}CO) begin to saturate at high I(C^{18}O) (Figure 2.4b and 2.4c). I(^{12}CO)/I(C^{18}O) and I(^{13}CO)/I(C^{18}O) range from 26 to 42 and from 2.5 to 4, respectively. I(^{13}CO)/I(C^{18}O) is smaller than a typical Galactic center value of 10 (Dahmen et al., 1998). This result suggests that either there is a small filling factor of C^{18}O to ^{13}CO, or that ^{13}CO has an intermediate optical depth (see equation 2.1). If we assume that C^{18}O is optically thin due to its low abundance, we may derive H_2 column densities directly from I(C^{18}O) following equation 2 in Meier & Turner (2001). For $T_{\rm ex}$ between 10–30 K, we derive $N(\mathrm{H_2}) =$ 1.2$\sim$3.1$\times$10^{22} cm^{-2}. We can constrain the column density that corresponds to the measured $I_{^{13}\mathrm{CO}}/I_{\mathrm{C}^{18}\mathrm{O}}$ better by using LVG models, but the results are comparable.

HCN vs. HCO^{+}: I(HCN) and I(HCO^{+}) have a tighter relation, yielding a line intensity ratio $\mathcal{R}$, which is defined as I(HCN)/I(HCO^{+}), of 1.2 ± 0.1 (Figure 2.4d). The ratio, which is larger than one, also suggests that both lines likely have intermediate optical depths. The small scatter applies across the entire 1 kpc bar region. Because the interstellar medium, and particularly the interstellar medium of a bar region, is complex and fractal, gas is likely to exist in a variety of states. Therefore, such a constancy of $\mathcal{R}$ indicates that $\mathcal{R}$ in the bar region of IC 342 is insensitive to locally varying physical conditions. We emphasize that the HCN(1–0) and HCO^{+}(1–0) lines cannot be subthermally excited at the same time, because emissions from subthermal excitation conditions are easily influenced by the varying environment across the entire nuclear bar. We discuss the certain set of environmental conditions that the constant $\mathcal{R}$ constrains further in Sec. 2.5.1.

^{13}**CO and C^{18}O, vs. HCN and HCO^{+}:** We present I(^{13}CO)-I(HCN) and I(C^{18}O)I(HCN) correlations in Figure 2.4e and 2.4f. Only HCN emission is included in the comparison, because I(HCO^{+}) has a tight correlation with I(HCN) and nearly identical correlations to the intensities of ^{13}CO and C^{18}O. As Figure 2.4e and 2.4f show, although I(^{13}CO) saturates at high I(HCN), I(C^{18}O) and I(HCN) have a linear correlation. We conclude that the saturation of I(^{13}CO) in high I(HCN) is due to the optical depth effect on ^{13}CO. As we have shown above, ^{13}CO has an intermediate optical depth and traces a morphology similar to that of ^{12}CO. Both ^{12}CO and ^{13}CO suffer from radiative trapping, and are more sensitive to the surface layer ($\tau \sim 1$) of the molecular gas. As a comparison, C^{18}O, HCN, and HCO^{+} trace the true distribution of the molecular gas, rather than the surface. C^{18}O constrains the column density of the dense molecular gas better than HCN and HCO^{+}, because the C^{18}O emission is optically thin.

2.5 Discussion

2.5.1 I(HCN)/I(HCO^{+}) As a Relative Abundance Tracer

As are summarized in § 2.4.2, our observations have revealed a nearly constant intensity ratio $\mathcal{R}$ of 1.2±0.1 across the ~1 kpc nuclear bar of IC 342 of a spatial resolution of 8″ (100 pc). We investigate three questions in this section to further understand the constraints that $\mathcal{R}$ may have over the physical conditions and discuss the inherent degeneracy. First, what is the relation between the parameter space of the physical conditions and a specific value $\mathcal{R}$ (specifically, $\mathcal{R}$ of 1.2 in IC 342, see § 2.5.1.1)? Second, is a permitted parameter space also physically realistic? Here we search for a parameter space that is "forgiving" to modest changes of physical conditions over a large region (§ 2.5.1.2). Third, how do we reconcile conclusions from the two questions above with the $\mathcal{R}$-L_{IR} relation seen in other galaxies, particularly as it relates to AGN versus starburst (§ 2.5.1.3), when the constant $\mathcal{R}$ over a 1 kpc scale in IC 342 provides constraints from a new perspective? Although $\mathcal{R}$ is ~1.2 in IC342, this value ranges from 0.8 to 2 in other galaxies

(Krips et al., 2010). We discuss each of the questions in subsections below, and conclude that $\mathcal{R}$ is a good relative abundance tracer of HCN and HCO^+in IC342 and that the similar trends seen in the ratios of HCN/HCO^+ of other galaxies suggest that these ratios may also be tracking abundance patterns there.

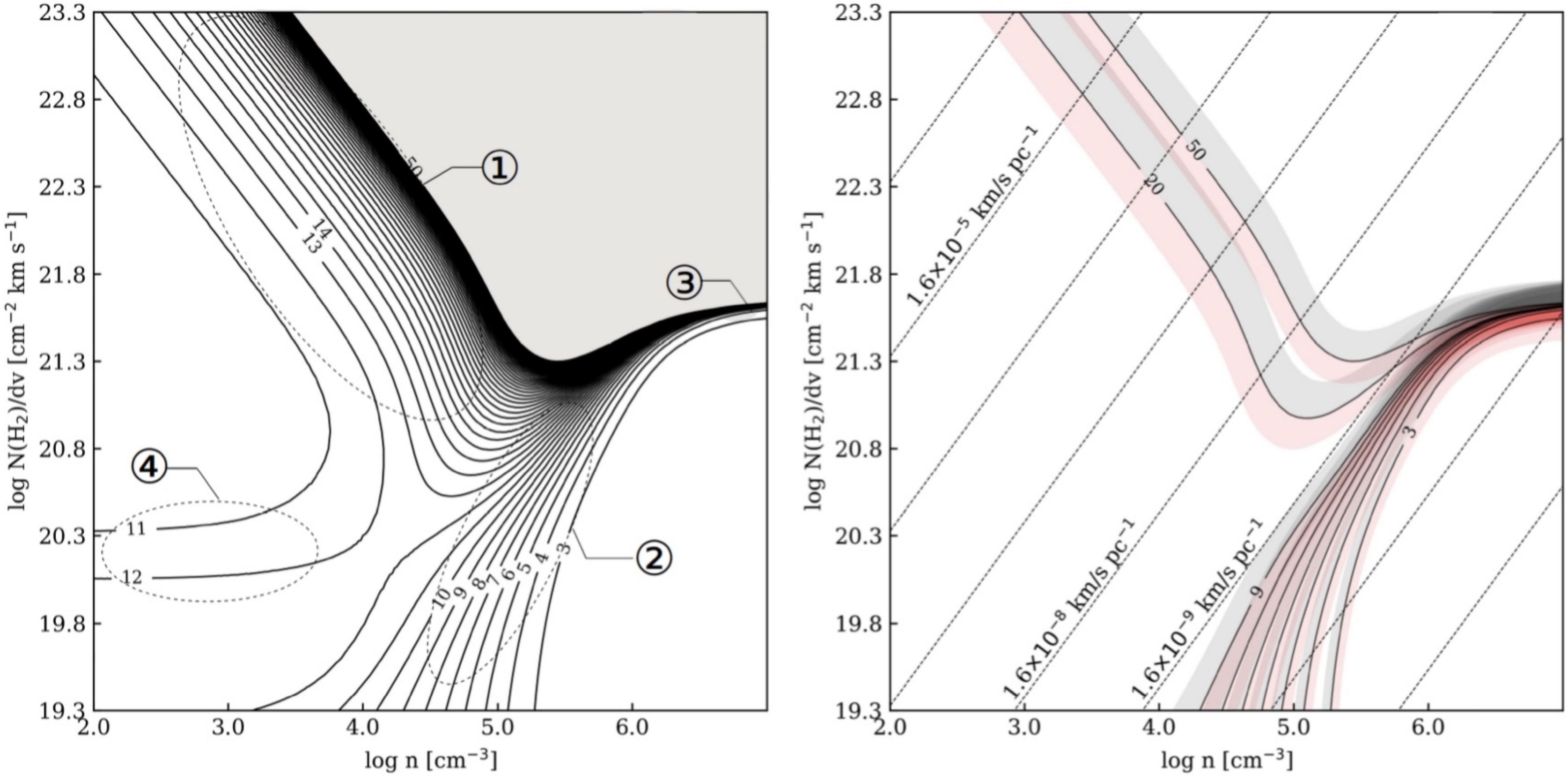

Figure 2.5: *Left:* assuming a one-component model, the available parameter space (the non-shadowed regions) corresponding to the intensity ratio of HCN to HCO^+ of 1.2 at 30 K. Contours represent the relative column density of HCN to HCO^+, i.e. the abundance ratio. The abundance of HCO^+ is fixed at $[HCO^+/H_2] = 2\times10^{-8}$; changing this value will shift the contour pattern along the y-axis, but the pattern shape will be the same. Four circled numbers indicate representative physical conditions that give rise to the observed intensity ratio. *Right:* the available parameter space for intensity ratio between 1.1 to 1.3. The red shade represents the ratio between 1.1 to 1.2 and the grey shade represents 1.2 to 1.3. Dashed straight lines represent $[HCO^+/H_2]dv/dr$ in order-of-magnitude contours.

2.5.1.1 Permitted Parameter Space for a Fixed $\mathcal{R}$

We investigate how a fixed value of $\mathcal{R}$ of 1.2, the intensity ratio observed in IC 342, is realized, assuming that HCN and HCO^+ coexist and that the (1–0) emission lines originate from the same regions at the same temperatures and densities. The assumption is based on the similar morphology and line profiles between HCN and HCO^+ (see § 2.4.2). We apply an escape probability formalism for a uniform sphere geometry, and use a one-component radiative transfer model with RADEX (Van der Tak et al., 2007) to explore the value of $\mathcal{R}$ over a grid of solutions in the space of the density ($n_{\mathrm{H_2}}$) and the column density (N/dv). The optical depths and the brightness temperatures are calculated under the corresponding parameter space to determine $\mathcal{R}$ (see Appendix B for details). Specifically, $n_{\mathrm{H_2}}$, N/dv, and τ are all taken as constant properties within a beam. We find that the results are insensitive to temperatures from 10 to 100 K, and show calculations for 30 K, which is close to the temperature of the molecular gas suggested by Meier & Turner (2001). The range of $n_{\mathrm{H_2}}$ is chosen from 10^2–10^7 cm^{-3}, and N/dv is from 10^{21-25} cm^{-2}/50 km s^{-1}. The abundance of [HCO^+/H_2] is fixed at 2×10^{-8} (the Galactic value adopted by Krips et al., 2008), and the abundance of HCN is scaled relative to HCO^+. We note that changes in the value of the abundance of HCO^+ shift the grid of solutions along the y-axis (see discussions below), but do not influence our conclusions.

We present in the left panel of Figure 2.5 the grid of solutions in the parameter space that produces $\mathcal{R} = 1.2$. The axes are $n_{\mathrm{H_2}}$ and N/dv, with contours in the non-shadowed regions representing the column density ratios of HCN to HCO^+ or, equivalently, the abundance ratios that give a fixed constant $\mathcal{R}$ of 1.2. The shadowed regions represent the parameter space without a solution.

Table 2.2: Physical conditions of the four marked regions in Figure 2.5. "sub" and "($\sim$)therm" represent subthermalization and (near-)thermalization. See Appendix. B for the detailed pattern of τ and $T_{\rm ex}$ over the ($n_{\rm H_2}$, N/dv) grid.

Region	Optical depth		Excitation condition	
	HCN	HCO$^+$	HCN	HCO$^+$
1	$\tau \gg 1$		sub	sub
2	$\tau \sim 1$		$\sim$therm	therm
3	$\tau \gg 1$	$\tau \sim 1.8$	therm	therm
4	$\tau \gg 1$	$\tau \gtrsim 1$	sub	sub

Not all solutions, however, are physically realistic. We investigate the constraints on the excitation conditions or optical depth for four different regions marked with circled numbers on the left-hand panel of Figure 2.5. These constraints are summarized in Table 2.2. In region 1, both lines are subthermalized, and the level populations are controlled by collisions. Both lines are optically thick, and the intensity ratio is determined by the ratio of the excitation temperature $T_{\rm ex}$. Region 2, in contrast, controls $\mathcal{R}$ through the relative optical depth together with $T_{\rm ex}$. In region 2, both HCN and HCO$^+$ have intermediate optical depth, and HCO$^+$ emission is thermalized. Region 3 requires a fixed τ(HCO$^+$), for which $1 - e^{\tau}$ = 1/1.2, because HCN emission is optically thick and $T_{\rm ex}$ of HCN and HCO$^+$ are equal. Such a tight constraint rules out region 3 as a realistic solution. Finally, contours in region 4 are parallel to the horizontal axis. Although both HCN and HCO$^+$ are subthermalized in this region due to the low value of $n_{\rm H_2}$, both τ(HCO$^+$) and the $T_{\rm ex}$ ratio are independent of $n_{\rm H_2}$ in this region. Similarly to region 3, we consider the constant τ in region 4 to be unrealistic.

Because both regions 1 and 2 are the permitted parameter spaces for a fixed $\mathcal{R}$ with a value of 1.2, we further compare the two regions in § 2.5.1.2 to see whether the two regions can apply to the whole bar region of IC 342.

Table 2.3: Key criteria for identifying the physically more feasible parameter space in the bar region of IC 342.

Comparison with ...	Criteria	Better Region
Models	Range of $[\mathrm{HCO^+/H_2}]dv/dr$	Region 2
	Allowed uncertainties for a specific $\mathcal{R}$	Region 2
Observations	Column density measured by $\mathrm{C^{18}O}$(1−0)	Region 2
	τ(HCN) derived through $\mathrm{H^{12}CN}$(1−0)/$\mathrm{H^{13}CN}$(1−0)	Region 2
	τ(HCN) estimated by comparing ... ... single-dish/interferometer maps	Region 2
	The abundance ratio of HCN to $\mathrm{HCO^+}$	N/A

2.5.1.2 Thermal vs. Subthermal in the Bar of IC 342

Our RADEX modeling results show that for the constant HCN(1−0)-to-$\mathrm{HCO^+}$(1−0) ratio across the IC 342 bar, there is a degeneracy of the parameter space in both region 1 and region 2. We discuss below whether the degeneracy may be further broken by comparing the theoretical predictions with the observations, including the column densities, the optical depths, and the abundance ratios derived from current and/or past studies as direct evidence for comparison. We show in this subsection that region 2 (thermal excitation) serves this requirement better than region 1 (subthermal excitation) does, and summarize in Table 2.3 the key criteria.

Theoretical constraints from the RADEX modeling: A constant $\mathcal{R}$ in the grid of ($n_{\mathrm{H_2}}$, N/dv) is produced along the abundance ratio contours (Figure 2.5). As the orientation of the contours reflects the relationship of $n_{\mathrm{H_2}}$ and N/dv, we argue below that the pattern of the contours is more feasible in region 2. In region 1, this corresponds to $n_{\mathrm{H_2}} \cdot N \sim$ constant. In region 2, the contours resemble more of the condition that dv/dr is constant, because $N/dv{\cdot}dv/dr \sim N_{\mathrm{H_2}}/dr \sim n_{\mathrm{H_2}}$. This point is illustrated as a group of parallel straight lines with a slope of one in the right panel of Figure 2.5, in which the intercept of each line corresponds to a different [HCO^+/H_2]dv/dr. As is shown in Figure 2.5, although [HCO^+/H_2]dv/dr only spans one order of magnitude, from 1.6×10^{-10} to 1.6×10^{-9} km s^{-1} pc^{-1}, in region 2, in region 1 the range is as high as four orders of magnitude. Therefore, the $n_{\mathrm{H_2}}$-N/dv relation in region 2 is more realistic for a fixed $\mathcal{R}$.

The "indirect" evidence of a constant HCN(1–0)-to-HCO^+(1–0) ratio across the IC 342 bar fits the movement of points along the abundance ratio contours of region 2 better. If points on the ($n_{\mathrm{H_2}}$, N/dv) space move along the constant dv/dr direction in the grid, region 1 has a smaller tolerance on the uncertainties to the solutions of a specific $\mathcal{R}$. We illustrate this point in the right panel of Figure 2.5, in which we only keep contour lines in regions 1 and 2, for clarity. Specifically, the red- and grey-shadowed regions represent $\mathcal{R}$ from 1.1 to 1.2, and from 1.2 to 1.3, a range that represents the uncertainty level we have observed in IC 342. Although the wider shaded region in region 1 seems to allow for a larger permitted parameter space under $\mathcal{R}$ from 1.1 to 1.3, the permitted range along the constant dv/dr is actually much smaller than that of region 2.

Observational constraints: We also compare with observational constraints on the column densities, the optical depths, and the abundance ratio to discuss which region on the grid of ($n_{\mathrm{H_2}}$, N/dv) is the preferred parameter space for the bar of IC 342.

To compare column densities and decide which excitation region better represents the conditions in IC 342, we make the assumption that $C^{18}O$ and HCN (or HCO^+) are tracing the same gas. As we have shown in § 2.4.2, the corresponding $N_{\mathrm{H_2}}$ (or N/dv) is $\sim 10^{22}$ cm^{-2} (or $10^{20.3}$ cm^{-2} km s^{-1}). The column density inferred from region 2 is thus more realistic.

Past observations of isotopologues of HCN in IC 342 show that HCN has an intermediate optical depth, also suggesting that region 2 is preferable (Downes et al., 1992; Schinnerer et al., 2008; Schulz et al., 2001; Wilson, 1999). Schulz et al. (2001) measured the intensity ratio of $H^{12}CN(1{-}0)$ to $H^{13}CN(1{-}0)$ over GMCs in the center of IC 342 and found a value of $\sim$40. This value is larger than one but smaller than the local [$^{12}C/^{13}C$] ratio of ~ 60 (Wilson, 1999). These measurements indicate that both $H^{12}CN$ and $H^{13}CN$ have intermediate optical depths, and thus are neither thick nor thin.

The comparison between the single-dish GBT/Argus image and the interferometric images (Downes et al., 1992; Schinnerer et al., 2008) also shows that HCN has an intermediate optical depth. If τ were much larger than one, it would then wash away substructures. The giant molecular clouds (GMCs) observed by interferometers in scales of $\sim$80 pc at the center of IC 342 (Downes et al., 1992; Schinnerer et al., 2008) would be behind an opaque screen, and would therefore be invisible. One alternative explanation to the extended HCN emission observed by the GBT is that optically thick small clouds form a foreground screen with gaps that are much smaller than the GBT beam, but such a scenario is not seen in the interferometer images and is therefore unrealistic.

The abundance ratio of HCN to HCO^+ would distinguish regions 1 and 2 if the range of the value of the ratio could be constrained to order unity (region 2) or order ten (region 1). However, neither theoretical models nor observations support such a constraint in the bar of IC 342. In the nucleus of IC 342, the central starburst produces both bar-induced shocks and PDR regions (Meier & Turner, 2005). Shocked molecular clouds allow possible endothermic reactions to occur, and gas-phase ion–molecule reactions to proceed in the compressed layers, so the abundance of HCO^+ could be suppressed by at most two orders of magnitude (see Figure 1 in Iglesias & Silk, 1978). As a comparison, models of PDRs mostly yield [HCN/HCO^+]>1 (Papadopoulos, 2007). Therefore, we cannot distinguish region 1 and 2 through the predictions on the abundance ratio.

2.5.1.3 Thermal vs. Subthermal in the General Case

As we have discussed in § 2.5.1.1 and Table 2.3, we favor region 2 more than region 1 in the nuclear bar region of IC 342. However, in either the $\mathcal{R}$-L_{IR} or the $\mathcal{R}$-AGN/SB relation as described in the introduction, it is the condition in region 1, subthermal excitation and large optical depth, the common interpretation inferred from unresolved or low spatial resolution observations (e.g., Jiménez-Donaire et al., 2017; Krips et al., 2008).

We investigate (1) whether region 1 is the unique solution to single-beam observations on samples of external galaxies, and (2) whether solutions in region 2 apply if external galaxies are spatially resolved and still keep a constant $\mathcal{R}$ (e.g., $\mathcal{R}$=1.4 across the spatially resolved bar of NGC 253 in Knudsen et al., 2007).

First, we analyze the line intensity ratios of higher-J to J=1–0 transitions of IC 342 with the LVG model, following the work of Knudsen et al. (2007). In Knudsen et al. (2007), NGC 253 was reported to have spatially resolved and indistinguishable HCN(1–0) and HCO^+(1–0) with $\mathcal{R}$=1.4. By comparing with single beam J=3–2 data, they conclude that both HCN(1–0) and HCO^+(1–0) are optically thick and are subthermally excited (n_{H_2} = $10^{5.2}$ cm^{-3} at 50 K).

For IC 342, J=4–3 transitions observed with the James Clerk Maxwell Telescope (JCMT) (Tan et al., 2018) are available for HCN and HCO^+. We convolved the J=1–0 image to the 14″ beam resolution of HCN(4–3), and found that the line intensity ratio of (1–0)/(4–3) (hereafter referred as r_{41}) is ∼3–10 and ∼2.5–6 for HCN and HCO^+, respectively. Using the same parameters in RADEX as § 2.5.1.1 over the one-component model, the range of r_{41} corresponds to

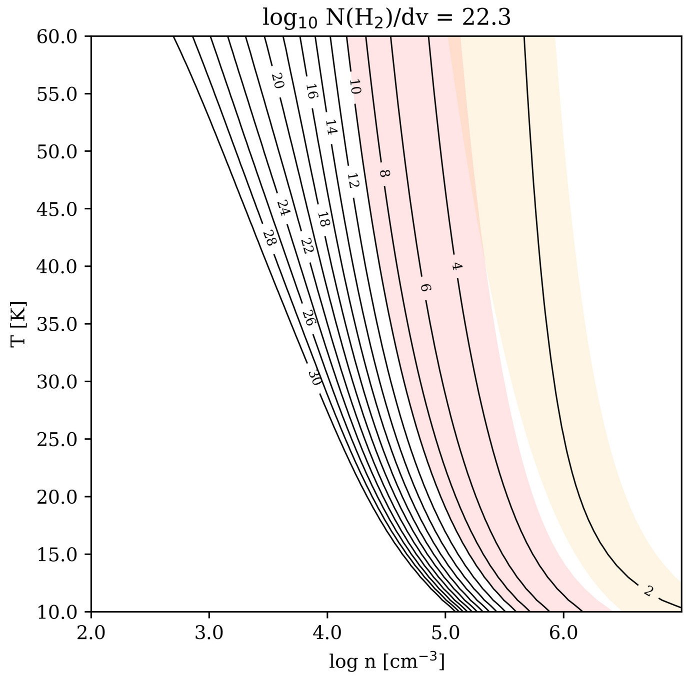

Figure 2.6: Contours represent $r_{10/43}$ of HCN over the grid (n, T) for $\log_{10}N(H_2)/dv$ = 22.3. The red region shows where $r_{10/43}$ is from 3 to 10. The orange area shows the solution for $r_{10/43}$ from 3 to 10 when $\log_{10}N(H_2)/dv$ = 21.3, which has a 10 times lower column density.

$n_{\mathrm{H_2}}$ from $10^{4.5}$–$10^{5.5}$ cm^{-3} (Figure 2.6) if HCN(1–0) were optically thick ($\tau \gg 1$). Although this result seems to be consistent with the condition that Knudsen et al. (2007) have suggested, and is located at region 1 (see Figure 2.5), such a combination of the column density and the particle density is not the unique solution that comes from single-beam observations. For example, a combination of a column density that is 10 times lower, an intermediate optical depth close to one, and a high $n_{\mathrm{H_2}}$ at which HCN(1–0) is thermalized also produces r_{41} in range of $\sim$3 to 10 (see the orange area in Figure 2.6).

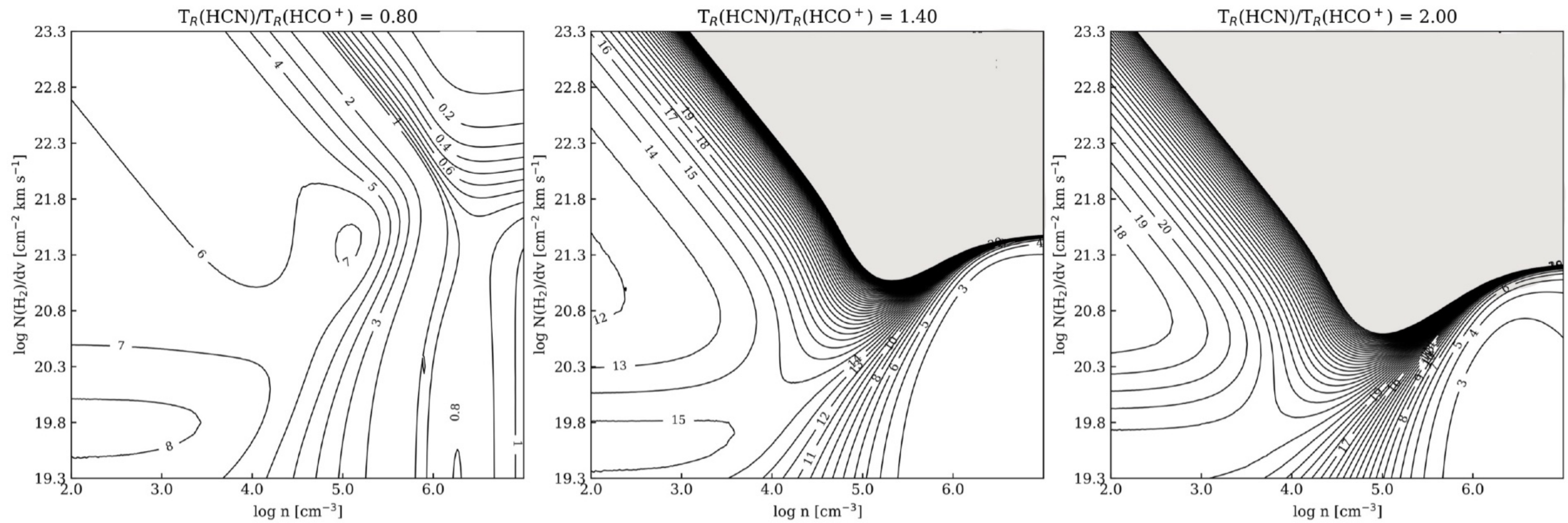

Figure 2.7: Assuming a one-component model, the available parameter space (the non-shadowed regions) corresponding to the intensity ratio of HCN to HCO^+ of 0.8, 1.4, and 2 under 30 K. Contours represent the relative column density of HCN to HCO^+, i.e. the abundance ratio.

Second, to explore whether the range of plausible solutions above for IC342 would apply to spatially resolved observations of other galaxies, we present in Figure 2.7 the solutions to the parameter space when $\mathcal{R}$ = 0.8, 1.4, and 2. The range between 0.8 and 2 is typical in a sample of galaxies when the $\mathcal{R}$-L_{IR} or $\mathcal{R}$-AGN/SB relation is discussed (e.g., Krips et al., 2010). If $\mathcal{R}$ is smaller than one, each ($n_{\mathrm{H_2}}$, N/dv) pair has a solution of the abundance ratio, because HCO^+ has a smaller critical density and is thermalized more easily than HCN. If $\mathcal{R}$ is larger than one, the solution in the ($n_{\mathrm{H_2}}$, N/dv) grid is similar to that of $\mathcal{R}$ = 1.2 (see Figure 2.5). Specifically, as $\mathcal{R}$ increases, the upper limit of allowed solution, N/dv at $n_{\mathrm{H_2}} < 10^5$ cm^{-3}, decreases, and the corresponding abundance ratio for ($n_{\mathrm{H_2}}$, N/dv) at $n_{\mathrm{H_2}} < 10^5$ cm^{-3} increases (see Figure 2.7). Such a behavior explains why the value of $\mathcal{R}$ as large as, for example, 5, is not seen in external galaxies. For such a high value of $\mathcal{R}$, there is no solution in the ($n_{\mathrm{H_2}}$, N/dv) grid at $n_{\mathrm{H_2}} < 10^5$ cm^{-3}. At $n_{\mathrm{H_2}} > 10^5$ cm^{-3}, the ($n_{\mathrm{H_2}}$, N/dv) solution requires an abundance-ratio of $\sim$50 that is too high to achieve.

The discussion above illustrates the implications of Figure 2.7, that region 2 is concluded as the preferable parameter space for a variety of $\mathcal{R}$, and that $\mathcal{R}$ is more sensitive to abundance ratio than to particle density after the degeneracy of the parameter space is partly broken. We note that one assumption here is that the abundance ratio does not vary by a factor of few with position by large factors, so the varying physical conditions tend to move along the constant abundance ratio contour (§ 2.5.1.2).

The idea that the HCN to HCO^+ intensity ratio traces abundance is related to using $\mathcal{R}$ as a potential diagnostic tool to distinguish AGN from starbursts in galactic nuclei. It has been argued that the abundance ratio of HCN to HCO^+ is sensitive to the environment that hosts an AGN or a starburst (e.g., Graciá-Carpio et al., 2006; Imanishi et al., 2006, 2007). First, HCN can be enhanced chemically either by far-ultraviolet radiation from young massive star-forming regions or through strong X-ray radiation from an AGN. AGNs are therefore likely to have a higher HCN abundance, because X-ray radiation penetrates more deeply into gas clouds than does UV radiation. Second, evolved starbursts tend to have a lower HCN to HCO^+ abundance ratio, due to the ionization effects from cosmic rays from SNEs. The ionization effects potentially increase the HCO^+ abundance and decrease the HCN abundance (e.g., Nguyen-Q-Rieu et al., 1992).

In conclusion, (1) region 1 is an inaccurate solution to the single-beam observations, and (2) for samples of external galaxies in the $\mathcal{R}$-L_{IR} or $\mathcal{R}$-AGN/SB relation, if the galaxies are mapped with finer resolution, those galaxies might still have a constant $\mathcal{R}$ across HCN/HCO^+ emitting region, with region 2 being the preferable parameter space. The ambiguities arising from the analysis of high-J lines reflect the fact that $\mathcal{R}$ and r_{41}, are actually probing different conditions. Although r_{41} is tracing more of the bright J=4–3 lines, this ratio probes more of the fraction of high excitation materials within the beam, or equivalently, the mean particle density. In contrast, $\mathcal{R}$ is insensitive to the exact condition of the two species, and is revealing more of the relative abundance of the two species, which may relate to the existence of AGNs or starbursts.

2.5.2 Breakdown of the HCN-IR Correlation at High Spatial Resolution

On a galactic scale, a scale-dependent scatter was previously observed for CO in the relationship between the molecular gas surface density and the SFR on a galactic scale (e.g., Kreckel et al., 2018; Kruijssen & Longmore, 2014; Pan et al., 2022; Schruba et al., 2010). Such a relationship breaks down at some scale due to incomplete sampling of star-forming regions. Argus on the GBT provides a unique opportunity to inspect such a scale-scatter breakdown in the closest HCN-bright galaxies. Although the EMPIRE survey (Jiménez-Donaire et al., 2017) reveals that the ratios of HCN/CO and HCN/IR show various clear correlations with galaxy structure, we are now able to investigate how a finer spatial resolution influences the scatter in HCN–IR relations.

We present in Figure 2.8a and 2.8b the L_{IR}–L_{HCN} and the $L_{\mathrm{IR}}/L_{\mathrm{HCN}}$-$L_{\mathrm{HCN}}$ relation on scales of 170 pc ($\sim$10″), 340 pc ($\sim$20″), and 510 pc ($\sim$30″) observed by convolving our Argus HCN image to different beam sizes. The HCN luminosity, L_{HCN}, was derived from the integrated intensities following Gao & Solomon (2004a), and L_{IR} was calibrated from the brightness of the $Herschel$ 70 μm images (Kennicutt et al., 2011) following Galametz et al. (2013). All of the data points on scales from 170 to 510 pc fall nicely on the Gao & Solomon (2004a) relation with a slope of one (see Figure 2.8a and 2.8b). This agreement is unsurprising, because IC 342 was one of the galaxies in the Gao & Solomon (2004a) sample.

In addition to individually sampled points from IC 342, Figure 2.8a and 2.8b also show the global L_{IR}–L_{HCN} relation measured on bright centers of external galaxies reported by Gao & Solomon (2004a). In Gao & Solomon (2004a), IC 342 as a whole galaxy follows the L_{IR}–L_{HCN} trend on galactic scales. Individual regions within IC342 from our high-resolution observations follow a similar trend. We confirm that the measurements of the line intensities from the two studies are consistent by presenting in Figure 2.8c the HCN spectra observed from a 72″ beam at the same position, although we note that there is a blue-shifted wing in the Gao & Solomon (2004a) spectrum that we do not detect. Furthermore, (L_{HCN}, L_{IR}) falls within the uncertainty level of $\pm$0.23 dex of Gao & Solomon (2004a) relation.

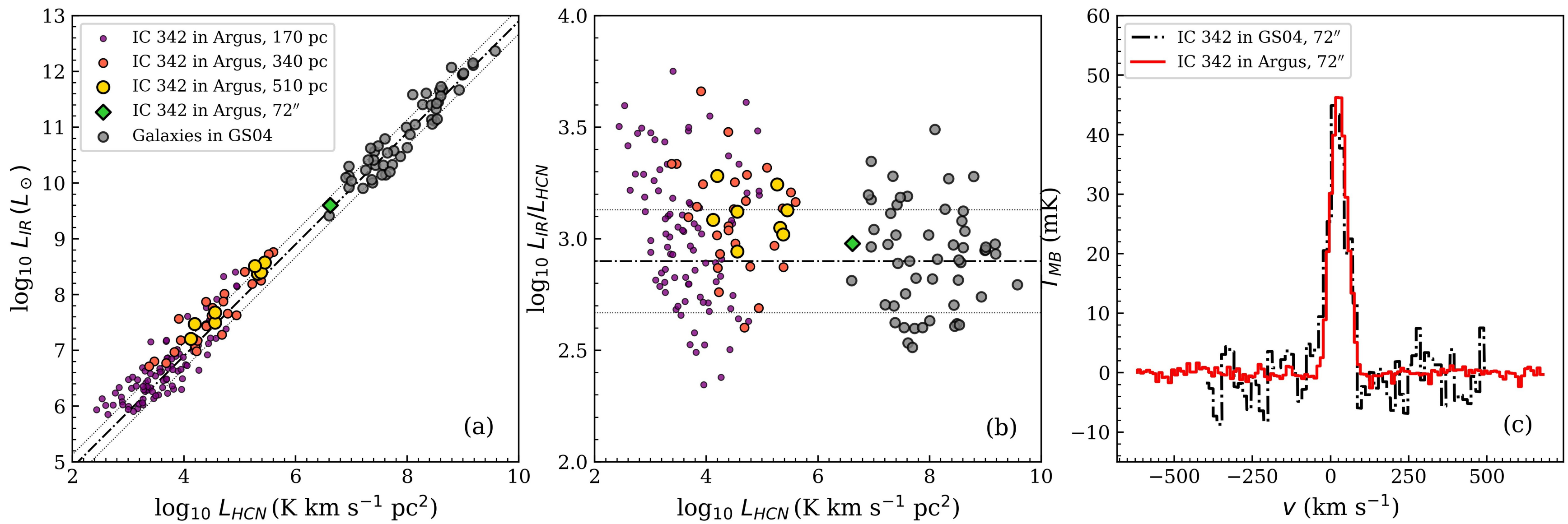

Figure 2.8: (a) and (b): L_{IR}–L_{HCN} relations from individual sampling points on the IC 342 Argus image on a scale of 170 (*purple*), 340 (*orange*), and 510 pc (*yellow*). Each individual point in the figure show luminosities of individually sampled apertures. The central 72″ beam in the Argus image (∼1150 pc, *green*); L_{HCN} of which is converted from the red spectrum on Figure 2.8(c) is set to compare with the beam size of measurements in Gao & Solomon (2004a) (*grey*). (c) Spectra observed by Argus and by Gao & Solomon (2004a) in T_{MB} scale from a 72″ beam at the center of IC 342 at RA = 3:46:48.30795, DEC = +68:05:48.8251 (J2000).

Table 2.4: The average and the scatter in $\log_{10}(L_{\rm IR}/L_{\rm HCN})$ in different spatial scales.

Regions	$\langle\log_{10}(L_{\rm IR}/L_{\rm HCN})\rangle$	$\sigma(\log_{10}(L_{\rm IR}/L_{\rm HCN}))$
170 pc	3.02	0.31
340 pc	3.10	0.23
510 pc	3.11	0.10
GS04[a]	2.92	0.23

[a] Values adopted from Gao & Solomon (2004a).

Table 2.4 summarizes the variation of the scatter of Argus data to the $L_{\rm IR}$–$L_{\rm HCN}$ relation of which the power is one under different sampling sizes. The scatter drops as the spatial scale increases. The scatter for the smallest (170 pc) scale of the corresponding $L_{\rm IR}$–$L_{\rm HCN}$ relation is only 1.3 times greater than the scatter for beam-averaged external galaxies, which is comparable for a 340 pc scale. As Figure 2.1 shows, Argus has resolved the angular offset between the IR emission and molecular gas emission at 100 pc resolution. The scatter on a 340 pc scale therefore intrinsically reflects this angular offset.

The scale-scatter breakdown observed in CO was interpreted as an incomplete sampling of star-forming regions. Specifically, Schruba et al. (2010) proposed that the breakdown reflects a temporal evolution process of gas depletion in star formation revealed at different spatial scales. However, we stress that we are not inferring the information of dense gas depletion efficiency in the $L_{\rm IR}$–$L_{\rm HCN}$ relation of IC 342, because the evolution is possibly influenced by the passing density wave. Therefore, we can only conclude that the HCN(1–0) emission is more strongly correlated with star formation when averaged over large regions of IC 342. The high-resolution observations suggest that the relationship begins to break down on smaller 340 pc regions. As a reference, we note that Murphy et al. (2015) has reported a spatial offset between HCN (and HCO^+) with the continuum tracing star-formation by a physical scale of $\sim$130 pc in NGC 3627.

We conclude that HCN(1–0) emission can serve as a useful star formation tracer if a certain spatial sampling criterion is satisfied. We stress that such a tracer may not fully reflect a dense gas-to-star formation relation. More samples with spatially resolved HCN emission from the DEGAS survey should provide a further understanding of the criteria that sustain the tight global $L_{\rm IR}$–$L_{\rm HCN}$ relation.

2.6 Summary

We have observed J=1–0 transitions of ^{12}CO, ^{13}CO, C^{18}O, HCN, and HCO^{+} from the external galaxy IC 342 with the 16-pixel spectroscopic focal plane Argus on the 100-m GBT. The gaseous nuclear bar was mapped in all five transitions, and ^{12}CO(1–0) observations revealed the two inner spiral arms. These data are important, because they provide single-dish measurements at high spatial resolution while interferometer maps can miss the extended molecular emission and previous single-dish maps lack the resolution to resolve the IR and molecular gas regions. The morphology of molecular gas traced by ^{12}CO(1–0) and ^{13}CO(1–0) differs from that of HCN(1–0) and HCO^{+}(1–0), indicating different sensitivity of these molecular gas tracers to different physical conditions. ^{13}CO(1–0) traces the surface layer, as ^{12}CO(1–0) does, due to radiative trapping. HCN emission correlates well with infrared emission tracing recent star formation as long as a sufficiently large sampling scale (e.g. $>$340 pc for IC 342) is satisfied.

The intensity of spatially resolved HCN(1–0) and HCO^{+}(1–0) emission have a remarkably tight correlation with independent measurements over a $\sim$100 pc scale. This tight correlation suggests that the line ratio of HCN(1–0) to HCO^{+}(1–0) is insensitive to local varying physical conditions across the center of IC342. We used RADEX with a one-component model to explore the permitted parameter space over this constant line ratio and the preferred region to realize the insensitivity of the line ratio to the environments. Our investigation also looked for available parameter space for HCN(1–0)/HCO$^+$(1–0) ratios observed among other external galaxies. For IC 342, we conclude that the HCN(1–0) and HCO$^+$(1–0) emission from the 1 kpc gaseous bar of IC 342 likely have intermediate optical depth and $n_{\mathrm{H_2}}$ in $10^{4.5}$–10^6 cm^{-3}, where HCO$^+$(1–0) is thermalized and HCN(1–0) is close to thermalization. This result is compatible with results derived from analyses with higher-J transitions, although it also indicates that the HCN(1–0) and HCO$^+$(1–0) emission from external galaxies may have physical conditions other than large optical depth and specific particle densities that cause subthermalization. The insensitivity of the HCN(1–0)-to-HCO$^+$(1–0) intensity ratio across the center of IC342 indicates that it is more sensitive to the relative abundance ratio rather than particle densities. We suggest that a multi-component radiative transfer model would help the analysis with higher-J lines, and observationally more realized constraints to the physical conditions of HCN(1–0) or HCO$^+$(1–0) emission can be conducted with more precise measurements of the isotopologues.

Chapter 3: High-resolution M-band Spectroscopy of CO toward the Massive Young Stellar Binary W3 IRS 5

3.1 Chapter Preface

Chapter 3 is presented with minimal changes since publication in ApJ as "High-Resolution M-band Spectroscopy of CO towards the Massive Young Stellar Binary W3 IRS5" (Li et al., 2022). The authors are Jialu Li, Adwin Boogert, Andrew G. Barr, and Alexander G. G. M. Tielens.

3.2 Introduction

Although massive stars profoundly affect the evolution of the universe, their formation and evolution processes are not well understood. Massive stars are rare, deeply embedded in the early stage, and seldom found to form in isolation. Therefore, the large distances to the observers, the high extinction at optical and near-infrared wavelengths, and the highly clustered environment impede a clear understanding of their formation and evolution processes.

Theoretical models for massive star formation have remained controversial. Compared to the well-established formation process of low-mass stars (McKee & Ostriker, 2007), massive stars do not form through an exact scaled-up mechanism due to the strong radiation pressure, which dramatically influences the accretion rate and the final stellar mass (Wolfire & Cassinelli, 1987). Several approaches have been followed to overcome this problem: the generation of radiatively driven bubbles and the disk-mediated accretion (Krumholz et al., 2009; Rosen & Krumholz, 2020) in monolithic collapse models (Krumholz et al., 2005; McKee & Tan, 2003) have been developed as a way to overcome the radiation pressure barrier; the coalescence scenario (Bally & Zinnecker, 2005; Bonnell et al., 1998) in high stellar density environments avoids the radiation pressure issues; and the competitive accretion model (Bonnell et al., 2004; Bonnell & Bate, 2006) suggests that the forming stars accrete material that is not gravitationally bound to the stellar seed. Each of these different scenarios has implications for cluster formation and binary formation involving disks.

For high-mass star-forming cores, the current proposed theoretical evolutionary sequence is: high-mass starless cores (HMSCs) $\rightarrow$ high-mass cores harboring accreting low-/intermediate-mass protostar(s) destined to become a high-mass star(s) $\rightarrow$ high-mass protostellar objects (HMPOs) $\rightarrow$ final stars (Beuther et al., 2007). Observationally, the embedded phases of massive protostellar objects are subdivided into infrared dark clouds (IRDC), hot molecular cores (HMCs), hypercompact- and ultracompact-HII regions (HCHIIs and UCHIIs), and compact and classical HII regions (Beuther et al., 2007). As the formation and evolution proceed, the central object warms and ionizes the environment and drives a rich chemistry. Complex physical activities are involved in the evolution as well, such as accretion disks, outflows, shocks, and disk winds (Cesaroni et al., 2007; Zinnecker & Yorke, 2007).

In the proposed evolutionary sequence of massive star formation, each stage has its own characteristic physical conditions. Mid-infrared (MIR) spectroscopy is sensitive to the presence of warm gas (several hundreds of degrees) that is very close to the protostar, often at a distance between 100 and 1000 au. Observing at MIR wavelengths, therefore, fills the gap in between the cooler and more extended regions ($>$ 1000 au) emitting in the submillimeter/millimeter and the innermost ionized HII regions traced by observations at radio wavelengths. The MIR spectroscopy also traces important characteristic chemistry during massive star formation. At these high temperatures, grain mantles have sublimated, and neutral-neutral reaction channels have opened up, resulting in a rich inventory of organic molecules (Agúndez et al., 2008; Bast et al., 2013; Herbst & van Dishoeck, 2009; van der Tak et al., 2003).

Molecular rovibrational transitions in the MIR provide a unique opportunity to study the physical conditions and chemical inventory of embedded phases in massive star formation. The size of the MIR continuum emission region provides the effective spatial resolution of such spectroscopic observations because the observed absorption components are exactly located in front of the infrared source and are along the line of sight. The full set of rovibrational lines can be covered in a short bandwidth without the multiple frequency settings that submillimeter observations require. Molecules without dipole moments such as C_2H_2 and CH_4, which are among the most abundant carbon-bearing molecules, can only be observed through their rovibrational spectra in infrared. Therefore, MIR spectroscopy at high resolution allows us to study the properties of physical components close to massive protostars and understand the interactions of the massive protostars with their environment in a better way.

The active star-forming region W3 IRS 5 is in the Perseus arm at a distance of $2.3^{+0.19}_{-0.16}$ kpc (Gaia DR2; Navarete et al., 2019). The high IR luminosity and the presence of radio sources reveal the presence of high-mass protostars. Object W3 IRS 5 is a binary (Megeath et al., 1996), and we refer to the northeastern component as MIR1 and the southwestern one as MIR2, following the nomenclature in van der Tak et al. (2005). Near-IR images reveal that MIR1 and MIR2 are separated by $\sim$1.2$''$ and coincident with the bright submillimeter sources MM1 and MM2

(Megeath et al., 2005; van der Tak et al., 2005). In this chapter, we present a rich high-resolution spectrum of W3 IRS 5 in the 4.7 μm M band covering the rovibrational transitions of ^{12}CO and its isotopologs ^{13}CO, C^{18}O, C^{17}O. In contrast to early observations by Mitchell et al. (1991) at the same wavelength, MIR1 and MIR2 are now spatially resolved, and we are therefore able to separate the different kinematic components in the complex absorption line profiles, tracing the immediate environment of each source in the W3 IRS 5 binary. We describe our observations and data reduction in Section 3.3, and our analysis method includes a simple optically thin foreground, as well as a photospheric disk model slab model in Section 3.4. We present the identification process and the derived physical conditions of different kinematic components in Section 3.5 and discuss the implications of our observations for our understanding of high-mass star formation in W3 IRS 5 in Section 3.6.

3.3 Observations and Data Reduction

We observed W3 IRS 5 with the iSHELL spectrograph (Rayner et al., 2022) at the NASA InfraRed Telescope Facility (IRTF) 3.2 m telescope as part of program 2018B095 on UT 09:00 2018 October 5. The instrument was used in its spectral mode M1 (see Table 1 in Rayner et al., 2022) with a slit width of 0.375″. This provides a resolving power of $R = \lambda/\Delta\lambda = 88,100 \pm 2,000$ (Rayner et al., 2022) over a wavelength range of 4.52–5.25 μm, excluding small gaps between the echelle orders. The total on-source integration time was 30 minutes, and the airmass was in the range of 1.535–1.443. The 15″ long slit was oriented along a position angle of 37 degrees, so that the binary components of W3 IRS 5 were observed simultaneously. The seeing conditions allowed for the 1.2″ binary to be well separated in the M band. The targets were nodded along the slit, allowing for the subtraction of the sky and hardware background emission. The Spextool package (version 5.0.2, Cushing et al., 2004) was used to reduce the spectra. This includes wavelength calibration using the sky emission lines and custom extraction apertures to separate the binary components. The binary components are of similar brightness in the M band. In the extracted spectra, the contamination by the flux from the other binary component is no more than $\sim$ 5–7%. This is estimated from the spectral features at velocities $v_{\rm LSR} < -70$ km/s (Figure 3.1), where we assume MIR1 only has continuum, and the absorption lines occur exclusively in MIR2. Telluric absorption lines were divided out using the program Xtellcor_model[1], which makes use of atmospheric models calculated by the Planetary Spectrum Generator (Villanueva et al., 2018). The echelle orders of iSHELL are strongly curved (blaze shape; cf., Figure 8 in iSHELL's observing manual[2]). This was corrected for by dividing by flat-field images taken with iSHELL's internal lamp. The Doppler shift due to the combined motion of the Earth on the date of the observations and the systemic velocity of W3 IRS 5 ($v_{\rm LSR}$ =-38 km s^{-1}; van der Tak et al., 2000) is -56 km s^{-1}. This is sufficient to separate the deep telluric CO lines from those in W3 IRS 5. Residual baseline curvature was divided out using a median filter. We shifted the wavelength scale by -18 km s^{-1} to remove the motion of the Earth in the direction of W3 IRS 5, converting it to an LSR scale. Finally, we used the HITRAN database (Kochanov et al., 2016) to identify the rovibrational transitions of ^{12}CO and its isotopologs.

Object W3 IRS5 was also observed with the SpeX spectrometer (Rayner et al., 2003) at the IRTF in order to obtain a wider-wavelength view of this binary system. The observations were done on UT 14:00 2020 August 14. The 15″ long SpeX slit was oriented along the binary position

[1] http://irtfweb.ifa.hawaii.edu/research/drresources/
[2] http://irtfweb.ifa.hawaii.edu/ishell/iSHELLobservingmanual20210827.pdf

angle of 37 degrees, and guiding was done in the K band on the slit spillover flux. Spectra were taken with the SpeX LXD_Long mode using the 0.5″ wide slit. This yields a resolving power of $R = 1,500$. The instantaneous spectral coverage is 1.95−5.36 μm. The standard star was HR 1641 (B3V). The IRTF/SpeX spectra were reduced using Spextool version 4.1 (Cushing et al., 2004). Flat-fielding was done using the images obtained with SpeX's calibration unit. The wavelength calibration procedure uses lamp lines at the shortest wavelengths and sky emission lines in much of the L and M bands. At the good seeing of ∼0.5″, the binary was well separated and could be extracted without significant contamination. The telluric correction was done using the Xtellcor program (Vacca et al., 2003). This uses a model of Vega to divide out the stellar photosphere. Vega's spectral type, A0V, differs from that of the standard star; thus, care must be taken with interpreting features near hydrogen lines.

3.4 Methods

For both MIR1 and MIR2, we have detected several hundred lines in the ν=0−1 band of ^{12}CO, ^{13}CO, C^{18}O, and C^{17}Oand the ν=1−2 band of ^{12}CO[3] at 4.7 μm in absorption. Figure 3.1 shows a selected group of lines that illustrate that each MIR source has a number of distinctive kinematic components that are characterized by different excitation conditions. For example, MIR2 shows highly blue-shifted gas, up to -90 km s^{-1}, but MIR1 does not. The ^{13}CO, C^{17}O, and C^{18}O lines of MIR2 are centered on the systemic velocity of $v_{\rm LSR} = -38$ km s^{-1}. In contrast, for MIR1 lines of the lowest J-levels center on $v_{\rm LSR} = -38$ km s^{-1}, while the high-J lines center on -46 km s^{-1}. To explore the properties of these components, we analyze the rovibrational lines of each species simultaneously. We regard the optically thin slab model in LTE as an appropriate

[3]In the rest of the chapter we consider ν=0−1 as the default band of ^{12}CO unless 'ν=1−2' is specified.

start for optically thin analysis (Section 3.4.1). In Section 3.4.2, we apply corrections when the effects of optical depth, covering factor, and radiative transfer are important.

3.4.1 Preliminary Analysis: Optically Thin Slab Model under LTE

Recovering the column density information from an absorption line is straightforward if emission from the molecular gas is negligible, and the relative intensity of the line to the continuum can be described by an attenuation factor, $e^{-\tau}$, in which τ is defined as the optical depth. This is the commonly considered slab model, where a cold, isothermal absorbing cloud is in front of a hot continuum source. In the context of the direct environment of a massive protostar, the foreground cloud can absorb the MIR emission from a disk or Hot Core. In the context of this chapter, we note that the Planck function peaks at 4.7 μm for a temperature of 600 K. Hence, the background continuum source will have to have a temperature of that order or higher. Moreover, in order to see absorption lines, the continuum source has to have an emission optical depth at least of order 1, while the foreground cloud has to be considerably cooler than 500 K (Barr et al., 2022b).

In a slab model, when the lines are optically thin, we can get the column density N_l in the lower state of a transition directly from the integrated line profile by

$$N_l = 8\pi/(A_{ul}\lambda^3)g_l/g_u \int \tau(v)dv, \tag{3.1}$$

in which A_{ul} is the Einstein coefficient, g_l and g_u are the statistical weight of the lower and upper level, and

$$\tau(v) = -\ln(I_{\text{obs}}/I_c), \tag{3.2}$$

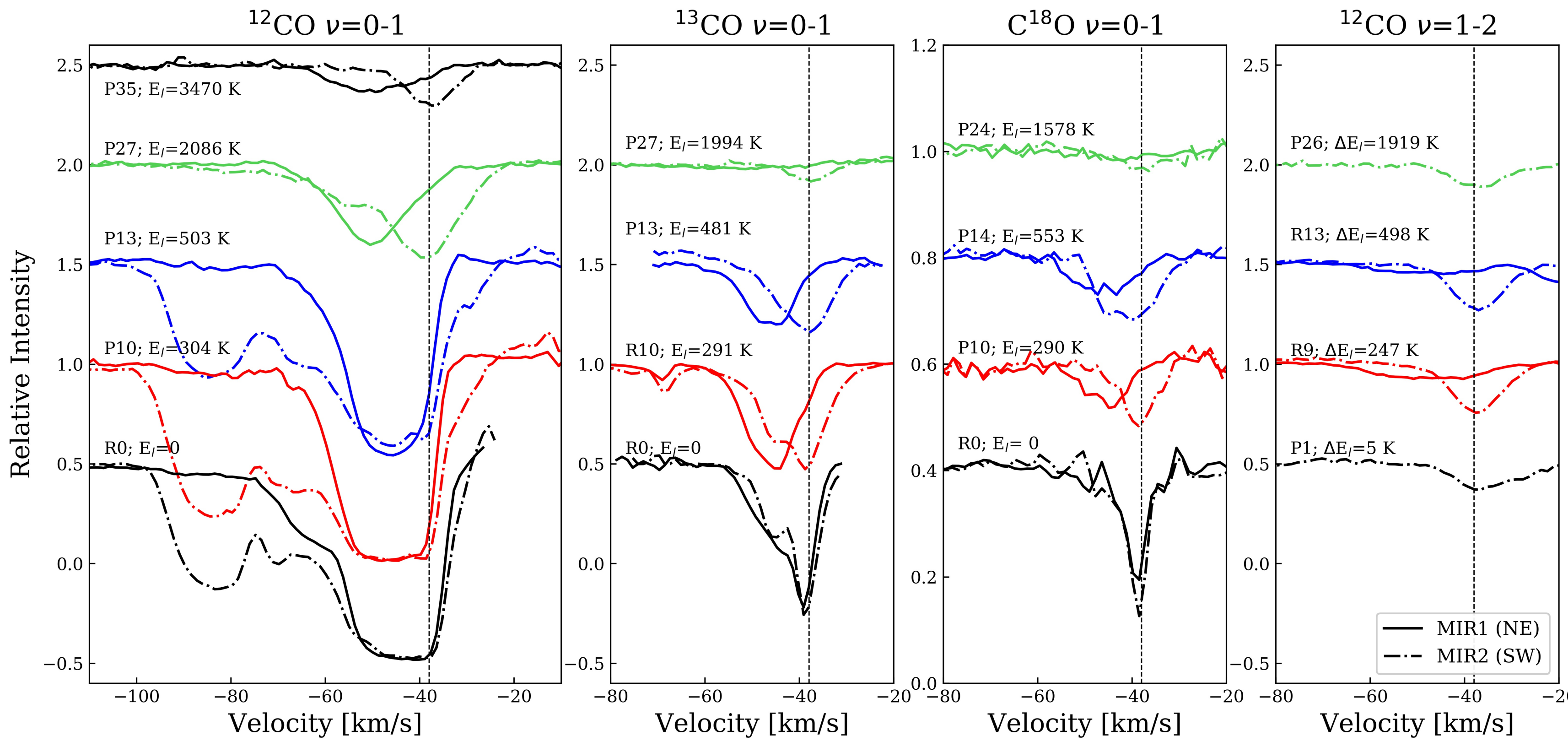

Figure 3.1: Selected ^{12}CO, ^{13}CO, and C^{18}O ν= 0−1 and ^{12}CO ν= 1−2 absorption lines observed toward MIR1 (*solid*) and MIR2 (*dash-dotted*). The dashed vertical lines at -38 km s^{-1} are the systematic velocities. In the panel of ^{12}CO ν= 1−2, $\Delta E_l = E_{\nu=1,J=J_l} - E_{\nu=0,J=0}$. Transitions with similar energy levels are represented by the same color. The ^{12}CO ν= 1−2 P1 and P26 of MIR1 are not plotted due to their poor spectral quality. C^{17}O ν=0−1 spectra were not plotted because of the limited energy levels of the observed lines. We note that the absorption at -60 km s^{-1} on the ^{12}CO ν=0−1 R0 of MIR1 is contaminated by ^{13}CO ν=0−1 R14, and we do not use the two transitions in our analysis.

where I_{obs} and I_c are the intensity of the absorption and the continuum.

If the absorbing gas is in LTE at an excitation temperature, T_{ex}, the population in the rotational level J is thermalized according to

$$\frac{N_l}{g(J)} = \frac{N_{\mathrm{tot}}}{Q(T_{\mathrm{ex}})} \exp\left(-\frac{E_l}{k_B T_{\mathrm{ex}}}\right), \tag{3.3}$$

where N_{tot} is the total column density, E_l is the excitation energy, $g(J)$ is the statistical weight of the level ($g(J) = 2J+1$ for a linear molecule), and $Q(T)$ is the partition function. For a uniform excitation temperature, the rotation diagram, $\ln(N_l/(2J+1))$ versus E_l/k_B, follows a straight line, with the inverse of the slope representing the temperature and the intercept representing the total column density over the partition function. We can therefore derive the temperature and the total column density of the molecular gas. If the slope on the rotation diagram is not a constant but has a gradient, we regard the component as a compound of multiple temperatures and fit $\ln(N_l/(2J+1))$ versus E_l/k_B with

$$\frac{N_l}{2J+1} = \sum_i \frac{N_{\mathrm{tot},\,i}}{Q(T_{\mathrm{ex},\,i})} \exp\left(-\frac{E_l}{k_B T_{\mathrm{ex},\,i}}\right), \tag{3.4}$$

where *i* represents the *i*th temperature component.

3.4.2 Curve-of-growth Analysis

3.4.2.1 Slab Model of a Foreground Cloud

For an absorbing foreground slab, corrections for the line saturation are necessary for optically thick lines. We can use the measured equivalent width,

$$W_\lambda = \int (1 - I_{\text{obs}}/I_c) d\lambda = \int (1 - \mathrm{e}^{-\tau}) d\lambda, \tag{3.5}$$

to obtain the column density of each state from the curve-of-growth (Rodgers & Williams, 1974):

$$\frac{W_\lambda}{\lambda} \approx \begin{cases} \frac{\sqrt{\pi} b}{c} \frac{\tau_p}{1+\tau_p/(2\sqrt{2})} & \text{for } \tau < 1.254 \\ \frac{2b}{c}\sqrt{\ln(\tau_p/\ln 2) + \frac{\gamma\lambda}{4b\sqrt{\pi}}(\tau_p - 1.254)} & \text{for } \tau > 1.254 \end{cases}. \tag{3.6}$$

where the peak optical depth is given by

$$\tau_p = \frac{\sqrt{\pi} e^2}{m_e bc} N_l f_{lu} \lambda. \tag{3.7}$$

In the equations above, f_{lu} is the oscillator strength, and γ is the damping constant of the Lorentzian profile. For CO rovibrational lines, γ due to radiative damping is of order $\sim$10 s^{-1}. The Doppler parameter in velocity space, b, is related to the FWHM of an optically thin line by $\Delta v_{\text{FWHM}} = 2\sqrt{\ln 2} b$. We stress that the Lorentzian line width that γ corresponds to (10^{-9} $\mathrm{km\,s^{-1}}$) is negligible compared to the observed Doppler width (a few $\mathrm{km\,s^{-1}}$).

As observations revealed that strong absorption lines did not go to zero intensity, Lacy (2013) recognized several issues that require cautions when applying an absorbing slab model.

One is that if emission from the foreground molecular cloud is not negligible, the line intensity tends to approach the source function and does approach the source function at a sufficient optical depth. The source function equals the Planck function at the line wavelength if the molecular gas is at LTE, which requires sufficient density if no other scattering opacity is considered inside the molecular cloud. As a reference, for a representative background temperature above 600 K, the foreground emission contributes an $\sim 4\%$ residual intensity at $\tau \sim 5$ in a 400 K cloud. The emission is therefore negligible in cooler clouds with smaller columns.

Another problem that may occur is that the foreground cloud does not cover the entire observing beam. The absorption feature saturates at a nonzero intensity as well because of the dilution, even if the emission from the gas is not important. Should a covering factor f_c be considered, equation 3.2 is modified to

$$I_{\mathrm{obs}} = I_{\mathrm{c}}(1 - f_c(1 - \mathrm{e}^{-\tau(v)})). \tag{3.8}$$

Similarly, the left-hand side of equation 3.6 is modified to $W_\lambda/(\lambda f_c)$.

3.4.2.2 Stellar Atmosphere Model of a Circumstellar Disk

The absorption may also occur if the dust thermal continuum is mixed with the molecular gas, and there is an outward-decreasing temperature gradient. This scenario is similar to the stellar atmosphere model when the continuum and the line are coupled, in which the residual flux,

$$R_\nu \equiv I_\nu / I_c, \tag{3.9}$$

can then be approximated by the Milne-Eddington model (Mihalas, 1978, Ch 10), which assumes a gray atmosphere. In the system of a forming massive star, such a model can be realized in a circumstellar disk that has a heating source in the midplane. In this scenario, saturated absorption lines approach a constant depth, and there is no need to consider a covering factor. We refer to Appendix A in Barr et al. (2020) for details of the expected line residual flux in this model.

Following Mihalas (1978), for the stellar atmosphere model, when there is pure absorption in the lines, the curve-of-growth is constructed by considering the equivalent width versus β_0, the ratio of the line opacity at line center, $\kappa_L(\nu = \nu_0)$, to the continuum opacity κ_c:

$$\begin{aligned}\frac{W_\nu}{2\Delta\nu_D} &= \int_0^{+\infty}(1 - R_v)dv \\ &= A_0\int_0^{+\infty}\beta_0 H(a,v)[1+\beta_0 H(a,v)]^{-1}dv,\end{aligned} \tag{3.10}$$

in which

$$\frac{W_\nu}{2\Delta\nu_D} = \frac{W_v}{2b} = \frac{c}{2b}\frac{W_\lambda}{\lambda}, \tag{3.11}$$

and

$$\begin{aligned}\beta_0 &= \frac{\kappa_L(\nu = \nu_0)}{\kappa_c} \\ &= \frac{A_{ul}\lambda^3}{8\pi\sqrt{2\pi}\sigma_v}\frac{g_u}{g_l}\frac{N_l}{\sigma_c N_H}\left(1 - \frac{g_l}{g_u}\frac{N_u}{N_l}\right).\end{aligned} \tag{3.12}$$

In the equations above, v is the frequency shift with respect to the line center in units of the Doppler width, and $H(a, v)$ is the Voigt function that gives the line profile, in which the damping factor $a = \gamma\lambda/b$ is of the order of 10^{-8} for CO rovibrational lines. The parameter A_0 is the central depth of an opaque line, and its exact value is determined by the radiative transfer model of the surface of the disk. The value of A_0 is related to the gradient of the Planck function, $dB/d\tau_c/B(T_o)$, where B is the Planck function, τ_c is the continuum optical depth, and T_o is the surface temperature of the disk. For a gray atmosphere, A_0 is $\sim$ 0.5–0.9 from 900 to 100 K (see Appendix A in Barr et al., 2020). The dispersion in velocity space, σ_v, is transformed from the Doppler parameter, $b/\sqrt{2}$. The continuum opacity, κ_c, is given by the dust cross section per H atom σ_c. We adopt a value of 7×10^{-23} cm^2/H-nucleus for σ_c following Barr et al. (2020), as it is appropriate for coagulated interstellar dust (Ormel et al., 2011). We can eliminate the bracketed item in equation 3.12 if the stimulated emission is negligible.

Similarly, for molecular gas under LTE, we may express β_0 as

$$\beta_0 = \left(\frac{A_{ul}\lambda^3}{8\pi\sqrt{2\pi}\sigma_v\sigma_c}\frac{g_u}{g_l}\right)\frac{g_l N_{tot}}{Q(T)N_H}e^{-E_l/(kT)}, \tag{3.13}$$

where $Q(T)$ is the partition function, and N_{tot}/N_H is the relative abundance of the molecules to hydrogen. If LTE sustains, we can thereby retrieve $(N_{tot}/N_H, T)$ through a grid search method by comparing the observable $W_\nu/2\Delta\nu_D$ (or transform into W_λ/λ) with the theoretical curve-of-growth and looking for the smallest χ_r^2. We note that our choice of σ_c influences the derived absolute abundance, although we may still use the derived abundance to calculate the relative abundance of different species in the same kinematic component.

3.4.2.3 Comparing the Two Curve-of-growth Analyses

Although the two curve-of-growth analyses assume intrinsically different radiative transfer models, the absorption profiles evolve in a similar way as the optical depth increases. The line profile firstly grows like a Gaussian (the linear part) and then saturates the intensity at the line center and thus slowly increases the equivalent width through absorption in the (Gaussian) wings (the logarithmic part). Finally, the equivalent width grows quickly again when the

Lorentzian wing takes over (the square root part). The latter case does not apply to the physical conditions in this chapter because the Lorentzian parameters γ and a (see § 3.4.2.2) are too small.

The main difference between the two models exists in the lower limit of the center depth of a line. In the stellar atmosphere model, A_0 does not approach zero; in a slab model with a 100% covering factor, the line depth does saturate at zero intensity. This is due to a mixture of the origin of the absorption line and the continuum and results in a difference in the equivalent width. However, for a slab model with a partial covering factor, its curve-of-growth may be alike to that of the stellar atmosphere model under certain conditions.

To illustrate this point, we first examine both models in the optically thin limit. In the foreground slab model, W_λ/λ goes to $f_c\tau_p$ (see eqn 3.6), and in the atmosphere model, it goes to $A_0\beta_0$ (see eqn 3.10). If we scale β_0 and τ_p by $\beta_0 = \tau_p/\tau_c = \tau_p/(\sigma_c N_H)$, and choose f_c equal to A_0, the two curves of growth can be shifted on top of each other.

We construct the curves of growth from the two models above (eqn 3.6 and 3.10) in W_λ/λ versus $N_l f_{lu}\lambda$ in Figure 3.2. As an example, the curve-of-growth in Figure 3.2 adopts $T = 660$ K and σ_v = 4.3 $\mathrm{km\,s^{-1}}$ ($b = 6.1$ $\mathrm{km\,s^{-1}}$), which are relevant for the ^{13}CO component of MIR2-H1 at -38 $\mathrm{km\,s^{-1}}$(see § 3.5.1). Figure 3.2 also presents the slab model with and without a covering factor ($f_c = A_0$). We can formulate β_0 analogous to eqn 3.7 by assuming that $\sigma_c N_H$ is 1 as for weak lines, which essentially indicates that we see down to a continuum optical depth of unity:

$$\beta_0 = \frac{1}{8\pi\sqrt{2\pi}}\frac{A_{ul}\lambda^2}{f_{lu}\sigma_v}\frac{g_u}{g_l}(N_l f_{lu}\lambda). \tag{3.14}$$

Figure 3.2 illustrates how the two approaches are shifted on top of each other. The curves

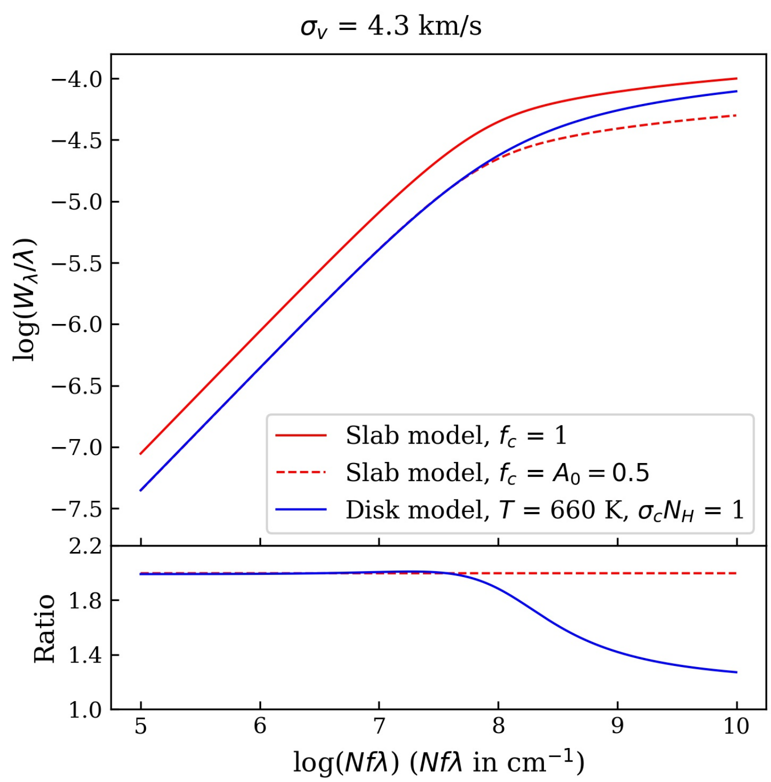

Figure 3.2: *Upper panel:* Curves of growth representing a slab model with and without a covering factor ($f_c = A_0$), and a stellar atmosphere model on a circumstellar disk adopting $\sigma_c N_H$=1. Both models were constructed with $\sigma_v = 4.3$ km s^{-1}, and $T = 660$ K adopted from the rotation diagram analysis of ^{13}CO is applied to the disk model. The central depth of an opaque line, A_0 under 660 K is 0.5. *Lower panel:* the ratio of each curve relative to that of the slab model without a covering factor.

shift along the X-axis because of the difference between β_0 and τ_p and the curves shift along the Y-axis because of the f_c versus A_0 factor. Specifically, when the two curves of growth overlap in the optically thin limit, $\tau_c = \sigma_c N_H = 1$. For a large optical depth, the lines in the slab model will saturate at f_c, while for the atmosphere, they go to A_0. However, even if we choose $f_c = A_0$, the approach to these limits is slightly different (Figure 3.2).

In summary, for highly optically thick lines, the rotation diagram will severely underestimate the column density/abundance of the absorbing species, and a curve-of-growth approach is required. In a foreground cloud scenario, high optical depth transitions can be recognized by saturated line profiles with zero intensity. However, if the cloud only partially covers the continuum source, the line profile will not go to zero intensity, even for highly optically thick lines. For absorption originating in the disk surface, a temperature gradient will naturally lead to nonzero intensity in the depth of the line. Introduction of an appropriate covering factor can make the two curve-of-growth approaches overlap, and the two approaches show only subtle differences for modestly optically thick lines (Figure 3.2).

3.5 Results

As we have summarized the analysis methods in Section 3.4, we present in this section the identification processes and the derived physical conditions of different components. We conduct the preliminary identification by iterating the decomposition of the line profiles and the rotation diagrams in Section 3.5.1, and present in Section 3.5.2 the procedures of modifications with the two curve-of-growth analyses. We discuss the properties of each identified component in Section 3.5.3.

3.5.1 Optically Thin Slab Modeling

Because most velocity components in our data are blended, we first attempt to use multiple Gaussians to fit and decompose the nonsaturated absorption profiles, assuming that the line is optically thin and its profile only consists of a Doppler core. We derive the physical conditions of each identified kinematic component via rotation diagrams in Figure 3.3 (and in Fig. C.1 for supplementary plots). Assuming a slab model in LTE, we get the τ and N_l of each absorption line (see Table C.1 in the Appendix) with equation 3.3 and 3.4, depending on whether the

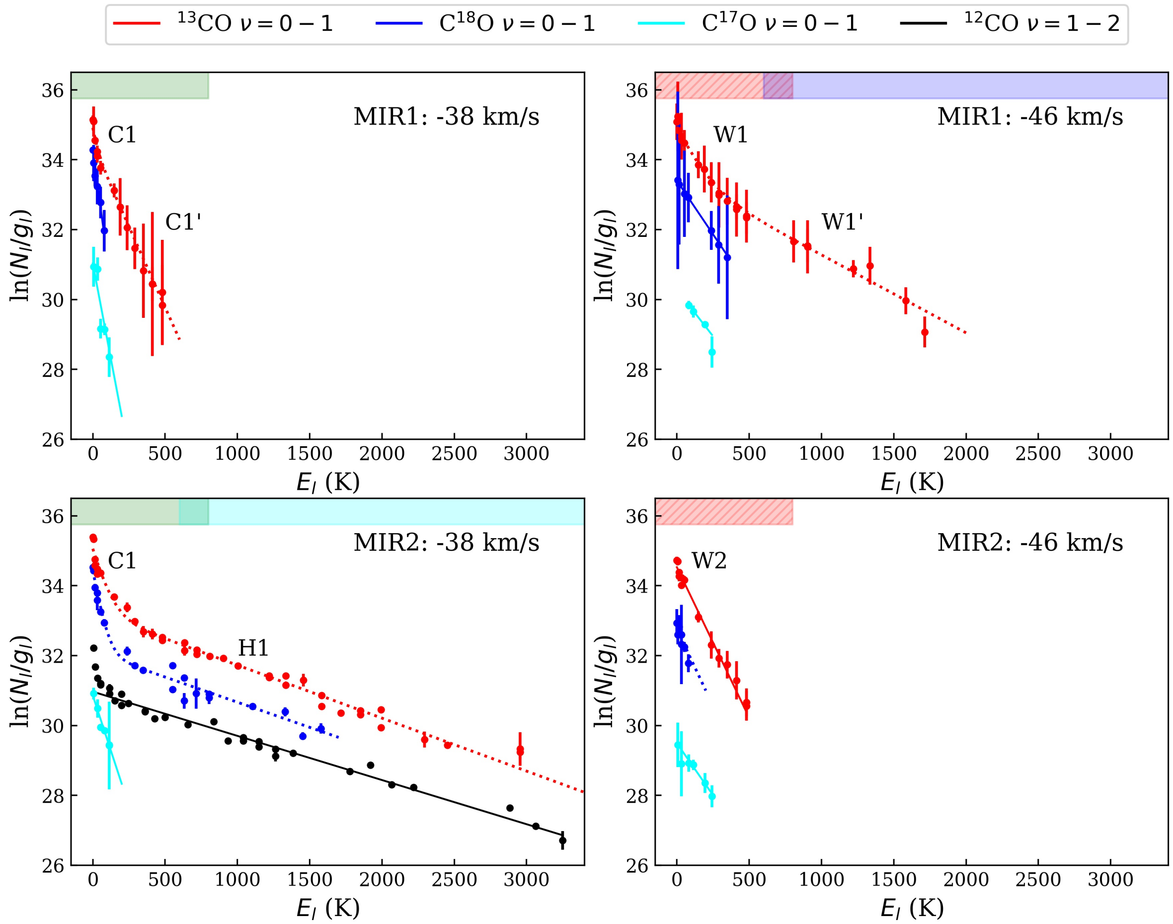

Figure 3.3: Rotation diagrams of ^{13}CO (*red*), C^{18}O (*blue*), C^{17}O (*cyan*), and ^{12}CO ν=1–2 (*black*) of a selected group of kinematic components. The colors of each component are consistent with those designated in Figure 3.4 (see supplementary rotation diagrams of other identified components in Figure C.1). N_l are derived from equation 3.2 with Gaussian fitting. Solid lines represent fitting results of equation 3.3 and dotted lines are of equation 3.4. The derived $T_{\rm ex}$ and $N_{\rm tot}$ are listed in Table 3.1.

$\ln(N_l/(2J+1))$-E_l/k_B relation on the rotation diagram has a constant gradient or not. Ideally, the identified kinematic components seen in the different isotopes with the same velocity center should originate from the same physical component and have consistent properties, such as line width and temperature.

We present the identified kinematic components in Figure 3.4 and list the line properties and derived physical conditions in Table 3.1. We grouped and named kinematic components from different species at consistent velocities with similar velocity widths based on their temperatures. In those names, “C”, “W”, and “H” stand for “cold”, “warm”, and “hot”. “B” represents the high-velocity components that appear exclusively in the ^{12}CO ν=0−1 transition in MIR2 (“B” stands for bullets; see § 3.5.3.5). For components of MIR1 at $-38\ \mathrm{km\,s^{-1}}$ (MIR1-C1/C1′) and $-46\ \mathrm{km\,s^{-1}}$ (MIR1-W1/W1′), and of MIR2 at $-38\ \mathrm{km\,s^{-1}}$ (MIR2-C1/H2), we see slope variation on the rotation diagrams. We address below in Section 3.5.3 whether this is due to an optical depth effect or a real temperature variation between different physical components.

Properties of distinctive components among different species in Table 3.1 cannot be easily reconciled. First, for all components with measurable ν=0−1 and ν=1−2 lines (MIR1-W1′, MIR2-H1, and MIR2-H2), the temperatures derived from ^{12}CO are much higher than those derived from isotopes. Second, the measured relative abundance ratios of isotopes are usually much smaller than the value found in the local ISM (see Table 3.2). Third, the velocity widths in different species do not always match. All of these issues reflect that optical depth effects are important. We justify below in Section 3.5.3 that for some components, those inconsistencies can be reconciled by introducing a curve-of-growth analysis, covering factors, and absorption in a disk photosphere.

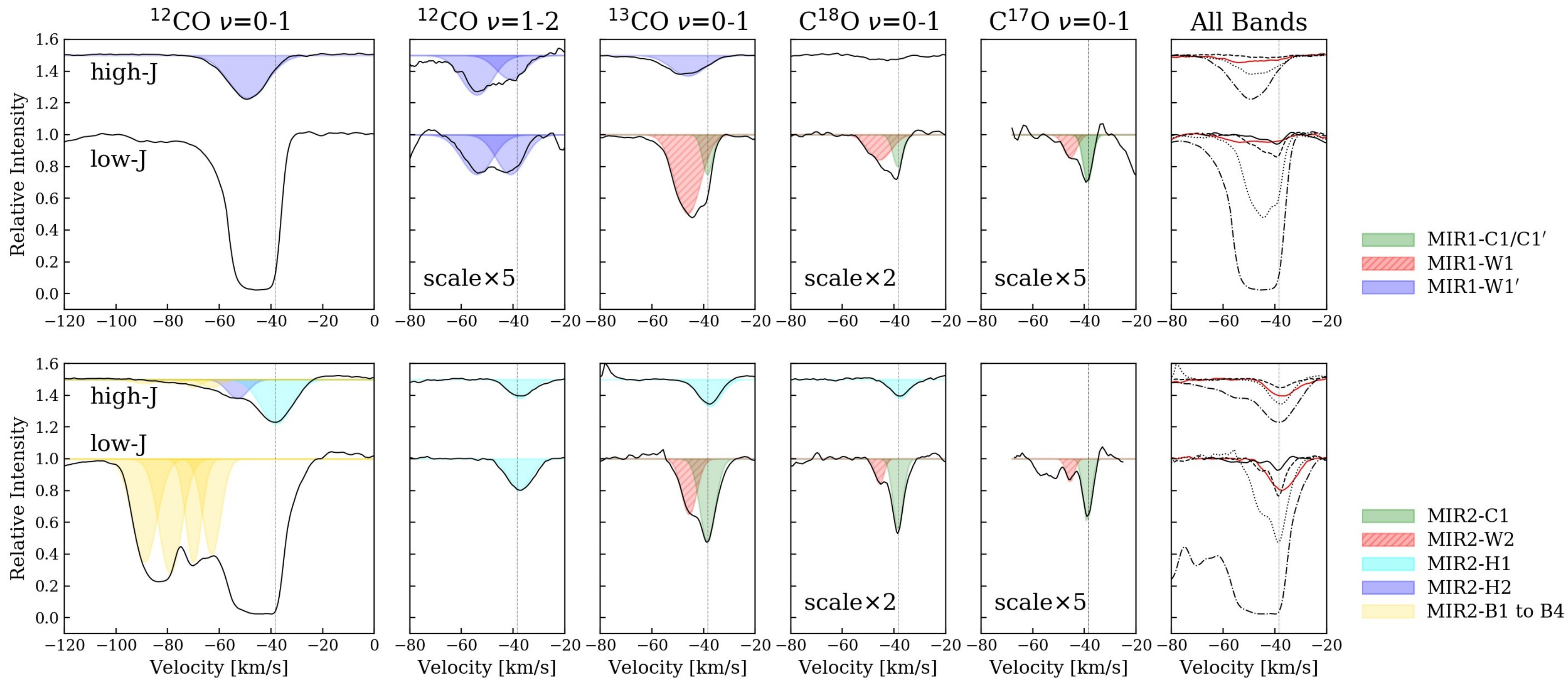

Figure 3.4: Identified kinematic components of MIR1 and MIR2 on the average spectra of low- and high-energy transitions. The detailed line information, as well as the derived physical properties of each kinematic component, are listed in Table 3.1. Here "C", "W", "H" stand for "cold", "warm", "hot" and "C1/C1′", "W1/W1′" indicate a change of temperature shown on the rotation diagrams. No components in the saturated part of ^{12}CO spectra in low-J are identified because we are not able to decompose distinct components there. The panels in the rightmost column summarize the identified components in the averaged spectra of all bands. The vertical dashed lines represent v_{sys}=-38.5 km s^{-1}.

3.5.2 Two Curve-of-growth Analyses

We discuss in this section the detailed analysis procedure for all identified components in Table 3.1. MIR2-W2 is not included, because its $N(^{13}\text{CO})/N(\text{C}^{18}\text{O})$ is even greater than the galactic [^{13}CO/C^{18}O] value. It is likely that there is an unresolved ^{13}CO component of which the C^{18}O component is buried in the noise, as indicated by the much broader ^{13}CO width in Table 3.1.

3.5.2.1 Slab Model of a Foreground Cloud

Assuming a foreground slab model, we use the curve-of-growth analysis to account for optical depth effects and determine the column density, temperature, and covering factor of a kinematic component of bands from all relevant CO isotopes. When a component is observed in multiple species, the smallest line width observed in ^{12}CO, ^{13}CO, or C^{18}O is used to estimate the Doppler parameter. We do not use the line widths observed in C^{17}O lines because rather large uncertainties would be introduced given the too few data points and poor baseline fitting. When a partial covering factor is necessary, it is bounded by the upper limit of the absorption intensity in the data sets. We obtain (T_{ex}, N_{tot}) by looking for the smallest reduced χ^2 in fitting the observable W_λ/λ to the curve-of-growth (equation 3.6), and estimate the 1σ uncertainty by looking for the $\chi^2_{r,\,min}$+Δ/dof contour in the (T_{ex}, N_{tot}) grid, where Δ is the χ^2 critical value for a significance level of 68.3%, and dof is degree of freedom, $n-2$ (n is the sample size). We summarize the results in Figure 3.5 and Table 3.3.

Table 3.1: Physical Conditions of Components in Fig. 3.3 Derived Directly from Gaussian Fitted Profiles and Rotation Diagrams.

Component (1)	Transitions (2)	E_l (K) (3)	J (4)	$v_{\rm LSR}$ ($\rm km\,s^{-1}$) (5)	σ_v ($\rm km\,s^{-1}$) (6)	$T_{\rm ex}$ (K) (7)	$N_{\rm tot}$ ($\times 10^{16}$ cm^{-2}) (8)
				MIR1			
MIR1-C1	^{13}CO ν=0−1	0−53	0−4	-38.5	2.0	$35.7^{+16.8}_{-16.9}$	$2.5^{+1.5}_{-1.0}$
	C^{18}O ν=0−1	0−79	0−5	-39.0	1.8	$49.1^{+33.2}_{-15.9}$	$1.3^{+0.6}_{-0.3}$
	C^{17}O ν=0−1	5−113	1−6	-39.0	1.5	$45.8^{+24.7}_{-13.3}$	$0.31^{+0.11}_{-0.07}$
MIR1-C1′	^{13}CO ν=0−1	148−481	7−13	-38.8	2.0	$120.2^{+18.5}_{-17.0}$	$5.5^{+1.6}_{-1.5}$
MIR1-W1	^{13}CO ν=0−1	0−481	0−13	-46.0	5.0	$103.2^{+43.7}_{-43.4}$	$9.0^{+4.6}_{-4.0}$
	C^{18}O ν=0−1	0−553	0−14	-46.0	4.0	163.6±4.1	2.1±0.1
	C^{17}O ν=0−1	81−243	5−9	-46.0	2.5	188.3±36.4	0.6±0.1
MIR1-W1′	^{13}CO ν=0−1	719−1994	16−27	-46.0	6.5	$448.5^{+86.5}_{-70.0}$	$12.1^{+4.1}_{-3.2}$
	^{12}CO ν=0−1	1937−5201	26−43	-49.0	7.5	956.3±56.7	74.2±15.4
	^{12}CO ν=1−2	3100−4347	2−21	-40.0	5.5	860.2±159.7	1.2±0.2
		3100−4347	2−21	-54.0	6.0	827.3±245.4	1.4±0.4
				MIR2			
MIR2-C1	^{13}CO ν=0−1	0−148	0−7	-38.5	2.8	31.4± 5.2	5.4± 0.7
	C^{18}O ν=0−1	0−79	0−5	-38.5	2.0	45.0± 3.2	1.7± 0.2
	C^{17}O ν=0−1	5-113	1−6	-38.5	1.6	$79.2^{+13.8}_{-15.4}$	$0.44^{+0.07}_{-0.06}$
MIR2-W2	^{13}CO ν=0−1	0−481	0−13	-45.5	3.0	116.1±6.9	8.8±0.5
	C^{18}O ν=0−1	0−79	0−5	-45.5	1.7	$97^{+33.4}_{-32.9}$	$0.7^{+0.2}_{-0.2}$
	C^{17}O ν=0−1	31−243	1−9	-45.5	1.6	168.0±19.0	0.24± 0.02
MIR2-H1	^{13}CO ν=0−1	634−2956	13−33	-37.5	4.3	$659.5^{+35.2}_{-40.8}$	$13.8^{+0.9}_{-0.8}$
	C^{18}O ν=0−1	237−1578	9−24	-37.5	3.4	$695.9^{+115.4}_{-89.3}$	$2.3^{+0.2}_{-0.2}$
	^{12}CO ν=0−1	1937−5687	26−45	-38.0	6.0	1162.1±55.1	65.3±8.6
	^{12}CO ν=1−2	3088−6331	1−33	-37.5	4.3	790.9±45.7	6.0±0.5
MIR2-H2	^{13}CO ν=0−1	808−1336	17−22	-52.0	4.0	484.9±98.3	2.4±1.2
	^{12}CO ν=0−1	1937−4293	26−45	-53.0	3.9	979.7±115.6	17.0±5.6
MIR2-B1	^{12}CO ν=0−1	0−1275	0−21	-89.0	3.5	265.2±11.5	24.9±1.6
MIR2-B2	^{12}CO ν=0−1	0−2085	0−27	-79.0	3.0	245.6±7.8	22.8±1.1
MIR2-B3	^{12}CO ν=0−1	0−2085	0−27	-70.0	3.0	229.8±6.2	13.6±0.6
MIR2-B4	^{12}CO ν=0−1	0−2564	0−30	-63.0	4.5	351.7±12.9	18.2±1.0

Column (1): Identified components. 'C1′' and 'W1′' represent the temperature gradient seen in component 'C1' and 'W1'. (5) Velocity of the line center. (6) σ_v: the standard deviation of the Gaussian core, and equals to $b/\sqrt{2}$. (7) & (8): Derived temperatures and total column densities. Values with asymmetrical uncertainties were the 16th and 84th percentiles derived from MCMC when there is a temperature gradient seen in the rotation diagram (dashed lines in Fig. 3.3).

Table 3.2: Column Density Ratios Derived from Rotation Diagram Analysis

Component	$N_{^{12}CO}/N_{^{13}CO}$	$N_{^{13}CO}/N_{C^{18}O}$	$N_{C^{18}O}/N_{C^{17}O}$
Galactic Ratios	66 ± 4[a]	$9.1^{+3.7}_{-3.3}$[b]	4.16 ± 0.09[c]
MIR1-C1	–	$1.9^{+2.1}_{-1.1}$	$4.2^{+3.7}_{-1.8}$
MIR1-W1	–	$4.3^{+2.5}_{-2.0}$	$3.5^{+0.9}_{-0.6}$
MIR1-W1′	$6.1^{+3.9}_{-2.3}$	–	–
MIR2-C1	–	$3.2^{+0.9}_{-0.7}$	$3.9^{+1.1}_{-0.9}$
MIR2-W2	–	$12.6^{+6.0}_{-3.3}$	$2.9^{+1.2}_{-1.0}$
MIR2-H1	$4.7^{+1.0}_{-0.9}$	$6.0^{+1.0}_{-0.8}$	–
MIR2-H2	$7.1^{+11.8}_{-3.9}$	–	–

[a] [^{12}C/^{13}C] of W3(OH) measured in (Milam et al., 2005).
[b] [^{16}O/^{18}O] = (58.8 $\pm$ 11.8) $\times D_{\rm GD}$ + (37.1 ± 82.6) (Wilson & Rood, 1994), which is 601.6±195.9 for W3 IRS 5. We adopt N(^{13}CO)/N(C^{18}O) = [^{12}CO/C^{18}O]/[^{12}CO/^{13}CO] = [^{16}O/^{18}O]/[^{12}C/^{13}C] in the table.
[c] Wouterloot et al. (2008).

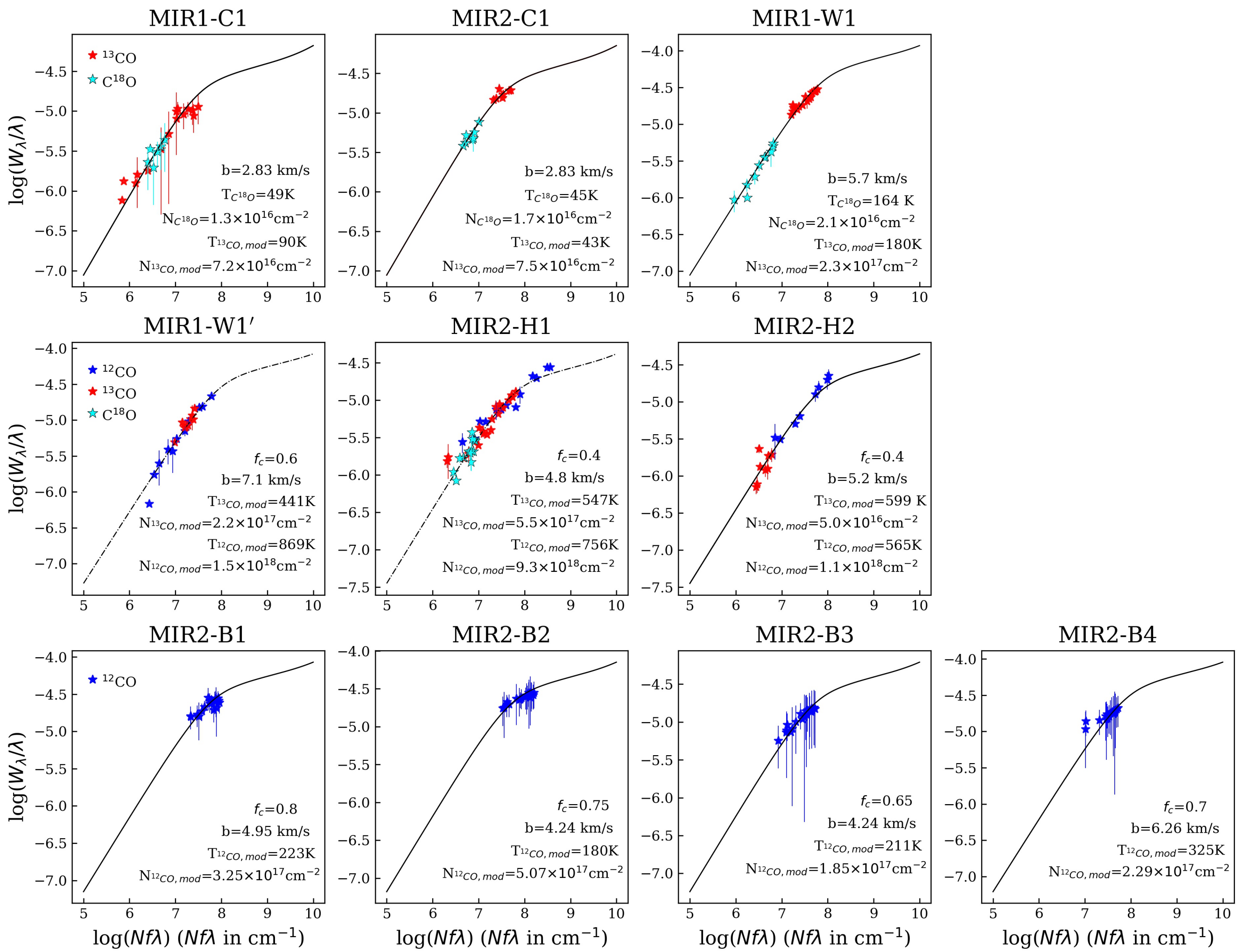

Figure 3.5: Best-fitting results of the observed $\log_{10}(W_\lambda/\lambda)$ versus $\log_{10}(Nf\lambda)$ and the theoretical curve-of-growth of a slab model on each individual component. The theoretical curve-of-growth and the values of $Nf\lambda$ are calculated based on the best-fit column density and temperature. Dashed curves of growth plotted on MIR1-W′ and MIR2-H1 indicate certain problems in the fitting results (§ 3.5.3.2 and § 3.5.3.3).

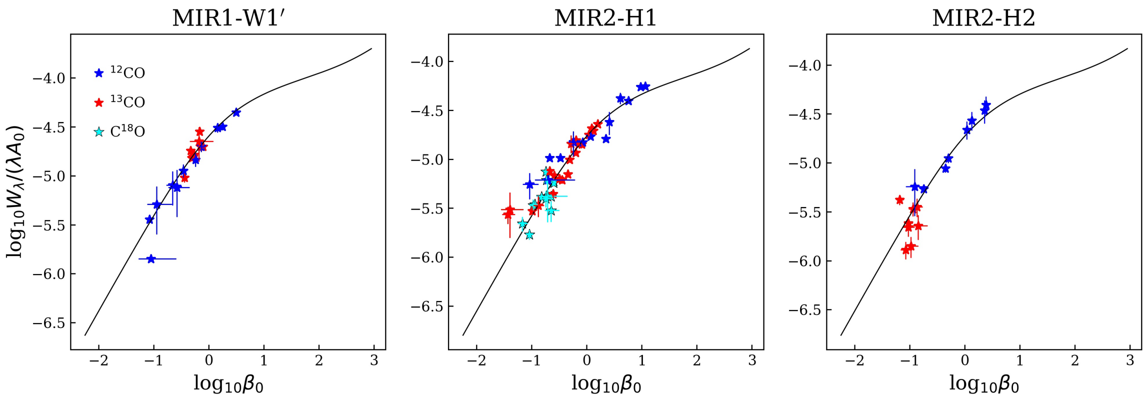

Figure 3.6: Best-fitting results of $\log_{10}(W_\lambda/(\lambda A_0))$-$\log_{10}(\beta_0)$ and the theoretical curve-of-growth of a stellar atmosphere model on MIR1-W1′, MIR2-H1, and MIR2-H2. The equivalent width in velocity space, W_λ (= $\lambda W_v/c$) of each molecular dataset is observable, and the Doppler width, b, is adopted from the smallest line width observed in ^{13}CO or C^{18}O (see texts in Section 3.5.2.2). The theoretical curve-of-growth, the values of β_0 and A_0 are calculated based on the best-fit N_{tot}/N_H and temperature.

3.5.2.2 Stellar Atmosphere Model of a Disk

Section 3.5.1 reveals three hot components (MIR1-W1′, MIR2-H1, and MIR2-H2) with temperatures between 500 and 700 K. This range is close to the dust temperature required to produce the observed continuum emission of the MIR disks. We therefore consider the possibility that three components are present in the photosphere of the disk and are absorbing against the continuum there. Similar to the curve-of-growth analysis on a foreground slab model, we apply the grid search method by fitting the observable W_v/c that equals W_λ/λ to the curve-of-growth (eqn 3.10) assuming pure absorption (see § 3.4.2.2). In the fitting procedure, we also reconcile the properties of different species by fitting with a Doppler width that is the smallest width measured among different species, i.e. ^{13}CO for MIR1-W1′ and MIR2-H2 and C^{18}O for MIR2-H1. We present the fitting results in Figure 3.6 and Table 3.4. We note that since the exact value of σ_c influences the derived absolute abundance ratio, we only present the relative abundance of different species in the same component in Table 3.4. If we assume that ^{12}CO has a constant relative abundance of 1.6×10^{-4} (Cardelli et al., 1996; Sofia et al., 1997), we may derive σ_c as listed in Table 3.5. The variation of σ_c for about an order of magnitude may convey information on the dust aggregation characteristics, for example, the dominant size in the aggregation distribution (Ormel et al., 2011).

3.5.3 Properties of Individual Components

3.5.3.1 MIR1-C1 and MIR2-C1

The two narrow low-J components (< 3 km s^{-1}) detected in ^{13}CO, C^{18}O, C^{17}O at -38 km s^{-1} sharing similar physical conditions are MIR1-C1 and MIR2-C1. Considering the results from the rotation diagram analysis (Table 3.1), for MIR1-C1, the ^{13}CO/C^{18}O column density ratio, $1.9^{+2.1}_{-1.1}$ is much less than the expected value of 9.1 (Table 3.2). Besides, the lines are not fit with a single temperature; the high-J levels reveal the presence of CO gas with a much higher excitation temperature. Hence, optical depth effects are indicated. The curve-of-growth analysis reconciles the temperatures of ^{13}CO and C^{18}O. As we present in Table 3.3, for MIR1-C1/C1$'$, a temperature of 90 K resolves the temperature difference for the C1/C1$'$ components in the ^{13}CO data. However, the C^{18}O excitation temperature is still discrepant (49 K; Table 3.1). For MIR1-C1/C1$'$, the isotopic column density ratios agree within the uncertainty level.

Table 3.3: Results From the Slab Model, Using a Curve-Of-Growth Analysis

Component	f_c	σ_v ($\mathrm{km\,s^{-1}}$)	$T_{^{12}\mathrm{CO,\,mod}}$ (K)	$T_{^{13}\mathrm{CO,\,mod}}$ (K)	$N_{^{12}\mathrm{CO,\,mod}}$ ($\times 10^{17}\,\mathrm{cm^{-2}}$)	$N_{^{13}\mathrm{CO,\,mod}}$ ($\times 10^{16}\,\mathrm{cm^{-2}}$)	$N_{^{12}\mathrm{CO}/^{13}\mathrm{CO,\,mod}}$	$N_{^{13}\mathrm{CO/C^{18}O,\,mod}}$
MIR1-C1	1.0	1.8	–	90^{+70}_{-27}	–	$7.2^{+6.4}_{-3.0}$	–	$5.4^{+8.1}_{-3.3}$
MIR2-C1	1.0	2.0	–	43^{+27}_{-13}	–	$7.5^{+3.7}_{-1.6}$	–	$4.4^{+3.1}_{-1.3}$
MIR1-W1	1.0	4.0	–	180^{+11}_{-14}	–	$23.0^{+2.5}_{-1.1}$	–	$10.9^{+1.8}_{-1.0}$
MIR1-W1′	0.6	5.0	869^{+155}_{-131}	441^{+94}_{-65}	$14.8^{+6.1}_{-3.8}$	$21.7^{+4.7}_{-2.2}$	$6.8^{+3.9}_{-2.7}$	–
MIR2-H1	0.4	3.4	756^{+49}_{-45}	547^{+44}_{-37}	$92.5^{+27.7}_{-20.5}$	$55.0^{+4.9}_{-6.1}$	$16.8^{+7.8}_{-4.8}$	$9.6^{+0.9}_{-1.1}$
MIR2-H2	0.4	3.7	565^{+122}_{-92}	599^{+518}_{-186}	$11.0^{+9.2}_{-3.9}$	$5.0^{+2.6}_{-1.4}$	$22.0^{+36.6}_{-11.5}$	–
MIR2-B1	0.8	3.5	223	–	3.25	–	–	–
MIR2-B2	0.75	3.0	180	–	5.07	–	–	–
MIR2-B3	0.65	3.0	211	–	1.85	–	–	–
MIR2-B4	0.7	4.5	325	–	2.29	–	–	–

For MIR2-B1 to B4, decomposing the blended line profiles may introduce large uncertainties. Hence, we do not report the uncertainty level in the derived physical conditions.

Table 3.4: Results for the Disk Atmosphere Model

Component	σ_v ($\mathrm{km\,s^{-1}}$)	$T_{^{12}\mathrm{CO,\,mod}}$ (K)	$T_{^{13}\mathrm{CO,\,mod}}$ (K)	$T_{\mathrm{C^{18}O,\,ex}}$ (K)	$X[^{12}\mathrm{CO}]/X[^{13}\mathrm{CO}]$	$X[^{13}\mathrm{CO}]/X[\mathrm{C^{18}O}]$
MIR1-W1′	5.0	709^{+136}_{-101}	474^{+152}_{-96}	–	$17.1^{+9.3}_{-5.9}$	–
MIR2-H1	3.4	662^{+33}_{-28}	507^{+47}_{-37}	676^{+230}_{-128}	$41.1^{+11.8}_{-9.8}$	$11.4^{+3.4}_{-3.3}$
MIR2-H2	3.7	482^{+97}_{-70}	542^{+795}_{-201}	–	$24.6^{+36.1}_{-16.4}$	

The absolute abundance of a species, $X[\mathrm{mol}]$, is defined as N_{mol}/N_H. Values of $X[\mathrm{mol}]$ in this table are dependent on the chosen dust opacity; therefore, we only report the relative abundance of different species in the table.

Table 3.5: Values of σ_c Derived from the Curve-of-growth Analysis in the Disk Model

Component (1)	σ_c (cm^2/H-nucleus) (2)	$N(^{12}\mathrm{CO})$ (cm^{-2}) (3)
MIR1-W1′	$2.7^{+1.0}_{-0.8} \times 10^{-23}$	$5.9^{+2.5}_{-1.6} \times 10^{18}$
MIR2-H1	$6.6^{+1.3}_{-1.2} \times 10^{-24}$	$2.4^{+0.5}_{-0.5} \times 10^{19}$
MIR2-H2	$1.2^{+0.8}_{-0.5} \times 10^{-22}$	$1.4^{+1.2}_{-0.6} \times 10^{18}$

Column (2): assuming a constant $X[^{12}\mathrm{CO}]$ of 1.6×10^{-4}, we derive values of σ_c via $(N_{\mathrm{mol}}/N_H)(\sigma_c/\sigma_{c0}) = 1.6 \times 10^{-4}$, in which $\sigma_{c0} = 7\times10^{-23}$ cm^2/H-nucleus following Barr et al. (2020).
Column (3): assuming that we are looking at the column density depth where the dust opacity approaches 1 (and, equivalently, $\sigma_c N_{\mathrm{H}} = 1$), $N_{\mathrm{mol}} = 1.6 \times 10^{-4}/\sigma_c$.

Table 3.6: Parameters of the Toy Model for MIR1-W1′

Component	f_c	b (km s^{-1})	T (K)	$N(^{12}\mathrm{CO})$ (cm^{-2})
MIR1-W1′-B	0.2	5.5	449	3.3×10^{19}
MIR1-W1′-N	0.5	4.0	449	2.7×10^{18}

Assuming $N(^{12}\mathrm{CO})/N(^{13}\mathrm{CO})$=66 (Milam et al., 2005).

For MIR2-C1, although the column density ratio is sufficiently uncertain that they could be in agreement, the excitation temperatures of these two isotopologs differ. Hence, here too, optical depth effects might be important. Taking these into account, the temperature becomes 43 K but the isotopolog abundance ratio, $4.4^{+3.1}_{-1.3}$, remains low compared to the expected ratio in the ISM (Table 3.3).

3.5.3.2 MIR1-W1 and MIR1-W1′

The two components at ~ -60 to -40 km s^{-1} are MIR1-W1 and MIR1-W1′. Their difference in temperature is indicated by the slope variation seen in the rotation diagram. MIR1-W1 is the cooler component. Although the rotation diagram analysis results in a much lower temperature of ^{13}CO (103 K) than that of C^{18}O (164 K) and an $N(^{13}\text{CO})/N(\text{C}^{18}\text{O})$ of only $4.3^{+2.5}_{-2.0}$ (Table 3.2), we can reconcile the properties of the two species by adopting the Doppler width of C^{18}O to ^{13}CO with the curve-of-growth analysis. The modified temperature of ^{13}CO is 180^{+11}_{-14}, and the modified relative column density is $10.9^{+1.8}_{-1.0}$ (Table 3.3).

The properties of the warmer component MIR1-W1′ are more complicated. Firstly, the line profiles in different transition bands are not consistent. As Table 3.1 shows, both low- and high-J lines in ^{13}CO center at -46 km s^{-1}, while the centers of unsaturated high-J ^{12}CO ν=0−1 lines are at -49 km s^{-1}. The ^{12}CO ν=1−2 lines have double peaks, with one at -40 km s^{-1} and one at -54 km s^{-1}. The comparison is more clearly illustrated in the final plot in the first row of Figure 3.4, where the average spectra of all bands are overlaid. The ^{12}CO and ^{13}CO seem to share the red wing for high-J lines.

The complexity seen in the line profiles indicates that they arise in somewhat different kinematic components; hence, we do not expect them to fall on a single rotation diagram or have an abundance ratio consistent with the isotope ratio. We present below the analysis over MIR1-W1 and MIR1-W1′ for completeness.

With the rotation diagram analysis, the temperature of ^{13}CO (449 K) is much less than that of ^{12}CO (956 K), and the relative column density ratio is only $6.1^{+3.9}_{-2.3}$ (Table 3.2). Adopting a Doppler width of 7.1 km s^{-1} and a fractional covering factor of ∼0.6, the saturated intensity, does not help to solve this problem. As we illustrate in Figure 3.5, after the modification with b and f_c, the ^{12}CO and ^{13}CO are still located on the linear part of the curve-of-growth. Therefore, we cannot reconcile the properties of ^{12}CO and ^{13}CO with a slab model assuming that the ^{12}CO and ^{13}CO lines each contain a single component. Considering substructures can work. For example, fixing the temperature of ^{12}CO to that of ^{13}CO derived from the rotation diagram and adopting an $N(^{12}\text{CO})/N(^{13}\text{CO})$ ratio of 66 (Milam et al., 2005), we may artificially fit the line profiles with a narrow component (MIR1-W1′-N, f_c=0.2) dominating the line peak and a broad component (MIR1-W1′-B, f_c=0.5) dominating the wing (see Table 3.6).

Applying a stellar atmosphere model can unify the temperatures of ^{12}CO and ^{13}CO. As we present in Figure 3.6 and Table 3.4, the dataset of ^{12}CO moves to the logarithmic part of the curve-of-growth. The 1σ temperature ranges of ^{12}CO and ^{13}CO are also comparable. However, we were only able to increase $X[^{12}\text{CO}]/X[^{13}\text{CO}]$ to $17.1^{+9.3}_{-5.9}$. Adopting a smaller σ_v increases the ratio further by at most up to twice; therefore, it reinforces that ^{12}CO and ^{13}CO do not originate from exactly the same component.

3.5.3.3 MIR2-H1

Component MIR2-H1 is close to v_{sys} at $-38\ \text{km s}^{-1}$ the same velocity as MIR1-C1/MIR2-C1, but it is intrinsically different. It appears in high-J lines and has a much broader line width (σ_v = 4.3 km s^{-1}) than MIR1-C1 and MIR2-C1 do. This component is hot enough to excite the vibrational band ^{12}CO ν=1−2. If we assume that the total N_0, the column density in the ν=0 level, for ^{12}CO is 66 times that of ^{13}CO, and compare it with N_1, the total column derived from ^{12}CO ν=1−2 in Table 3.1, we can derive a vibrational excitation temperature, T_{vib} of 613 K via the Boltzmann equation,

$$N_1/N_0 = \exp(-3083.11/T_{\text{vib}}). \tag{3.15}$$

This vibrational excitation temperature is consistent with the rotational excitation temperature and firmly links the absorption in the 0−1 and 1−2 transitions.

While the temperatures of MIR2-H1 derived from the rotation diagram analysis of the

^{13}CO, C^{18}O, and ^{12}CO ν=1−2 of the MIR2-H1 components are consistent with each other, they do not agree with the derived properties of the ^{12}CO ν=0−1 component. The temperature of ^{12}CO ν=0−1 derived from the rotation diagram is $\sim$ 1000 K compared to 650−750 K for the isotopologs and vibrationally excited transitions. In addition, the derived $N(^{12}\mathrm{CO})/N(^{13}\mathrm{CO})$ is only $4.7^{+1.0}_{-0.9}$ (Table 3.2). Similar to the MIR1-W1′ component, a slab model with f_c = 1 is not correct. Otherwise, we would expect the absorption intensity of this component to approach zero in low-J lines, which is also not seen in our observed spectra.

We present in Figure 3.5 and 3.6 the curve-of-growth analysis of MIR2-H1 on a modified slab model (f_c=0.4, σ_v=4.8 $\mathrm{km\,s^{-1}}$) and a stellar atmosphere model. As the ^{12}CO ν=0−1 dataset moves to the logarithmic part with both analyses, we confirm that the ^{12}CO ν=0−1 absorption profiles saturate in the Doppler core. We consider that, when the temperatures agree within 1σ, the different isotopologs probe the same gas (Table 3.3 and 3.4). The $N(^{12}\mathrm{CO})/N(^{13}\mathrm{CO})$ increases to $16.8^{+7.8}_{-4.8}$ and $41.1^{+11.8}_{-9.8}$, and $N(^{13}\mathrm{CO})/N(\mathrm{C^{18}O})$ increases to $9.6^{+0.9}_{-1.1}$ and $11.4^{+3.4}_{-3.3}$ (Table 3.3 and 3.4). For the slab model, the increased new column densities result in a lower T_{vib} of ^{12}CO ν=1−2 of 513 K, suggesting that the particle density in the foreground cloud does not reach the critical density of the vibrational band. The vibrational level is likely subthermalized.

Although the equivalent widths fit nicely with the curve-of-growth, we found a mismatch between the profiles of the modeled spectra and the observed spectra for both models. This is illustrated in Figure 3.7 which takes the modified slab model as an example. For the J <30 lines, the saturated modeled (green) spectra do not match the red wing of the observed spectra at $v_{\mathrm{sys}} > -38$ $\mathrm{km\,s^{-1}}$. We interpret this mismatch with an extra emission component in the red wing region, which is in emission. This component was also evident in the data of Mitchell et al. (1991, component E).

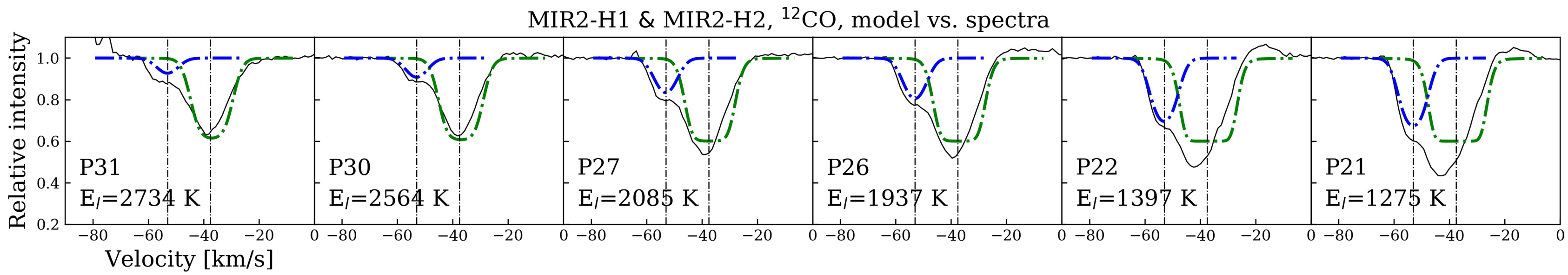

Figure 3.7: Comparison between the observed ^{12}CO spectra (*black*) and the modeled spectra (*green and blue dashed*) under the curve-of-growth modification with a slab model on MIR2-H1 (Section 3.5.3.3) and MIR2-H2 (Section 3.5.3.4).

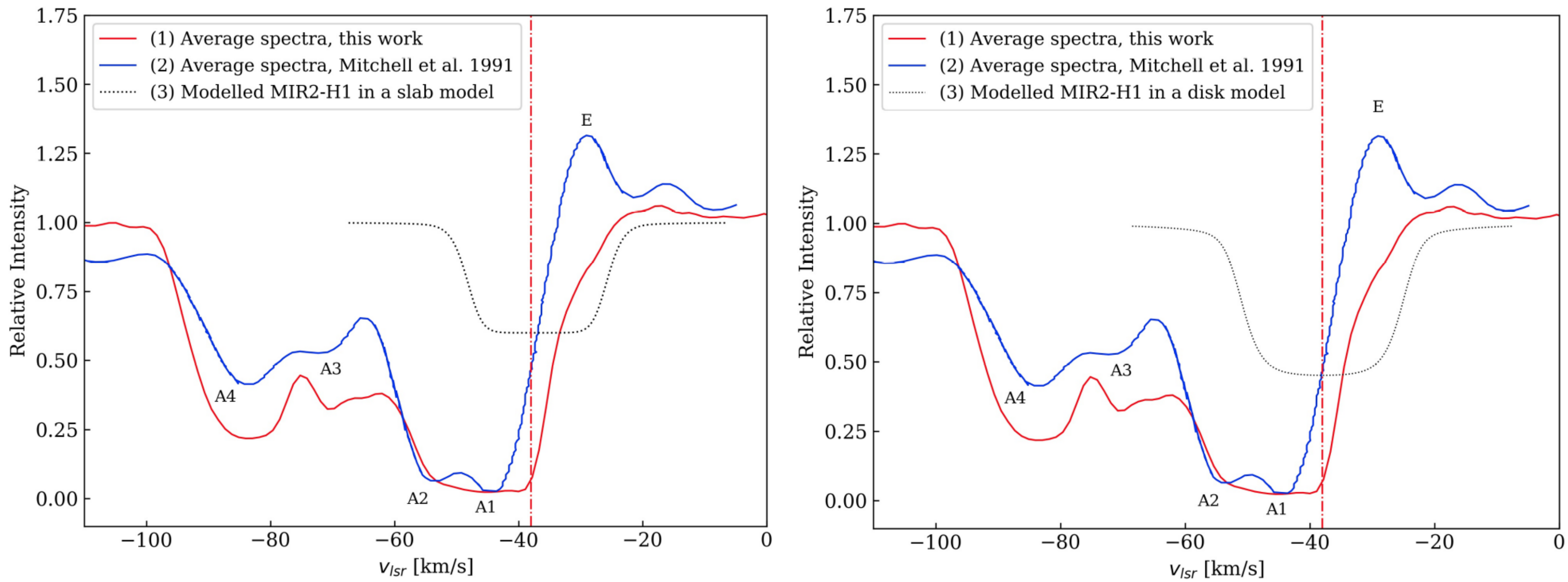

Figure 3.8: Comparison between the residual of the average of observed MIR2 spectra (P3, P6, P7, P8, P9, P12, R1, R3, and R7) minus that of the modeled MIR2-H1 spectra (*left*: the slab model; *right*: the disk model) and the average spectra reported in Mitchell et al. (1991), in which MIR1 and MIR2 were not distinguished. Both panels show that the difference between the observed spectra and the model may be a correspondence of the emission component "E" found in Mitchell et al. (1991).

We plot the average modeled spectra of MIR2-H1, the observed spectra of MIR2, and the average spectra of W3 IRS 5 from Mitchell et al. (1991) in Figure 3.8. All of the spectra were of ^{12}CO and were averaged over P3, P6, P7, P8, P9, P12, R1, R3, and R7 following Mitchell et al. (1991), in which MIR1 and MIR2 were not distinguished, and a potential emission component "E" at $\sim -30\ \mathrm{km\,s^{-1}}$ was reported. Although the modeled MIR2-H1 in both models does not match the observed spectra at $> -38\ \mathrm{km\,s^{-1}}$, the residual between the models and the observed spectra indicates an emission component. Compared to the observed spectra in Mitchell et al. (1991), this emission component may correspond to the "E" component there. This emission component is visible up to J=22, suggesting that it is rather warm. If this component is real, the comparable intensity indicates a comparable ratio between the emission area relative to the observation fields, which is a 2.5″ aperture covering the whole binary in Mitchell et al. (1991) and a 0.375″ wide slit in front of MIR2 in this study. Further spatially resolved spectroscopy is required to confirm the reality of this emission component and its physical characteristics.

3.5.3.4 MIR2-H2

The other component observed in ^{12}CO and ^{13}CO simultaneously is MIR2-H2. The value of $N(^{12}\mathrm{CO})/N(^{13}\mathrm{CO})$ of $7.1^{+11.8}_{-3.9}$ derived from the rotation diagram analysis (Table 3.2) also indicates an underestimation of the ^{12}CO column density. We reconcile the properties of ^{12}CO and ^{13}CO by adopting f_c = 0.4 and b = 3.7 $\mathrm{km\,s^{-1}}$ (Figure 3.5 and 3.7) in the slab model. We adopt b = 3.7 $\mathrm{km\,s^{-1}}$ for the atmosphere model. For both models, the modified temperatures of ^{12}CO and ^{13}CO are comparable. The corrected $N(^{12}\mathrm{CO})/N(^{13}\mathrm{CO})$ increases to $22.0^{+36.6}_{-11.5}$ and $24.6^{+36.1}_{-16.4}$ (Table 3.3 and 3.4), and the large uncertainties are due to the very few measurements of ^{13}CO lines on this component.

3.5.3.5 MIR2-B1 to B4

As iSHELL observations distinguish spectra that originated from the binary separately, the absorption features of ^{12}CO ν=0–1 between ~ -60 and -90 km s^{-1} were found to be exclusively associated with MIR2. No absorption lines of isotopologs were detected in this velocity range, indicating that these "B" components have much lower column densities than those between -38 to -60 km s^{-1}. We decompose the blended profile by four Gaussians (MIR2-B1 to B4) and derive similar temperatures (∼230–350 K) and total column densities ($\sim 2 \times 10^{17}$ cm^{-2}) from rotation diagram analysis.

For low-J lines of MIR2-B1 to B4, the steep slopes in the rotation diagrams, together with the flap-top line profiles, suggest line saturation in the Gaussian cores. We apply a covering factor of 0.8, 0.75, 0.65, and 0.7 based on the upper limit of the absorption intensities in the curve-of-growth analysis. We stress that there is a ∼5–7% uncertainty due to contamination of the binaries in the spectral extraction process (Section 3.3). As shown in Figure 3.5, all the four components are on the logarithmic part. The corrected temperatures (180–325 K) have a minor decrease, and the column densities of each component are increased by less than a factor of 2. We stress that our decomposition on the blended line profiles introduces a quite large uncertainty in these estimates and therefore do not report them in Table 3.3.

3.6 Discussion

The picture that emerges from the M-band spectroscopic study is of a shared foreground envelope, several high-velocity clumps, and a few warm and/or hot components in the immediate environment of the binary (Table 3.7). Identification of the origin of the absorption components requires more extensive analysis. In the subsequent subsections, we will place the observed CO absorption components in the framework of the known structures in the W3 IRS 5 star-forming region.

3.6.1 Known Structures of W3 IRS 5

Object W3 IRS 5 is a very active region of massive star formation, and the binary is oriented along the northeast-to-southwest direction. The binary is enclosed by a 10^4 au hot core detected in CS (van der Tak et al., 2000) and a rotating toroid or envelope of a similar size detected in SO_2 (Rodón et al., 2008; Wang et al., 2012, 2013). Outflows were observed at different scales; a bipolar outflow in CO(2–1) along the northeast-to-southwest direction was observed by the James Clerk Maxwell Telescope (JCMT) ($>10^5$ au; Mitchell et al., 1991) ranging from a v_{LSR} of -20 to $-60\ \mathrm{km\,s^{-1}}$, and two outflows along the line of sight were detected in SiO(5–4) ($0.39'' \times 0.34''$ beam at 1.4 mm, Rodón et al., 2008) by the Plateau de Bure Interferometer (PdBI) from a v_{LSR} of -30 to $-50\ \mathrm{km\,s^{-1}}$. A cavity in front of the binary cleared by the outflows was suggested to exist due to the low estimated foreground extinction (van der Tak et al., 2005). Along the northeast-to-southwest direction, a few fast-moving, compact, non-thermal radio continuum sources were found. As these jet lobes indicate jet-disk systems ($\sim 10^3$ au), MIR1 and MIR2 with thermal radio emission are disk candidates (Purser et al., 2021; Wilson et al., 2003). Moreover, hundreds of water maser spots are widely distributed in the same region (Imai et al., 2000; Menten et al., 1990), suggesting active clumps-surrounding gas interactions in the nearby region to the binary.

We present in Figure 3.9 the envelope, the conical region cleared by the outflows, the non-thermal continuum sources, and water masers to illustrate the important structures of W3 IRS 5. It is against this backdrop that we have to identify the origin of the different absorption components observed at MIR wavelengths in MIR1 and MIR2.

3.6.2 The Foreground Envelope: Gas and Ice

Because MIR1-C1 and MIR2-C1 have almost the same column density ($N_{^{13}\mathrm{CO}} \simeq 7.2 \times 10^{16}$ cm^{-2}; Table 3.3) and are at the same velocity, it is reasonable to designate them in the envelope surrounding the binary. The derived temperatures are cool (~40–90 K), suggesting that the envelope layer is rather far away from the protostars.

The total H column density of the envelope can be derived to be $N_H = 2{\times}10^{23}$ cm^{-2} ($A_V = 108$) from the observed 9.7 μm silicate optical depth ($\tau_{9.7\ \mu m} \simeq 5.8$; Gibb et al., 2004), the $A_V/\tau_{\rm sil}$ = 18.6, and $N_H/A_V = 1.9 \times 10^{21}$ cm^{-2} (Bohlin et al., 1978; Roche & Aitken, 1984). Therefore, adopting a ^{12}C/^{13}C elemental abundance ratio of 65 (Milam et al., 2005), this H column density (A_V = 108) implies an abundance of gaseous CO in the envelope of 2×10^{-5}. With a gas phase C abundance of 1.6×10^{-4} (Cardelli et al., 1996; Sofia et al., 1997), gaseous CO is not the main reservoir of carbon along these sight lines.

Table 3.7: Physical Conditions of Identified Components

Comp. (1)	$v_{\rm LSR}$ ($\rm km\,s^{-1}$) (2)	$T_{\rm k}$ (K) (3)	f_c (4)	$N_{\rm H_2}$ ($\times 10^{22}\,\rm cm^{-2}$) (5)	$J_{\rm max}$ (6)	log($n_{\rm crit}$) ($\rm cm^{-3}$) (7)	d (au) (8)	$\sigma_{\rm obs}$ ($\rm km\,s^{-1}$) (9)	σ_v ($\rm km\,s^{-1}$) (10)	Heating (11)	Ref. (12)
Shared Envelope											
MIR1-C1	-38.5	90	1.0	2.9	–	–	–	2.0	1.4	Radiation	3.6.2
MIR2-C1	-38.5	43	1.0	3.1	–	–	110	2.0	1.4	Radiation	3.6.2
MIR2 Bullets											
MIR2-B1	-89	223	0.8	0.21	21	7.27	7.4	3.5	3.2	J-shock	3.6.3
MIR2-B2	-79	180	0.75	0.32	27	7.60	5.3	3.0	2.6	J-shock	3.6.3
MIR2-B3	-70	221	0.65	0.12	27	7.60	2.0	3.0	2.6	J-shock	3.6.3
MIR2-B4	-63	325	0.7	0.14	30	7.73	1.8	4.5	4.3	J-shock	3.6.3
MIR1-MIR2 Immediate Environment (Warm)											
MIR1-W1	-43	180	0.6	1.4	13[a]	>6.52	<289	4.0	2.0	Radiation	3.6.4.1
MIR2-W2	-45.5	116	–	3.6	13[a]	>6.52	<720	1.7	0.9	Radiation	3.6.4.1
MIR1-MIR2 Immediate Environment (Hot): Foreground Interpretations											
MIR1-W1′	-46∼-49	449	0.5 & 0.2	1.7 & 20.6	ν=1-2	>10	–	2.8 & 3.9	2.5 & 3.7	–	3.6.4.2
MIR2-H1	-37.5	756	0.4	5.8	ν=1-2	>10	0.4	4.3	4.1	–	3.6.4.2
MIR2-H2	-52	565	0.4	0.7	37	8.01	4.1	3.7	3.5	–	3.6.4.2
MIR1-MIR2 Immediate Environment (Hot): Disk Interpretations											
MIR1-W1′	-46∼-49	709	–	3.7	ν=1-2	>10	–	5.0	4.8	Disk	3.6.4.3
MIR2-H1	-37.5	662	–	15.3	ν=1-2	>10	–	4.3	4.1	Disk	3.6.4.3
MIR2-H2	-52	482	–	0.9	37	8.01	–	3.7	3.5	Disk	3.6.4.3

[a] $J_{\rm max}$ identified in ^{13}CO. This is a very underestimated value because the ^{12}CO data at this velocity are saturated and not usable. For ^{13}CO, we use $n_{\rm crit} = 1.5 \times 10^3 J^3\,\rm cm^{-3}$.

Column (1): identified components. Column (5): $N_{\rm H_2} = N_{\rm CO}/(1.6 \times 10^{-4})$ (Cardelli et al., 1996; Sofia et al., 1997). Column (7): $n_{\rm crit}$ corresponds to the critical density that the highest J level requires to be thermalized. For ^{12}CO, $n_{\rm crit} = 2 \times 10^3 J^3\,\rm cm^{-3}$. This is a lower limit when estimating n. Column (8): $d = N_{\rm H_2}/n_{\rm crit}$; this is an upper limit for estimating the slab thickness. Column (10): deconvolved observed velocity dispersion, $\sigma_v = \sqrt{(\sigma_{\rm obs})^2 - (\sigma_{\rm res})^2}$. $\sigma_{\rm res} = c/(2\sqrt{2\ln 2}R)$.

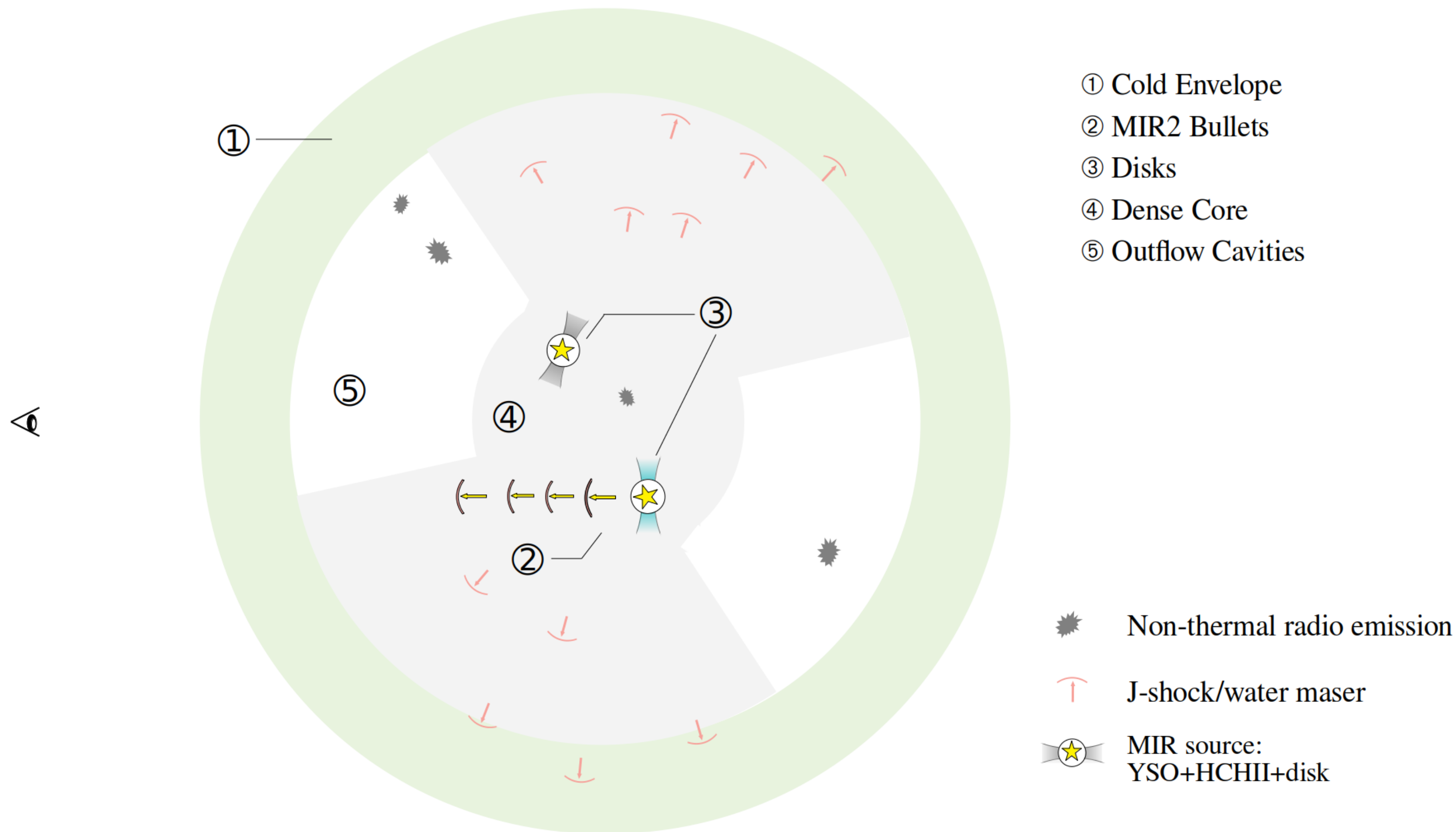

Figure 3.9: Schematic view of the potential environment of W3 IRS 5. Important structures from past studies, including the envelope, the conical region cleared by the outflows, the nonthermal continuum sources, and water masers, are presented. We locate the origins of new structures we identify in CO absorption, such as high-velocity bullets and disks, against this backdrop.

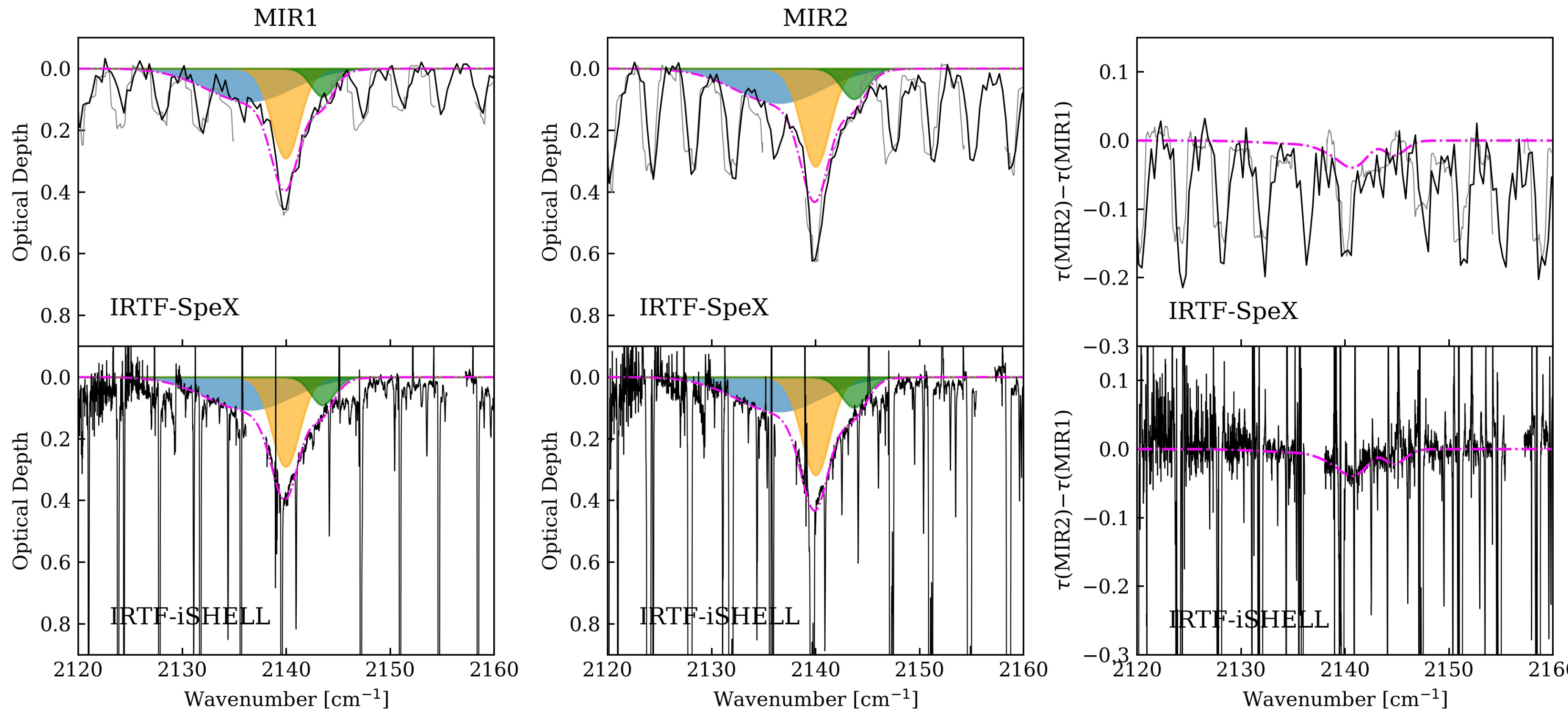

Figure 3.10: IRTF-SpeX (*upper panel*; R=1200) and IRTF-iSHELL spectra (*bottom panel*; R=88,100) toward MIR1 and MIR2 at 4.67 μm showing the CO ice band. IRTF-iSHELL spectra convolved to the resolution of 1200 (*grey*) are overlaid on SpeX spectra. The ice absorption profiles are fitted by three Gaussians over the iSHELL spectra: non-polar CO (*blue*, 2136.5 cm^{-1}), polar CO (*yellow*, 2139.9 cm^{-1}), non-polar CO (*green*, CO_2/CO>1, 2143.7 cm^{-1}). Gaussian fittings on iSHELL spectra are overlapped on SpeX spectra, as gaseous CO absorption lines there contaminate the ice absorption. The bottom right panel shows that the difference of the optical depth of features between MIR1 and MIR2 is smaller than 5%.

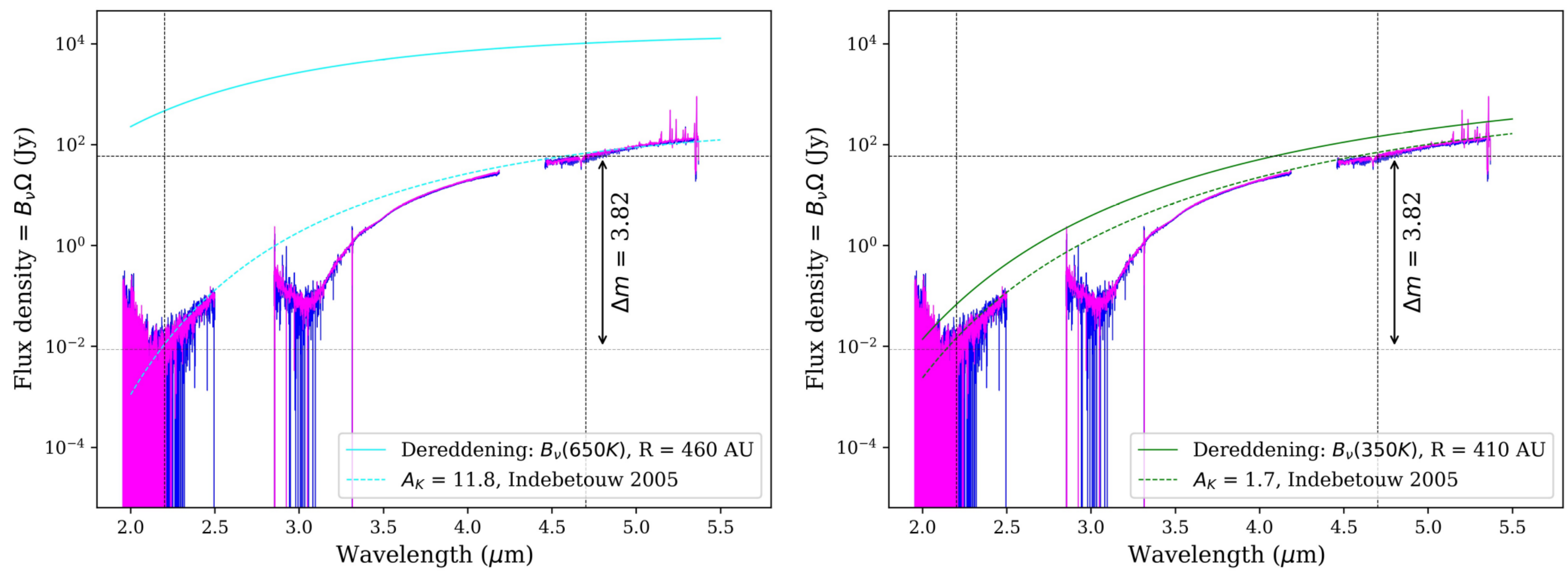

Figure 3.11: IRTF-SpeX spectra from 2–5 μm of MIR1 (*magenta*) and MIR2 (*blue*) compared to the flux density from two disks emitting in black body. Both the black body model (*solid*) and the reddened spectra (*dashed*) following the extinction law in Indebetouw et al. (2005) are presented. The extinction on the left panel is consistent with the 9.7 μm optical depth ($A_K = 11.8$), and that on the right panel is consistent with the column ($A_K = 1.7$) derived from the gaseous CO absorption adopting a CO abundance of 1.6×10^{-4}.

An independent view of the gas and dust columns toward W3 IRS5 is given by the IRTF/SpeX 2–5 μm micron spectra. We find that the foreground column density is consistent with the 9.7 μm optical depth if we consider that the near-IR and MIR continuum originates from the blackbody emission of the disks. Figure 3.11 shows that the magnitude difference Δm between the K and M bands is 3.82. Adopting the extinction curve from Indebetouw et al. (2005) and $A_K = 11.8$ ($A_V = 108$) derived from the 9.7 μm silicate band, the spectrum is consistent with a disk in a radius of 460 au emitting at 650 K, a typical temperature we have derived for the hot CO components (see Table 3.7 and § 3.6.4.2). On the contrary, if we use the foreground extinction that we measured from gaseous CO ($A_K = 1.7$, or, equivalently, $\sim 3 \times 10^{22}$ cm^{-2}; Table 3.7) adopting the canonical ^{12}CO abundance of 1.6×10^{-4} (e.g., all the gas phase C in CO), this leads to a blackbody temperature of 350 K with a radius of 410 au. However, we consider that the latter disk model is less likely because hot components above 600 K (e.g. MIR2-H1) will have emission rather than absorption lines against the 350 K disk (see Appendix A in Barr et al. 2022, *submitted*). Hence, this analysis of the near-infrared spectral energy distribution also implies that the measured CO column density of the cool foreground gas is only a good measure of the total hydrogen column density if we adopt a low (2×10^{-5}) abundance for ^{12}CO. We suggest that MIR interferometry observations may be able to distinguish between the different models at much lower temperature and much smaller foreground extinction.

The iSHELL/IRTF provides a direct handle on the solid CO ice along the same sight lines (see Figure 3.10). The CO-ice absorption profiles toward MIR1 and MIR2 are almost identical, supporting our conclusion that there is a shared cool envelope in front of the binary. Adopting a band strength $A = 1.1 \times 10^{-17}$ (Pontoppidan et al., 2003), $N_{\rm CO,\,ice}$ = 2.1$\times$10^{17} cm^{-2}. Specifically, nonpolar (centered at 2136.5 cm^{-1}) and polar (centered at 2139.9 cm^{-1}) CO have comparable column densities, suggesting that half of the solid CO ice is in H_2O- or CH_3OH-rich ice. Moreover, taking the column of CO_2 ice, 7.1×10^{17} cm^{-2} (Gibb et al., 2004), into account of the carbon inventory, carbon in solid phase is 19.6% of H_2O ice and 19.8% of gaseous CO. The column of H_2O ice is measured through the 3 μm absorption feature and is 5.1×10^{18} cm^{-2} (Gibb et al., 2004). Hence, the identified carbon-containing ice species cannot account for the missing C in the envelope. We may speculate that prolonged UV photolysis has converted the carbon containing ice compounds into an organic residue (Bernstein et al., 1995, 1997; Vinogradoff et al., 2013).

Taking into account that dust and gas will be well coupled thermally, we note that the derived temperature of the cold gaseous component (40−90 K) is well above the sublimation temperature of pure CO. Likewise, much of the CO trapped as a trace species in H_2O ice will sublimate at a temperature of $T_d \simeq 50$ K. We surmise that the polar CO-ice component coexists with the gaseous CO MIR1- and MIR2-C1 components in the warmer parts of the envelope, while the nonpolar component likely resides further away in a region where dust temperatures are below 20 K (see Figure 7.9 in Tielens, 2021).

3.6.3 The Foreground Bullets of MIR2

Although submillimeter observations have seen multiple molecular outflows in W3 IRS5, none of them are direct counterparts of MIR2-B1 to B4, which are at ∼20−50 km s^{-1} relative to a v_{sys} of -38.5 km s^{-1} (see Section 3.6.1). The range of the radial expansion velocity of water masers observed at 22 GHz (up to 60 km s^{-1}; Imai et al., 2000), on the other hand, is comparable with that of the MIR2 "bullets". As maser action is limited to regions of long velocity coherence, the bullets could be related to the water masers if they are directed more toward us and their maser action is directed away from us. In the remainder of this section, we will examine this possibility. As maser emission originates from either J- or C-type shocks driven by protostellar outflow (Hollenbach et al., 2013), we will consider the implications of each of these possibilities separately.

3.6.3.1 A J-Shock Origin

In fast J-shocks, the gas is instantaneously heated to an extremely high temperature, up to 10^5 K, that completely dissociates molecules and partially destroys dust behind the shock. As the material cools down, H_2 reforms on the surviving dust and is collisionally de-excited. The H_2 reforming stage provides a heating source and maintains the gas on a temperature plateau of $\sim$300–400 K (Hollenbach et al., 2013). This warm gas is very conducive to molecule formation, and the H_2O maser emission and CO absorption could originate in this temperature plateau region.

We can compare the physical properties of the absorbing bullets with what the J-shock model would predict. First, in the J-shock model for the H_2O maser emission, the CO column density of the heated plateau is as large as 3×10^{17} to 3×10^{18} cm^{-2} (Neufeld & Hollenbach, 1994), and is consistent with the derived column densities of MIR2-B1 to B4 in Table 3.7. Second, the postshock plateau density can be as high as 10^8–10^9 cm^{-3} (Hollenbach et al., 2013), and is also compatible with that of the bullets. As we have observed energy levels in LTE up to J = 30, the corresponding critical density is $\sim 3 \times 10^3\ J^3 \sim 8.1 \times 10^7$ cm^{-3}. This is a lower limit. In short, the temperature, the column density, and the particle density are in the favored parameter space for the masing regions produced by J-shocks.

3.6.3.2 A C-Shock Origin

In contrast to J-shocks, H_2 is not dissociated in C-shocks, and its relatively constant temperature plateau is kept by the frictional heating between ions and neutrals. The temperature of the shocked gas is typically much higher (>1000 K; Kaufman & Neufeld, 1996a) than observed for the MIR2-B1 to B4 CO absorption components. In the masing plateau, the warm hydrogen column is $\sim 10^{21}$ cm^{-2} (1.6×10^{17} cm^{-2} for CO; Kaufman & Neufeld, 1996a). Similar to J-shocks, densities of $10^8 - 10^9$ cm^{-3} are required for H_2O maser action in C-shocks (Hollenbach et al., 2013).

Therefore, interpreting the warm gas in the B components in MIR2 as C-shocks faces some issues. First, the observed temperature under 400 K is rather low and would restrict the shocks to a velocity less than 10 km/s (Kaufman & Neufeld, 1996a). Second, the observed column densities are a factor of 1–3 larger than C-shocks can produce. This is irrespective of whether these bullets are truly water maser counterparts.

3.6.3.3 Linking the Bullets to Water Masers

If MIR2-B1 to B4 indeed originate from the post-J-shock gas, the physical properties we obtain along the line-of-sight direction are complementing what water masers convey on the sky plane. The CO absorption lines and the water masers are depicting different perspectives of the geometry of the postshock gas. Water masers are beamed emissions that require enough coherence path length in our direction. While masers formed in a compressed shell of postshock gas swept up by outflows, observable masers are typically viewed from an "edge-on" direction that is perpendicular to the motion of the shock. Therefore, while the brightest masers have the lowest line-of-sight velocities, CO components detected in our absorption spectra complement information along the line of sight, and the maser emissions are the weakest.

The water masers have a smaller velocity width and size than the B components; in Table 3.7, the velocity widths (2.6–4.3 $\mathrm{km\,s^{-1}}$) and the thickness (2–10 au) of the absorbing bullets are larger than but not incompatible with the average velocity width, from 0.8 to 1.6 $\mathrm{km\,s^{-1}}$ in 1997 and 1998, and the average size of 1 au of 22 GHz water masers observed in the region surrounding MIR1 and MIR2 in W3 IRS5 (Imai et al., 2002). We may expect that the water masers have a smaller velocity width because of the required velocity coherence. We are observing them perpendicular to the propagation direction, while the bullets are coming more toward the observer. Besides, the estimated thickness of the bullet is an upper limit derived simply by $N_{\mathrm{H_2}}/n_{\mathrm{crit}}$. As a reference, the thickness of the masing region predicted by the shock model (Hollenbach et al., 2013) is $\sim 10^{14}$ cm (6.7 au). Hollenbach et al. (2013) has proved that, although the value of the maser thickness predicted by the J-shock model depends on exact shock properties, strong water maser emission is a robust phenomenon that can be generated from a wide range of physical conditions without a fine-tuning of parameters.

We have to consider the likelihood that the four bullets are intercepting the narrow pencil beam set up by the background IR source. For the hundreds of water masers, Imai et al. (2002) found that the two-point spatial correlation function among 905 maser spots can be fitted by a power law. With an index of -2 in a linear-scale range of 1.1–540 au, this indicates that in this scale range, the features are clustered and have a "fractal" distribution. Considering that adding four more radially identified data points (MIR2-B1 to B4) over the $0.375'' \times 1.2''$ continuum from our observations does not have a significant influence over the correlation function, the correspondent $\sim$10 spots per square arcsecond corresponds to a spatial separation of $\sim$0.2″($\sim$450 au), which fits with the maser geometry (Imai et al., 2000). However, we note that those seemingly nice fits do not answer why the spatial distribution of the masers is clustered. As for the direction along the line of sight, Imai et al. (2002) also found a power-law on the velocity correlation function. The measured difference in Doppler velocity and the spatial separation was fit with an index of 0.29$\pm$0.03 and was putatively linked to Kolmogorov-type turbulence in the interiors of the masers. It was suggested that small-scale turbulence was left in the subsonic part of the postshock region (Gwinn, 1994). Consistent with a postshock origin, MIR2-B1 to B4 fit into this power-law correlation.

3.6.4 The Immediate Regions of MIR1 and MIR2

All absorbing components in our MIR spectra other than MIR2-B1 to B4 are located in the range ~ -38 to -60 $\mathrm{km\,s^{-1}}$. Although our analyses of the isotope lines have shown that the components within this range are different, saturated ^{12}CO low-J lines still share a fortuitous similar line profile, with its red edge contributed by MIR1-C1 and MIR2-C1, the surrounding envelope at $v_{\rm sys}$, and its blue edge contributed by MIR1-W1/W1′ and MIR2-H2. Such a profile shared by MIR1 and MIR2 indicates the underlying correlation of the two sources, and we investigate how components within ~ -38 to -60 $\mathrm{km\,s^{-1}}$ constitute the immediate regions of MIR1 and MIR2. As the observations are consistent with absorption arising either in foreground clumps or in the disk, we will consider these in turn.

3.6.4.1 Radiative Heating

Assuming the gas and dust are thermally coupled, we use equation 5.44 and equation 5.43 in Tielens (2005) to estimate the distance of the gas to the protostars if the gas is radiatively heated,

$$T_d \simeq 53 \left(\frac{0.1\ \mu m}{a}\right)^{0.2} \left(\frac{G_0}{10^4}\right)^{0.2}, \tag{3.16}$$

and

$$G_0 = 2.1 \times 10^4 \left(\frac{L_*}{10^4 L_\odot}\right) \left(\frac{0.1\ \mathrm{pc}}{d}\right)^2, \tag{3.17}$$

in which G_0 is the radiation field in terms of the Habing field, a is the grain size, L_* is the stellar luminosity, and d is the distance. Taking 0.1 μm as a typical size for interstellar grains,[4], and that MIR1 and MIR2 have a similar L_* of $4{\times}10^4 L_\odot$ (van der Tak et al., 2005), we arrive at a d of 280, 140 au for the 450 K (MIR1-W1′) and ∼600 K (MIR2-H1, MIR2-H2) components and d of at least 2000 au for the cooler components (MIR1-W1, MIR2-W2, < 200 K).

However, locating the hot components at such a small distance to the protostars is in conflict with the similarity of the 1991 and 2018 CO absorption line profiles (see § 3.5.3.3). Considering that MIR1-W1′ and MIR2-H2 have a constant relative velocity of 10 and 15 km s^{-1}, the two components moved outward along the line of sight for 60 and 100 au in the past 30 yr. As the moving distances are quite large, radiative heating cannot keep MIR1-W1′ and MIR2-H2 at the observed high temperature. As for MIR2-H1, which is at v_{sys}, it would have to stay static at a distance of only 140 au for 30 yrs and yet be close to a massive forming protostar. It could be

[4] We recognize that grains may have grown to ∼0.3–0.5 μm in dense clouds due to coagulation (Ormel et al., 2011), but that will have a very little effect on the MIR absorption compared to the far-IR emission. We estimated it will change the temperature by 20–30%.

Table 3.8: Keplerian Parameters of Hot Blobs on the Disk

Component	v_{lsr}(MIR1) ($\mathrm{km\,s^{-1}}$)	v_{lsr}(MIR2) ($\mathrm{km\,s^{-1}}$)	$v - v_{lsr}$ ($\mathrm{km\,s^{-1}}$)	d (au)	P (yrs)	Note
MIR1-W1′	-38	–	$>$10	$<$180	$<$540	Blob on an inclined disk
MIR1-W1′	-46	–	0	–	–	Annular structure
MIR2-H1	–	-38	0	–	–	Blob on a face-on disk
MIR2-H2	-38	-38	$>$15	$<$80	$<$180	Blob on an inclined disk

part of a disk associated with the protostar.

3.6.4.2 A J-shock/C-shock Origin

Alternatively, a shock origin for the hot components is attractive, as the vibrationally excited lines observed toward MIR1-W1′ and MIR2-H1 indicate a very high density, $\sim 10^{10}$ cm^{-3} for thermalization at the ν=1 level. However, because J-shocks cannot heat the masing gas to temperatures greater than about 400 K (Hollenbach et al., 2013), and the column density is far too large to be consistent with C-shocks (see § 3.6.3.2), neither a J-shock nor a C-shock model fits.

3.6.4.3 A Disk Origin

In Section 3.5.3, we illustrate that the curve-of-growth analysis on a disk model can reconcile the temperatures measured from the observed CO isotope spectra of MIR1-W′, MIR2-H1, and MIR2-H2 at a 1σ level. Other than being a feasible model, such a disk origin of hot gas has been proposed in other massive protostellar systems. Take AFGL 2591 and AFGL 2136 as examples. In Barr et al. (2020), absorption features against the MIR continuum were detected in CO, CS, HCN, C_2H_2, and NH_3, and all have a temperature of ~600 K. The disk origin was motivated by the abundance difference on both HCN and C_2H_2 at 7 and 13 μm; e.g., the abundance derived from HCN as well as C_2H_2 lines at 13 μm is about an order of magnitude smaller than that derived from lines at 7 μm, even though the lines originate from the same ground state. This was attributed to a dilution effect at 13 μm, as the outer parts of the disk radiate predominantly at 13 μm, and these outer layers have lower abundances of these species (Barr et al., 2020). MIR interferometry has shown that the IR emission originates from a structure with a size of $\sim$100−200 au for both AFGL 2136 (de Wit et al., 2011; Frost et al., 2021a; Monnier et al., 2009) and AFGL 2591 (Monnier et al., 2009; Olguin et al., 2020) and this is likely a disk. This scenario is also supported by Atacama Large Millimeter/submillimeter Array (ALMA) (AFGL2136; Maud et al., 2019) and NOEMA (AFGL2591; Suri et al., 2021) observations in which Keplerian disks are revealed. Clumpy substructures that may be associated with the absorbing components were resolved on the disk of AFGL 2136 in the 1.3 mm continuum (Maud et al., 2019), supporting the model that a cooler component is absorbing against the continuum from the disk.

We hereby attribute the absorption to blobs in a disk in accordance with studies of other massive protostars. However, given the unknown inclination and systematic velocity of the disk, the location of the blobs on the disk is difficult to pinpoint. We present the Keplerian parameters of the three hot components in Table 3.8 to illustrate the difficulty in interpreting the kinematics, and specifically note that we measure a radial velocity and the blobs could be much further away if the disks are not in the plane of the sky and radial velocities contain little information on Keplerian motion. We emphasize that the velocity difference between the blobs in MIR1 and MIR2 is the interplay of the orbital motion of the blobs in these disks and the difference in space motion between the two protostars where we note that the orbital motion of a double star system (each has 20 $M_\odot$) at 1000 au is $\sim$ 3 km/s. Therefore, disks in MIR1 and

MIR2 need to be spatially and spectrally resolved to a fully understand of the structures in this region.

We stress in the end that, while such a model is feasible to interpret the observed absorption profiles, we still lack definite evidence to link the absorbing gas in the MIR with the disks in W3 IRS 5. We recall that in Section 3.6.2, for both MIR1 and MIR2, we fit the 2–5 μm spectrum with a 650 K disk in a radius of 360 au. We acknowledge that this is an oversimplified model, and the dust composition, the extinction correction, or the actual disk geometry may influence the fitting result. This radius is compatible with the disk radii (500–2000 au) that Frost et al. (2021b) found for some massive young stellar objects using multiscale and multiwavelength analysis. However, we recognize that the derived radius is slightly larger than the size of MIR1 and/or MIR2 of 350-–500 au at 4–10 μm (van der Tak et al., 2005). This value is also quite large compared to the $\sim$100 au size measured by MIR interferometry for other massive protostellar systems (Beltrán & de Wit, 2016; Monnier et al., 2009), although Frost et al. (2021b) discussed that the MIR emission is mostly dominated by emission from the inner rim of the disk and therefore may not constitute the size of the whole disk. We suggest that complementary observations in MIR and millimeter interferometry will help to disentangle the issues above.

3.6.5 Comparison with Hot Core Tracers

The hot core at $v_{\rm sys}$ of -38 km s^{-1} in the W3 IRS 5 system revealed by submillimeter molecular lines is a spatially (10^3–10^4 au) and spectrally (σ_v $\sim$5 km s^{-1}) extended structure (van der Tak et al., 2000; Wang et al., 2013). As a comparison, the absorbing components in the MIR are observed in "pencil" beams (subarcsecond scale, or a few hundred au). Since we have decomposed the different CO absorbing components by their velocities and temperatures (Table 3.7), it is of interest to compare the molecular components in emission and in absorption. We note that the postshock bullets do not leave any signatures on the hot core tracers, possibly because their beam-averaged column densities in the large submillimeter beams are very small.

The submillimeter CO observations reveal emission at $-38\ \mathrm{km\,s^{-1}}$ with a ^{12}CO column density derived from C^{17}O observations of 3.7×10^{19} cm^{-2}. This column density is much higher than that of the cold envelope, $-38\ \mathrm{km\,s^{-1}}$ components (MIR1-C1/MIR2-C1 and MIR2-H1) probed in the MIR ($N_{^{12}\mathrm{CO}} = 4.7 \times 10^{18}$ cm^{-2}, Table 3.3, ^{12}C/^{13}C = 65). This may well be because the submillimeter includes emission from the core (Figure 3.9) which is not traversed by the MIR pencil beam.

Other submillimeter molecular tracers, such as SO, HCN, and CS rotational transitions, also reveal the hot core at a rather extended scale of ∼3000–5000 au (beam size of 1.1″×0.8″, Wang et al., 2013). While the exact measurements of the column densities are lacking, as the lines are heavily filtered out at v_{sys}, these tracers are all in the velocity range (-30 to $-50\ \mathrm{km\,s^{-1}}$) characteristic of the molecular core. The submillimeter continuum dust emission provides a beam-averaged H_2 column density of the core of 1.5×10^{23} cm^{-2} (Wang et al., 2013). Coincidentally, this is similar to the H_2 column density derived from the envelope derived from the pencil beam observations of the strength of the 9.7 μm silicate feature (2×10^{23} cm^{-2}, Section 3.6.2). Therefore, similar to the discussion of CO emission lines above, neither the SO, HCN, and CS rotational lines nor the dust continuum trace the envelope components MIR1-C1/MIR2-C1 and MIR2-H1 probed in the MIR but rather entire core region.

The SOFIA HyGal survey (Jacob et al., 2022) provides constraints on hydride molecules (such as CH) and atomic constituents (C^+ and O) against the far-IR/submillimeter continuum, as well with beam sizes of from 6–14″. The CH, C^+, and O are all in the velocity range of the envelope. Adopting a CH abundance of 3.5×10^{-8}, appropriate for diffuse clouds (Sheffer et al., 2008), Jacob et al. (2022) inferred an H_2 column density of 2.7×10^{21} cm^{-2}. Even if we adopt an abundance of 10^{-8}, typical for dark cloud cores (Loison et al., 2014), the inferred H_2 column density is only 10^{22} cm^{-2}. This is small compared to either the pencil beam column density derived for the envelope from the 9.7 μm silicate feature or the average column density of the core derived from the submillimeter dust. Perhaps much of the carbon has frozen out in the envelope and/or core in the ice mantles. The CH observed by HyGal may then mainly trace the surface layers of the cloud. It is reasonable to assume that the [CII] 1.9 THz fine-structure line traces the photodissociated surfaces of the molecular cloud. Taking a fractional gas phase carbon abundance of 1.6×10^{-4} (Sofia et al., 1997), this corresponds to a column of hydrogen of 3.7×10^{21} cm^{-2}, a typical value for a photodissociation region (PDR) surface (Tielens & Hollenbach, 1985). The column density of O measured at 63 μm (2.2×10^{18} cm^{-2}) is rather comparable to the amount of oxygen in water ice (5×10^{18} cm^{-2}) measured at 3 μm, and a large fraction of the elemental oxygen is locked up in water ice in the envelope.

3.7 Summary

In this chapter, we report the results of a high-resolution (R=88,100) MIR spectroscopy study of W3 IRS 5 at 4.7 μm, in which hundreds of absorption lines of ^{12}CO and its isotopologs, including ^{13}CO, C^{18}O, C^{17}O were resolved. The main results are summarized as follows.

1. Different spectroscopic properties of MIR1 and MIR2 are spatially resolved for the first time, and the high-velocity components between -60 and -90 km s^{-1} are attributed exclu-

sively to MIR2.

2. In low-J lines, MIR1 and MIR2 share very similar saturated ^{12}CO line profiles between -38 and -60 $\mathrm{km\,s^{-1}}$, but we decomposed and identified components from the blended profiles with very different physical properties.

3. For components identified with Gaussian fittings, their physical conditions derived from the rotation diagram analyses show that optical thin assumptions fail. The derived column density ratios are much lower than the expected CO isotope ratios, indicating that optical depth effects have affected the rotation diagram analyses.

4. To reconcile the physical properties derived from different isotopes from the same velocity component, we have analyzed the data using a curve-of-growth approach. In this, we consider two scenarios: (1) absorption by foreground blobs that partially cover the background continuum source and (2) absorption in the photosphere of a circumstellar disk that has a decreasing temperature gradient in the vertical direction.

5. We applied the slab model to all of the components and constrained the corresponding covering factor and Doppler width. We found that this slab model fits nicely to most of the components other than two very hot ones with large column densities (MIR1-W1$'$ and MIR-H2).

6. We applied the stellar atmosphere model to all of the hot components ($>$400 K) and were able to reconcile all of the related molecular lines to a single curve. This procedure provides abundance ratios relative to the MIR continuum opacity of the dust.

7. We assign the identified components to the immediate environment of W3 IRS 5, including

the shared envelope, the foreground clumps produced by either J- or C-shocks, and the disk. Direct radiation can be a heating mechanism for some components.

8. Components MIR1-C1 and MIR2-C1 originate from a shared cool envelope in front of the binary. However, the rather low abundance of gaseous CO suggests that gaseous CO is not the main reservoir of carbon in the envelope. The identified carbon-bearing ice species cannot account for the missing C in the envelope.

9. Components MIR2-B1 to B4 ("bullets") are possibly J-shock-compressed regions akin to the regions that produce the water maser emission. Our observations in CO lines likely complement the constraints on the physical conditions of water masers from a different geometry perspective. As bright water maser spots are usually beaming in a direction that is perpendicular to their motions, CO absorption lines reveal their properties along the line of sight when water masers have the weakest brightness.

10. The modeled spectra of MIR2-H1 from both modifications do not match the observed spectra of MIR2 in its red wing at $v_{\rm sys} > -38$ km s^{-1}. However, we found that the residual between the model and the measurement matches the potential emission component reported by Mitchell et al. (1991) at -35 km s^{-1} in velocity position and intensity. If the residual represents a real emission component, this is a P Cygni profile indicative of an outflow on a scale of $\sim$1000 au.

11. Our curve of analyses favor the hot components (400–700 K) located at the two circumstellar disks. However, given the unknown inclination and the unknown systematic velocity of the disk, the location of the blobs on the disk is difficult to pinpoint. Spatially and spec-

trally resolving the disks in MIR1 and MIR2 will help fully understand the structures in this region.

Chapter 4: High-resolution SOFIA/EXES Spectroscopy of Water Absorption in the Massive Young Binary W3 IRS 5

4.1 Chapter Preface

Chapter 4 is presented with minimal changes and has been submited to ApJ as "High-resolution SOFIA/EXES Spectroscopy of Water Absorption Lines in the Massive Young Binary W3 IRS 5". At the stage of the submission of this thesis, the author is working on the referee report. The authors are Jialu Li, Adwin Boogert, Andrew G. Barr, Curtis DeWitt, Maisie Rashman, David Neufeld, Nick Indriolo, Yvonne Pendleton, Edward Montiel, Matt Richter, J. E. Chiar, and Alexander G. G. M. Tielens.

4.2 Introduction

Massive stars reach the main sequence while they are deeply embedded and are still accreting. While rich chemistry is driven as the central object warms and ionizes the environment, complicated physical activities such as accretion disks, outflows, shocks, and disk winds are involved (Beuther et al., 2007; Cesaroni et al., 2007; Zinnecker & Yorke, 2007). However, the large distances to the observers, the high extinction at optical and near-infrared wavelengths, and the highly clustered environment impede a clear understanding of their formation and evolution processes.

High spectral resolution, pencil beam absorption line studies at mid-infrared (MIR) wavelengths provide a unique opportunity to probe the embedded phases in massive star formation (Lacy, 2013). On the one hand, the MIR continuum originates from the photosphere of the disk at a distance of tens to a few hundreds of au (Beltrán & de Wit, 2016; Frost et al., 2021a). The effective pencil beam, therefore, avoids beam dilution issues that submillimeter observations are subject to. On the other hand, molecules without dipole moments such as C_2H_2 and CH_4, which are among the most abundant carbon-bearing molecules, can only be observed through their rovibrational spectra in the infrared. MIR spectroscopy at high resolution, therefore, is a critical tracer of the physical conditions, the chemical inventory, and the kinematics of structures close to the massive protostars.

Among the rich chemical inventory in the regions associated with the protostars, water is of fundamental importance because it is one of the most abundant molecules in both the gas and ice phase. As its abundance varies largely between warm and cold gas (e.g., Bergin et al., 2002; Draine et al., 1983; Kaufman & Neufeld, 1996b), water has a powerful diagnostic capability in probing physical conditions (van Dishoeck et al., 2021). However, due to its prevalence in the Earth's atmosphere, water is very difficult to observe from the ground. We present in this work the power of combining the Stratospheric Observatory for Infrared Astronomy (SOFIA, Young et al., 2012) that flies observes between 39,000 and 45,000 feet and the Echelon Cross Echelle Spectrograph (EXES, Richter et al., 2018) spectrometer which resolves lines to several km/s to make the most of the diagnostic capability of water.

Previous studies of the MIR water absorption spectrum toward massive protostars (Boonman & van Dishoeck, 2003; Boonman et al., 2003a) have revealed a rich spectral content. High spectral resolution observations can provide much insight into the characteristics of these regions. (e.g., Barr et al., 2022a; Indriolo et al., 2020). Water has also been studied at high spectral resolution via pure rotational transitions, using the heterodyne instruments on board SWAS, Odin, and *Herschel* Space Observatory (e.g., Chavarría et al., 2010; Karska et al., 2014; Snell et al., 2000; Wilson et al., 2003). Because of their limited spatial resolution, these observations mainly probed the large-scale environment of these sources.

We conducted high spectral resolution (R=50,000) spectroscopy from 5–8 μm with EXES on board SOFIA toward the hot core region close to the massive binary protostar W3 IRS 5. W3 IRS 5 is a luminous, massive protostellar binary with a separation of 1.2$''$ ($\sim$2800 au at $2.3^{+0.19}_{-0.16}$ kpc, Navarete et al., 2019) that is in transition from the embedded to the exposed phase of star formation (van der Tak et al., 2000, 2005). Millimeter studies reveal complex structures, including a hot molecular core with large-scale outflows, shocks, and a circumbinary toroid (Imai et al., 2000; Rodón et al., 2008; Wang et al., 2012, 2013). High spectral (R=88,100) and spatial resolution observations in the M-band (4.7 μm) also show a complex structure, and Li et al. (2022) use this to determine the physical conditions.

In this chapter, we present the rich spectrum of rovibrational (the ν_2 band) water lines observed in absorption toward W3 IRS 5. The high spectral resolution spectroscopy allows us to separate and identify individual velocity components that are linked to different stars in the W3 IRS 5 binary and to derive the temperatures, the level-specific column densities as well as the total column densities (and/or the abundances). We describe our observations and data reduction in Section 4.3 and our analysis methods with both the rotation diagram and the curve-of-growth in Section 4.4. We present the properties of multiple dynamical components in Section 4.5 and discuss the implications of the results in Section 4.6.

Table 4.1: Observational Parameters

Source (1)	Date (UT) (2)	Time (UT) (3)	λ (μm) (4)	$v_{\rm geo}$ (km s^{-1}) (5)	Long. (deg) (6)	Lat. (deg) (7)	Alt. (feet) (8)	ZA (deg) (9)	Slit Height ($''$) (10)	PA (°) (11)
W3 IRS 5	2022-02-24	09:01:10	5.36–5.51	-20.8	-117.11	49.11	41772	63.97	2.11	293.3–312.5
	2021-12-04	08:57:30	5.48–5.67	-36.8	-124.41	29.93	43072	46.06	1.74	318.3–335.2
	2021-12-04	08:01:15	5.65–5.84	-36.8	-132.92	26.80	43075	40.21	1.74	42.4–67.3
	2021-12-02	06:46:07	5.83–6.02	-37.5	-91.80	34.73	41513	40.66	1.74	17.4–36.3
	2021-12-01	07:26:18	6.01–6.20	-37.9	-104.60	38.89	40113	35.51	1.93	19.9–37.7
	2021-06-16	07:11:54	6.01–6.20	-51.5	-98.82	45.37	42475	62.47	1.93	236.0
	2021-06-16	06:00:33	6.18–6.37	-51.5	-113.11	48.40	41056	67.76	2.31	259.0
	2021-12-01	08:10:29	6.19–6.37	-37.9	-98.06	41.39	40607	40.87	2.31	3.0–14.8
	2021-06-11	19:37:02	6.35–6.61	-50.1	-111.17	48.82	41004	61.99	1.36	226.9–245.3
	2021-06-18	06:40:39	6.35–6.61	-52.1	-100.56	45.11	41079	64.06	1.36	226.9–241.5
	2021-06-18	05:37:44	6.59–6.85	-52.1	-114.09	47.81	41002	67.61	1.55	247.8–263.7
	2021-06-10	19:55:04	6.59–6.85	-49.7	-98.07	45.88	42010	59.82	1.56	218.1–234.1
	2021-06-09	18:45:41	6.79–7.06	-49.4	-123.32	51.26	41023	64.68	1.75	242.2–265.1
	2020-02-06[a]	08:38:37	7.02–7.21	-21.0	-126.47	46.66	43007	55.00	3.06	318.7–331.3
	2022-02-24	07:53:55	7.19–7.45	-20.8	-131.46	45.93	40589	57.87	2.33	318.3–335.2
	2018-10-31[b]	03:26:20	7.34–7.52	-49.4	-102.79	33.33	38020	39.28	3.25	152.7–173.0
	2020-02-07[a]	09:10:52	7.49–7.68	-21.0	-152.16	49.01	41024	45.90	3.43	312.5–341.6
	2021-06-09	20:06:39	7.67–7.92	-49.4	-107.06	48.97	43011	59.73	2.51	226.3–238.9
Sirius	2022-02-24	06:45:01	7.18–7.46	–	-135.36	41.32	39098	62.13	–	–

[a] AOR_ID: 07_0063.

[b] AOR_ID: 76_0004.

Column (1): Sirius is the standard star for the observation session on 2022-02-24 at 7.19–7.45 μm. Column (5): velocity of the target relative to the Earth. Column (6)–(9): the longitude, latitude, altitude, and zenith angle of the telescope of the observation session. Column (10)–(11): the height and the position angle (from north to east) of the slit. Note that the shortest slit height (1.36$''$) is longer than the distance between the binary of W3 IRS 5 (1.2$''$). For all settings, the slit width is fixed to 3.2$''$.

4.3 Observations and Data Reduction

Object W3 IRS 5 was observed with the EXES spectrometer (Richter et al., 2018) on board SOFIA observatory from 2021 June to 2022 February as part of programs 08_0136, 09_0072. Archival data observed in programs 07_0063 and 76_0004 were included in this study as well. The full spectral survey covers a wavelength range of 5.3–7.9 μm in 18 observational settings and was observed under the HIGH-LOW cross-dispersed mode. The observational parameters of all 18 settings are listed in Table 4.1. For all settings, the slit width is fixed to 3.2″ to limit slit losses perpendicular to the slit (at a SOFIA PSF FWHM of ∼3.0–3.5″), which provides a spectral resolution of $R \sim 50,000$, or equivalently, a velocity resolution of 6 $\mathrm{km\,s^{-1}}$. The slit length is dependent on the wavelength and the angle of the echelle grating and is in the range of 1.36–3.43″ after accounting for the anamorphic magnification (Figure 4.1). Off-slit nodding was applied to remove the background night sky emission and the telescope thermal emission.

The EXES data were reduced with the SOFIA Redux pipeline (Clarke et al., 2015), which has incorporated routines originally developed for the Texas Echelon Cross Echelle Spectrograph (Lacy et al., 2003). The science frames were despiked and sequential nod positions subtracted, to remove telluric emission lines and telescope/system thermal emission. An internal blackbody source was observed for flat fielding and flux calibration and then the data were rectified, aligning the spatial and spectral dimensions. The wavenumber solution was calibrated using sky emission spectra produced for each setting by omitting the nod-subtraction step. We used wavenumber values from HITRAN (Rothman et al., 2013) to set the wavelength scale. The resulting wavelength solutions have 1σ errors of 0.5 $\mathrm{km\,s^{-1}}$.

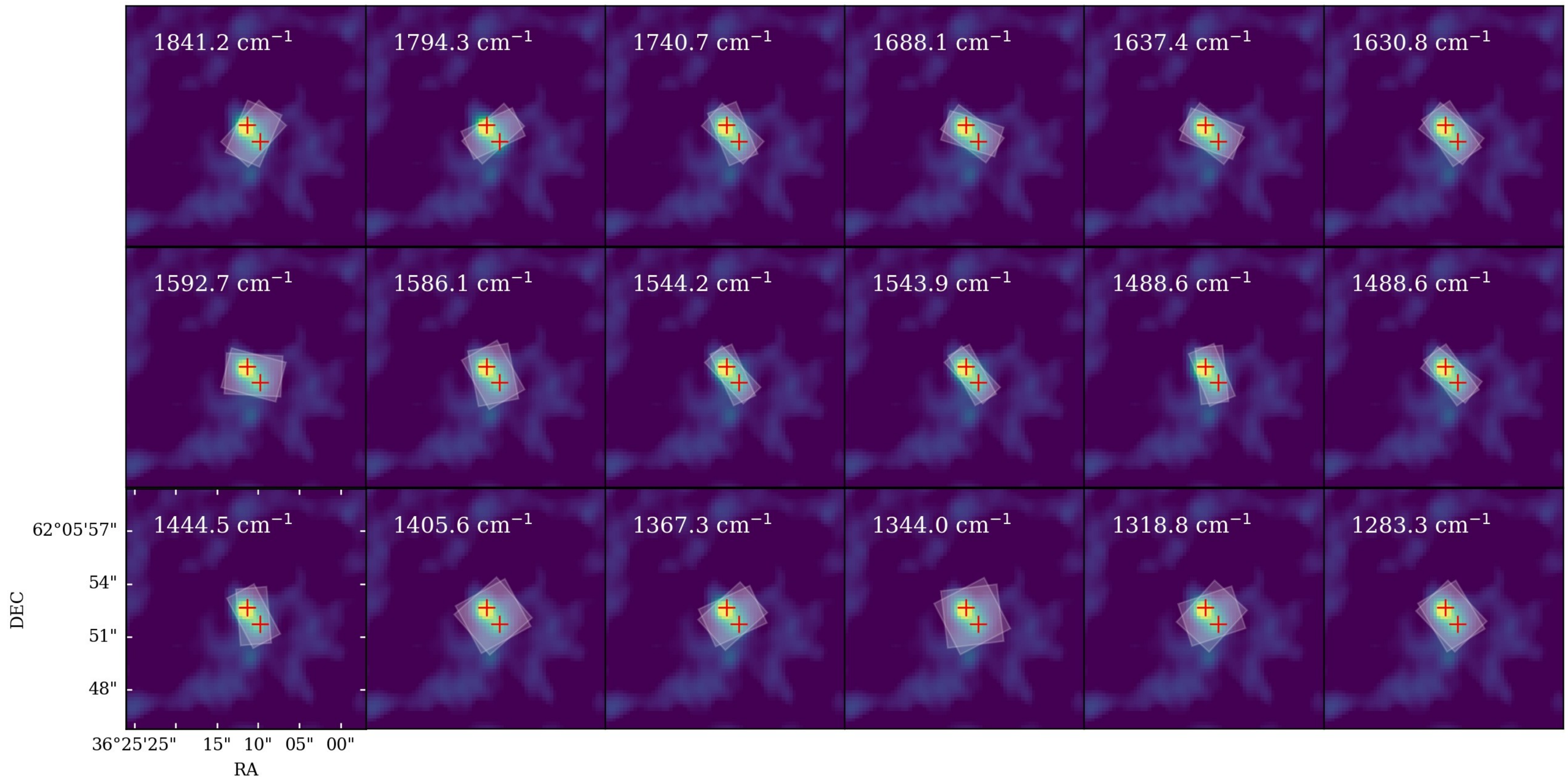

Figure 4.1: Slit coverage (white rectangles) on top of W3 IRS 5 at different observational settings. Only the initial and final positions are plotted in the figure. The range of the position angles is listed in Table D.1. The three settings centered at 1405.6, 1344.0, and 1318.8 cm^{-1} are the archival data. The background is the PdBI 3.4 mm image of W3 IRS 5 adopted from Rodón et al. (2008) and the two red crosses mark the positions of the proto-binary stars.

Before measuring intrinsic lines in the source, the spectra had to be corrected for telluric absorption. Ideally, this is done by taking a spectrum of a featureless hot star immediately before or after the target observation, so that the atmospheric characteristics are as close as possible between the target and calibrator. This method also has the advantage of removing instrumental baseline effects present in both spectra. Unfortunately, it was impractical to schedule calibrators for every part of the W3 IRS 5 survey due to limitations of airborne observation scheduling, and thus only one survey setting was observed with the adjacent calibrator star Sirius (7.28–7.46 μm, Table D.1). For the rest of the survey, we relied on carefully tuned atmospheric transmittance models created with PSG (Planetary Spectrum Generator, Villanueva et al., 2018). Compared to a standard star spectrum, an atmospheric model only predicts the telluric features by assuming certain parameters including the molecular species, the pressure, the altitude, etc (see Appendix D.1). After a PSG model is considered, further data reduction such as removing the local baseline is still required. We utilized the 7.28–7.46 μm calibrator comparison to establish the reliability of the procedure (see Appendix D.2), and apply the PSG models to all the observed settings.

Since the distance between the binary (1.2$''$) is smaller than the SOFIA PSF ($\sim$3–3.5$''$), W3 IRS 5 is not spatially resolved in the observed spectra. As both sources contribute to the observed flux in our slit, the derived equivalent width of an absorption associated with one IR source will be diminished by the continuum emission from the other source. The two sources have very comparable MIR brightness (see the SpeX observations in Li et al., 2022) and we include a factor 2 in our analysis to account for this effect throughout this study unless otherwise stated. It should be mentioned that the actual contribution of the non-absorbing source will depend on the slit orientation over the source and this changes slightly between the different

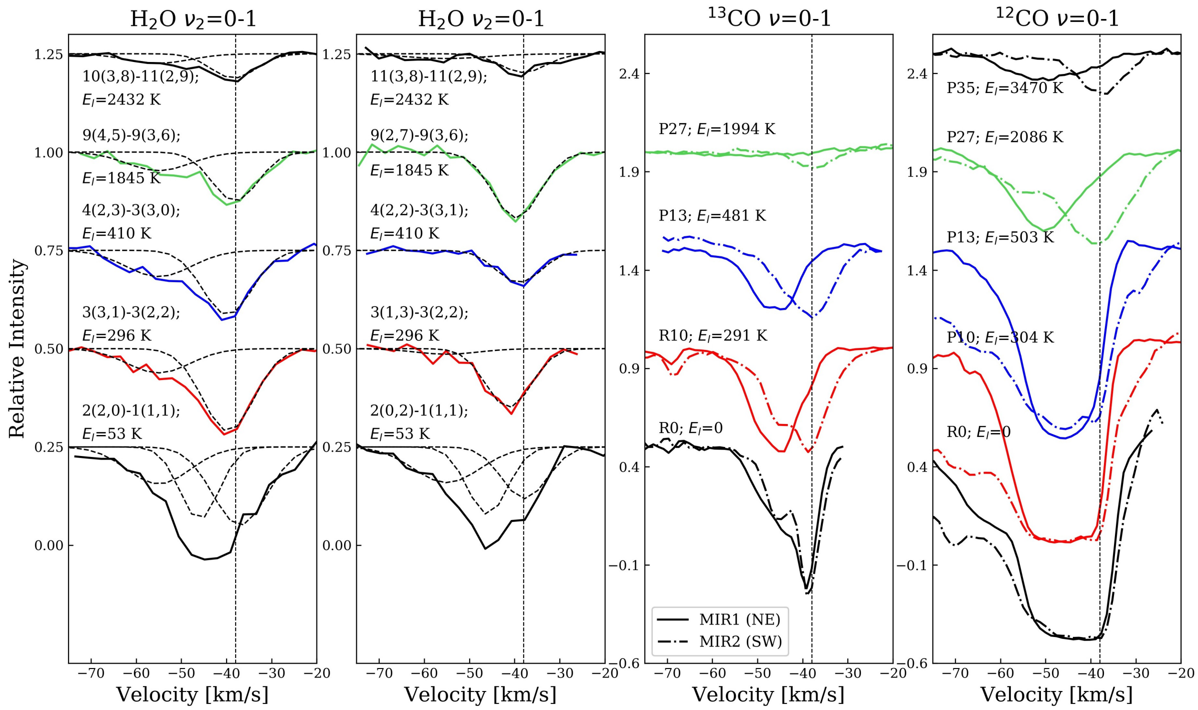

Figure 4.2: Selected H_2O ν_2=0−1, ^{13}CO ν=0−1, and ^{12}CO ν=0−1 (adopted from Li et al., 2022) absorption lines observed toward W3 IRS 5, which is spatially resolved to MIR1 and MIR2 by IRTF but not by SOFIA. The dashed vertical lines at -38 km s^{-1} are the systematic velocities. Transitions with similar energy levels are represented by the same color. Distinct kinematic components in H_2O transitions are present under different excitation conditions. Gaussian fitting profiles on top of H_2O lines are centered at -55, -46, and $-40 \sim -38$ km s^{-1}. We note that H_2O line profiles originate from states with comparable energies and may differ significantly due to the opacity effect (see § 4.4.1).

grating settings (see Figure 4.1). We have decided to accept this additional source of uncertainty to the results in view of the uncertain brightness distribution of the two sources on the sky.

4.4 Data Analysis

By comparing with the spectra constructed via the existing laboratory line information (HITRAN, Rothman et al., 2013) and LTE models, we identified over 180 H_2O ν_2=1−0 and about 90 H_2O ν_2=2−1 absorption lines in this survey. As shown in Figure 4.2, the velocity ranges of the absorbing components are very similar to those present in ^{13}CO or in high-J ^{12}CO lines (Li et al., 2022). All components are blueshifted compared to or are located at the cloud velocity v_{LSR}= $-38\ \mathrm{km\,s^{-1}}$ (van der Tak et al., 2000). Each kinematic component is characterized by different excitation conditions.

We fit the ν_2=1–0 absorption line profiles with a sum of multiple Gaussians using the `curve_fit` function in `scipy`. The fitting results are determined by restricting the range of the free parameters. Specifically, two components centered at $\sim -39.5\ \mathrm{km\,s^{-1}}$ and $-54.5\ \mathrm{km\,s^{-1}}$ are present across all energy levels, while the component centered at $-45\ \mathrm{km\,s^{-1}}$ only appears in transitions originating from relatively low energy states (<800 K). We name the three components provisionally as the "red, "blue", and "middle" ones based on their velocities. For very low energy states (<200 K), an extra component at $-39.5\ \mathrm{km\,s^{-1}}$ is possibly needed for a better fitting result (see Appendix D.3), and we discuss its existence and the implications in § 4.6.1.

Therefore, we fit two and three Gaussians above and below 800 K, separately. Above 800 K, we constrain the velocity center to -43 to $-36\ \mathrm{km\,s^{-1}}$ for the red component, and the blue component with a relative velocity of -17 to $-14\ \mathrm{km\,s^{-1}}$ guided by an initial guess. The line widths, σ_v, were constrained to 4–6 and 7–$9\ \mathrm{km\,s^{-1}}$. We apply the same constraints to the ν_2=2–1 absorption line profiles. In the low energy transitions (<800 K), the middle and the blue component is fixed with the central velocity, v_{cen}, of $-45\ \mathrm{km\,s^{-1}}$ and -54.5, and the velocity dispersion parameter, σ_v from 4–$5\ \mathrm{km\,s^{-1}}$. We note that the blue ($-54.5\ \mathrm{km\,s^{-1}}$) component disappears in some of the low-energy transitions (see the second panel in Figure 4.2) as a result of the opacity effect (see § 4.4.1). In this case, we only fit the line profile with one Gaussian. The parameters of each individual component such as the central velocity, velocity width, and equivalent widths are listed in detail in Appendix D.5.

4.4.1 Rotation Diagram Analysis and the Opacity Problem

After the distinct velocity components are determined, we use a rotation diagram to provide a first view of their characteristics. If the absorption lines are optically thin, we can get the column density N_l in the lower state of a transition directly from the integrated line profile by

$$N_l = 8\pi/(A_{ul}\lambda^3)g_l/g_u \int \tau(v)dv, \tag{4.1}$$

in which A_{ul} is the Einstein A coefficient, g_l and g_u are the statistical weight of the lower and upper levels, and

$$\tau(v) = -\ln(I_{\text{obs}}/I_c), \tag{4.2}$$

where I_{obs} and I_c are the intensity of the absorption and the continuum. All spectral line parameters used in this study are adopted from HITRAN (Rothman et al., 2013).

If the foreground absorbing gas is in LTE, the population of one rotational level can be described with the Boltzmann equation,

$$\frac{N_l}{g_l} = \frac{N_{\text{tot}}}{Q(T_{\text{ex}})}\exp\left(-\frac{E_l}{k_B T_{\text{ex}}}\right), \tag{4.3}$$

in which T_{ex} is the excitation temperature, N_{tot} is the total column density, E_l is the excitation energy, and $Q(T)$ is the partition function. Specifically, ln(N_l/g_l) and E_l/k_B of all absorption lines constructs the so-called rotation diagram. For a uniform excitation temperature, ln(N_l/g_l) and E_l/k_B fall on a straight line. The inverse of the slope represents the temperature and the intercept represents the total column density over the partition function.

We present the rotation diagrams of the rovibrational H_2O lines from W3 IRS 5 in Figure 4.3. For the three velocity components centered at -39.5, -45, and -54.5 $\mathrm{km\,s^{-1}}$, the derived temperatures are 807$\pm$58, 200$\pm$18, and 669$\pm$57 K. The total column densities are (1.2$\pm$0.6)$\times 10^{18}$, (3.3$\pm$2.0)$\times 10^{17}$, and (6.2$\pm$3.4)$\times 10^{17}$ $\mathrm{cm^{-2}}$, respectively. However, it is noticeable that the large scatter in the rotation diagram exceeds what the error bars can account for in the two hot components at -39.5 and -54.5 $\mathrm{km\,s^{-1}}$. Specifically, as shown in Figure 4.3, for transitions that share the same lower state (and the same g_l), the difference in the derived N_l is up to an order of magnitude.

We can further illustrate this problem by directly comparing the line profiles of the transitions that have a common lower energy level. As presented in Figure 4.2 and 4.4, lines that share the same lower level do not necessarily have the same absorption intensity and/or the equivalent width, which is defined as

$$W_\nu = \int (1 - I_{\mathrm{obs}}/I_c) d\nu \tag{4.4}$$

in the frequency space. This behavior where transitions with high Einstein A's fall systematically below the relation provided by transitions with low Einstein A's in the rotation diagram (Figure 4.3) is characteristic for opacity effects. Specifically, when transitions are optically thick, an increase in absorption strength (due to an increase in Einstein A) results in only a small increase in line width (not in depth) and hence marginally increase the equivalent width. This effect was noted earlier in Indriolo et al. (2020) and Barr et al. (2022a) in studies of MIR H_2O rovibrational lines toward massive protostars AFGL 2136 and AFGL 2591.

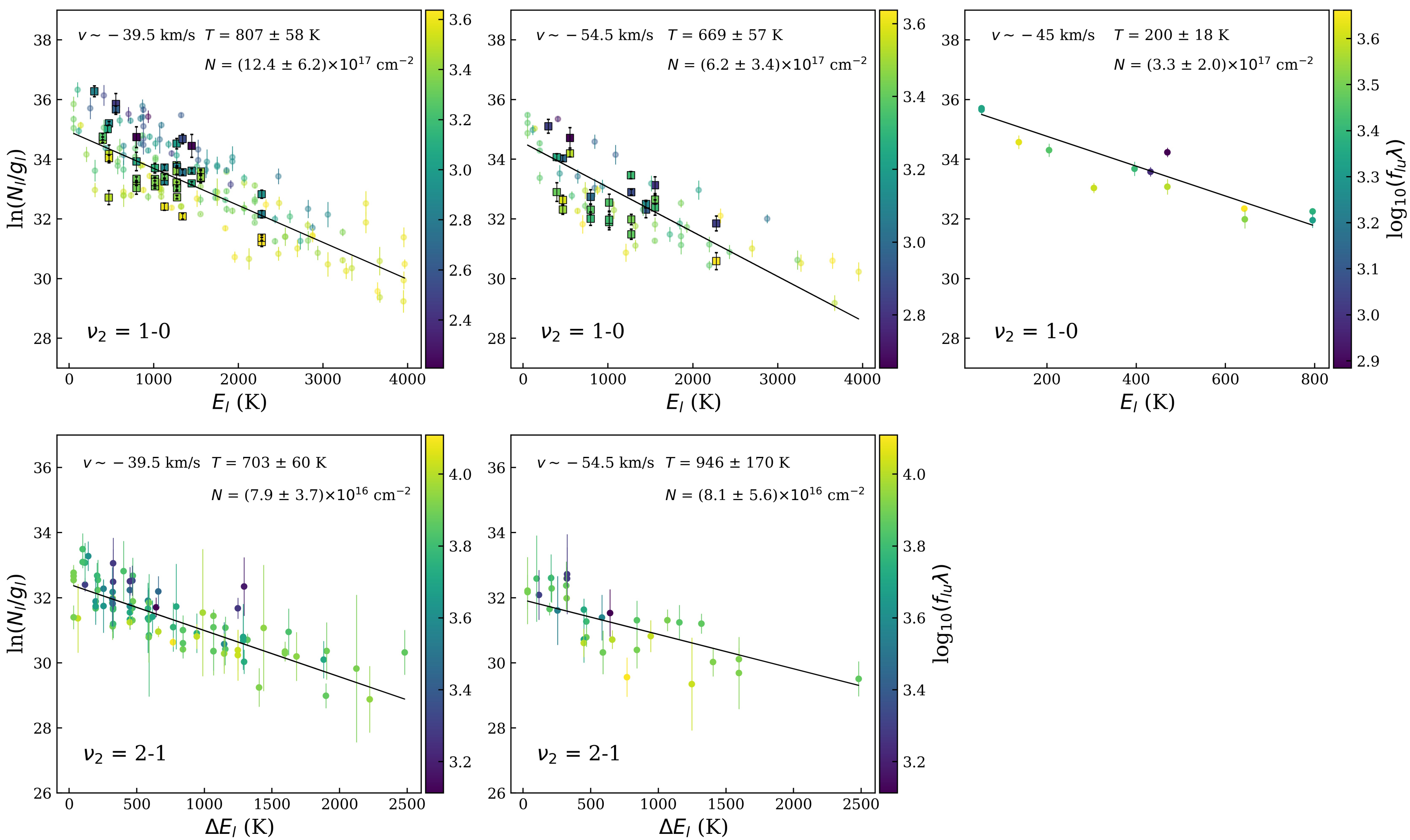

Figure 4.3: Rotation diagrams of H_2O ν_2=1−0 (*upper panels*) and ν_2=2−1 (*lower panels*) transitions from the decomposed velocity components: -39.5, -45, and -54.5 km s^{-1}. For ν_2=2−1 transitions, E_l in the x-axis are ΔE_l relative to the ground state energy of $\nu_2 = 1$ ($J_{K_a,K_c} = 0_{0,0}$, 2294.7 K). Square data points represent a collection of lines as shown in Figure 4.4, that share the same lower level. The N_l are derived from equation 4.1 with Gaussian fitting on the line profiles assuming optically thin absorption. The color code is $\log_{10}(f_{lu}\lambda)$, which is representative of the intrinsic strength (see § 4.4.2). The parameter f_{lu} is the oscillator strength and λ is the wavelength.

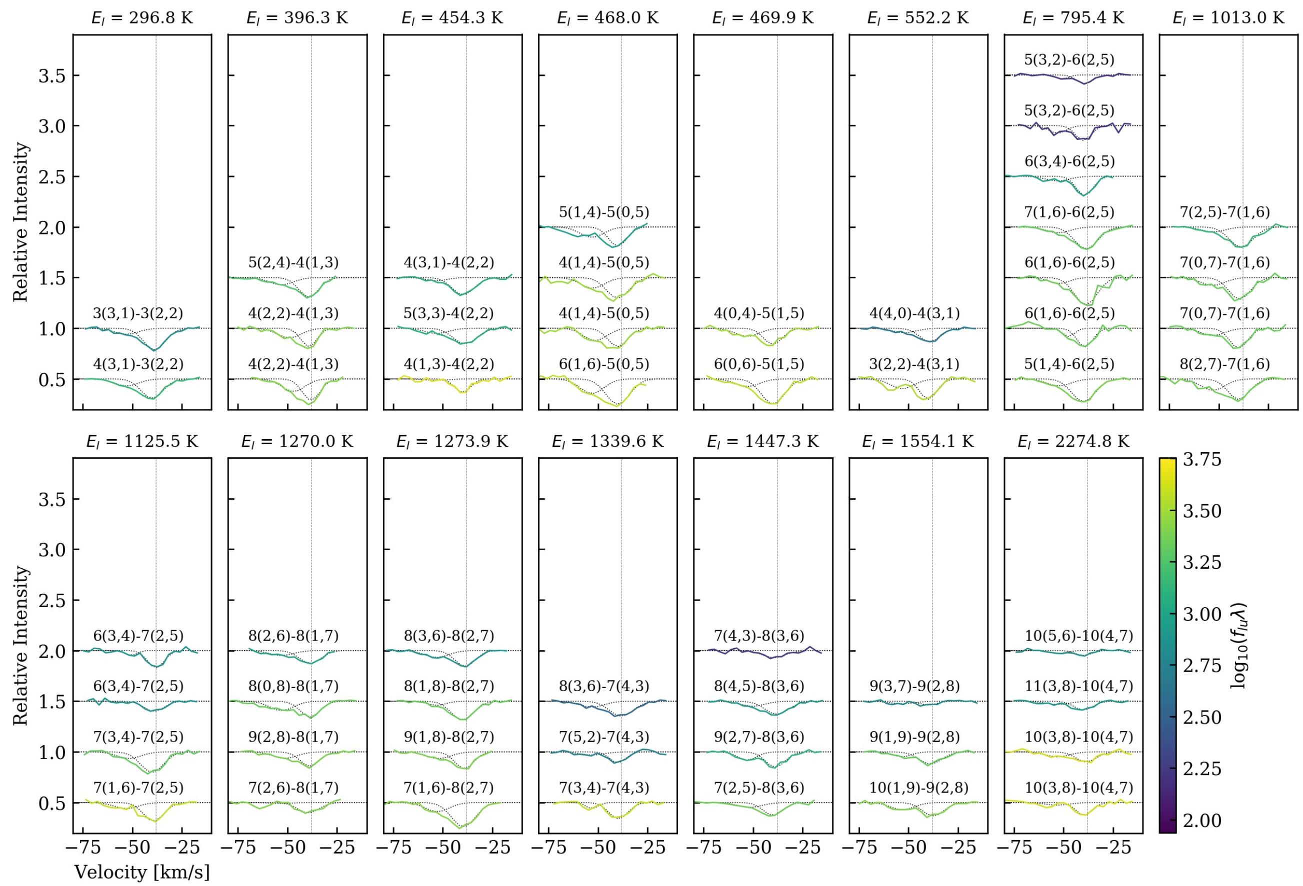

Figure 4.4: Selected H_2O ν_2=1−0 absorption lines observed toward W3 IRS 5. In each panel, all rovibrational lines share the same lower energy state but show different absorption depths or/and equivalent widths. Some transitions appear in more than one setting and result in duplicated entries in the figure. The line profiles are color-coded following the color bar in Figure 4.3 (see Section 4.4.2), and are listed in each panel from top to bottom with increasing $\log_{10}(f_{lu}\lambda)$, which is representative of the opacity. While the lines in each panel refer to the same column density, these transitions show that the equivalent width increases with the intrinsic strength of the transitions. Gaussian fitting at ~ -53 and ~ -38 km s^{-1} are presented together with each absorption line. The dashed vertical lines at -38 km s^{-1} indicate the systematic velocity of W3 IRS 5 (van der Tak et al., 2000).

4.4.2 Curve-of-growth Analysis

Considering that $\tau(v)$ in equation 4.1 does not represent an optically thin Gaussian core, the definition of the equivalent width in equation 4.4 can be written as

$$\begin{aligned} W_\nu &= \int (1 - I_{\text{obs}}/I_c) d\nu = \int (1 - \mathrm{e}^{-\tau(\nu)}) d\nu \\ &= \int (1 - \mathrm{e}^{-\tau_p H(a,\nu)}) d\nu. \end{aligned} \tag{4.5}$$

The ν in H, the Voigt profile, represents the shift from the line center in Doppler units while the ν in the integral is the frequency. The parameter a is the damping factor. The peak optical depth τ_p is

$$\tau_p = \frac{\sqrt{\pi} e^2}{m_e b c} N_l f_{lu} \lambda. \tag{4.6}$$

In equation 4.6, e is the electron charge, m_e is the electron mass, and f_{lu} is the oscillator strength. The Doppler parameter in velocity space, b, is related to the full width at half maximum of an optically thin line by $\Delta v_{\text{FWHM}} = 2\sqrt{\ln 2} b$.

Equation 4.6 clearly shows that for lines that share the same lower level and have the same N_l, a difference in $f_{lu}\lambda$ will lead to different τ_p. Defining $\log_{10}(f_{lu}\lambda)$ as the representative for the line strength, lines with a larger line strength have larger equivalent widths (as shown in Figure 4.4), and as a result, the N_l derived via equation 4.1 will be underestimated (as shown in Figure 4.3).

4.4.2.1 Slab Model of a Foreground Cloud

A curve-of-growth analysis (Rodgers & Williams, 1974) is required to reconcile the opacity problem and to correctly derive N_l and N_{tot}:

$$\frac{W_\lambda}{\lambda} \approx \begin{cases} \frac{\sqrt{\pi}b}{c}\frac{\tau_p}{1+\tau_p/(2\sqrt{2})} & \text{for } \tau < 1.254 \\ \frac{2b}{c}\sqrt{\ln(\tau_p/\ln 2) + \frac{\gamma\lambda}{4b\sqrt{\pi}}(\tau_p - 1.254)} & \text{for } \tau > 1.254 \end{cases}. \tag{4.7}$$

We specifically note that this correction applies to an absorbing foreground slab model. In the equations above, the definitions of all parameters follow equation 4.6. The parameter γ is the damping constant of the Lorentzian profile and is of order 10 for radiative damping. We stress that for H_2O lines discussed in this paper, the Lorentzian line width that γ corresponds to is 10^{-9} km s^{-1}, and is negligible compared to the observed Doppler width (a few km s^{-1}).

For such an absorbing slab model, the emission from the foreground is negligible against the representative background temperature of $\sim$600 K in this study (see Section 3.2.1 in Li et al., 2022). Furthermore, if the foreground cloud does not cover the entire observing beam, a covering factor f_c ($0 \leq f_c \leq 1$) has to be accounted for and equation 4.2 is modified to:

$$I_{\text{obs}} = I_{\text{c}}(1 - f_c(1 - \mathrm{e}^{-\tau(v)})), \tag{4.8}$$

and the left-hand side of the equation 4.7 is modified to $W_\lambda/(\lambda f_c)$.

4.4.2.2 Stellar Atmosphere Model of a Circumstellar Disk

The absorption can also occur in an accretion disk scenario in the system of a forming massive star (Barr et al., 2020, 2022a; Li et al., 2022). Specifically, the disk has an outward-decreasing temperature gradient from the mid-plane to the surface. Such disks show absorption lines because the thermal continuum from the dust is mixed with the molecular gas. For such a scenario, we adopt the curve-of-growth of the stellar atmosphere model in which the continuum and the line opacities are coupled. The residual flux,

$$R_\nu \equiv I_\nu / I_c, \tag{4.9}$$

can then be approximated by the Milne-Eddington model (Mihalas, 1978, Ch 10) which assumes a grey atmosphere. The absorption line profile may originate in pure absorption or scattering. The parameter ϵ characterizes the line formation, and can take the form of 1 (pure absorption), 0 (pure scattering) or between 0 and 1 (a combination of scattering and absorption). We refer to Appendix A in Barr et al. (2020) for details of the line residual flux expected from this model.

The curve of growth in the stellar atmosphere model is constructed via the equivalent width versus β_0, the ratio of the line opacity at the line center, $\kappa_L(\nu = \nu_0)$, to the continuum opacity κ_c:

$$\begin{aligned} \frac{W_\nu}{2\Delta\nu_D} &= \int_0^{+\infty} (1 - R_v)dv \\ &= A_0 \int_0^{+\infty} \beta_0 H(a, v)[1 + \beta_0 H(a, v)]^{-1} dv, \end{aligned} \tag{4.10}$$

in which

$$\beta_0 = \frac{\kappa_L(\nu = \nu_0)}{\kappa_c} = \frac{A_{ul}\lambda^3}{8\pi\sqrt{2\pi}\sigma_v}\frac{g_u}{g_l}\frac{N_l}{\sigma_c N_H}\left(1 - \frac{g_l}{g_u}\frac{N_u}{N_l}\right). \tag{4.11}$$

In the equations above, v is the frequency shift with respect to the line center in units of the Doppler width, and $H(a, v)$ is the Voigt function that gives the line profile. The damping factor $a = \gamma\lambda/b$ is of the order of 10^{-8} for H_2O ro-vibrational lines. The parameter A_0 is the central depth of an opaque line. Its exact value is determined by the radiative transfer model of the surface of the disk and is related to the gradient of the Planck function. For a grey atmosphere and lines in pure absorption, A_0 is $\sim$ 0.5–0.9 from 900 to 100 K (see Appendix A in Barr et al., 2020). The continuum opacity, κ_c, is given by the dust cross-section per H-atom σ_c. The dispersion in velocity space, σ_v, is transformed from the Doppler parameter, $b/\sqrt{2}$, with which we convert W_ν to the velocity space:

$$\frac{W_\nu}{2\Delta\nu_D} = \frac{W_v}{2b}. \tag{4.12}$$

We can disregard the bracketed item in equation 4.11 if stimulated emission is negligible.

We adopt a value of 7×10^{-23} cm^2/H-nucleus for σ_c following Barr et al. (2020), as it is appropriate for coagulated interstellar dust (Ormel et al., 2011). Theoretical fits to these curves of growth will provide abundances relative to the dust opacity. As this value of σ_c is adopted in the CO analysis (Li et al., 2022) as well, we are able to derive an absolute water-to-CO ratio once the CO correspondent component to water is identified via the kinematic information (see § 4.5.2).

4.5 Results

As shown in § 4.4, the H_2O ν_2=1–0 lines are decomposed into three velocity components at -45, -39.5, and -54.5 $\mathrm{km\,s^{-1}}$, while the ν_2=2–1 absorption lines are decomposed into two components at -39.5 and -54.5 $\mathrm{km\,s^{-1}}$. Since the rotation diagram analysis under the optically thin assumption provides a preliminary estimation of their temperatures (see § 4.4.1 and Table 4.2), we name these components accordingly as 'W', 'H1', and 'H2', in which 'W' and 'H' stands for "warm" and "hot" following the nomenclature in Li et al. (2022).

We hereafter apply the curve-of-growth analyses to the ν_2=1–0 transitions from 'H1 and 'H2' and ν_2=2–1 from 'H1'. Their rotation diagrams illustrate a large scatter thus the opacity problem in § 4.5.1. In § 4.5.2, all the water components are compared to and connected with warm and/or hot CO components. The implications of the vibrationally excited water lines are presented in § 4.6.1.2.

4.5.1 Two Hot Components: H1 and H2

We conduct the grid search method (Li et al., 2022) on the ($T_{\rm ex}$, $N_{\rm tot}$) and ($T_{\rm ex}$, abundance) grid in the curve-of-growth analyses for the slab model and the disk model, respectively. While ($T_{\rm ex}$, $N_{\rm tot}$) determines τ_p, or $N f_{ul} \lambda$, and ($T_{\rm ex}$, abundance) determines β_0, we search for the smallest reduced χ^2 in the two grids to look for the best fitting between the observable W_λ/λ, or equivalently, W_ν/c to the theoretical curves-of-growth.

Table 4.2: Physical Conditions of Decomposed Components

Component	‘W’, -45 km s^{-1}	‘H1’, -39.5 km s^{-1}		‘H2’, -54.5 km s^{-1}	
Transitions	ν_2 = 1–0	ν_2 = 1–0	ν_2 = 2–1	ν_2 = 1–0	ν_2 = 2–1
			Rotation Diagram		
$T_{\rm ex}$ (K)	200 ± 18	807 ± 58	703 ± 60	669 ± 57	946 ± 170
$N_{\rm tot}$ (cm^{-2})	$(6.6 \pm 4.0) \times 10^{17}$[a]	$(1.2 \pm 0.6) \times 10^{18}$	$(7.9 \pm 3.7) \times 10^{16}$	$(6.2 \pm 3.4) \times 10^{17}$	$(8.1 \pm 5.6) \times 10^{16}$
			Slab Model		
f_c	...	0.4	0.4	0.3	...
b (km s^{-1})	...	2.8	2.8	3.5	...
$T_{\rm ex}$ (K)	...	471^{+14}_{-15}	654^{+135}_{-191}	542^{+33}_{-35}	...
$N_{\rm tot}$ (cm^{-2})	...	$2.5^{+0.3}_{-0.2} \times 10^{19}$	$2.8^{+0.5}_{-0.7} \times 10^{17}$	$5.7^{+0.7}_{-0.7} \times 10^{18}$	...
$\chi^2_{r,min}$	..	1.7	0.65	3.8	...
			Disk Model[b]		
b (km s^{-1})	...	2.8	2.8	3.5	...
$T_{\rm ex}$	...	491^{+13}_{-14}	691^{+122}_{-212}	612^{+27}_{-30}	...
Abun. (w.r.t H, $\times 10^{-3}$)	...	$2.6^{+0.1}_{-0.2} \times 10^{-3}$	$5.0^{+1.4}_{-3.5} \times 10^{-5}$	$5.1^{+0.4}_{-0.5} \times 10^{-4}$	...
$\chi^2_{r,min}$	...	1.7	0.34	2.3	...

[a] This value is corrected by assuming that ‘W’ covers both proto-binary and the absorption intensity is not diluted (see § 4.5.2).
[b] Pure absorption with parameter ϵ of 1 are assumed in this table. See Table 4.3 for results with ϵ of 0 and 0.5.

When fitting the observed W_λ/λ to the theoretical curve-of-growth of a slab model, we fix the partial coverage, f_c, to 0.4 and 0.3 for 'H1' and 'H2', separately. Values of f_c are constrained by twice the lower limit of the line intensities considering a dilution factor of two (see § 4.3). We set the Doppler width b (=$\sqrt{2}\sigma_v$) to 2.8 and 3.5 $\mathrm{km\,s^{-1}}$, as the upper limit of σ_v is constrained by the observed line width, and the chosen value of b provides the smallest χ^2_r. As a reference, for gas of 500 K, $\sigma_{\rm th} = \sqrt{(k_{\rm B}T)/(\mu m_{\rm H})}$ = 9.12×10^{-2} $\mathrm{km\,s^{-1}}$ (T/K)$^{0.5}\mu^{-0.5} \approx 0.5$ $\mathrm{km\,s^{-1}}$. This value corresponds to 2.6 $\mathrm{km\,s^{-1}}$ after convolving with the instrument resolution $\sigma_{\rm res}$ = $c/(2\sqrt{2\ln 2}R)$ = 2.5 $\mathrm{km\,s^{-1}}$.

For the ν_2=1−0 transition, we illustrate the best-fitting results of the 'H1' component for both the foreground and disk model in Figure 4.5 (results of 'H2' are presented in Figure D.6 in Appendix D.4) and summarize the derived properties in Table 4.2, assuming that the lines are formed in pure absorption ($\epsilon = 0$). In either the slab or the disk model, about half of the data points are located on the logarithmic part of the curve-of-growth, confirming that the corresponding absorption lines are optically thick. In the slab model, the curve-of-growth analysis "corrects" the underestimated total column densities in the rotation diagram by a factor of 21 and 9 for 'H1' and 'H2', respectively. The derived temperatures are lowered to 471 K and 542 K, respectively (Table 4.2). In the disk model, as relative abundances are derived, the correction in column densities is quantified once the connection between CO and water components is established (see § 4.5.2). The derived temperatures from the disk model are comparable to those derived from the slab model (Table 4.2). As for the ν_2=2−1 transition on 'H1', the correction after the curve-of-growth analysis on the temperature and column density is insignificant (Table 4.2), indicating that the optical depth effect is not severe.

We note that in the disk model, the 1σ uncertainty for given ϵ and given σ_v is very small

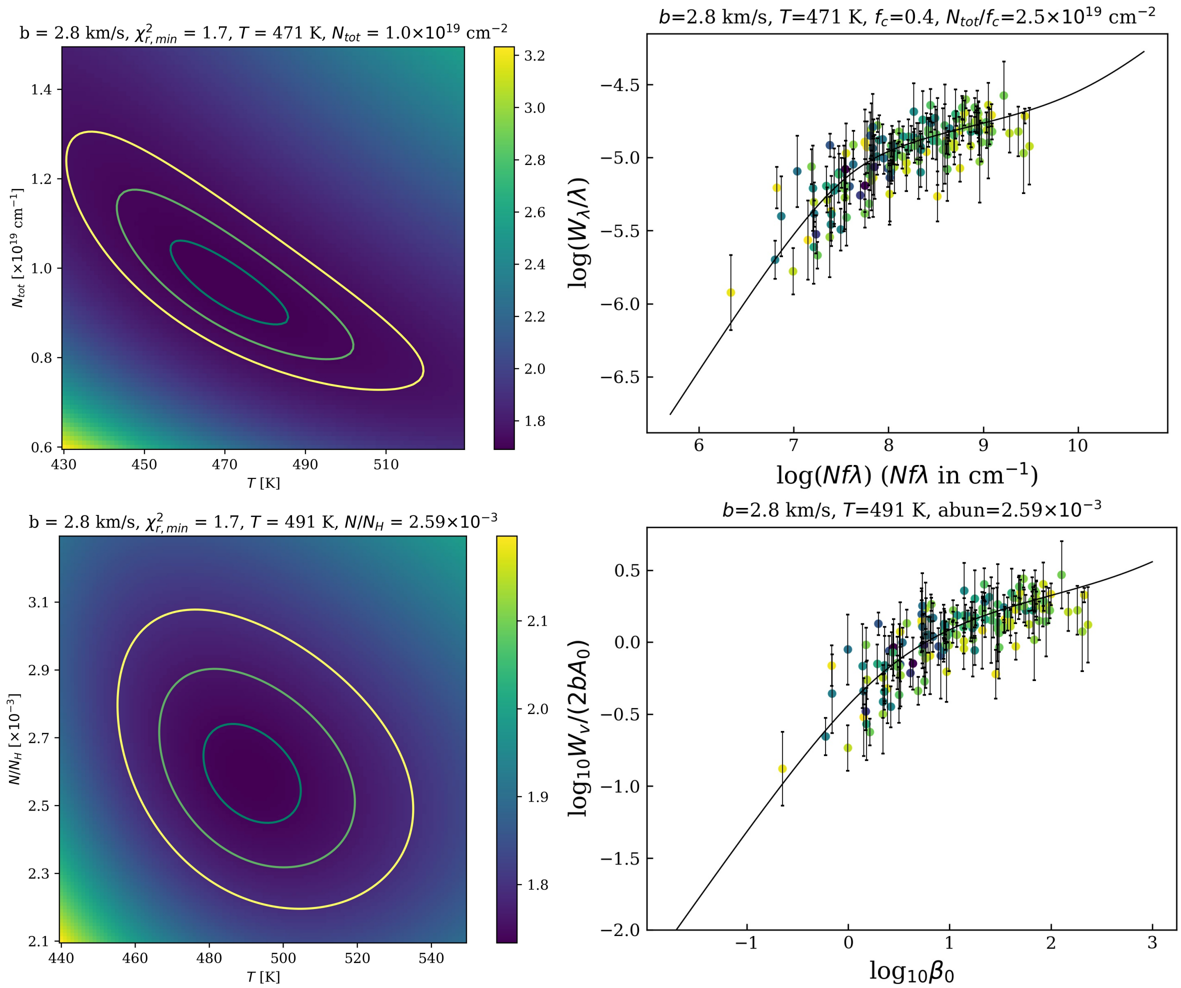

Figure 4.5: Curve-of-growth analysis for the slab (top) and disk (bottom) models. *Left panels:* Grid-search results for both the slab and the disk model illustrating the best-fitting results. The contours represent the 1σ, 2σ, and 3σ uncertainty levels. *Right panels*: the curves of growth for the slab and the disk model. The color scale of the data points is the same as those in the rotation diagram.

(Figure 4.5). However, if take the 'H1' component as an example, as presented in Table 4.3, the results do depend on the adopted σ_v and ϵ. While there is a degeneracy between σ_v and ϵ, combinations of different σ_v and ϵ may provide comparable $\chi^2_{r,min}$. While we may have some control over σ_v, the value of ϵ is unconstrained. We, therefore, provide Table 4.3 as a reference for conditions when the lines are not due to pure absorption.

Table 4.3: Results of the Physical Component ‘H1’ Derived From Different ϵ And σ_v In the Disk Model

	ϵ=0			ϵ=0.5			ϵ=1		
	$\chi^2_{r,min}$	$T_{\rm ex}$ (K)	$X_{\rm H_2O}/X_{\rm CO}$	$\chi^2_{r,min}$	$T_{\rm ex}$ (K)	$X_{\rm H_2O}/X_{\rm CO}$	$\chi^2_{r,min}$	$T_{\rm ex}$ (K)	$X_{\rm H_2O}/X_{\rm CO}$
σ_v=1.5 km s^{-1}	2.02	579	1.19	1.79	449	2.45	1.88	419	3.71
σ_v=2.0 km s^{-1}	2.54	565	0.78	1.84	510	1.30	1.77	474	1.81
σ_v=2.5 km s^{-1}	3.14	598	0.61	1.99	560	0.90	1.88	521	1.20
σ_v=3.0 km s^{-1}	3.72	622	0.52	2.37	594	0.72	1.98	564	0.92

(1) The 1σ uncertainty for the derived temperatures is in order of ±10 K. (2) $X_{\rm H_2O}/X_{\rm CO}$ is derived by assuming that ‘H1’ and ‘MIR2-H1’ in CO coexist.

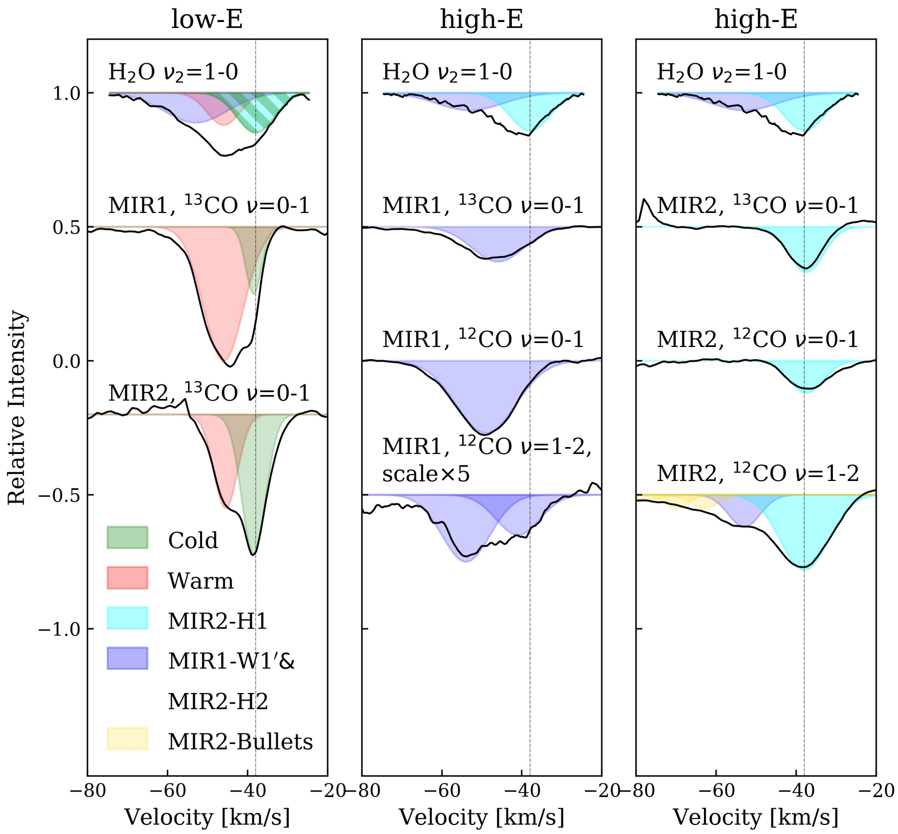

Figure 4.6: Comparison between averaged H_2O and CO components in low (<400K) and high (>400K) energy levels. The dashed vertical line represents $v_{\rm sys} = -38$ km s^{-1}, and the decomposed components are colored following Li et al. (2022).

4.5.2 Connecting the Absorbing Components in H_2O and CO

High spectral resolution M-band absorption spectroscopy (R=88,100) toward W3 IRS 5 at 4.7 μm revealed multiple kinematic components in ^{12}CO and its isotopologues (Li et al., 2022). Specifically, IRTF/iSHELL spatially resolved the two protostars in W3 IRS 5. As CO lines also trace ambient gaseous components that absorb against the MIR background, building a connection between the components identified in H_2O and CO will help us to understand the origins of the gaseous H_2O components.

The velocity resolution of EXES (6 km s^{-1}) and iSHELL (3.4 km s^{-1}) enables the compar-

Table 4.4: Comparing Water and CO Components

Comp.	Species	v_{LSR} ($\mathrm{km\,s^{-1}}$)	$T_{\rm ex}$ (K)
'W'	H_2O	-46	200 ± 18
MIR1-W1	CO	-43	180^{+11}_{-14}
MIR1-W2	CO	-45.5	116 ± 7
'H1'	H_2O (Slab)	-39.5	471^{+14}_{-15}
	H_2O (Disk)	-39.5	491^{+13}_{-14}
MIR2-H1	CO	-37.5	662^{+23}_{-28}
'H2'	H_2O (Slab)	-54.5	542^{+33}_{-35}
	H_2O (Disk)	-54.5	612^{+27}_{-30}
MIR2-H2	CO	-52	482^{+97}_{-70}
MIR1-W1′	CO	$-40, \sim -54$	709^{+136}_{-101}

ison between H_2O and CO components through their kinematic information. We, therefore, present in Figure 4.6 the comparison between the absorption profiles. As the different velocity components are characterized by different excitation temperatures, both the profiles of the H_2O and CO spectra are averaged in low-energy (<400 K) and high-energy (>400 K) transitions. As we have described in § 4.4, we identified three components centered at $-39.5, -45$, and -54.5 $\mathrm{km\,s^{-1}}$ in low-energy transitions, and two centered at -39.5 and -54.5 $\mathrm{km\,s^{-1}}$ in high-energy transitions. We note that half of the transitions (6 of 12) with a -45 km/s component are at energies between 400 and 800 K.

In low-energy levels, two components are revealed in CO, with one centered at the $v_{\rm sys} = -38$ $\mathrm{km\,s^{-1}}$, and the other centered at -46 $\mathrm{km\,s^{-1}}$. No low-energy CO components were found at -55 $\mathrm{km\,s^{-1}}$. Since both the -38 and -46 $\mathrm{km\,s^{-1}}$ components are detected toward MIR1 and MIR2 and are revealed to have similar physical properties (Li et al., 2022), they are regarded to cover MIR1 and MIR2 simultaneously. Specifically, as marked in Figure 4.6, the "cold" component at -38 $\mathrm{km\,s^{-1}}$ is ∼50 K, while the "warm" component at -46 $\mathrm{km\,s^{-1}}$ is

$\sim$180 K. Therefore, we consider that the 'W' component, which is centered at $-45\ \mathrm{km\,s^{-1}}$ and whose T_{ex} is 200 K (Table 4.2), is the H_2O correspondent to the "warm" CO component. Because this warm CO component was found to be in front of both binary stars in Li et al. (2022), for this component in H_2O, we do not consider dilution in the relative intensity when doing the rotation diagram analysis in § 4.4.

We note that for the 'H1' H_2O component which is centered at $-39.5\ \mathrm{km\,s^{-1}}$ and is close to υ_{sys}, the existence of ν_2=2−1 transitions and its derived high temperature exclude a connection between it and the cold CO component ('MIR1-C/MIR2-C'). It is possible that in the low energy CO transitions, the CO counter part of this hot H_2O component at $-38\ \mathrm{km\,s^{-1}}$ may be hidden underneath a lower temperature component at that velocity. We will discuss this possibility in § 4.6.2.1.

At high-energy levels, MIR1 and MIR2 contribute differently toward the absorbing components. The component MIR2-H1 in CO is centered at $-37.5\ \mathrm{km\,s^{-1}}$ and is characterized by 600–700 K. We link this to the 'H1' water component. It is more difficult to determine the origin of the $-54.5\ \mathrm{km\,s^{-1}}$ 'H2' H_2O component. The CO component MIR1-W′ has a more complicated origin, as is indicated by the varying average line profiles in ^{13}CO, ^{12}CO, and ^{12}CO ν=2−1. In view of the similarity in excitation temperature, it might be tempting to link the $-54.5\ \mathrm{km\,s^{-1}}$ H_2O 'H2' component ($\sim$500 K) to the CO MIR1-W′ component (400–700 K, Li et al., 2022). However, the CO MIR1-W′ component is a complex amalgam of several components as indicated by the two peaks in ^{12}CO ν=2−1. Specifically, one of the two peaks in the ^{12}CO ν=2−1 profile (at $-54\ \mathrm{km\,s^{-1}}$) of the MIR1-W′ component coincides more or less with the $-54.5\ \mathrm{km\,s^{-1}}$ H_2O 'H2' component but the other one (at $-39.5\ \mathrm{km\,s^{-1}}$) has no counterpart in the H_2O spectrum. Likewise the ^{12}CO and ^{13}CO MIR1-W′ components are centered at -46 and $-49\ \mathrm{km\,s^{-1}}$, respec-

Table 4.5: Comparison of H_2O Characteristics Derived From *ISO-SWS* and SOFIA/EXES Observations

Properties	ISO-SWS	SOFIA-EXES			
		H1 (Slab)	H1 (Disk)	H2 (Slab)	H2 (Disk)
$T_{\mathrm{ex}}(H_2O)$ (K)	400^{+200}_{-150}	471^{+14}_{-15}	491^{+13}_{-14}	542^{+35}_{-33}	612^{+27}_{-30}
$N(H_2O)$ (cm^{-2})	$3^{+1}_{-1} \times 10^{19}$	$2.5^{+0.3}_{-0.2} \times 10^{19}$	$3.6 \pm 1.2 \times 10^{19}$	$5.7 \pm 0.7 \times 10^{18}$	$8.9 \pm 0.3 \times 10^{18}$
$X[H_2O]/X[CO]$	0.05	$1.1^{+0.4}_{-0.4}$	1.5 ± 0.5	$4.1^{+3.9}_{-2.1}$ *or* $1.0^{+0.5}_{-0.4}$	0.9 ± 0.3

tively. Hence, we consider that the H_2O 'H2' component is related to one of the CO MIR1-W′ components.

In conclusion, the water component 'H1' is much stronger and it better matches MIR2-H1 in CO. The water component 'H2' is weaker and its origin is less clear. We present the derived relative abundance of H_2O and CO in Table 4.2 by connecting 'W' to the warm component at -45 $\mathrm{km\,s^{-1}}$ in CO, 'H1' to MIR2-H1, and 'H2' to either MIR2-H2 or MIR1-W′. Once the hot components in H_2O are linked to those in CO, we can derive the H_2O/CO abundance ratio (Table 4.5). Adopting a CO abundance of 1.6×10^{-4} (Cardelli et al., 1996; Sofia et al., 1997), we derive H_2O column densities under the disk model of 3.6×10^{19} and 8.9×10^{18} $\mathrm{cm^{-2}}$ for 'H1' and 'H2', respectively (Table 4.5).

4.6 Discussion

Under the framework of the known structures in W3 IRS 5, the M-band spectroscopic study on CO pictures the kinematic and physical properties of the gaseous environment. Specifically, it includes a shared foreground envelope at -38 $\mathrm{km\,s^{-1}}$, several high-velocity clumps (referred to as "bullets") from -60 to -100 $\mathrm{km\,s^{-1}}$, and a few warm and/or hot components in the immediate environment of the binary from -38 to -60 $\mathrm{km\,s^{-1}}$ (Li et al., 2022). While we have connected 'W', 'H1', and 'H2' in water to MIR1-W1/MIR2-W1, MIR2-H1, and MIR2-H2 (or MIR1-W′) in CO (§ 4.5.2), gaseous water is not detected in the shared cold envelope or the bullets. We refer to past water studies for a more complete view toward W3 IRS 5 (see Table 4.5) in this section and discuss the implications of these "detections" and "non-detections" from the perspective of both the kinematics and the chemical abundances.

4.6.1 Hot Gaseous Water in W3 IRS 5

4.6.1.1 Physical Origins of the Hot Components

As we have built the connections of H_2O 'H1' and 'H2' components to the hot CO components via the kinematic information, it is natural to consider that, as for the corresponding CO components, the two H_2O components have a disk rather than a foreground cloud origin. Although the observed W_λ/λ can be successfully fitted to the theoretical curve-of-growth of either model (see § 4.4 and § 4.5.1), and the two models derive comparable column densities (see § 4.5.2) and temperatures, we nevertheless consider the disk model as the more preferred one for the following reasons.

If the hot components have a foreground origin, the heating mechanisms are either due to the radiative heating or due to shocks. On the one hand, if the water components are radiatively heated, the temperature range from 450–600 K corresponds to a distance of 280–140 au in the W3 IRS 5 system (Li et al., 2022). As 'H1' is at the systemic velocity, this would imply that this component is static in radial velocity in the highly dynamic environment close to a high mass protostar. The 'H2' component has the opposite issue as it is moving at a radial velocity of $-15\ \mathrm{km\,s^{-1}}$ relative to the system, and would move outward by some 100 au in 30 years. As the physical conditions derived from CO observations in 2020 are very similar to those derived in 1991 (Mitchell et al., 1991), this distance range does not work for H2, either, because of its relative velocity of 15 $\mathrm{km\,s^{-1}}$, and it shall move outward along the line of sight for a large distance ($\sim$100 au). On the other hand, interpreting the warm temperature of these two components as the results of shocks has issues too. For J-shocks, the derived temperatures are quite high. J-shocks initially heat the gas to very high temperatures larger than 10^4 K. The gas then cools to $\sim$400 K before molecules reform in the so-called "plateau region" (Hollenbach et al., 2013). C-type shocks can yield temperatures of 450–600 K for shock velocity of $\sim$10 $\mathrm{km\,s^{-1}}$ (Kaufman & Neufeld, 1996b). However, a C-shock produces warm hydrogen of $\sim 10^{21}$ $\mathrm{cm^{-2}}$, which is far too small to be consistent with the column density we derived for the hot components.

If 'H1' and 'H2' are in the disks, the H_2O (and CO) excitation temperatures are similar (but slightly lower than) the dust continuum temperature. Hence, heating is not an issue. However, the problem now resides in the exact positions of the two components on the disk based on their projected velocity information along the line of sight. As pointed out in Li et al. (2022), it is difficult to pinpoint the locations of the blobs on the disk because the inclination angles of both MIR1 and MIR2 and the systematic velocity of MIR1 are unknown. For 'H1', while it was connected with 'MIR2-H1' because of the similar velocity and temperature, we note that there is a $\sim$2 $\mathrm{km\,s^{-1}}$ velocity difference between them. Such a velocity difference is significant compared with the uncertainty level of v_{cen} of 'H1'. Since MIR2-H1 is at v_{sys} and CO observations reveal that it has had very similar conditions for at least 30 yr, MIR2 is rather a face-on disk. A small velocity discrepancy of 2 $\mathrm{km\,s^{-1}}$ may therefore reflect a significant spatial offset of one blob where both CO and water reside in. For 'H2', it is not even clear whether it is associated with MIR1 or MIR2, as the binary protostars are not spatially resolved by SOFIA, and both binary stars show hot components at the same velocity close to -55 km s^{-1}. As shown in Figure 4.6, in MIR1, the hot component shows up in ^{12}CO ν=2–1 vibrationally excited transitions which indicate a high-density region, $\sim 10^{10}$ cm^{-3}. In MIR2, the component is possibly a blob on an inclined disk at a distance smaller than 80 au to the central protostar, but such a scenario poses questions on the inclination of the disk MIR2 again. We, therefore, emphasize that disks in MIR1 and MIR2 need to be both spatially and spectrally resolved to fully understand the structures in this region. Observations of vibrationally excited lines via submillimeter interferometers may be very instrumental in settling these issues.

Analysis of AFGL 2136 and AFGL 2591 observations have faced the same issues in determining whether the hot 600 K absorbing components reside in the foreground slab or in the disk (Barr et al., 2022a). A foreground slab model places very strong constraints on the geometry. In AFGL 2136, if the slab has a water maser origin, the spatial coverage is even larger than the MIR disk, inconsistent with the required covering factor in order to explain the saturation of absorption lines at non-zero flux. In AFGL 2591, wavelength-dependent covering factors are needed to interpret the difference of the spatial coverage derived from the 7 and 13 μm spectroscopy, while the component does not cover the source at all at 3 μm (Barr et al., 2022b). Continuum emission size and chemistry need to be radius dependent, possibly due to the temperature gradient, to interpret the different covering factors. Moreover, similar to W3 IRS 5, too high a density, and too high an abundance argue against a shock origin. In contrast, Keplerian disks as well as clumpy substructures were spatially resolved by Atacama Large Millimeter/submillimeter Array (AFGL 2136; Maud et al., 2019) and NOEMA (AFGL 2591; Suri et al., 2021), supporting the scenario that the absorption arises in blobs in the disk.

In summary, from a broad view, it is a prevalent scenario that hot absorption gas is detected against the MIR continuum backgrounds in massive protostars (e.g. Boonman & van Dishoeck, 2003; Cernicharo et al., 1997; Lahuis & van Dishoeck, 2000; van Dishoeck & Helmich, 1996). Locating a blob on a disk that has a vertical outward-decreasing temperature gradient requires fewer constraints on the geometry than a foreground slab model does. However, disk models face challenges in realizing such an internal heating mechanism. As discussed in Barr et al. (2022a), the flashlight effect may ensure the disk is not externally heated (Kuiper et al., 2010; Nakano, 1989; Yorke & Bodenheimer, 1999). However, if one proposes the dissipation of gravitational energy, the accretion rate would be orders of magnitude higher than the expected accretion rate (Caratti o Garatti et al., 2017; Hosokawa et al., 2010; Kuiper et al., 2011; McKee & Tan, 2003). Hence dissipation of turbulent and/or magnetic energy inherited from the prestellar core would be required, implying a very early and active stage in the formation of these massive protostars.

4.6.1.2 Vibrationally Excited H_2O

We presented in Figure 4.3 the rotational temperatures of 'H1' and 'H2' in the first excited vibrational state ($\nu_2 = 1$), which are 703±60 K and 946±170 K, respectively. Applying curve-of-growth analyses to 'H1', the corrected rotational excitation temperatures are 654^{+135}_{-191} K in the slab model and 691^{+122}_{-212} K in the disk model (Table 4.2) and are not far away from the result derived from the rotation diagram. The increment of the total column density of 'H1' after correction is ∼3–4 times, much less than that of ∼20 times on the $\nu_2 = 0$ state, indicating a less severe optical depth effect.

One can derive the vibrational excitation temperature, $T_{\rm vib}$ via the Boltzmann equation by

Table 4.6: Vibrational Excitation Temperatures

	H1	H2
T_{vib}(thin) (K) [a]	843^{+553}_{-233}	1127^{+2083}_{-498}
T_{vib}(slab) (K) [b]	511^{+30}_{-42}	539^{+99}_{-127}
T_{vib}(disk) (K) [c]	581^{+52}_{-139}	488^{+66}_{-100}

[a] Values of N_1 and N_0 in equation 4.13 are derived from rotation diagram analysis (see Table 4.2; same for the columns below).
[b] N_1 and N_0 are corrected under the slab model. Since no curve-of-growth analysis is applied for the ν_2=1 state of 'H2', we adopt N_1 from the rotation diagram analysis. Same for the 'H2' result under the disk model.
[c] N_1 and N_0 are corrected under the disk model.

comparing the column density in the $\nu_2 = 0$ level, N_0, with N_1 in the $\nu_2 = 1$ level:

$$N_1/N_0 = \exp(-2294.7/T_{\text{vib}}). \tag{4.13}$$

We list in Table 4.6 multiple vibrational excitation temperatures for 'H1' and 'H2', using N_0 and N_1 before and after corrections on the optical depth effects. Results in Table 4.6 indicate that such a correction also decreases the derived vibrational excitation temperatures by a few hundred Kelvin. Comparing the corrected T_{vib} with the corrected rotational excitation temperature for the population in the $\nu_2 = 0$ state (Table 4.2) or in the $\nu_2 = 1$ state, we conclude that those temperatures are in relatively good agreement within the error and that the vibrational equilibrium is reached.

The existence of vibrationally excited H_2O implies that the physical conditions of the hot absorbing gas are extreme as the $\nu_2 = 1$ state lies 2295 K above the ground vibrational state. The two main excitation mechanisms are collisional excitation due to warm, dense gas and radiative excitation by infrared radiation due to warm dust. If the $\nu_2 = 1$ state is collisionally populated, a density exceeding 10^{10} cm^{-3} is required for thermalization. This order takes account of a critical density[1] of 10^{11} cm^{-3} and a radiative trapping effect with β of ~ 0.1 for an optically thick line ($\tau \sim 10$). Since the vibrational equilibrium is reached, the density must be higher than 10^{10} cm^{-3}. As a comparison, Barr et al. (2020) estimated a blob density of 10^9 cm^{-3} in the disk systems of AFGL 2136 and AFGL 2591.

Other than the collisional excitation, one can estimate the relative importance of the excitation due to the strong radiation field. As is described in Tielens (Ch 2.3.3, 2005), with a dilution factor W (W <1) on the radiation,

$$\frac{T_{\rm ex}}{T_R} = 1 + \frac{kT_{\rm ex}}{h\nu}{\rm ln}W, \tag{4.14}$$

in which T_R is the radiation temperature and can be characterized by a dust temperature T_d inside a blackbody. Taking that the hot components are on the surface of the disk and are receiving radiation with $W = 0.5$ (half of the disk), that $T_{\rm ex}$ is from 400–500 K (equation 4.13), and that $h\nu$ are larger than 2295 K, we derive $T_{\rm ex}/T_R > 0.85$. This result indicates that the radiation field does drive the gas to the radiative temperature. We note that at the high implied densities ($\sim 10^{10}$ cm^{-3}), collisions between gas and dust will lead to gas kinetic temperatures that are coupled to but slightly lower than the dust temperature (Takahashi et al., 1983).

Li et al. (2022) detected vibrationally excited CO transitions and derived a rotational excitation temperature, 791 K, of CO $\nu = 1$ state for the MIR2-H1 component. The similarity excitation temperatures of the vibrational band of water (703 K) and CO support that the excitation temperature is more representative of the color temperature of the radiation field than

[1] Take the transition $\nu_2 = 1, J_{K_a,K_c} = 1_{0,1}$ as an example, the critical densities from 200 to 1000 K are $\sim 6\times10^{10}$ to 10^{11} cm^{-3}. Values of the Einstein A and the collisional rate of relevant energy states are adopted from Tennyson et al. (2001) and Faure & Josselin (2008).

the kinetic temperature because water has a much larger dipole moment than CO and therefore much more rapid spontaneous radiation. Finally, we emphasize that the scenario that the kinetic temperature is less than the dust temperature is inherent to our results as otherwise one would observe emission rather than absorption lines against the MIR continuum of the observed sources (see Appendix A in Barr et al., 2022a).

4.6.1.3 Comparison with Past Observations

The temperature range of 'H1' and 'H2' at -39.5 and -54.5 $\mathrm{km\,s^{-1}}$ from 400–500 K is comparable with that derived from the ISO-SWS observations in Boonman & van Dishoeck (2003). In the ISO-SWS study, the individual velocity components were not spectrally resolved, separate transitions were blended ($R = 1400$, 214 $\mathrm{km\,s^{-1}}$), and a Doppler width b of 5 $\mathrm{km\,s^{-1}}$ was assumed in modeling the absorption features. As presented in Table 4.5, the column density of hot gaseous components derived from our SOFIA/EXES study is about two orders of magnitude larger than the ISO-SWS results. This is a significant increment and much more that the 2.4 and 4.3 times increments derived for AFGL 2136 and AFGL 2591 (Barr et al., 2022a). We interpret this from two aspects: firstly, the absorption intensities of W3 IRS 5 measured by ISO-SWS are much lower than those for AFGL 2136 and AFGL 2591 (Boonman & van Dishoeck, 2003). This indicates a more significant opacity effect than in AFGL 2136 and AFGL 2591. As a result, the column densities in W3 IRS 5 corrected by the curve-of-growth analysis are much higher than those corrected values in AFGL 2136 and AFGL 2591 (Barr et al., 2022a). Secondly, saturated lines do not go to 0 but rather reach a non-zero intensity because of either the temperature gradient in a disk atmosphere or a covering factor less than 1 for a foreground cloud.

4.6.2 Other Foreground Gaseous Components

4.6.2.1 The Radiatively Heated Foreground Clouds

Comparison between the average low-energy CO and H_2O lines (Figure 4.6) reveals a warm component 'W' at -45.5 $\mathrm{km\,s^{-1}}$ which has a H_2O-to-CO relative abundance of 4.4%. While 'W' is considered as a shared component in front of MIR1 and MIR2, according to Li et al. (2022), this component is radiatively heated and is located at least as close as 2000 au to the protostars. In contrast, the cold CO component at -38 $\mathrm{km\,s^{-1}}$, which is regarded as a shared foreground envelope of ∼50 K, is not present in H_2O. If the water in the cold envelope has a comparable column density to that of CO, saturated absorption lines will be detected (see Appendix D.3). We conclude that the non-detection of water is due to a too-low column density ($< 4.7 \times 10^{15}$ $\mathrm{cm^{-2}}$). Therefore, both the warm and the cold components have a low H_2O/CO relative abundance.

Past observations of water lines, however, reveal the rather cool (∼50 K) component but did not observe the warm component (∼200 K). Observations in the pure rotational ortho-lines of water by SWAS (Snell et al., 2000) and Odin (Wilson et al., 2003) derive very comparable results. Adopting a temperature of 40 K, both studies reveal a relative ortho-H_2O abundance of order 1–2$\times 10^{-9}$, or column densities of $\sim$ 10^{13} $\mathrm{cm^{-2}}$. These results are also comparable with the column density of 10^{13} $\mathrm{cm^{-2}}$ derived by *Herschel*-HIFI observations (Chavarría et al., 2010), albeit that the latter result is rather model dependent. Therefore, we are reporting an EXES upper limit that is much higher than the column density observed by SWAS, Odin, and *Herschel*. We suggest that both the SWAS and Odin beams are very large and they may be measuring the large-scale core, which has a low average column density. If there is a density gradient rising toward the central source, then the submillimeter observations would measure column density that could be much less than along a pencil beam. With a pencil beam, it is difficult to come up with a clear picture of the structural relationship of these three components and with the larger scale structure of the source.

4.6.2.2 The Foreground Bullets

The four high-velocity "bullets" from -100 to -60 $\mathrm{km\,s^{-1}}$ in CO (200–300 K) were not detected in the water observations. Those bullets have been attributed to shocked gas intercepted by the pencil beam (Li et al., 2022). Specifically, Li et al. (2022) quantified the column density, the density, the velocity, and the thickness of these bullets and concluded that they are possibly correlated with the maser clumps moving toward us. As a comparison, assuming that water has a comparable column density to CO, one would expect to see water absorption lines with a depth of ∼80% relative to the continuum. However, among all the identified water lines, the only transition that has a potential absorption feature with an intensity depth of 5% at ~ -80 $\mathrm{km\,s^{-1}}$ is $2_{2,1} - 3_{1,2}$, which has an expected line depth of $\sim 30\%$. Therefore, CO bullets are indeed not detected in water lines.

J and C shocks are expected to lead to high abundances of H_2O, comparable to CO (Hollenbach et al., 2009, 2013). Hence, the absence of water absorption lines associated with this high-velocity gas sheds some doubt in their interpretation as shocked bullets and a potential link to water masers. We emphasize that we do recognize other factors that are related to non-detections of the bullets, although those factors are insignificant. For example, we may define the baseline beyond ~ -75 km s^{-1} poorly where the bullets are expected. In addition, those foreground bullets were exclusively found in front of MIR2 in the CO observations and may suffer from extra dilution in the SOFIA observations. However, these factors are insignificant for the high abundances of H_2O-to-CO, as one would expect to observe prominent saturated H_2O absorption features.

4.6.3 Chemical Abundances along the Line of Sight

The availability of data on column densities of different species such as gaseous CO and ices along the line of sight toward W3 IRS 5 makes it an appropriate example to address the oxygen and carbon budget. We discuss below the reservoirs of the two elements in different environments of the W3 IRS 5 system and other massive protostars including the hot disks as well as the cold foreground clouds.

As described in § 4.6.1, SOFIA observations derived much higher column densities of hot gaseous water than that of hot gaseous CO in W3 IRS 5 as well as AFGL 2136 and AFGL 2591 (Barr et al., 2022a). While iSHELL measurements (Barr et al., 2020; Li et al., 2022) provide a better constrain on the amount of gaseous CO from the same region, we derive high relative abundances of H_2O to CO; e.g., ~ 1 to 1.5 for W3 IRS 5, 1.6 for AFGL 2136, and 7.4 for AFGL 2591. Such a high relative H_2O to CO abundance is expected for warm, dense gas where gas phase chemistry rapidly converts the available O not in CO into H_2O (Kaufman & Neufeld, 1996b). As a comparison, these values are much higher than the H_2O/CO = 10^{-4} derived from submillimeter observations by *Herschel*-HIFI toward the hot core region of AFGL 2591 (Kaźmierczak-Barthel et al., 2014), or the value of 4.4% from the warm 200 K component identified in this water study (see

Table 4.2). On the other hand, a high relative H_2O to CO abundance from 1 to 2 was observed toward T Tauri and Herbig disks (Carr & Najita, 2008; Salyk et al., 2011).

In the cold dense ISM, there is a well-documented problem of the missing oxygen budget (Whittet, 2010). While Hollenbach et al. (2009) predicted that oxygen not in silicates or oxides should be eventually converted into gaseous CO and ices, a substantial shortfall of oxygen is observed. In the study of the Taurus complex dark clouds (Whittet, 2010), the combined contributions of gaseous CO, ice, and silicate/oxide account for less than 300 ppm of the elemental oxygen compared to the solar value of 490 ppm (Asplund et al., 2009). We observed a similar missing oxygen reservoir in W3 IRS 5: assuming 284 ppm of the O in diffuse clouds (Cartledge et al., 2004), we only see a value of 58.1 ppm (20.4%) in cold, dense clouds (see Table 4.7). If one uses local B stars as the interstellar standard, the total budget of the elemental abundance of oxygen is even higher (575 ppm rather than 490 ppm, Nieva & Przybilla, 2012). Therefore, a budget close to the oxygen abundance in silicate (~ 200 ppm, Tielens & Allamandola, 1987) is missing or is locked up in an unidentified form, which is referred to as "the unidentified depleted oxygen (UDO)" in Whittet (2010).

The intrinsic properties of the reservoir of the missing oxygen remain mysterious. Refractory dust compounds like carbonates are implausible, as they will survive and appear in the diffuse medium as well. Neither gas-phase nor solid-phase O_2 are possible as well. While SWAS observations (Goldsmith et al., 2000) towards massive protostars provide an upper limit of 0.1 ppm on the gaseous O_2, solid O_2 is too volatile in the line of sight of W3 IRS 5. Oxygen-bearing organics in solid ice would be a potential carrier, although no significant detection of the related bonds has yet been detected at infrared wavelengths (Gibb et al., 2004). We suggest that the MIRI spectrograph on board the *JWST* is well-suited to study such an organic inventory. One other possibility of the UDO is a population of very large water ice grains ($> 1\ \mu$m) in the cold gas (Jenkins, 2009). These large grains are nearly opaque to infrared radiation and are hard to detect.

Similar to the "oxygen crisis", a depletion problem in elemental carbon exists in the envelope of W3 IRS 5 (see Table 4.7). The total amount of carbon (32 ppm) comprises only 19.7% of the value expected in diffuse clouds (160 ppm, Cardelli et al., 1996; Sofia et al., 1997). As discussed in Li et al. (2022), one speculation is that the carbon-containing ice compounds were converted into an organic residue by prolonged UV photolysis (Bernstein et al., 1995, 1997; Vinogradoff et al., 2013).

Both the "oxygen crisis" and the "carbon crisis" were observed in AFGL 2136 and AFGL 2591 as well. In contrast to previous studies that relied on a comparison of pencil beam IR absorption line studies with sub-millimeter emission observations, for these massive protostars, the IR pencil beam samples the same material in absorption. As shown in Table 4.7, the depletion problems are more severe for AFGL 2591, but less severe for AFGL 2136. We suggest that further studies of the different oxygen reservoirs could help pinpoint the processes involved in the missing oxygen or carbon reservoirs by studying a large enough sample with diverse characteristics.

Table 4.7: The Repository of Elemental Carbon and Oxygen in the Cold Regions of Massive Protostars

	W3 IRS 5			AFGL 2136			AFGL 2591		
	N (cm^{-2})	X_C (ppm)	X_O (ppm)	N (cm^{-2})	X_C (ppm)	X_O (ppm)	N (cm^{-2})	X_C (ppm)	X_O (ppm)
Hydrogen	2.0(23)			7.4(22)			8.0(22)		
CO (gas)[a]	4.7(18)	23.5	23.5	5.1(18)	68.9	68.9	2.5(18)	31.3	31.3
H_2O (gas)[b]	<4.7(15)	...	<0.02	...	...	...	...	...	...
CO (ice)[c]	2.1(17)	1.1	1.1	2.7(17)	3.6	3.6	...	...	...
CO_2 (ice)[c]	7.1(17)	3.6	7.1	7.8(17)	10.5	21.1	1.6(17)	2.0	4.0
CO_2 (ice)[c]	7.1(17)	3.6	7.1	7.8(17)	10.5	21.1	1.6(17)	2.0	4.0
H_2O (ice)[c]	5.1(18)	...	25.5	5.1(18)	...	68.9	1.2(18)	...	15.0
CH_3OH (ice)[c]	1.7(17)	0.9	0.9	2.6(17)	3.5	3.5	1.7(17)	2.1	2.1
Sum (ice)	...	5.6	34.6	...	17.6	97.1	...	4.1	21.1
Sum (total)	...	29.1	58.1	...	86.5	166.0	...	35.4	52.4
Diffuse Clouds (gas)		160[d]	284[e]		160	284		160	284
Silicate Abundance[f]			200			200			200
Solar Abundance[g]		269	490		269	490		269	490
B-Stars Abundance[h]		214	575		214	575		214	575

[a] Results of gaseous CO are adopted from Li et al. (2022) for W3 IRS 5, and are from Barr et al. (2020) for AFGL 2136 and AFGL 2591. The temperatures of the cold regions are ~50 K, 27 K, and 49 K for W3 IRS 5, AFGL 2136, AFGL 2591, separately (Barr et al., 2020; Li et al., 2022).
[b] Results from this work. [c] All measurements on ice are adopted from Gibb et al. (2004).
[d] Cardelli et al. (1996); Sofia et al. (1997). [e] Cartledge et al. (2004). [f] Tielens & Allamandola (1987).
[g] $\log\epsilon_C = 8.43$, $\log\epsilon_O = 8.69$ (Asplund et al., 2009). [h] Nieva & Przybilla (2012).
(1) For column densities, powers of 10 are given in parentheses. (2) X_C and X_O are the relative abundances derived from N_C/N_H and N_O/N_H.

4.7 Summary

We conducted high spectral resolution ($R \sim$50,000; 6 $\mathrm{km\,s^{-1}}$) spectroscopy from 5–8 μm with EXES on board SOFIA toward the hot core region associated with the massive binary protostar W3 IRS 5. By comparing with the LTE models constructed with the existing laboratory line information, we identified about 180 $\nu_2 = 1 - 0$ and 90 $\nu_2 = 2 - 1$ absorption lines. Preliminary Gaussian fittings and rotation diagram analyses reveal two hot components with $T >$ 600 K and one warm component of 190 K. However, the large scatter in the rotation diagrams of the two hot components reveals 1) opacity effects, 2) that the absorption lines are not optically thin, and 3) the total column densities derived from the rotation diagrams are underestimated.

We adopted two curve-of-growth analyses to account for the opacity effects of the hot components. One model considers absorption in a foreground slab that partially covers the background emission. The other model assumes absorption in the photosphere of a circumstellar disk with an outward-decreasing temperature in the vertical direction. In both models, about half of the data points converted from the $\nu_2 = 1 - 0$ transitions are located on the logarithmic part of the curve-of-growth, confirming that the corresponding absorption lines are optically thick. The two curve-of-growth analyses correct the column densities by at least atn order of magnitude and lower the derived excitation temperatures accordingly. We note that for the disk model, the results of the curve-of-growth analysis depend on the adopted velocity width σ_v and the parameter ϵ that characterizes absorption and scattering of the absorption line. We provide a reference table for different σ_v and ϵ as the two parameters are poorly constrained.

Although our SOFIA-EXES observations do not spatially resolve the binary protostars in W3 IRS 5, using the kinematic and temperature characteristics, we link each H_2O component to a spatially separate CO component identified in IRTF/iSHELL observations (R=88,100). Specifically, the warm H_2O component 'W' is linked to the shared warm CO component MIR1-W1/MIR1-W2, the hot H_2O component 'H1' is linked to the MIR2-H2 in CO, and the hot H_2O component 'H2' is considered to be related to one of the CO MIR1-W′ components.

Once the connections of H_2O components and CO components were established, we discussed the physical origins of H_2O components in light of the better understood of CO components. From our analysis, we conclude that the disk model is the preferred one over the slab model out of the considerations of the geometry constraints, although disk models face challenges in realizing such an internal heating mechanism.

We derive the H_2O/CO abundance ratio based on the results of the disk model and discuss the chemical abundances along the line of sight based on the H_2O-to-CO connection. For the hot gas, we derive a high H_2O/CO abundance ratio of 0.9. Such a high relative H_2O to CO abundance is expected for warm, dense gas where gas phase chemistry rapidly converts the available O not in CO into H_2O. For the cold gas, we observe a substantial shortfall of oxygen in agreement with earlier studies of cold dense clouds. We suggest that organics in solid ice are the potential carrier.

Chapter 5: Summary and Future Outlook

This thesis presents studies of molecular clouds in systems that are either close and cold, or far and hot, with instruments advanced in sensitivity and spatial/spectral resolution. This chapter summarizes some takeaway messages for the reader and presents a future outlook for projects finished in the thesis.

5.1 The Takeaway

5.1.1 *Argus* for Resolved Molecular Gas

Half of the thesis (Chapter 2 and Appendix A) introduces the behavior of the first array receiver functioning at 3 mm *Argus* on the GBT and the knowledge we learned from molecular gas in IC 342 in *Argus*' initial extragalactic observations. The main results are as follows:

- The multi-beam receiver *Argus* can map molecular clouds of several arcmins efficiently with a high spatial resolution of $6''$–$9''$ in a fast raster scanning mode.
- For the GBT with a $\sim$100 m dish, observations under strong winds ($>$5 m s^{-1}) can result in pointing errors as large as a beam and should thus be avoided. Cross-correlation with correct known maps can to some extent help register the positional offset.
- The beam pattern of *Argus* rotates while the GBT is tracking. Therefore, observations on

targets whose declination is close to 38° (the latitude of the GBT) should not be taken when the hour angle (HA) is smaller than 0.5 hr. Otherwise, the unevenness of the map sampling can be severe.

- *Argus* made the first ^{12}CO(1−0) map of an external galaxy, IC 342, from the GBT over a $4' \times 5'$ region in only 11 hours (including the overheads). The sensitivity and the spatial resolution (6.3″) are sufficient to resolve giant molecular clouds of approximately a hundred parsecs in the inner spiral arms.

- The resolved maps of HCN and HCO$^+$ on the galactic bar of IC 342 show a constant ratio of 1.2$\pm$0.1 across a 1 kpc region. In the past, single-beam observations toward the brightest center of external galaxies found similar HCN-HCO$^+$ ratios averaged over the entire nucleus. The ratios were commonly interpreted as the lines being subthermally excited. This interpretation does not work for the result in IC 342. We argue the HCN-HCO$^+$ ratio therein is more sensitive to the relative abundance of the two species.

- The breakdown of the $L_{\rm IR} - L_{\rm HCN}$ correlation at high spatial resolution due to the effect of incomplete sampling of star-forming regions in IC 342 is observed. The scatter of the $L_{\rm IR} - L_{\rm HCN}$ relation decreases as the spatial scale increases from 10″–30″ (170–510 pc) and is comparable to the scatter of the global relation at the scale of 340 pc.

Overall, observations with high spatial resolution on (dense) molecular clouds further break down the degeneracy problems in understanding the physical conditions. The ability of *Argus* to map large samples of galaxies efficiently will solidify the findings in IC 342, and help establish the quantitative link between gas density and star formation (the DEGAS survey, Kepley et al., in prep).

5.1.2 MIR Absorption Spectroscopy and Massive Star Formation

The other half of the thesis (Chapters 3 and 4) uses MIR absorption spectroscopy to study a massive protobinary, W3 IRS 5, which is at its hot core phase. In Chapter 3, I report the results of observation at 4.7 μm toward the rovibrational lines of CO and its isotopologues from iSHELL at IRTF. The narrow and long slit of iSHELL spatially resolves the binary and allows the characterization of each protostar respectively. Chapter 4 presents observations of EXES/SOFIA toward W3 IRS 5 from 5–8 μm with a high spectral (therefore, also a high velocity) resolution comparable to that of iSHELL, and specifically analyzes water rovibrational transitions at this wavelength range. The main findings are as follows:

- The iSHELL/ITRF study reveals different kinematic components in each protostar, including a cool (~ 50 K) foreground envelope shared by the two, several high-velocity clumps (200–300 K) exclusively belonging to one protostar, and a few warm and/or hot components (400–700 K) in the immediate environment of the binary.

- Analyses of spectrally resolved molecular lines show that many of the lines are optically thick. Curve-of-growth analyses are used to interpret the line intensities and to derive correct column densities, which can be two orders of magnitude higher than that derived by studies with much less spectral resolution.

- Either a foreground slab model or a disk model is used in the curve-of-growth analyses to interpret the data. For hot components, the disk model is preferred because it requires fewer assumptions and provides a universal interpretation of hot-absorbing components ubiquitously found in other hot cores.

- To interpret the absorption lines, the disk scenario in the massive protostar requires an vertically-decreasing temperature from mid-plane. This is a significant difference compared to the disk structures observed in a T Tauri star or a Herbig AeBe star because disks in those systems have a hotter surface due to the illumination from the central star.

- The high-velocity components found in CO in one of the protostars are likely to have a J-shock origin and are likely related to water maser spots in the same region. In this way, the physical information of water masers along the direction of their movements can be complemented. However, those components are not observed in the EXES water studies and this result sheds doubts on the proposed link above.

- The iSHELL observations toward CO build the framework of substructures in the W3 IRS 5. We are therefore able to directly compare the kinematically resolved water and CO components along the line of sight and address the oxygen and carbon budget under different physical conditions. We find that in the hot gas, all oxygen that is not locked in CO resides in water. In the cold gas, we observe a substantial shortfall of oxygen and suggest that organics in solid ice is the potential carrier.

Overall, MIR absorption spectroscopy provides a critical and unique diagnostic of the physical conditions and chemical inventory in the hot core phase of the not-well-understood massive protostellar systems.

5.2 Future Work

5.2.1 *Argus* in Its Commission

I have been involved in three large *Argus* surveys that are still ongoing since its deployment on the GBT: DiSCo[1], GBT EDGE[2], and DEGAS[3]. DiSCo studies the kinematics of all starless and Class 0 protostellar cores in Perseus down to $\sim$0.01 pc scales with $<$0.05 km s^{-1} velocity resolution using the widely-used dense gas tracer N_2H^+. GBT EDGE aims to conduct CO(1–0) observations toward a sample of 150 galaxies that is representative of the local population to answer fundamental questions regarding galaxy growth and quenching, star formation regulation, and the structure of the molecular component. The goal of DEGAS is to map four dense molecular gas tracers (HCN(1–0), HCO^+(1–0), ^{13}CO(1–0), and C^{18}O(1–0)) over the central 4 arcmin^2 of 36 nearby galaxies to set the dense molecular gas-star formation relation. The Green Bank Observatory and the original *Argus* team are now collaborating on an Argus144[4] project, which would take advantage of the technical development afforded by Argus to produce a camera of 144 beams with ten times the mapping speed.

IC 342 in Chapter 2 is one of the 36 samples of the DEGAS survey. The scanning coverage calculator (Appendix A) was used for DiSCo and GBT EDGE for calculating the required integration time and designing the observation strategy at the stage of proposing. Observations of these two surveys are still ongoing and I take participate in regular observing processes.

[1]Dynamics in Star-forming Cores: https://greenbankobservatory.org/science/gbt-surveys/disco-gas/
[2]Extragalactic Database for Galaxy Evolution: https://greenbankobservatory.org/science/gbt-surveys/edge/
[3]Dense Extragalactic GBT+Argus Survey: https://greenbankobservatory.org/science/gbt-surveys/degas-survey/
[4]*Argus* 144: https://greenbankobservatory.org/science/instruments-2020-2030/argus144/

5.2.2 Disks in the Embedded Massive Protostellar Phase

I present in the rest of this section some questions that arose naturally when conducting work in Chapters 3 and 4. Those questions point out interesting future directions to pursue and will further shed light on our understanding of massive star formation processes.

Is there a disk during the massive star formation process? As is introduced in § 1.1.1.3, the formation of massive stars is not as well understood because the accretion is counteracted by strong radiation pressure and harsh ionization fields. A disk-mediated accretion scenario, nevertheless, has been gradually established both theoretically (Bonnell & Bate, 2006; McKee & Tan, 2003) and observationally: Submillimeter/millimeter observations provide direct, accumulating evidence of the presence of Keplerian disks surrounding massive protostars from sub-100 to sub-1000 AU (e.g., Ginsberg et al., 2018; Ilee et al., 2016; Johnston et al., 2015, 2020; Moscadelli & Goddi, 2014; Moscadelli et al., 2019; Zapata et al., 2019). However, it is worth noting that different disk tracers were applied among these studies while the detected Keplerian disks vary in their spatial scale as well as the energy regime (Table5.1). Understanding the role and properties of an accretion disk is still at a stage that requires *thorough case studies* of different hot cores.

Are there disks in the massive protobinary system, W3 IRS 5? MIR spectroscopy studies in this thesis revealed hot, dense absorbing in W3 IRS 5. But whether to locate the hot absorbing gas on the disk remains uncertain: absorption lines may originate from gas clumps in front of the disk, or from the photosphere of the disk whose surface layer is cooler than the mid-plane. The two scenarios are indistinguishable if one compares the theoretically predicted line intensities to the observed ones. To break down the foreground-gas/disk degeneracy, it

Table 5.1: Detection of Keplerian Disks in MYSOs

MYSO	d (kpc)	Disk	Tracers	E_u (K)	Disk Scale (AU)	Beam Size (AU×AU)	Ref
AFGL 2136	2.2	Y	H_2O $5_{5,0}-6_{4,3}$ $\nu_2=1$	3462	<50	44×33	(1)
AFGL 2591	3.3	Y	HCN J = 4–3 ν_2 = 1	1067	<1000	627×561	(2)
AFGL 4176	4.2	Y	CH_3CN	80–900	4000	1176×1008	(3)(4)
NGC 7538 IRS1	2.7	Y	CH_3OH masers	...	500	27×14	(5)
W3 IRS5	1.8	?	HCN J = 4–3 ν_2 = 1	1067		500–1000?	

Notes: (1): Maud et al. 2019; (2): Suri et al. 2021; (3–4): Johnston et al. 2015, 2020; (5) Moscadelli & Goddi 2014.

is essential to know the velocity of each contributor to the mid-IR continuum, which is likely a disk, through spectroscopic imaging of high excitation energy transitions at sub-mm/mm wavelengths. An SMA proposal has been successfully proposed to observe vibrationally excited molecular lines at 354 GHz to spatially and spectrally resolve the disks in this 1.2″ protostellar binary. The spatial resolution of the SMA's extended configuration (0.8″×0.75″) is sufficient for this goal.

Are there disk-disk interactions in W3 IRS 5? W3 IRS 5 is likely to have multiple disks. A big hot molecular core with large-scale outflows, shocks, and circumbinary toroid is detected in this binary (Imai et al., 2000; Rodón et al., 2008; van der Tak et al., 2000, 2005; Wang et al., 2012, 2013). The presence of disks is referred from rotating structures that were found orthogonal to the jet axis indicated by linearly-aligned non-thermal compact radio knots (Purser et al., 2021; Wang et al., 2013). Multiple ∼600 K components are found at different velocities against the 350–500 AU mid-IR circular continuum (van der Tak et al., 2005) in both sources/elements in the binary (Chapters 3 and 4). It is unclear whether they originate from circumstellar or circumbinary disks. The SMA study thus also provides a unique opportunity to probe disk-disk interactions directly.

How is the temperature scenario of disks in massive protostellar systems realized, and what is its implication? As is summarized in § 5.1.2, the disk scenario used in the curve-of-growth analysis requires an vertically-decreasing temperature from mid-plane. But it remains a challenge in realizing such an internal heating mechanism. As discussed in Barr et al. (2022a), the "flashlight effect" may allow the disk to be not externally heated (Kuiper et al., 2010; Nakano, 1989; Yorke & Bodenheimer, 1999). If one proposes the dissipation of gravitational energy as the heating source, however, the accretion rate implied would be orders of magnitude higher than the expected accretion rate. Additional dissipation of turbulent and/or magnetic energy inherited from the prestellar core would be required. This implies a very early and active stage in the formation of these massive protostars. It is worth noting that viscous heating in the disk mid-plane has started to be taken into account in studies of massive star formation (e.g., Nazari et al., 2022), specifically in calculations of radiative transfer. But reconciling the different heating mechanisms and realizing the actual temperature scenario is still an intriguing task.

What is the organic inventory of the disks? The temperature stratification in the disks will result in chemical stratification. As is shown in Figure 5.1, high temperatures in disks opens up reactions with high energy barriers that produce simple molecules such as CH_4, C_2H_2, NH_3, and HCN (Agúndez et al., 2008; Bast et al., 2013). These species drive a rich organic chemistry and a high abundance of complex molecules. While Chapter 4 only analyzes water lines from 5–8 μm, absorption bands of the simple molecules mentioned above are also expected in this wavelength region (e.g., Barr et al., 2018, 2020, on AFGL 2591 and AFGL 2136). Specifically, C_2H_2 and HCN absorption spectra have already been detected by *ISO-SWS* among W3 IRS 5 and many other massive protostars (e.g., Boonman & van Dishoeck, 2003). With the high spectral resolution and curve-of-growth analyses, we expect to derive the physical conditions and abundances

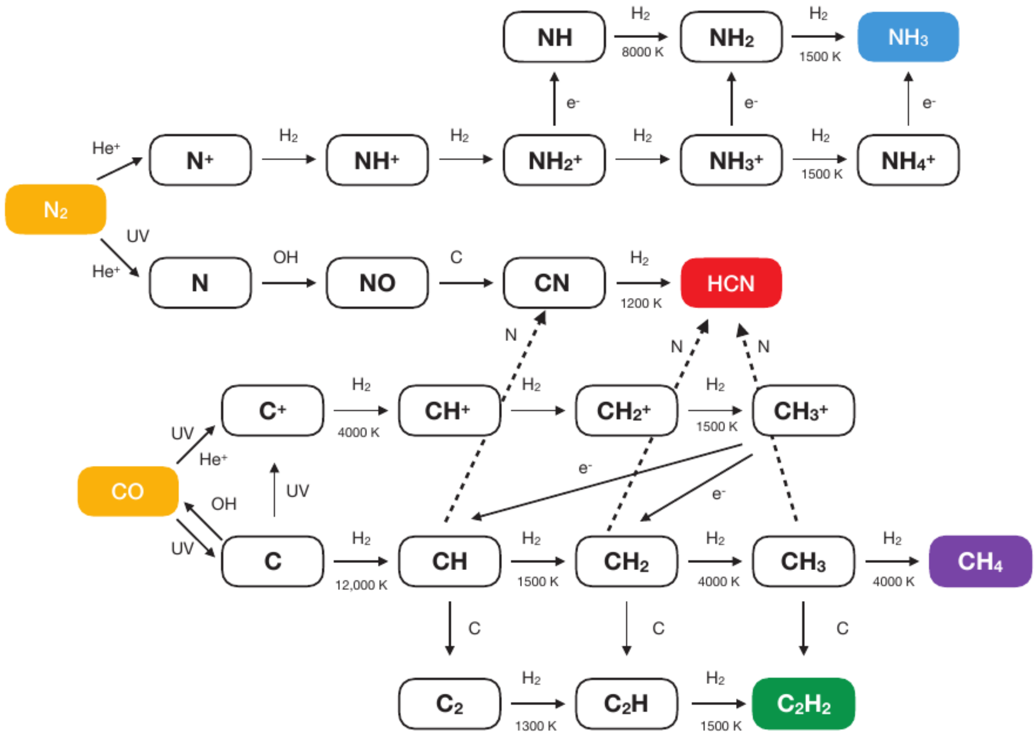

Figure 5.1: Chemical network of the main reactions with high activation energies to produce HCN, C_2H_2, CH_4, and NH_3. Figure directly taken from Barr's thesis (Barr et al. 2022), and is adapted from Bast et al. (2013) and Agúndez et al. (2008).

of the absorbing molecules. Anticipated work related to this perspective includes: (1) analyzing C_2H_2 and HCN band of W3 IRS 5 in the complete 3–13 μm range observed by EXES/SOFIA and the ground facility, TEXES/Gemini. (2) Investigate the EXES/SOFIA spectra of NGC 7538 IRS 1, another massive protostar with signatures of a disk, to complement the EXES hot core survey of massive protostars. The wavelength coverage is not limited to the 5–8 μm but also extends to the Q-band (above 20 μm), where OH, H_2O, and HCN lines are expected.

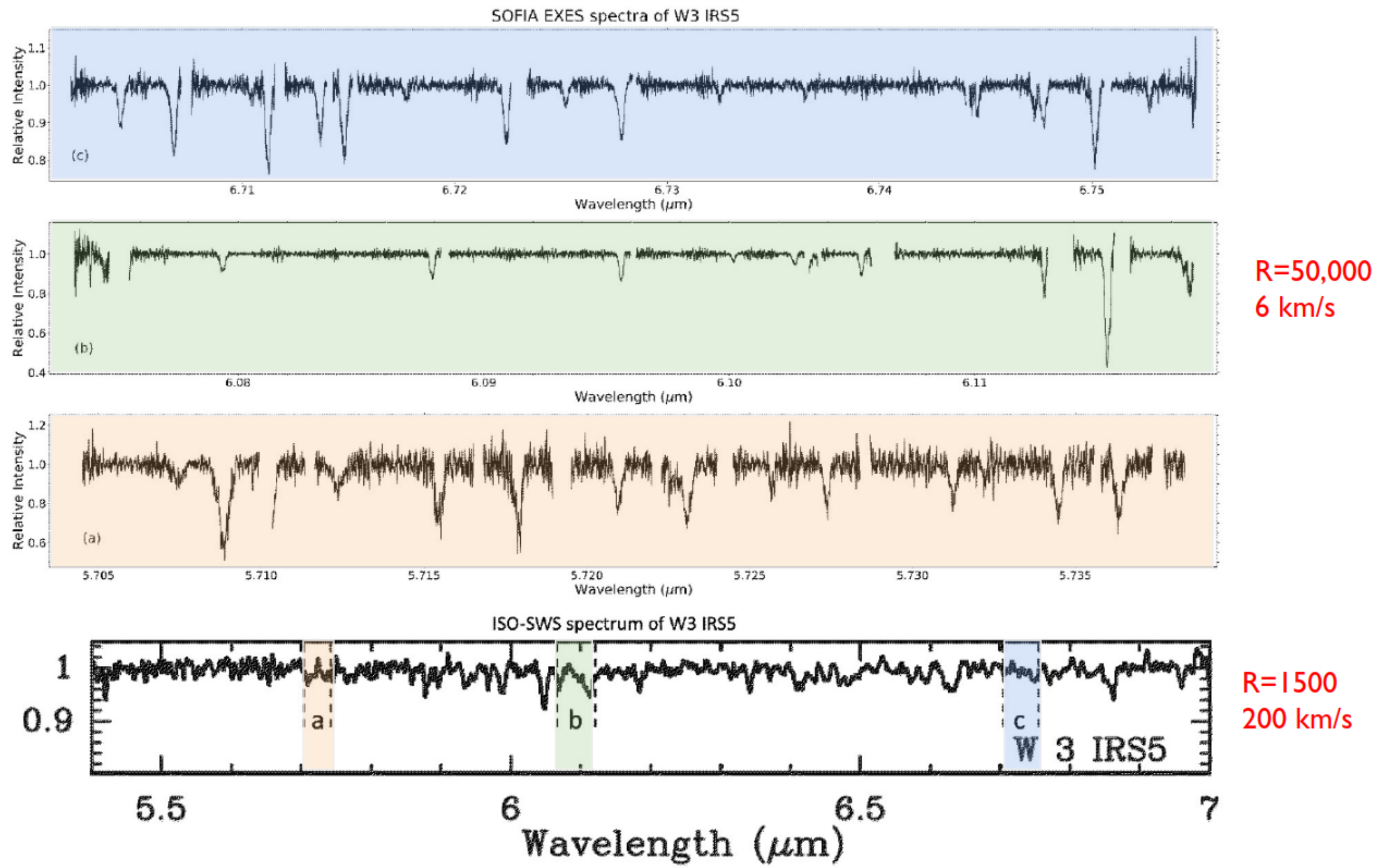

Figure 5.2: Adapted from Tielens (2021), Fig 4.10, with SOFIA/EXES spectra of W3 IRS 5 in colored band (Indriolo 2020, private comm) as a comparison to the low spectral resolution *ISO-SWS* spectra from Boonman & van Dishoeck (2003).

How do MIR observations on hot cores guide our knowledge of hot corinos? Other than the unknown properties of the embedded phase in massive star formation, one other motivation in investigating and surveying hot cores in detail is that those bright sources may provide plentiful information and serve as benchmarks to our understanding of hot corinos, the stage when low-mass protostars are in their embedded phase. As MIRI/*JWST* will study the evolution and chemical composition of protoplanetary disks around low-mass protostars, understanding the properties and physical/chemical processes of disks in massive protostellar systems will be insightful. However, it is worth noting that the inverse temperature gradient in disks of a massive protostellar system may lead to scenarios such as the "snowline" in low-mass systems being very far away from the central object. The formation scenario of planetesimals next to a massive protostar may therefore be quite different. From an observational perspective, however, the MIR survey on hot cores also provides important guidance for the interpretation of MIRI/*JWST* data on low-mass protostars. Firstly, MIRI*JWST* has a low (R=3000) spectral resolution, therefore many individual transitions within a given spectral resolution element will blend into one feature (see Figure 5.2). EXES/SOFIA spectra will point out regions where few spectral lines exist and can be safely used. Secondly, analyses of EXES data have revealed strong optical depth effects across many of the observed lines, and therefore provide important guidance on how to interpret the usable transitions and recover their column densities correctly.

Appendix A: Argus on the GBT

A.1 Mapping Strategy Analysis

Observations conducted with the 16 feeds *Argus* focal plane array spectroscopic imager Sieth et al. (2014) on board the alt-az-mounted telescope, GBT, usually adopts the OTF (On-The-Fly, Haslam et al., 1970; Mangum et al., 2007) mapping strategy. While good sampling of the source is desired, *Argus* cannot rotate following the change of parallactic angle during the scanning procedure. As a result, the actual scanning tracks are distorted, and the coverage of the 16 beams may not fully cover the desired mapping region. We present in this section the predicted distorted actual tracks of *Argus* and discuss the scanning strategy one should choose to improve the coverage.

A.1.1 Influence from the Change of the Parallactic Angle

Suppose that S is the position of the source, NP is the north pole and Z is the zenith, the angle between S-NP and S-Z is the parallactic angle. The change of the parallactic angle is the change of the direction of declination in an alt-az-mounted coordinate.

Ghigo (1990) gives the formula of the parallactic angle:

$$p = \tan^{-1}[\sin \mathrm{H}/(\cos\delta \tan\phi - \sin\delta \cos \mathrm{H})], \tag{A.1}$$

$$dp/d\mathrm{H} = 0.25(x \cos \mathrm{H} - \sin^2 \mathrm{H} \sin\delta)/(x^2 + \sin^2 \mathrm{H}). \tag{A.2}$$

In the formula above, H is the hour angle that changes as the source moves; δ is the declination of a source; ϕ is the latitude of the telescope, which is 38°26′ for Green Bank. Fig. $A.1$ indicates the function of p(H) of several sources. Since we also care about the level of the change of parallactic angle in 70 s, we present in Fig. $A.1$ p(H+70) - p(H) as well.

A.1.2 Image Distortion under Current Scanning Strategy

In our plot, 5 image pixels in length equal to 1 arcsec. I constructed a 2′ $\times$ 2′ region with 600 pixels $\times$ 600 pixels. The square Gaussian kernel used in this report has a FWHM of 6.5″ for the GBT at $\sim$115 GHz. Although the size of the kernel (number of pixels of the edge) only influences how we "crop" the convoluted result in size, an appropriate size is in need to balance the calculation time and a good representation of the image quality. To get one"detection" is to convolve the measurement of a 1 pixel $\times$ 1 pixel area with the kernel. The 4$\times$4 array *Argus* contains 16 beams in total, and the interval between centers of beams in a row (column) is 30.4″.

Because the parallactic angle changes during the observing process, one straight scanning track of one beam in the coordinates system of the *Argus* array will be projected to one curve in the RA-DEC coordinate system. We first check the tracks of the central positions of each beam, and will then convolve them with a Gaussian beam to reproduce the actual integration time.

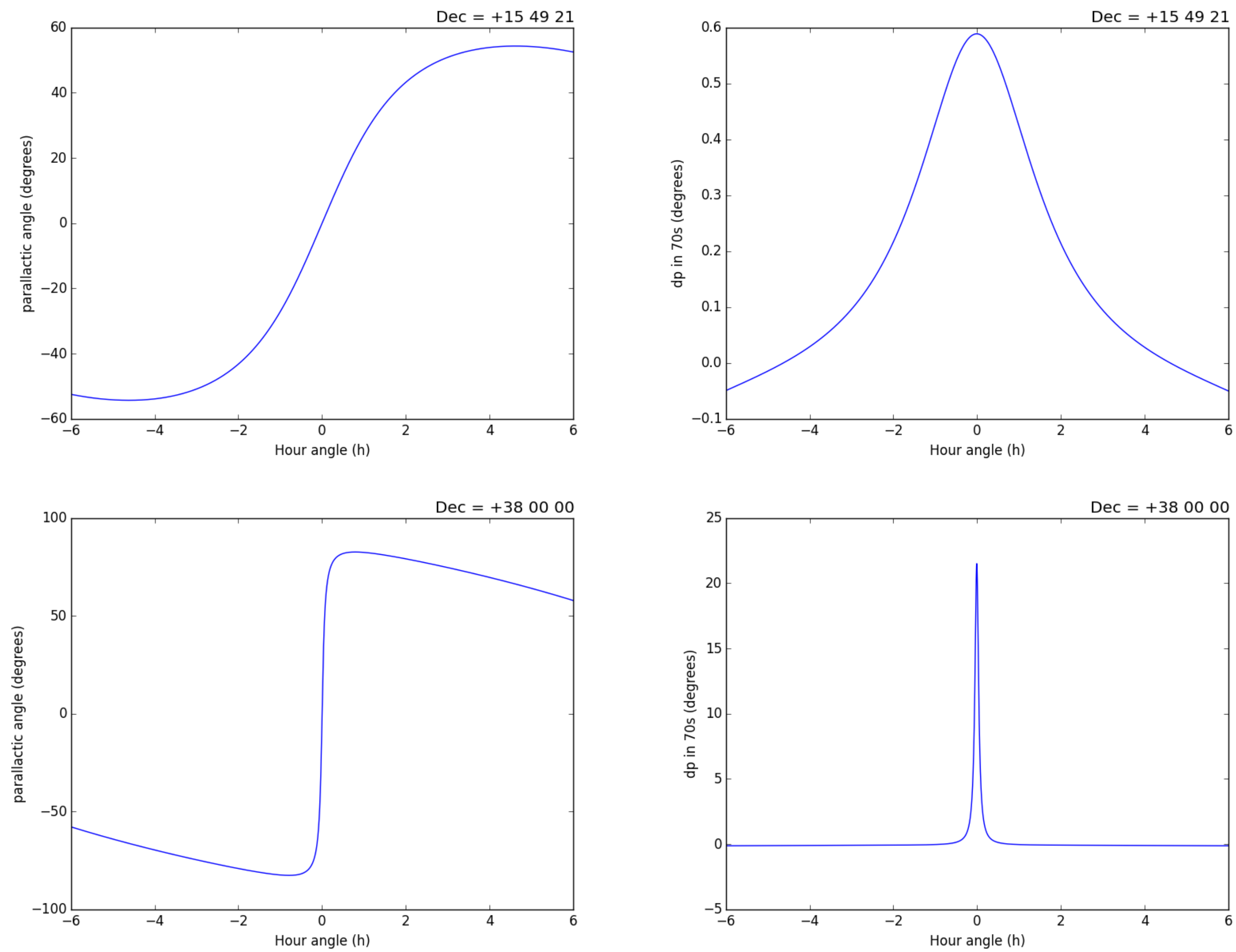

Figure A.1: p(H) and p(H+70) - p(H) of two sources are shown above. M100 has DEC = $+15°49'21''$, and the second source has a declination of 38°, which is close to the latitude of the GBT. We conclude from the plots that, the change of parallactic angle is very small for a source whose declination is far away from the latitude of Green Bank. Specifically, the change for M100 is smaller than 1°. However, the change can be very large if the declination is close to $38°26'$.

I am specifically concerned about two questions before conducting the convolution:

(1) Does the movement of the central position represent the movement of the first and the final beam that are in the same row?

(2) Does the movement of the central position represent the movement of the first and the final beam that are in the same column?

I present in Fig. A.2 the comparison of the resulted difference of dp in 70 s of different beams in direction of DEC or RA with an interval of 2 arcmin, respectively. M100, and the source with a declination of 38° are taken as the two examples. We can see that the difference in the direction of DEC is slightly larger than in the direction of RA, and the difference is larger when the declination is close to $38^\circ 26'$. From the plots, we can make the conclusion that, for sources whose declination is far away from the latitude of Green Bank, the difference of beams due to their position in either different DEC or RA can be neglected. When the declination of the source is close to $38^\circ 26'$, as long as the hour angle is not close to 0, it can be neglected, either. In conclusion, we may say that it's reasonable to convolve the 16 beams to the central position of the array directly when some specific conditions are satisfied.

Fig. A.3 shows the mapping commands used in the actual observation process.

- RALongMap: A Right Ascension/Longitude (RALong) map performs an OTF raster scan centered on a sky location. Scans are performed along the major axis of the selected coordinate system. The upper plot in Fig. A.3 shows a mapping that is scanning along the RA axis with a width of $2.5'$, a height of $2'$, a row spacing of $3.4251''$, and a scanning time of 72 s per row.

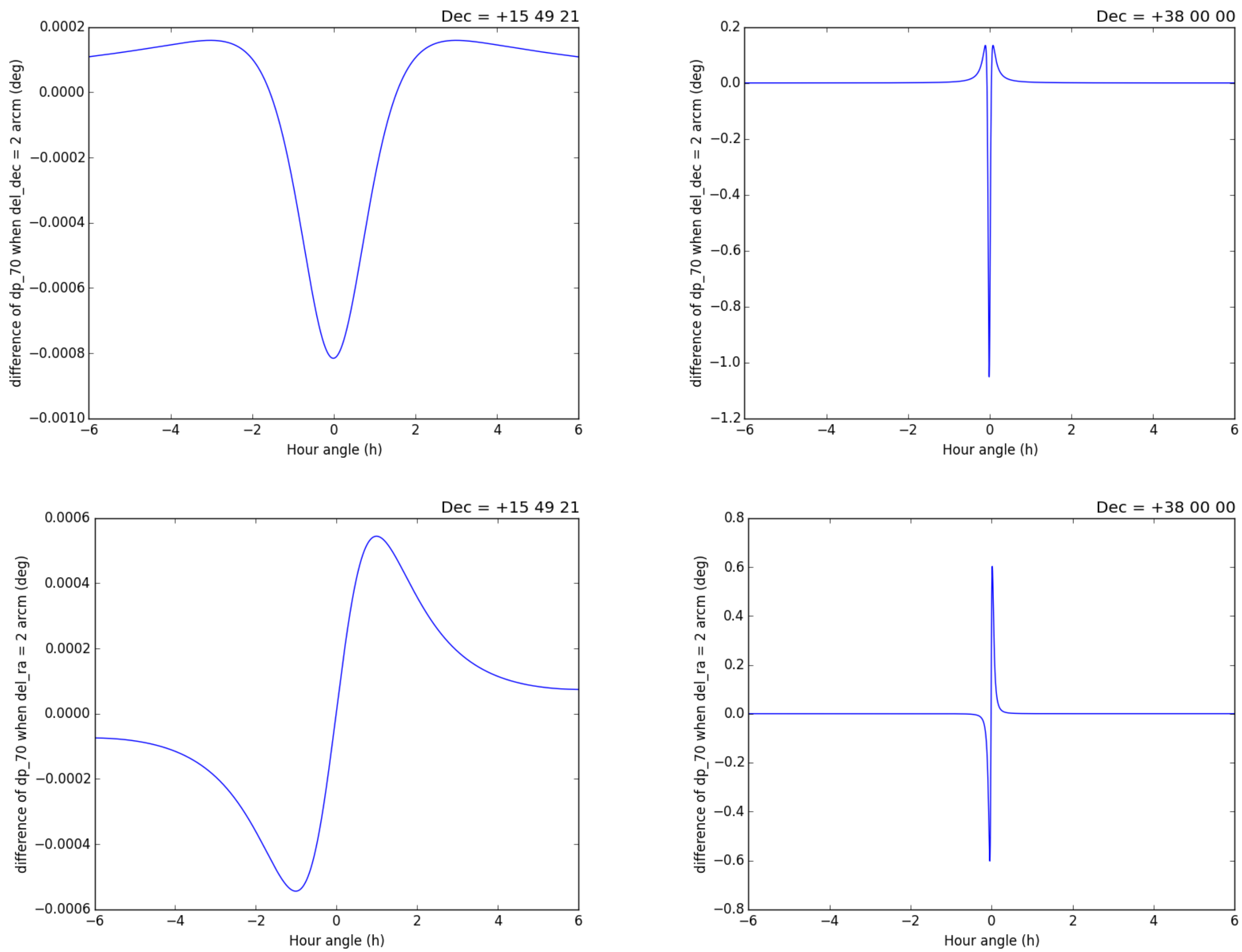

Figure A.2: Difference of dp in 70 seconds when the difference of DEC and RA are 2 arcmins, respectively for M100, and the source with dec of 38°.

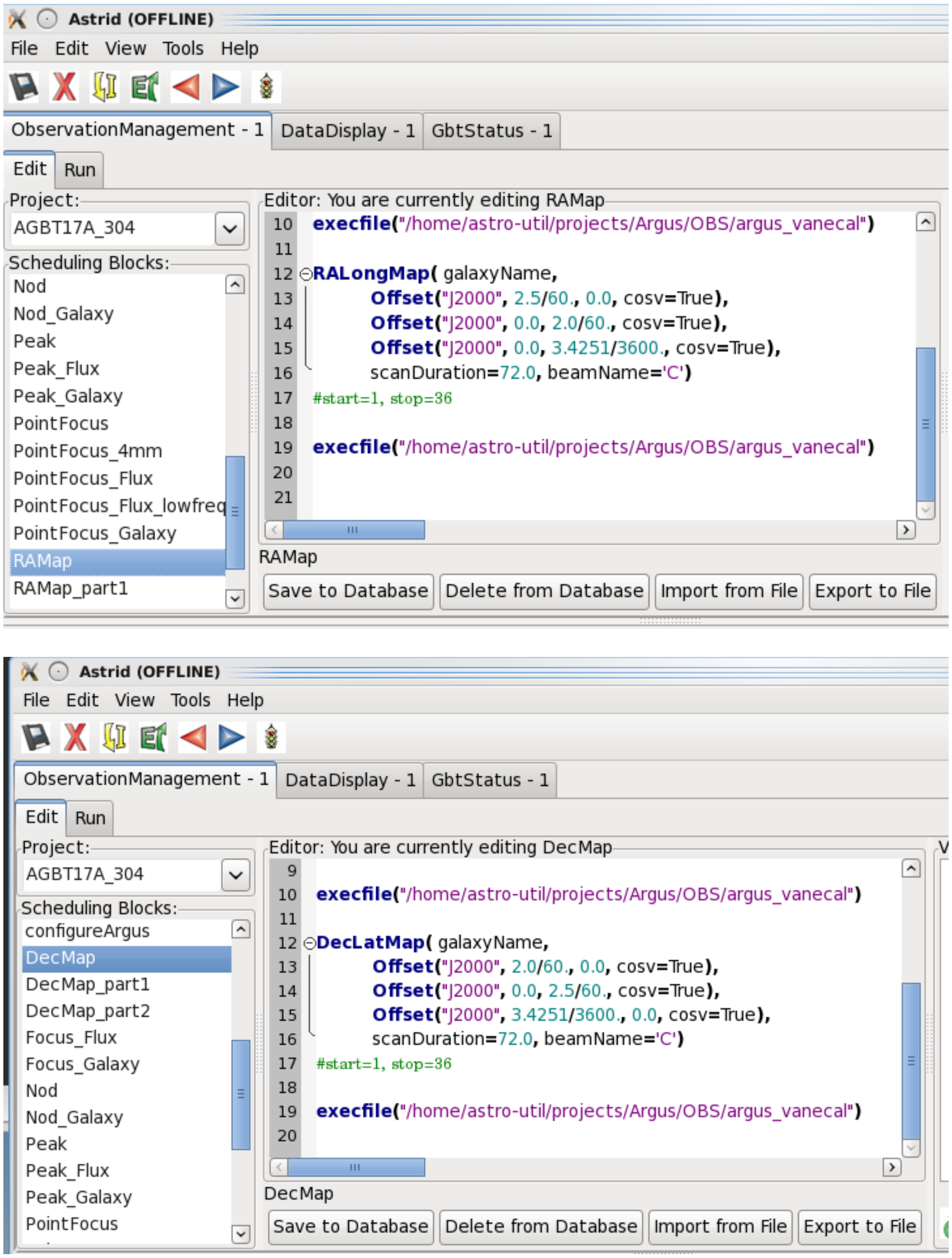

Figure A.3: Mapping commands used in actual observations. The left one is the type of RALongMap and the right one is of DecLatMap.

- DecLatMap: A Declination/Latitude map performs an OTF raster scan centered on a sky location. Scans are performed in declination, latitude, or elevation coordinates depending on the desired coordinate system. The lower plot in Fig. A.3 shows a mapping that is scanning along the Dec axis with a width of $2'$, a height of $2.5'$, a column spacing of $3.4251''$,

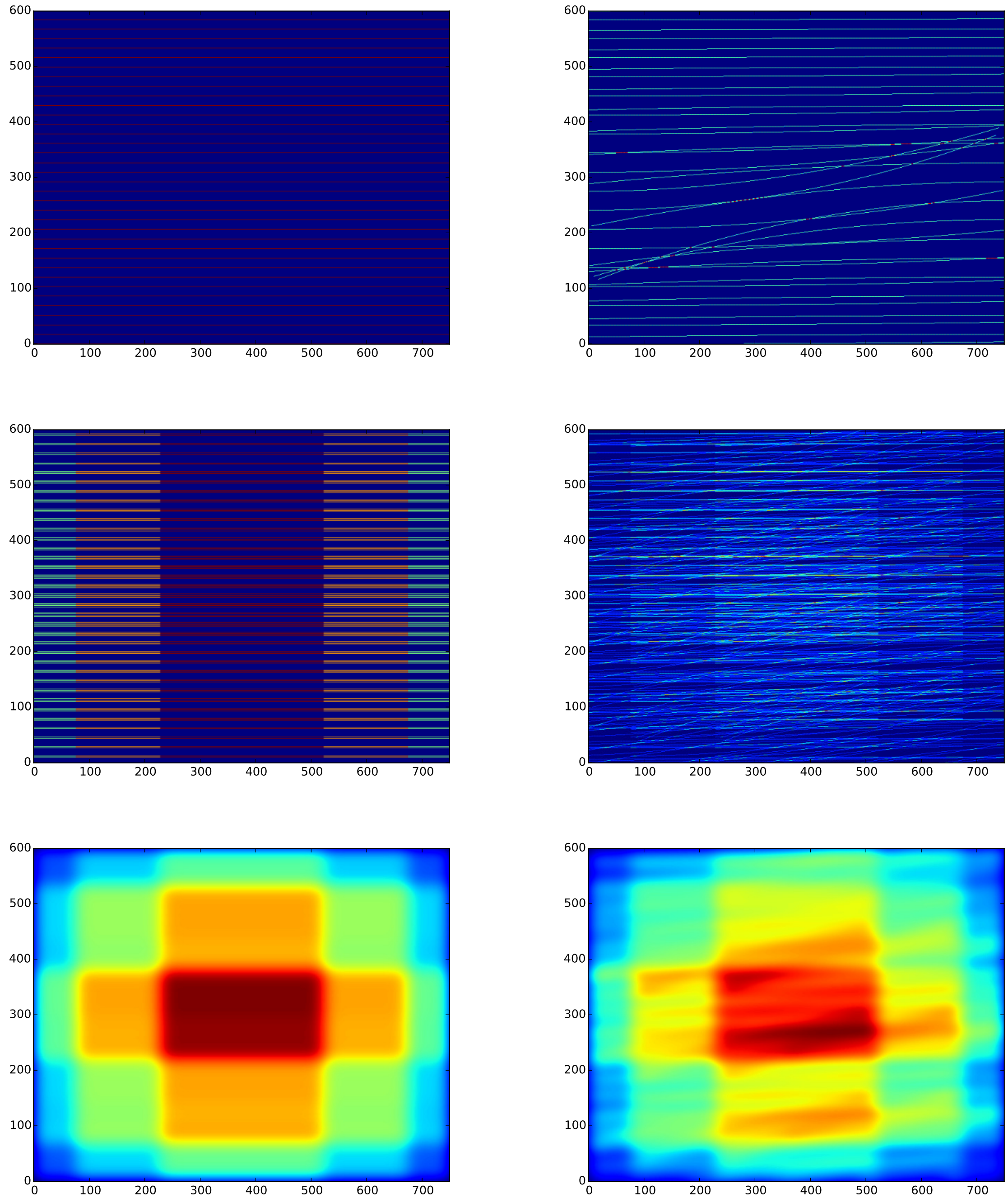

Figure A.4: The left plot shows an ideal track of the central position of the array and the right one shows the track of scanning that starts from HA = -0.3 hrs. The declination of the source is 38°.

and a scanning time of 72 s per row.

I plot the tracks on a full $2.5' \times 2'$ region to be consistent with the actual observation

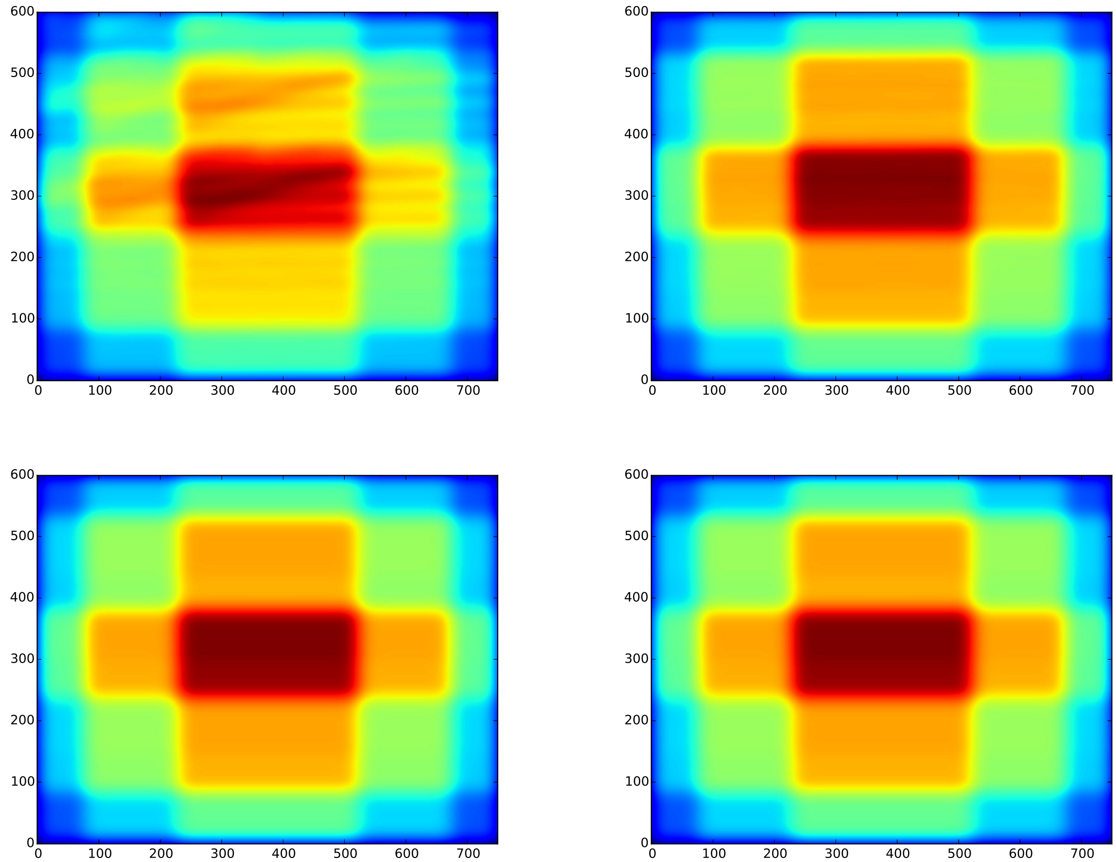

Figure A.5: From upper to lower, left to right, mapping with 2, 3, 4, 5 scannings $\times$ 43 mins are shown. The declination of the source is 38° as well.

commands, and present in Fig. A.4 both the ideal and the real tracks in a raster scanning. Specifically, plots on the second column correspond to scans starting from HA = -0.3 hrs. It is clear that at the beginning of the scan, the change of parallactic angle does not influence the tracks that much, and the curves appear until the source moves to around HA = 0.

One raster scan takes 72 s $\times$ 36 lines $\approx$ 43 min. To extend the observing time as well as the scanning times, we show in Fig. A.5 the tracks of 16 beams and the convoluted pattern, separately. It is quite clear that as the scanning time increases, the coverage is more evenly distributed.

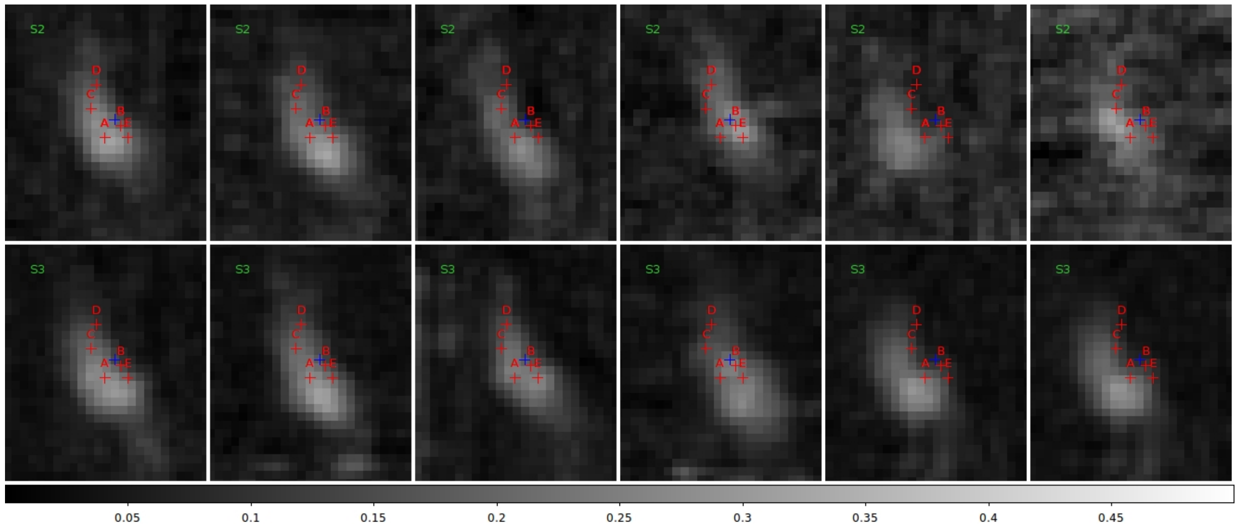

Figure A.6: Distorted nucleus region of IC 342 mapped in HCN(1−0) in selected different sessions. Each session last for 35−40 minutes and telescope pointing processes were conducted in between those sessions. Red crosses are positions of resolved giant molecular clouds observed by Downes et al. (1992) the and blue cross is the central position of IC 342. All images have the same intensity scale.

A.2 Registering Position Errors under Problematic Pointing

Strong wind (>5 m s^{-1}) results in pointing errors to our observation toward IC 342. Although re-pointing processes were conducted in between every 35−40 minutes session, the wind was strong enough to leave observable distortion on the image. As illustrated in Figure A.6), for twelve selected sessions observed in two nights, the nucleus region of IC 342 mapped in each session show a somewhat different structure and position. Combining all the distorted maps would result in a smeared map. A spatial cross-correlation was applied to quantify the image pixel offset. Figure A.7 presents the cross-correlation result in between different sessions. As a reference, the size of four image pixels equal to the size of the telescope beam. Figure A.7 shows that the largest offset is even larger than one beam, and correction on such a image distortion is necessary.

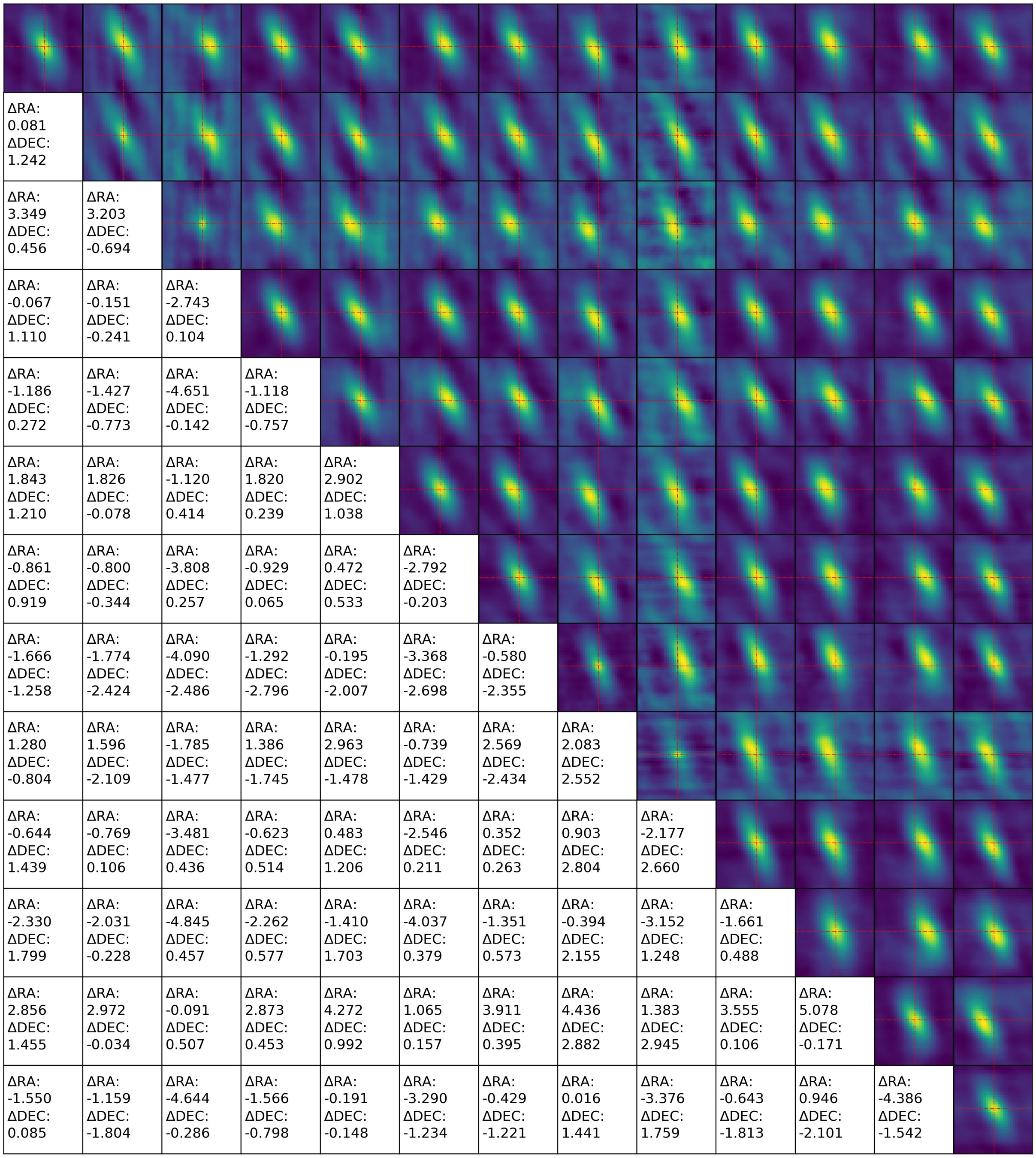

Figure A.7: Cross-correlation between sessions that are influenced by the strong wind. The offset are in units of image pixels. The size of four image pixels equal to the size of the telescope beam.

The image distortion is not limited to HCN observations. Cross-correlation with a known, correct image is required for fixing this problem. I took the IC 342 map from the BIMA-SONG

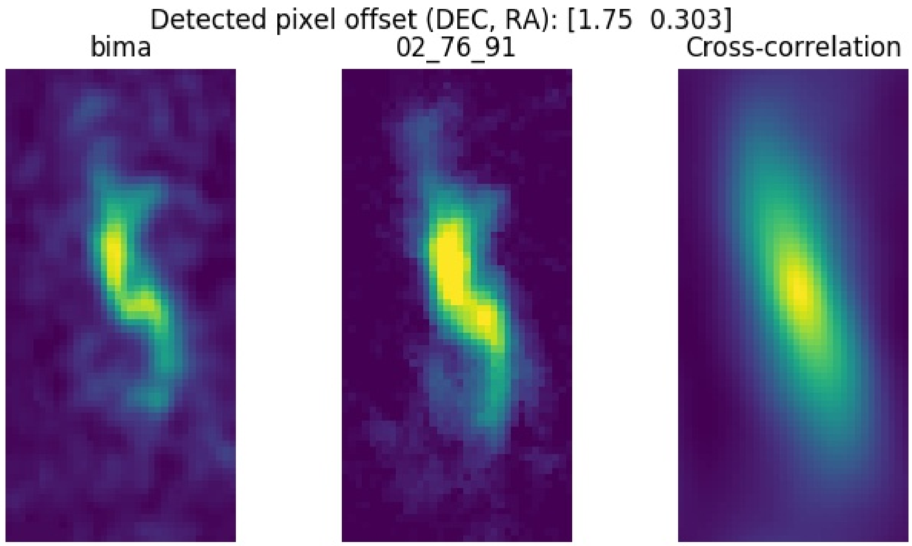

Figure A.8: Cross-correlation between the BIMA-SONG map of IC 342 and one of the ^{12}CO session observed by *Argus*.

survey (Helfer et al., 2003) for this purpose. BIMA is an interferometer, and the BIMA-SONG map has a comparable spatial resolution of $\sim 5''$. I present in Figure A.8 one example of the cross-correlation result, which quantifies the spatial offset in units of image pixel. Maps in Chapter 2 are all fixed in this way.

Appendix B: Appendix for Chapter 2

B.1 Solutions for a Specific Line Intensity Ratio

We plot in Figure B.1 the ratio of $(1 - e^{-\tau})$, and the ratio of $T_{\rm ex}$ between HCN(1–0) and $\rm HCO^+$(1–0) on the plots of the first and the second column. The optical depth effects and the excitation condition are represented, separately. Plots on the third column shows the joint result of τ and $T_{\rm ex}$, as $T_{\rm R} = (1 - e^{-\tau})J(T_{\rm ex})$. $J(T_{\rm ex})$ is the Rayleigh-Jeans corrected excitation temperature.

We overlay the contour representing $T_{\rm R}$ ratio of 1.2 on the first two columns to see the corresponding τ and $T_{\rm ex}$. The four representative regions discussed in Section 2.5.1 are labeled in circled numbers: (1) region 1 is contributed by very large optical depths, as it is located where the ratio of $(1 - e^{-\tau})$ of HCN and $\rm HCO^+$ is close to 1, and therefore the ratio of $T_{\rm R}$ equal to 1.2 is because the ratio of $T_{\rm ex}$ is 1.2, (2) region 2 spans across where HCN is less thermalized than $\rm HCO^+$, and its brightness is contributed by larger $(1 - e^{-\tau})$, (3) region 3 is where both HCN and $\rm HCO^+$ are thermalized, and the ratio of $(1 - e^{-\tau})$ is fixed to 1.2 regardless of the abundance ratio, and (4) region 4 follows the contours when the ratio of $T_{\rm ex}$ is slightly larger than 1 while both lines are subthermalized, and $(1 - e^{-\tau})$ is constant.

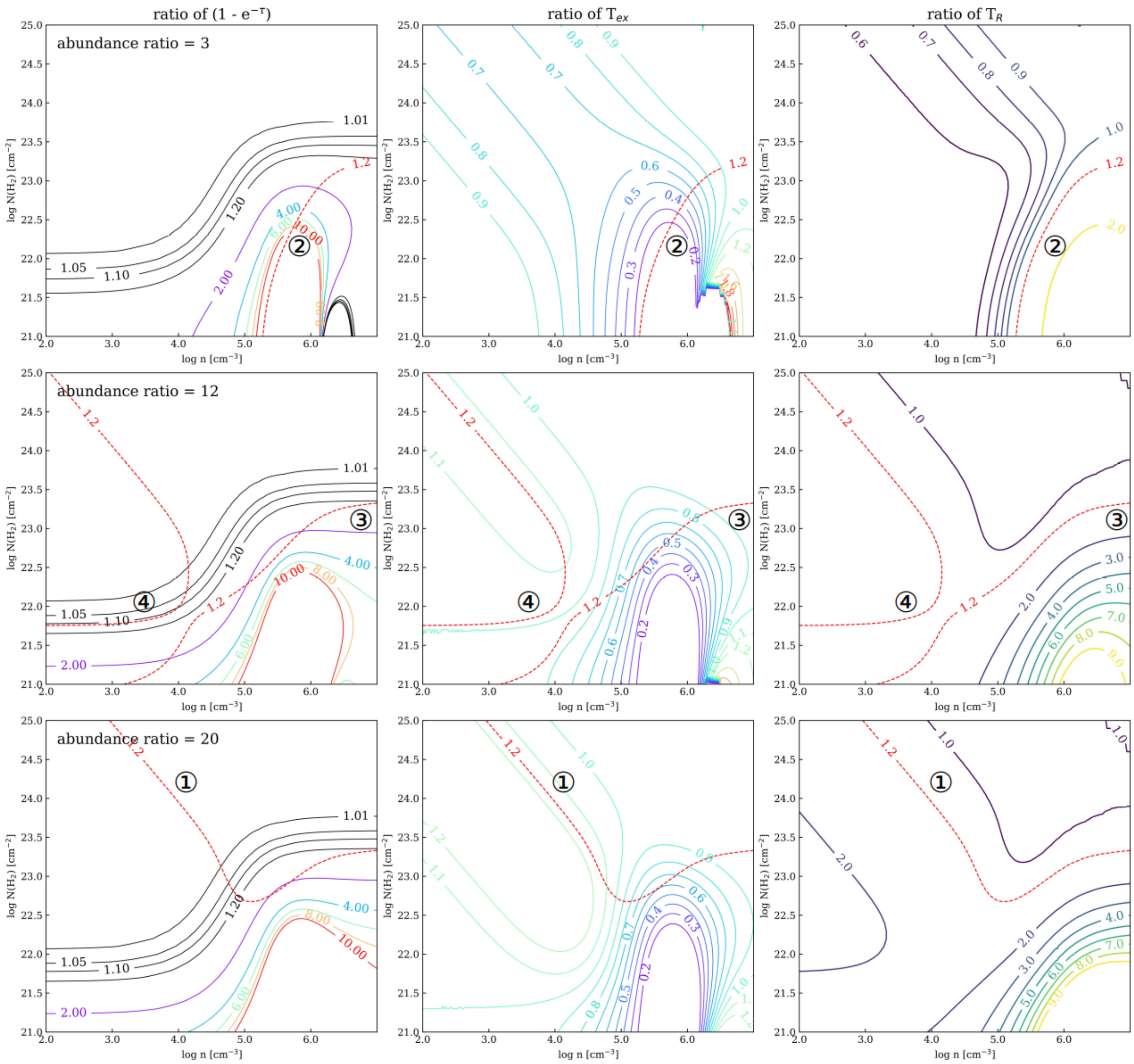

Figure B.1: The optical depth effects on the emission, and the excitation condition of HCN and HCO^+ in 30 K. Each row presents a representative relative column density of HCN to HCO^+ of 3, 12, and 20. The first column shows the ratio of $(1 - e^{-\tau})$ of HCN and HCO^+. The second column shows the ratio of the excitation temperature of both molecules, HCN to HCO^+. The third shows the ratio of the radiation temperature, which is $T_{ex}(1 - e^{-\tau})$. The red dashed line in each panel indicates where the line intensity ratio is 1.2, assuming that HCN and HCO^+ have the same line width. Labels of regions are consistent with those in Figure 2.7.

Appendix C: Appendices for Chapter 3

C.1 Additional Figures

We present in Figure C.1 the supplementary rotation diagrams of absorbing components listed in Table 3.3 that are not presented in Figure 3.4.

C.2 Supplementary Tables

Table C.1 lists the properties of all decomposed absorption lines, assuming that the lines are optically thin and the line profile only consists of a Doppler core (see Section 3.5.1).

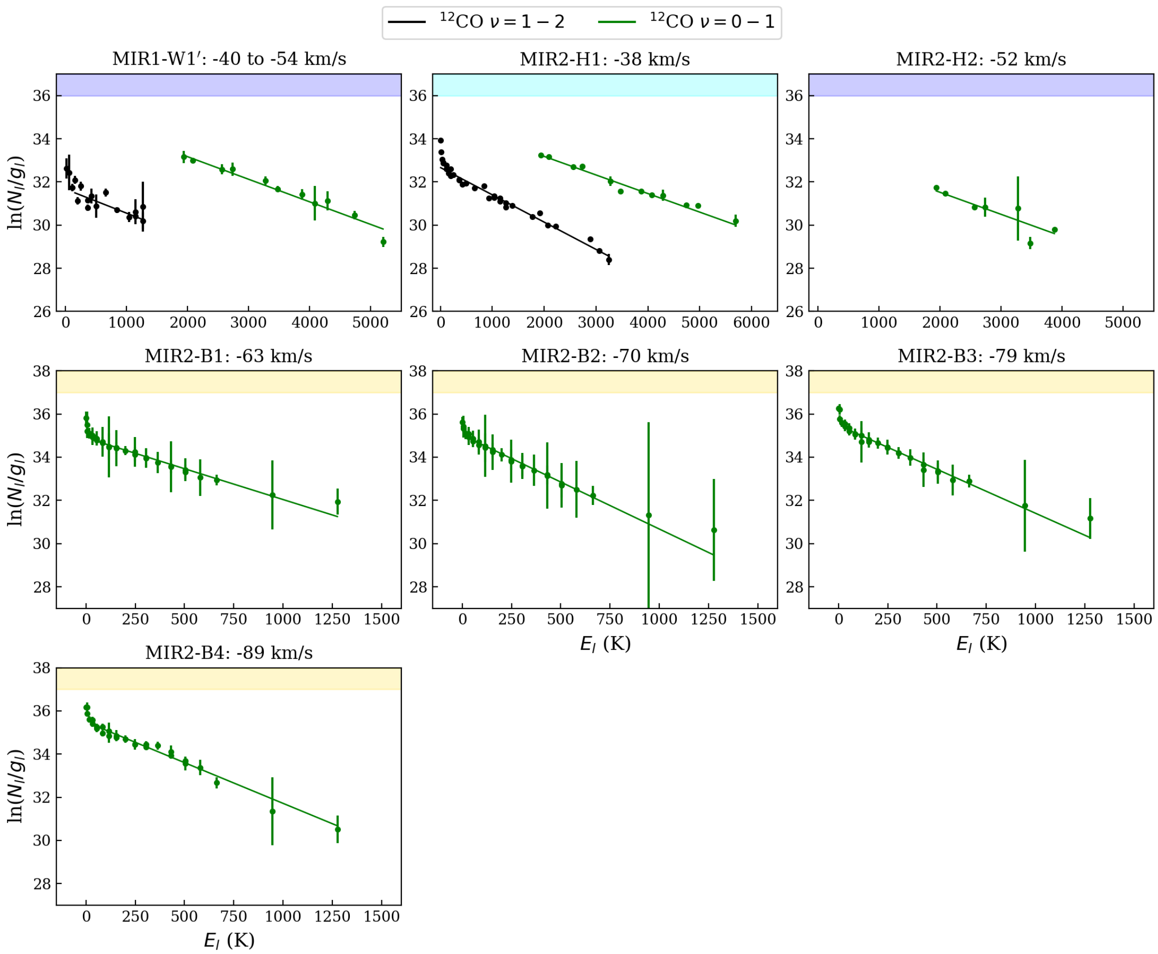

Figure C.1: Supplementary rotation diagrams of absorbing components. N_l are derived from Gaussian fitting. Solid lines represent fitting results of equation 4.3 and dotted lines are of equation 3.4, and the derived $T_{\rm ex}$ and $N_{\rm tot}$ are listed in Table 3.1. Each panel presents data from all different molecular species at a specific velocity component, and the color head on each figure follows the colors of distinct components in Figure 3.4.

Table C.1: MIR1: ^{13}CO Line Parameters of $v = -43\ \mathrm{km\,s^{-1}}$

Species	tr.s.	λ (μm)	E_l (K)	g_l	A_{ij} (s^{-1})	v_{LSR} (km s^{-1})	Δv (km s^{-1})	τ_0	N_l ($\times 10^{14}$ cm^{-2})	W_v (km s^{-1})
^{13}CO ν = 0–1	R0	4.7626	0	2	10.9	-43.4 ± 0.5	2.5 ± 0.9	0.593 ± 0.009	16.1 ± 11	2.271 ± 1.547
	P1	4.7792	5.3	6	32.4	-43 ± 1.4	2.5 ± 2.3	0.658 ± 0.005	53.4 ± 79.9	2.507 ± 3.752
	P2	4.7877	15.9	10	21.5	-43.4 ± 0.4	2.5 ± 0.7	0.942 ± 0.007	59.3 ± 26.6	3.226 ± 1.496
	P3	4.7963	31.7	14	19.2	-43.5 ± 0.9	2.5 ± 1.2	1.147 ± 0.015	56.8 ± 59.9	3.432 ± 3.616
	R3	4.7383	31.7	14	14.8	-43.2 ± 0.5	2.5 ± 1	1.387 ± 0.009	52.6 ± 32.8	3.877 ± 2.643
	P4	4.805	52.9	18	18.2	-43.2 ± 0.5	2.5 ± 1	1.167 ± 0.014	64 ± 37.6	3.667 ± 2.355
	P7	4.8317	148	30	16.9	-43.7 ± 0.5	2.4 ± 0.9	1.096 ± 0.01	46.9 ± 35	3.08 ± 2.299
	P8	4.8408	190.3	34	16.6	-43.7 ± 1.9	1.8 ± 2.1	0.973 ± 0.021	43.5 ± 65	2.116 ± 4.303
	P9	4.8501	237.9	38	16.4	-43.7 ± 1	2 ± 1.3	0.815 ± 0.009	39.4 ± 40.1	2.154 ± 2.670
	P10	4.8594	290.7	42	16.2	-44.4 ± 3.5	1.5 ± 3.6	0.565 ± 0.099	20.3 ± 50.1	1.092 ± 3.355
	R10	4.6853	290.7	42	16.5	-43.7 ± 0.6	2.2 ± 0.9	0.728 ± 0.006	32.9 ± 24.5	2.259 ± 1.815
	P11	4.8689	348.9	46	16.1	-43.8 ± 1	2.1 ± 1.4	0.535 ± 0.005	26.4 ± 32.9	1.712 ± 2.215
	P12	4.8784	412.3	50	15.9	-43.4 ± 1.2	2.2 ± 1.8	0.434 ± 0.005	24.1 ± 33.8	1.606 ± 2.284
	R12	4.6711	412.3	50	16.8	-43.2 ± 0.7	2.5 ± 0.7	0.506 ± 0.006	32.3 ± 14.8	2.168 ± 1.087
	P13	4.8881	480.9	54	15.8	-43.2 ± 0.6	2.5 ± 1	0.353 ± 0.006	23.3 ± 15.6	1.569 ± 1.057
	R13	4.6641	480.9	54	16.9	-43.3 ± 1.2	2.4 ± 1.8	0.386 ± 0.004	22.3 ± 27.5	1.599 ± 2.013

Table C.2: MIR1: ^{13}CO Line Parameters of $v = -49$ km s^{-1}

Species	tr.s.	λ (μm)	E_l (K)	g_l	A_{ij} (s^{-1})	v_{LSR} (km s^{-1})	Δv (km s^{-1})	τ_0	N_l ($\times 10^{14}$ cm^{-2})	W_v (km s^{-1})
^{13}CO ν = 0–1	R0	4.7626	0	2	10.9	-48.9 $\pm$ 1.6	3 $\pm$ 0.7	0.329 $\pm$ 0.007	18.5 $\pm$ 7.1	1.849 $\pm$ 1.006
	P1	4.7792	5.3	6	32.4	-49 $\pm$ 2.6	3 $\pm$ 1.3	0.399 $\pm$ 0.004	67.3 $\pm$ 40.9	2.308 $\pm$ 1.922
	P2	4.7877	15.9	10	21.5	-49 $\pm$ 1.1	3 $\pm$ 0.5	0.5 $\pm$ 0.006	74.5 $\pm$ 16.9	2.652 $\pm$ 0.950
	P3	4.7963	31.7	14	19.2	-49 $\pm$ 2.2	3 $\pm$ 1.3	0.762 $\pm$ 0.027	102.5 $\pm$ 46.8	3.65 $\pm$ 2.825
	R3	4.7383	31.7	14	14.8	-49 $\pm$ 1.1	3 $\pm$ 0.5	0.885 $\pm$ 0.006	89.6 $\pm$ 18.6	4.088 $\pm$ 1.501
	P4	4.805	52.9	18	18.2	-49 $\pm$ 1.2	3 $\pm$ 0.6	0.821 $\pm$ 0.011	106.1 $\pm$ 24	3.913 $\pm$ 1.501
	P7	4.8317	148	30	16.9	-49 $\pm$ 1.2	3 $\pm$ 0.6	0.858 $\pm$ 0.01	104.1 $\pm$ 23.2	4.035 $\pm$ 1.523
	P8	4.8408	190.3	34	16.6	-49 $\pm$ 1.7	3 $\pm$ 1.1	1.056 $\pm$ 0.017	107.9 $\pm$ 36.2	4.851 $\pm$ 2.398
	P9	4.8501	237.9	38	16.4	-49 $\pm$ 1.6	3 $\pm$ 1	0.708 $\pm$ 0.008	76.4 $\pm$ 26.2	3.731 $\pm$ 1.747
	P10	4.8594	290.7	42	16.2	-49 $\pm$ 2.2	3 $\pm$ 1.2	0.663 $\pm$ 0.033	69 $\pm$ 33.5	3.624 $\pm$ 2.245
	R10	4.6853	290.7	42	16.5	-49 $\pm$ 1.2	3 $\pm$ 0.6	0.608 $\pm$ 0.006	61 $\pm$ 15.7	3.269 $\pm$ 1.165
	P11	4.8689	348.9	46	16.1	-49 $\pm$ 1.7	3 $\pm$ 0.9	0.509 $\pm$ 0.004	55.5 $\pm$ 21.9	2.89 $\pm$ 1.472
	P12	4.8784	412.3	50	15.9	-49 $\pm$ 1.8	3 $\pm$ 1	0.423 $\pm$ 0.005	46 $\pm$ 20.5	2.504 $\pm$ 1.383
	R12	4.6711	412.3	50	16.8	-49 $\pm$ 1.1	3 $\pm$ 0.6	0.442 $\pm$ 0.006	43.7 $\pm$ 12.2	2.519 $\pm$ 0.896
	P13	4.8881	480.9	54	15.8	-49 $\pm$ 1.2	3 $\pm$ 0.6	0.339 $\pm$ 0.007	36.6 $\pm$ 11.4	2.036 $\pm$ 0.774
	R13	4.6641	480.9	54	16.9	-49 $\pm$ 1.9	3 $\pm$ 1	0.404 $\pm$ 0.004	40.3 $\pm$ 19.5	2.387 $\pm$ 1.432

Table C.3: MIR1: ^{13}CO Line Parameters of $v = -40\ \mathrm{km\,s^{-1}}$, high J

Species	tr.s.	λ (μm)	E_l (K)	g_l	A_{ij} ($\mathrm{s^{-1}}$)	v_{LSR} ($\mathrm{km\,s^{-1}}$)	Δv ($\mathrm{km\,s^{-1}}$)	τ_0	N_l ($\times 10^{14}\ \mathrm{cm^{-2}}$)	W_v ($\mathrm{km\,s^{-1}}$)
^{13}CO ν = 0–1	P17	4.928	808.3	70	15.2	-42.1 $\pm$ 2.7	5 $\pm$ 1	0.129 $\pm$ 0.003	18.3 $\pm$ 11.7	1.201 $\pm$ 0.803
	P18	4.9382	903.3	74	15.1	-41.3 $\pm$ 2.3	4.8 $\pm$ 1	0.11 $\pm$ 0.004	16.1 $\pm$ 8.5	1.059 $\pm$ 0.579
	R18	4.6306	903.3	74	17.5	-42.1 $\pm$ 3.4	5 $\pm$ 1.3	0.124 $\pm$ 0.004	17.5 $\pm$ 13.4	1.215 $\pm$ 0.978
	R19	4.6242	1003.5	78	17.6	-40.5 $\pm$ 0.6	4.3 $\pm$ 0.4	0.094 $\pm$ 0.004	11.8 $\pm$ 1.6	0.826 $\pm$ 0.120
	R21	4.6116	1219.8	86	17.8	-40.7 $\pm$ 1.1	3.9 $\pm$ 0.7	0.068 $\pm$ 0.003	7.7 $\pm$ 2.6	0.546 $\pm$ 0.192
	R22	4.6055	1335.8	90	17.9	-40.3 $\pm$ 2.4	5 $\pm$ 1.3	0.087 $\pm$ 0.005	13.8 $\pm$ 6.7	0.965 $\pm$ 0.486
	P24	5.0022	1583.5	98	14.4	-40 $\pm$ 1.8	3.8 $\pm$ 1.3	0.03 $\pm$ 0.005	3.6 $\pm$ 1.9	0.248 $\pm$ 0.131
	P25	5.0133	1715.2	102	14.3	-40.3 $\pm$ 1.2	3.4 $\pm$ 0.9	0.018 $\pm$ 0.003	2.1 $\pm$ 0.9	0.142 $\pm$ 0.061
	P27	5.0358	1994.2	110	14.1	-40.6 $\pm$ 2.1	2 $\pm$ 2.2	0.011 $\pm$ 0.004	0.6 $\pm$ 0.8	0.041 $\pm$ 0.054

Table C.4: MIR1: ^{13}CO Line Parameters of $v = -51$ km s^{-1}, high J

Species	tr.s.	λ (μm)	E_l (K)	g_l	A_{ij} (s^{-1})	v_{LSR} (km s^{-1})	Δv (km s^{-1})	τ_0	N_l ($\times 10^{14}$ cm^{-2})	W_v (km s^{-1})
^{13}CO ν = 0–1	P17	4.928	808.3	70	15.2	-50.6 $\pm$ 2.4	5 $\pm$ 1	0.139 $\pm$ 0.003	21.1 $\pm$ 11.9	1.343 $\pm$ 0.810
	P18	4.9382	903.3	74	15.1	-51 $\pm$ 2	5 $\pm$ 1.1	0.126 $\pm$ 0.004	20.7 $\pm$ 8.6	1.339 $\pm$ 0.592
	R18	4.6306	903.3	74	17.5	-51 $\pm$ 3.3	5 $\pm$ 1.5	0.127 $\pm$ 0.004	18.1 $\pm$ 13.6	1.247 $\pm$ 0.993
	R19	4.6242	1003.5	78	17.6	-51 $\pm$ 0.3	4.6 $\pm$ 0.2	0.189 $\pm$ 0.004	29 $\pm$ 1.7	1.96 $\pm$ 0.122
	R21	4.6116	1219.8	86	17.8	-51 $\pm$ 1	5 $\pm$ 0.9	0.087 $\pm$ 0.004	14.5 $\pm$ 2.9	1.017 $\pm$ 0.210
	R22	4.6055	1335.8	90	17.9	-51 $\pm$ 2.9	5 $\pm$ 1.7	0.075 $\pm$ 0.005	11.4 $\pm$ 6.9	0.803 $\pm$ 0.499
	P24	5.0022	1583.5	98	14.4	-51 $\pm$ 1.6	5 $\pm$ 1.4	0.037 $\pm$ 0.005	6.5 $\pm$ 2	0.445 $\pm$ 0.138
	P25	5.0133	1715.2	102	14.3	-51 $\pm$ 2.3	5 $\pm$ 2.4	0.012 $\pm$ 0.003	2.2 $\pm$ 1	0.148 $\pm$ 0.069
	P27	5.0358	1994.2	110	14.1	-51 $\pm$ 1.4	5 $\pm$ 2	0.02 $\pm$ 0.005	3.7 $\pm$ 1.1	0.253 $\pm$ 0.078

Table C.5: MIR1: $C^{18}O$ Line Parameters of $v = -38$ $km\,s^{-1}$

Species	tr.s.	λ (μm)	E_l (K)	g_l	A_{ij} (s^{-1})	v_{LSR} ($km\,s^{-1}$)	Δv ($km\,s^{-1}$)	τ_0	N_l ($\times 10^{14}$ cm^{-2})	W_v ($km\,s^{-1}$)
$C^{18}O$ ν = 0–1	R0	4.7716	0	1	10.8	-39 $\pm$ 0.2	1.9 $\pm$ 0.2	0.235 $\pm$ 0.004	7.7 $\pm$ 0.6	1.007 $\pm$ 0.083
	P1	4.7882	5.3	3	32.2	-38.7 $\pm$ 0.4	1.7 $\pm$ 0.2	0.193 $\pm$ 0.003	15.9 $\pm$ 8.2	0.693 $\pm$ 0.382
	P2	4.7967	15.8	5	21.3	-38.8 $\pm$ 0.3	1.7 $\pm$ 0.2	0.27 $\pm$ 0.004	18.3 $\pm$ 5.4	0.926 $\pm$ 0.303
	P3	4.8053	31.6	7	19.1	-38.9 $\pm$ 8.3	1.7 $\pm$ 4.5	0.312 $\pm$ 0.005	19.9 $\pm$ 123	1.06 $\pm$ 7.409
	R3	4.7473	31.6	7	14.7	-39 $\pm$ 0.7	1.9 $\pm$ 0.3	0.345 $\pm$ 0.005	19 $\pm$ 9.7	1.306 $\pm$ 0.783
	R4	4.7395	52.7	9	15.1	-38.6 $\pm$ 0.5	1.8 $\pm$ 0.3	0.314 $\pm$ 0.004	16 $\pm$ 6.7	1.082 $\pm$ 0.527
	R5	4.7317	79	11	15.4	-39 $\pm$ 1.1	1.8 $\pm$ 0.6	0.158 $\pm$ 0.006	8.4 $\pm$ 5	0.589 $\pm$ 0.386
	R9	4.7016	237	19	16.2	-37.1 $\pm$ 0.6	1.5 $\pm$ 0.4	0.052 $\pm$ 0.003	2.4 $\pm$ 1	0.174 $\pm$ 0.077

Table C.6: MIR1: $C^{18}O$ Line Parameters of $v = -43$ km s^{-1}

Species	tr.s.	λ (μm)	E_l (K)	g_l	A_{ij} (s^{-1})	v_{LSR} (km s^{-1})	Δv (km s^{-1})	τ_0	N_l ($\times 10^{14}$ cm^{-2})	W_v (km s^{-1})
$C^{18}O$ ν = 0–1	P1	4.7882	5.3	3	32.2	-43 ± 1.8	2.5 ± 5.4	0.053 ± 0.003	5.8 ± 16.1	0.271 ± 0.753
	P2	4.7967	15.8	5	21.3	-43.6 ± 1.6	2.5 ± 2.9	0.093 ± 0.003	9.1 ± 14.7	0.509 ± 0.828
	P3	4.8053	31.6	7	19.1	-43.5 ± 25.4	2.2 ± 47.9	0.116 ± 0.005	9.3 ± 264.9	0.552 ± 15.957
	R3	4.7473	31.6	7	14.7	-43.8 ± 1.9	2.5 ± 3.6	0.172 ± 0.004	11.1 ± 24.4	0.891 ± 1.96
	R4	4.7395	52.7	9	15.1	-43.3 ± 1	2.5 ± 2.3	0.179 ± 0.003	12.2 ± 14.7	0.953 ± 1.15
	R5	4.7317	79	11	15.4	-43.7 ± 0.8	2.1 ± 1.2	0.202 ± 0.005	11.9 ± 9.6	0.865 ± 0.738
	R9	4.7016	237	19	16.2	-43 ± 1	2.4 ± 1.1	0.109 ± 0.005	8.4 ± 4.4	0.607 ± 0.325
	R10	4.6943	289.6	21	16.4	-43.5 ± 1.2	2.2 ± 2	0.086 ± 0.003	5.7 ± 7.7	0.417 ± 0.572
	R11	4.6872	347.5	23	16.5	-43.9 ± 2.2	2.3 ± 2.7	0.064 ± 0.003	4.5 ± 8.1	0.329 ± 0.599

Table C.7: MIR1: $C^{18}O$ Line Parameters of $v = -49$ km s^{-1}

Species	tr.s.	λ (μm)	E_l (K)	g_l	A_{ij} (s^{-1})	v_{LSR} (km s^{-1})	Δv (km s^{-1})	τ_0	N_l ($\times 10^{14}$ cm^{-2})	W_v (km s^{-1})
$C^{18}O$ ν = 0–1	P1	4.7882	5.3	3	32.2	-48.3 $\pm$ 4.3	2.2 $\pm$ 1.8	0.036 $\pm$ 0.003	3.9 $\pm$ 8.5	0.174 $\pm$ 0.397
	P2	4.7967	15.8	5	21.3	-49 $\pm$ 4.8	2.5 $\pm$ 2.2	0.052 $\pm$ 0.003	5.3 $\pm$ 10.1	0.271 $\pm$ 0.568
	R4	4.7395	52.7	9	15.1	-49 $\pm$ 3.1	2.4 $\pm$ 1.5	0.099 $\pm$ 0.003	7.3 $\pm$ 8.8	0.502 $\pm$ 0.689
	R5	4.7317	79	11	15.4	-49 $\pm$ 1.7	2.5 $\pm$ 1	0.125 $\pm$ 0.004	9.8 $\pm$ 5.7	0.699 $\pm$ 0.436
	R9	4.7016	237	19	16.2	-48.3 $\pm$ 1.2	2.1 $\pm$ 0.7	0.095 $\pm$ 0.005	6.2 $\pm$ 3.7	0.435 $\pm$ 0.274
	R10	4.6943	289.6	21	16.4	-49 $\pm$ 2.3	2.5 $\pm$ 1.3	0.062 $\pm$ 0.003	5 $\pm$ 4.2	0.355 $\pm$ 0.307
	R11	4.6872	347.5	23	16.5	-49 $\pm$ 4.4	2.5 $\pm$ 2.1	0.048 $\pm$ 0.003	3.7 $\pm$ 6.4	0.261 $\pm$ 0.47

Table C.8: MIR1: $C^{17}O$ Line Parameters of $v = -38$ km s^{-1}

Species	tr.s.	λ (μm)	E_l (K)	g_l	A_{ij} (s^{-1})	v_{LSR} (km s^{-1})	Δv (km s^{-1})	τ_0	N_l ($\times 10^{14}$ cm^{-2})
$C^{17}O$ ν = 0–1	P1	4.7336	5.4	18	33.7	-39.3 $\pm$ 0.4	1.7 $\pm$ 0.6	0.056 $\pm$ 0.003	4.9 $\pm$ 2.8
	P3	4.7507	32.3	42	20	-38.4 $\pm$ 0.5	1.7 $\pm$ 0.5	0.159 $\pm$ 0.004	10.7 $\pm$ 3.6
	R4	4.6849	53.9	54	15.8	-39.3 $\pm$ 0.3	1.2 $\pm$ 0.3	0.066 $\pm$ 0.003	2.5 $\pm$ 0.7
	R5	4.6771	80.9	66	16.1	-39.1 $\pm$ 0.1	1.5 $\pm$ 0.2	0.083 $\pm$ 0.005	3 $\pm$ 0.5
	R6	4.6695	113.2	78	16.4	-39.3 $\pm$ 0.3	1.7 $\pm$ 0.5	0.051 $\pm$ 0.004	1.6 $\pm$ 0.9

Table C.9: MIR1: $C^{17}O$ Line Parameters of $v = -44$ km s^{-1}

Species	tr.s.	λ (μm)	E_l (K)	g_l	A_{ij} (s^{-1})	v_{LSR} (km s^{-1})	Δv (km s^{-1})	τ_0	N_l ($\times 10^{14}$ cm^{-2})
$C^{17}O$ ν = 0–1	R5	4.6771	80.9	66	16.1	-45.3 $\pm$ 0.5	4.8 $\pm$ 0.4	0.046 $\pm$ 0.005	6 $\pm$ 0.7
	R6	4.6695	113.2	78	16.4	-44.6 $\pm$ 0.9	4.6 $\pm$ 0.6	0.044 $\pm$ 0.004	5.9 $\pm$ 1
	R8	4.6544	194	102	16.8	-44.6 $\pm$ 0.4	4.8 $\pm$ 0.4	0.039 $\pm$ 0.003	5.3 $\pm$ 0.5
	R9	4.6471	242.5	114	17	-44.5 $\pm$ 1.6	3.2 $\pm$ 1.2	0.027 $\pm$ 0.004	2.7 $\pm$ 1.2

Table C.10: MIR1: ^{12}CO ν= 1–2 Line Parameters of $v = -40$ km s^{-1}

Species	tr.s.	λ (μm)	E_l (K)	g_l	A_{ij} (s^{-1})	v_{LSR} (km s^{-1})	Δv (km s^{-1})	τ_0	N_l ($\times 10^{14}$ cm^{-2})
^{12}CO ν = 1–2	P2	4.7413	3099.5	5	45.2	-37.4 $\pm$ 2.5	4.6 $\pm$ 2.7	0.037 $\pm$ 0.004	3.7 $\pm$ 1.8
	R4	4.6832	3137.9	9	32	-40.5 $\pm$ 3.8	4.9 $\pm$ 2.3	0.064 $\pm$ 0.005	4.4 $\pm$ 3.8
	P6	4.7769	3198.2	13	36.1	-39 $\pm$ 1.9	5.9 $\pm$ 1.7	0.151 $\pm$ 0.006	15.9 $\pm$ 5.8
	R7	4.6598	3236.5	15	33.7	-40.1 $\pm$ 0.8	5.2 $\pm$ 0.5	0.073 $\pm$ 0.003	5.7 $\pm$ 1
	P8	4.7954	3280.4	17	34.9	-37.4 $\pm$ 8.9	6 $\pm$ 5.4	0.102 $\pm$ 0.003	9.9 $\pm$ 16.3
	R9	4.6448	3329.7	19	34.4	-40.8 $\pm$ 1	5.5 $\pm$ 0.5	0.072 $\pm$ 0.003	5.9 $\pm$ 1.2
	P11	4.824	3444.7	23	33.7	-41.7 $\pm$ 0.6	5.4 $\pm$ 0.6	0.048 $\pm$ 0.004	4.6 $\pm$ 0.4
	R11	4.6302	3444.7	23	35	-38 $\pm$ 0.7	6 $\pm$ 0.9	0.04 $\pm$ 0.004	4 $\pm$ 0.5
	R12	4.623	3510.4	25	35.3	-37.4 $\pm$ 1.4	6 $\pm$ 2.2	0.054 $\pm$ 0.005	5.2 $\pm$ 2
	R13	4.616	3581.6	27	35.6	-41.5 $\pm$ 2.1	5.2 $\pm$ 1	0.044 $\pm$ 0.003	3.4 $\pm$ 1.7
	P15	4.8637	3740.3	31	32.5	-39.7 $\pm$ 1.2	5 $\pm$ 0.7	0.056 $\pm$ 0.004	4.6 $\pm$ 1.1
	P17	4.8843	3920.8	35	31.9	-39.1 $\pm$ 0.5	3.5 $\pm$ 0.4	0.044 $\pm$ 0.003	2.5 $\pm$ 0.4
	P19	4.9054	4123.2	39	31.4	-43 $\pm$ 1.1	5.4 $\pm$ 0.8	0.04 $\pm$ 0.003	3.8 $\pm$ 0.7
	P20	4.9161	4232.5	41	31.2	-40.5 $\pm$ 2.5	5.7 $\pm$ 1.4	0.047 $\pm$ 0.003	4.5 $\pm$ 2.1
	R20	4.5694	4232.5	41	37.2	-41 $\pm$ 0.8	6 $\pm$ 0.6	0.041 $\pm$ 0.004	4 $\pm$ 0.5
	P21	4.9269	4347.3	43	31	-43 $\pm$ 7.8	6 $\pm$ 3	0.049 $\pm$ 0.003	3.8 $\pm$ 6
	R21	4.5631	4347.3	43	37.4	-40.4 $\pm$ 2.3	3.9 $\pm$ 2	0.025 $\pm$ 0.005	1.5 $\pm$ 1

Table C.11: MIR1: ^{12}CO ν= 1–2 Line Parameters of $v = -54$ km s^{-1}

Species	tr.s.	λ (μm)	E_l (K)	g_l	A_{ij} (s^{-1})	v_{LSR} (km s^{-1})	Δv (km s^{-1})	τ_0	N_l ($\times 10^{14}$ cm^{-2})
^{12}CO ν = 1–2	P2	4.7413	3099.5	5	45.2	-50 $\pm$ 1.6	3.4 $\pm$ 1.6	0.049 $\pm$ 0.003	3.6 $\pm$ 1.6
	R4	4.6832	3137.9	9	32	-54 $\pm$ 2.7	6 $\pm$ 4.8	0.073 $\pm$ 0.005	6.6 $\pm$ 5.3
	R6	4.6675	3198.2	13	33.2	-54 $\pm$ 0.2	3.3 $\pm$ 0.3	0.036 $\pm$ 0.003	1.9 $\pm$ 0.1
	R7	4.6598	3236.5	15	33.7	-54 $\pm$ 0.7	6 $\pm$ 1	0.077 $\pm$ 0.003	7.3 $\pm$ 1.3
	R8	4.6523	3280.4	17	34.1	-52.8 $\pm$ 0.6	6 $\pm$ 1.1	0.044 $\pm$ 0.003	4.3 $\pm$ 0.6
	R9	4.6448	3329.7	19	34.4	-53.8 $\pm$ 1	6 $\pm$ 1.1	0.069 $\pm$ 0.003	6.4 $\pm$ 1.5
	P11	4.824	3444.7	23	33.7	-53 $\pm$ 0.3	3.3 $\pm$ 0.3	0.059 $\pm$ 0.004	3.2 $\pm$ 0.4
	R11	4.6302	3444.7	23	35	-54 $\pm$ 0.5	2.4 $\pm$ 0.5	0.039 $\pm$ 0.004	1.5 $\pm$ 0.3
	R12	4.623	3510.4	25	35.3	-53.2 $\pm$ 1.4	5.9 $\pm$ 1.6	0.054 $\pm$ 0.003	5.1 $\pm$ 1.6
	R13	4.616	3581.6	27	35.6	-54 $\pm$ 2.3	6 $\pm$ 2.8	0.038 $\pm$ 0.003	3.6 $\pm$ 2.1
	P15	4.8637	3740.3	31	32.5	-54 $\pm$ 0.6	6 $\pm$ 1.1	0.099 $\pm$ 0.008	10.4 $\pm$ 1.7
	P17	4.8843	3920.8	35	31.9	-52.8 $\pm$ 0.5	6 $\pm$ 0.9	0.047 $\pm$ 0.003	5 $\pm$ 0.6
	P19	4.9054	4123.2	39	31.4	-53.3 $\pm$ 0.8	3.8 $\pm$ 0.7	0.038 $\pm$ 0.003	2.2 $\pm$ 0.7
	P20	4.9161	4232.5	41	31.2	-54 $\pm$ 2.8	6 $\pm$ 3.3	0.037 $\pm$ 0.003	3.6 $\pm$ 2.6
	R20	4.5694	4232.5	41	37.2	-54 $\pm$ 0.7	4.7 $\pm$ 0.7	0.037 $\pm$ 0.005	2.6 $\pm$ 0.6
	P21	4.9269	4347.3	43	31	-53.8 $\pm$ 4.3	6 $\pm$ 2.5	0.073 $\pm$ 0.003	7 $\pm$ 6.4
	R21	4.5631	4347.3	43	37.4	-54 $\pm$ 1.8	6 $\pm$ 1.8	0.041 $\pm$ 0.005	4.1 $\pm$ 1.1

Table C.12: MIR1: ^{12}CO ν=0−1 Line Parameters of $v = -40$ km s^{-1}, high J

Species	tr.s.	λ (μm)	E_l (K)	g_l	A_{ij} (s^{-1})	v_{LSR} (km s^{-1})	Δv (km s^{-1})	τ_0	N_l ($\times 10^{14}$ cm^{-2})	W_v (km s^{-1})
^{12}CO ν = 0−1	P26	4.9204	1937.1	53	15.5	-39 ± 1.7	4.5 ± 1	0.155 ± 0.003	7.5 ± 5	0.53 ± 0.353
	P27	4.9318	2085.7	55	15.4	-39.3 ± 0.6	4 ± 0.4	0.165 ± 0.003	9.2 ± 2.6	0.653 ± 0.183
	P30	4.9668	2564.4	61	15.1	-39 ± 1	4.5 ± 0.6	0.136 ± 0.003	11.4 ± 4.1	0.807 ± 0.292
	P31	4.9788	2734.8	63	14.9	-39 ± 1	4.5 ± 0.6	0.153 ± 0.005	15.6 ± 5.2	1.063 ± 0.368
	P34	5.0154	3278.6	69	14.6	-40.2 ± 0.9	4.5 ± 0.5	0.121 ± 0.005	12.9 ± 4	0.889 ± 0.288
	P35	5.0279	3470.7	71	14.5	-40.7 ± 0.9	4 ± 0.7	0.09 ± 0.008	8.2 ± 3.7	0.569 ± 0.265
	P37	5.0532	3871	75	14.3	-39.8 ± 0.9	4.5 ± 0.5	0.075 ± 0.003	8.8 ± 2.7	0.61 ± 0.195
	P38	5.0661	4079.3	77	14.2	-40.2 ± 2.6	4.5 ± 1.5	0.056 ± 0.003	6.4 ± 6.7	0.451 ± 0.48
	P39	5.0792	4292.9	79	14.1	-39.8 ± 2	4.5 ± 1.1	0.071 ± 0.006	9 ± 5.5	0.626 ± 0.395
	P41	5.1057	4736.2	83	13.8	-42 ± 2.3	4 ± 1.7	0.034 ± 0.003	3.2 ± 4.2	0.228 ± 0.302
	P42	5.1191	4965.9	85	13.7	-41.2 ± 5	4.5 ± 2.6	0.035 ± 0.004	4.5 ± 8.7	0.317 ± 0.625
	P43	5.1328	5201	87	13.6	-41.3 ± 6.5	4 ± 3.4	0.014 ± 0.005	1.6 ± 2.9	0.112 ± 0.21

Table C.13: MIR1: ^{12}CO ν=0−1 Line Parameters of $v = -50$ km s^{-1}, high J

Species	tr.s.	λ (μm)	E_l (K)	g_l	A_{ij} (s^{-1})	v_{LSR} (km s^{-1})	Δv (km s^{-1})	τ_0	N_l ($\times 10^{14}$ cm^{-2})	W_v (km s^{-1})
^{12}CO ν = 0−1	P26	4.9204	1937.1	53	15.5	-50.3 $\pm$ 0.3	6.5 $\pm$ 0.3	0.589 $\pm$ 0.004	124.4 $\pm$ 5.5	7.225 $\pm$ 0.392
	P27	4.9318	2085.7	55	15.4	-50.6 $\pm$ 0.2	6.5 $\pm$ 0.2	0.509 $\pm$ 0.005	109.1 $\pm$ 3	6.48 $\pm$ 0.212
	P30	4.9668	2564.4	61	15.1	-50.7 $\pm$ 0.4	6.5 $\pm$ 0.4	0.338 $\pm$ 0.004	74 $\pm$ 4.7	4.625 $\pm$ 0.333
	P31	4.9788	2734.8	63	14.9	-51.2 $\pm$ 0.5	6.5 $\pm$ 0.6	0.327 $\pm$ 0.007	71.6 $\pm$ 6.2	4.508 $\pm$ 0.441
	P34	5.0154	3278.6	69	14.6	-51.9 $\pm$ 0.7	6.5 $\pm$ 0.6	0.199 $\pm$ 0.005	43.9 $\pm$ 4.6	2.895 $\pm$ 0.328
	P35	5.0279	3470.7	71	14.5	-51.9 $\pm$ 0.8	6.5 $\pm$ 0.9	0.141 $\pm$ 0.008	31.4 $\pm$ 4.4	2.129 $\pm$ 0.315
	P37	5.0532	3871	75	14.3	-51.9 $\pm$ 0.7	6.5 $\pm$ 0.8	0.108 $\pm$ 0.003	23.9 $\pm$ 3.3	1.642 $\pm$ 0.234
	P38	5.0661	4079.3	77	14.2	-51.5 $\pm$ 2.8	6.5 $\pm$ 2.6	0.072 $\pm$ 0.003	15.9 $\pm$ 7.7	1.105 $\pm$ 0.548
	P39	5.0792	4292.9	79	14.1	-51 $\pm$ 2.1	5.9 $\pm$ 1.7	0.085 $\pm$ 0.006	16.9 $\pm$ 6.1	1.168 $\pm$ 0.433
	P41	5.1057	4736.2	83	13.8	-53 $\pm$ 2.5	6.5 $\pm$ 3	0.047 $\pm$ 0.003	10.5 $\pm$ 5.2	0.745 $\pm$ 0.375
	P42	5.1191	4965.9	85	13.7	-53 $\pm$ 6.8	6.5 $\pm$ 9.2	0.033 $\pm$ 0.005	7.3 $\pm$ 11.2	0.521 $\pm$ 0.803
	P43	5.1328	5201	87	13.6	-50.4 $\pm$ 4.7	4.5 $\pm$ 2.9	0.019 $\pm$ 0.005	2.9 $\pm$ 3	0.206 $\pm$ 0.215

Table C.14: MIR2: ^{13}CO Line Parameters of $v = -38\ \mathrm{km\,s^{-1}}$ (1 of 2)

Species	tr.s.	λ (μm)	E_l (K)	g_l	A_{ij} ($\mathrm{s^{-1}}$)	v_{LSR} ($\mathrm{km\,s^{-1}}$)	Δv ($\mathrm{km\,s^{-1}}$)	τ_0	N_l ($\times 10^{14}\ \mathrm{cm^{-2}}$)	W_v ($\mathrm{km\,s^{-1}}$)
^{13}CO ν = 0–1	R0	4.7626	0	2	10.9	-38.3 ± 0.2	2.6 ± 0.2	1.275 ± 0.022	46.6 ± 2.5	4.549 ± 0.354
	P1	4.7792	5.3	6	32.4	-38.4 ± 0.2	2.6 ± 0.2	1.171 ± 0.009	132 ± 8.4	4.4 ± 0.393
	P2	4.7877	15.9	10	21.5	-38.2 ± 0.2	2.6 ± 0.1	1.342 ± 0.013	124.1 ± 6.2	4.656 ± 0.349
	R2	4.7463	15.9	10	14.2	-38.5 ± 0.4	3.2 ± 0.2	1.333 ± 0.03	104.5 ± 7.7	5.818 ± 0.648
	P3	4.7963	31.7	14	19.2	-38.5 ± 0.3	2.8 ± 0.2	1.384 ± 0.021	131.3 ± 7.8	5.153 ± 0.473
	R3	4.7383	31.7	14	14.8	-38.3 ± 0.3	3 ± 0.3	1.589 ± 0.014	114 ± 8.1	5.745 ± 0.649
	P4	4.805	52.9	18	18.2	-38.5 ± 0.5	3.1 ± 0.4	1.515 ± 0.023	150.7 ± 14.2	6.016 ± 0.891
	R7	4.7075	148	30	16	-38.5 ± 0.5	3.8 ± 0.4	1.207 ± 0.016	126.9 ± 10.8	6.494 ± 0.816
	R9	4.6926	237.9	38	16.4	-38.3 ± 0.9	4.5 ± 0.7	0.89 ± 0.01	119.2 ± 16.1	6.598 ± 1.197
	R10	4.6853	290.7	42	16.5	-38.5 ± 0.6	4.2 ± 0.4	0.683 ± 0.007	88.3 ± 8.3	5.157 ± 0.613
	P11	4.8689	348.9	46	16.1	-38.5 ± 0.9	4.2 ± 0.7	0.501 ± 0.005	72.1 ± 11.7	4.051 ± 0.786
	P12	4.8784	412.3	50	15.9	-38.3 ± 0.9	4.5 ± 0.7	0.469 ± 0.005	73.4 ± 11.2	4.197 ± 0.754
	P13	4.8881	480.9	54	15.8	-38.2 ± 0.4	4.5 ± 0.3	0.42 ± 0.009	66 ± 4.5	3.847 ± 0.306
	R13	4.6641	480.9	54	16.9	-38.4 ± 0.4	4.5 ± 0.3	0.495 ± 0.006	71.5 ± 4.7	4.373 ± 0.342
	P15	4.9078	634.1	62	15.5	-37.6 ± 0.8	4.5 ± 0.6	0.358 ± 0.006	56.4 ± 8.2	3.374 ± 0.559
	R15	4.6504	634.1	62	17.1	-38 ± 0.4	4.5 ± 0.3	0.487 ± 0.008	70.8 ± 4.9	4.317 ± 0.358
	P16	4.9178	718.6	66	15.3	-38 ± 0.3	4 ± 0.3	0.393 ± 0.005	54.2 ± 3.6	3.242 ± 0.247
	R16	4.6437	718.6	66	17.3	-38.2 ± 0.1	4.5 ± 0.1	0.426 ± 0.005	60.9 ± 1.5	3.892 ± 0.108
	P17	4.928	808.3	70	15.2	-38.1 ± 0.1	4.5 ± 0.1	0.35 ± 0.004	54.2 ± 1.1	3.323 ± 0.074
	R18	4.6306	903.3	74	17.5	-37.7 ± 0.1	4.5 ± 0.1	0.372 ± 0.006	54.1 ± 0.8	3.501 ± 0.057
	R19	4.6242	1003.5	78	17.6	-38.3 ± 0.1	4.4 ± 0.1	0.32 ± 0.006	45.8 ± 0.9	3.014 ± 0.065
	P21	4.9697	1219.8	86	14.8	-37.5 ± 0.1	4.5 ± 0.1	0.242 ± 0.004	38.1 ± 0.9	2.423 ± 0.06
	R21	4.6116	1219.8	86	17.8	-37.4 ± 0.1	4.2 ± 0.1	0.262 ± 0.005	36.1 ± 0.7	2.408 ± 0.05
	P22	4.9804	1335.8	90	14.7	-37.8 ± 0.1	4.3 ± 0.1	0.202 ± 0.006	30.6 ± 0.7	1.976 ± 0.049
	R22	4.6055	1335.8	90	17.9	-37.5 ± 0.1	4.5 ± 0.1	0.268 ± 0.007	39.8 ± 0.9	2.651 ± 0.065
	R23	4.5995	1457	94	18	-38.1 ± 0.8	4.5 ± 0.5	0.248 ± 0.007	36.8 ± 6.6	2.452 ± 0.479
	P24	5.0022	1583.5	98	14.4	-37.4 ± 0.3	4 ± 0.3	0.128 ± 0.007	18 ± 1.1	1.193 ± 0.074

Table C.15: MIR2: ^{13}CO Line Parameters of $v = -38$ km s^{-1} (2 of 2)

Species	tr.s.	λ (μm)	E_l (K)	g_l	A_{ij} (s^{-1})	v_{LSR} (km s^{-1})	Δv (km s^{-1})	τ_0	N_l ($\times 10^{14}$ cm^{-2})	W_v (km s^{-1})
^{13}CO ν = 0–1	R24	4.5935	1583.5	98	18.1	-37.6 $\pm$ 0.2	3.9 $\pm$ 0.2	0.189 $\pm$ 0.007	24.7 $\pm$ 1	1.685 $\pm$ 0.076
	P25	5.0133	1715.2	102	14.3	-37.4 $\pm$ 0.3	4.1 $\pm$ 0.3	0.107 $\pm$ 0.004	15.6 $\pm$ 1.1	1.042 $\pm$ 0.074
	P26	5.0245	1852.1	106	14.2	-38.5 $\pm$ 0.4	4.5 $\pm$ 0.4	0.108 $\pm$ 0.011	17.3 $\pm$ 1.3	1.151 $\pm$ 0.086
	R26	4.5819	1852.1	106	18.2	-38.5 $\pm$ 0.4	3.8 $\pm$ 0.3	0.119 $\pm$ 0.005	15.4 $\pm$ 1.5	1.074 $\pm$ 0.108
	P27	5.0358	1994.2	110	14.1	-37.8 $\pm$ 0.2	3.7 $\pm$ 0.3	0.085 $\pm$ 0.005	11.1 $\pm$ 0.7	0.75 $\pm$ 0.048
	R27	4.5762	1994.2	110	18.3	-38.5 $\pm$ 0.3	4.5 $\pm$ 0.3	0.122 $\pm$ 0.007	18.5 $\pm$ 1.3	1.286 $\pm$ 0.096
	P29	5.0589	2294.1	118	13.9	-37.4 $\pm$ 0.9	4.1 $\pm$ 0.8	0.057 $\pm$ 0.003	8.4 $\pm$ 1.9	0.573 $\pm$ 0.133
	P30	5.0706	2451.9	122	13.8	-37.4 $\pm$ 0.4	4 $\pm$ 0.4	0.052 $\pm$ 0.003	7.4 $\pm$ 0.6	0.503 $\pm$ 0.039
	P33	5.1065	2956.4	134	13.5	-37.4 $\pm$ 0.9	4.5 $\pm$ 1.1	0.042 $\pm$ 0.004	6.7 $\pm$ 1.3	0.462 $\pm$ 0.088
	R33	4.544	2956.4	134	18.9	-37.4 $\pm$ 1.9	4.3 $\pm$ 1.8	0.049 $\pm$ 0.009	7.3 $\pm$ 3.5	0.519 $\pm$ 0.25

Table C.16: MIR2: ^{13}CO Line Parameters of $v = -46\ \mathrm{km\,s^{-1}}$

Species	tr.s.	λ (μm)	E_l (K)	g_l	A_{ij} ($\mathrm{s^{-1}}$)	v_{LSR} ($\mathrm{km\,s^{-1}}$)	Δv ($\mathrm{km\,s^{-1}}$)	τ_0	N_l ($\times 10^{14}\ \mathrm{cm^{-2}}$)	W_v ($\mathrm{km\,s^{-1}}$)
^{13}CO ν = 0–1	R0	4.7626	0	2	10.9	-45.9 ± 0.4	3 ± 0.4	0.452 ± 0.008	24 ± 2.5	2.666 ± 0.356
	P1	4.7792	5.3	6	32.4	-46.2 ± 0.5	3 ± 0.4	0.442 ± 0.005	70 ± 7.9	2.629 ± 0.369
	P2	4.7877	15.9	10	21.5	-45.4 ± 0.3	2.9 ± 0.3	0.692 ± 0.007	85.3 ± 6.4	3.571 ± 0.362
	R2	4.7463	15.9	10	14.2	-46.4 ± 0.5	3 ± 0.6	0.976 ± 0.039	76.4 ± 10.9	4.414 ± 0.923
	P3	4.7963	31.7	14	19.2	-46 ± 0.4	3 ± 0.4	0.914 ± 0.024	102.7 ± 10	4.339 ± 0.605
	R3	4.7383	31.7	14	14.8	-46 ± 0.4	3 ± 0.4	0.978 ± 0.007	82.5 ± 8	4.487 ± 0.644
	P4	4.805	52.9	18	18.2	-47 ± 0.6	3 ± 0.5	1.182 ± 0.014	123.2 ± 14.6	5.071 ± 0.915
	R7	4.7075	148	30	16	-46.7 ± 0.6	3 ± 0.5	0.841 ± 0.013	71.5 ± 11.1	3.786 ± 0.837
	R9	4.6926	237.9	38	16.4	-47 ± 1.1	3 ± 0.9	0.519 ± 0.008	40.5 ± 15.8	2.377 ± 1.175
	R10	4.6853	290.7	42	16.5	-46.9 ± 0.7	3 ± 0.5	0.389 ± 0.005	30.7 ± 8.1	1.92 ± 0.598
	P11	4.8689	348.9	46	16.1	-46.8 ± 1.1	3 ± 0.7	0.318 ± 0.004	28 ± 11.1	1.648 ± 0.747
	P12	4.8784	412.3	50	15.9	-47 ± 1.3	3 ± 1	0.242 ± 0.005	19.4 ± 10.6	1.182 ± 0.717
	P13	4.8881	480.9	54	15.8	-46.6 ± 0.9	3 ± 0.6	0.158 ± 0.006	10.1 ± 4.3	0.66 ± 0.289
	R13	4.6641	480.9	54	16.9	-46.6 ± 0.8	3 ± 0.5	0.2 ± 0.004	11.2 ± 4.4	0.797 ± 0.325

Table C.17: MIR2: ^{13}CO Line Parameters of $v = -53\ \mathrm{km\,s^{-1}}$

Species	tr.s.	λ (μm)	E_l (K)	g_l	A_{ij} (s^{-1})	v_{LSR} ($\mathrm{km\,s^{-1}}$)	Δv ($\mathrm{km\,s^{-1}}$)	τ_0	N_l ($\times 10^{14}\ \mathrm{cm^{-2}}$)	W_v ($\mathrm{km\,s^{-1}}$)
^{13}CO ν = 0−1	P17	4.928	808.3	70	15.2	-52 ± 0.7	5 ± 0.8	0.048 ± 0.003	8.8 ± 1.2	0.558 ± 0.084
	R19	4.6242	1003.5	78	17.6	-52.6 ± 0.7	5 ± 1.1	0.031 ± 0.004	5.4 ± 1	0.362 ± 0.069
	R21	4.6116	1219.8	86	17.8	-53 ± 0.6	3.7 ± 0.6	0.044 ± 0.005	5.7 ± 0.8	0.399 ± 0.057
	P22	4.9804	1335.8	90	14.7	-50.7 ± 0.7	3.3 ± 0.7	0.028 ± 0.004	3.2 ± 0.6	0.213 ± 0.041
	R22	4.6055	1335.8	90	17.9	-50 ± 0.7	2.8 ± 0.7	0.039 ± 0.006	3.4 ± 0.7	0.232 ± 0.054

Table C.18: MIR2: $C^{18}O$ Line Parameters of $v = -38\ \mathrm{km\,s^{-1}}$

Species	tr.s.	λ (μm)	E_l (K)	g_l	A_{ij} (s^{-1})	v_{LSR} ($\mathrm{km\,s^{-1}}$)	Δv ($\mathrm{km\,s^{-1}}$)	τ_0	N_l ($\times 10^{14}$ $\mathrm{cm^{-2}}$)	W_v ($\mathrm{km\,s^{-1}}$)
$C^{18}O$ ν = 0–1	R0	4.7716	0	1	10.8	-38.5 ± 0.1	1.9 ± 0.1	0.308 ± 0.005	9.9 ± 0.6	1.259 ± 0.079
	P1	4.7882	5.3	3	32.2	-38.4 ± 0.1	1.9 ± 0.1	0.27 ± 0.004	26.8 ± 1.4	1.149 ± 0.067
	P2	4.7967	15.8	5	21.3	-38.5 ± 0.2	1.8 ± 0.3	0.375 ± 0.005	27.7 ± 2.9	1.383 ± 0.164
	P3	4.8053	31.6	7	19.1	-38.5 ± 0.6	1.8 ± 0.7	0.392 ± 0.007	27 ± 7.7	1.435 ± 0.463
	R3	4.7473	31.6	7	14.7	-38.5 ± 0.2	2.4 ± 0.2	0.49 ± 0.006	33.3 ± 1.9	2.3 ± 0.151
	R4	4.7395	52.7	9	15.1	-38.4 ± 0.1	2 ± 0.1	0.423 ± 0.005	24.9 ± 1.3	1.702 ± 0.102
	R5	4.7317	79	11	15.4	-38.4 ± 0.3	2.6 ± 0.3	0.27 ± 0.007	22.3 ± 2.2	1.57 ± 0.169
	R9	4.7016	237	19	16.2	-38 ± 0.5	3 ± 0.5	0.17 ± 0.005	17 ± 2.2	1.192 ± 0.166
	R10	4.6943	289.6	21	16.4	-38.5 ± 0.2	3.2 ± 0.2	0.118 ± 0.003	12.5 ± 0.7	0.889 ± 0.048
	R11	4.6872	347.5	23	16.5	-38.4 ± 0.2	3.2 ± 0.2	0.111 ± 0.004	12 ± 0.7	0.852 ± 0.053
	P14	4.9069	552.8	29	15.5	-38.5 ± 0.3	3.8 ± 0.3	0.124 ± 0.006	17.2 ± 1.3	1.114 ± 0.087
	R14	4.6662	552.8	29	16.9	-38.4 ± 0.2	3.3 ± 0.2	0.078 ± 0.004	8.7 ± 0.5	0.619 ± 0.036
	P15	4.9168	631.7	31	15.4	-38.5 ± 0.7	2.9 ± 0.8	0.063 ± 0.004	6.7 ± 1.5	0.446 ± 0.101
	R15	4.6594	631.7	31	17	-37.5 ± 0.3	3.8 ± 0.4	0.101 ± 0.004	13 ± 1	0.914 ± 0.07
	R16	4.6527	715.8	33	17.1	-37.5 ± 1.6	3.4 ± 1.9	0.076 ± 0.003	8.8 ± 3.8	0.623 ± 0.28
	P17	4.9369	805.2	35	15.1	-37.4 ± 0.3	3.8 ± 0.4	0.067 ± 0.005	9.2 ± 0.7	0.616 ± 0.047
	R17	4.6461	805.2	35	17.2	-38 ± 0.7	3.4 ± 0.8	0.071 ± 0.005	8.3 ± 1.5	0.592 ± 0.109
	P20	4.968	1104.8	41	14.8	-37.4 ± 0.3	3.8 ± 0.4	0.056 ± 0.003	7.6 ± 0.6	0.515 ± 0.042
	R22	4.6145	1330.7	45	17.7	-37.4 ± 0.5	3.4 ± 0.5	0.062 ± 0.005	7.1 ± 0.9	0.506 ± 0.064
	P23	5.0002	1451.5	47	14.4	-37.4 ± 0.4	3.3 ± 0.4	0.031 ± 0.004	3.7 ± 0.4	0.253 ± 0.026
	P24	5.0111	1577.5	49	14.3	-37.5 ± 0.6	3.8 ± 0.7	0.035 ± 0.004	4.8 ± 0.7	0.328 ± 0.052

Table C.19: MIR2: $C^{18}O$ Line Parameters of $v = -46\ \mathrm{km\,s^{-1}}$

Species	tr.s.	λ (μm)	E_l (K)	g_l	A_{ij} (s^{-1})	v_{LSR} ($\mathrm{km\,s^{-1}}$)	Δv ($\mathrm{km\,s^{-1}}$)	τ_0	N_l ($\times 10^{14}\ \mathrm{cm^{-2}}$)	W_v ($\mathrm{km\,s^{-1}}$)
$C^{18}O$ ν = 0–1	R0	4.7716	0	1	10.8	-45.4 $\pm$ 0.8	1.8 $\pm$ 0.8	0.062 $\pm$ 0.005	2 $\pm$ 0.8	0.269 $\pm$ 0.106
	P1	4.7882	5.3	3	32.2	-45.5 $\pm$ 0.4	1.3 $\pm$ 0.4	0.061 $\pm$ 0.004	4.3 $\pm$ 1.2	0.193 $\pm$ 0.057
	P2	4.7967	15.8	5	21.3	-45.5 $\pm$ 0.7	1.8 $\pm$ 0.8	0.112 $\pm$ 0.004	9 $\pm$ 3	0.477 $\pm$ 0.169
	P3	4.8053	31.6	7	19.1	-45.5 $\pm$ 2.5	1.8 $\pm$ 2.5	0.101 $\pm$ 0.006	7.6 $\pm$ 8.6	0.433 $\pm$ 0.517
	R3	4.7473	31.6	7	14.7	-45.4 $\pm$ 0.4	1.8 $\pm$ 0.5	0.184 $\pm$ 0.006	10 $\pm$ 2.1	0.726 $\pm$ 0.168
	R4	4.7395	52.7	9	15.1	-45.4 $\pm$ 0.3	1.8 $\pm$ 0.3	0.159 $\pm$ 0.004	9.1 $\pm$ 1.3	0.661 $\pm$ 0.105
	R5	4.7317	79	11	15.4	-45.5 $\pm$ 0.5	1.8 $\pm$ 0.5	0.125 $\pm$ 0.005	7 $\pm$ 1.8	0.501 $\pm$ 0.135

Table C.20: MIR2: $C^{17}O$ Line Parameters of $v = -38 \text{ km s}^{-1}$

Species	tr.s.	λ (μm)	E_l (K)	g_l	A_{ij} (s^{-1})	v_{LSR} (km s^{-1})	Δv (km s^{-1})	τ_0	N_l ($\times 10^{14}$ cm^{-2})	W_v (km s^{-1})
$C^{17}O$ ν = 0–1	P1	4.7336	5.4	18	33.7	-38.9 $\pm$ 0.3	1.4 $\pm$ 0.3	0.064 $\pm$ 0.003	4.8 $\pm$ 0.8	
	P3	4.7507	32.3	42	20	-38.8 $\pm$ 0.5	1.6 $\pm$ 0.5	0.111 $\pm$ 0.005	7.3 $\pm$ 1.9	
	R4	4.6849	53.9	54	15.8	-38.4 $\pm$ 0.1	1.5 $\pm$ 0.1	0.12 $\pm$ 0.004	5.5 $\pm$ 0.4	
	R5	4.6771	80.9	66	16.1	-38.8 $\pm$ 0.2	1.7 $\pm$ 0.2	0.113 $\pm$ 0.006	6.1 $\pm$ 0.5	
	P6	4.7771	113.2	78	17.9	-38.9 $\pm$ 2.4	1.7 $\pm$ 2.6	0.073 $\pm$ 0.008	4.7 $\pm$ 5.9	
	R6	4.6695	113.2	78	16.4	-38.5 $\pm$ 0.2	1.7 $\pm$ 0.2	0.087 $\pm$ 0.005	4.8 $\pm$ 0.4	

Table C.21: MIR2: $C^{17}O$ Line Parameters of $v = -46$ km s^{-1}

Species	tr.s.	λ (μm)	E_l (K)	g_l	A_{ij} (s^{-1})	v_{LSR} (km s^{-1})	Δv (km s^{-1})	τ_0	N_l ($\times 10^{14}$ cm^{-2})
$C^{17}O$ ν = 0–1	P1	4.7336	5.4	18	33.7	-45 $\pm$ 0.8	1 $\pm$ 0.9	0.019 $\pm$ 0.003	1.1 $\pm$ 0.7
	P3	4.7507	32.3	42	20	-45.5 $\pm$ 1.9	1.8 $\pm$ 2	0.02 $\pm$ 0.004	1.5 $\pm$ 1.4
	R5	4.6771	80.9	66	16.1	-45.5 $\pm$ 0.5	1.8 $\pm$ 0.5	0.042 $\pm$ 0.006	2.4 $\pm$ 0.6
	R6	4.6695	113.2	78	16.4	-45 $\pm$ 0.3	1.8 $\pm$ 0.4	0.047 $\pm$ 0.004	2.7 $\pm$ 0.4
	R8	4.6544	194	102	16.8	-45 $\pm$ 0.6	1.8 $\pm$ 0.6	0.035 $\pm$ 0.003	2.1 $\pm$ 0.6
	R9	4.6471	242.5	114	17	-45 $\pm$ 0.6	1.8 $\pm$ 0.7	0.027 $\pm$ 0.004	1.6 $\pm$ 0.5

Table C.22: MIR2: ^{12}CO ν=0−1 Line Parameters of $v = -38$ km s^{-1}, high J

Species	tr.s.	λ (μm)	E_l (K)	g_l	A_{ij} (s^{-1})	v_{LSR} (km s^{-1})	Δv (km s^{-1})	τ_0	N_l ($\times 10^{14}$ cm^{-2})	W_v (km s^{-1})
^{12}CO ν = 0−1	P26	4.9204	1937.1	53	15.5	-39 $\pm$ 0.2	6.9 $\pm$ 0.2	0.665 $\pm$ 0.003	144.6 $\pm$ 3.6	8.336 $\pm$ 0.256
	P27	4.9318	2085.7	55	15.4	-39 $\pm$ 0.2	7 $\pm$ 0.2	0.632 $\pm$ 0.003	140.5 $\pm$ 2.8	8.224 $\pm$ 0.199
	P30	4.9668	2564.4	61	15.1	-38 $\pm$ 0.1	6.3 $\pm$ 0.1	0.474 $\pm$ 0.003	96.7 $\pm$ 1.2	5.929 $\pm$ 0.086
	P31	4.9788	2734.8	63	14.9	-38.5 $\pm$ 1	7 $\pm$ 0.9	0.447 $\pm$ 0.292	102.1 $\pm$ 10.8	6.32 $\pm$ 0.768
	P34	5.0154	3278.6	69	14.6	-37.4 $\pm$ 1.4	5.4 $\pm$ 0.6	0.309 $\pm$ 0.004	56.2 $\pm$ 12.8	3.61 $\pm$ 0.908
	P35	5.0279	3470.7	71	14.5	-37.8 $\pm$ 0.2	4.8 $\pm$ 0.2	0.228 $\pm$ 0.008	36.7 $\pm$ 1.1	2.433 $\pm$ 0.082
	P37	5.0532	3871	75	14.3	-37 $\pm$ 0.1	5.3 $\pm$ 0.1	0.214 $\pm$ 0.003	38.7 $\pm$ 0.8	2.577 $\pm$ 0.057
	P38	5.0661	4079.3	77	14.2	-37 $\pm$ 0.2	5.5 $\pm$ 0.2	0.179 $\pm$ 0.003	33.3 $\pm$ 1.1	2.247 $\pm$ 0.081
	P39	5.0792	4292.9	79	14.1	-37.3 $\pm$ 1.9	6 $\pm$ 1.2	0.164 $\pm$ 0.006	33.3 $\pm$ 8.6	2.257 $\pm$ 0.615
	P41	5.1057	4736.2	83	13.8	-37.5 $\pm$ 0.4	5.6 $\pm$ 0.4	0.116 $\pm$ 0.004	22.5 $\pm$ 1.3	1.554 $\pm$ 0.095
	P42	5.1191	4965.9	85	13.7	-37.6 $\pm$ 0.4	6.3 $\pm$ 0.3	0.103 $\pm$ 0.005	22.4 $\pm$ 1	1.555 $\pm$ 0.075
	P43	5.1328	5201	87	13.6	-37.2 $\pm$ 4	4.9 $\pm$ 3.3	0.078 $\pm$ 0.006	13.2 $\pm$ 49.3	0.924 $\pm$ 3.534
	P45	5.1605	5687.1	91	13.4	-39 $\pm$ 1.8	5.3 $\pm$ 1.6	0.064 $\pm$ 0.005	11.8 $\pm$ 3.3	0.832 $\pm$ 0.24

Table C.23: MIR2: ^{12}CO ν=0−1 Line Parameters of $v = -53$ km s^{-1}, high J

Species	tr.s.	λ (μm)	E_l (K)	g_l	A_{ij} (s^{-1})	v_{LSR} (km s^{-1})	Δv (km s^{-1})	τ_0	N_l ($\times 10^{14}$ cm^{-2})	W_v (km s^{-1})
^{12}CO ν = 0−1	P22	4.876	1397.1	45	16	-52.6 ± 0.8	5 ± 0.6	0.456 ± 0.004	65.1 ± 10.6	3.782 ± 0.747
	P26	4.9204	1937.1	53	15.5	-54.2 ± 0.3	4.2 ± 0.3	0.256 ± 0.003	32.3 ± 2.7	1.931 ± 0.192
	P27	4.9318	2085.7	55	15.4	-54.7 ± 0.2	3.6 ± 0.2	0.23 ± 0.004	25.5 ± 1.8	1.518 ± 0.126
	P30	4.9668	2564.4	61	15.1	-54.1 ± 0.2	3.7 ± 0.2	0.122 ± 0.004	14.8 ± 0.8	0.94 ± 0.056
	P31	4.9788	2734.8	63	14.9	-55.4 ± 1.8	3.9 ± 1.6	0.129 ± 0.009	15.6 ± 6.9	0.992 ± 0.490
	P34	5.0154	3278.6	69	14.6	-52.1 ± 7.4	5 ± 2.7	0.097 ± 0.005	15.9 ± 23.8	1.07 ± 1.692
	P35	5.0279	3470.7	71	14.5	-52.8 ± 1.2	3.7 ± 1.3	0.025 ± 0.008	3.3 ± 0.9	0.22 ± 0.066
	P37	5.0532	3871	75	14.3	-54.3 ± 0.5	4.3 ± 0.5	0.043 ± 0.003	6.5 ± 0.6	0.445 ± 0.045
	P38	5.0661	4079.3	77	14.2	-52.5 ± 1.2	2.9 ± 1.2	0.023 ± 0.003	2.1 ± 0.7	0.143 ± 0.052
	P39	5.0792	4292.9	79	14.1	-54.7 ± 2.7	2.9 ± 2.8	0.022 ± 0.006	2.1 ± 1.7	0.146 ± 0.124

Table C.24: MIR2: ^{12}CO ν= 1–2 Line Parameters of $v = -38$ km s^{-1} (1 of 2)

Species	tr.s.	λ (μm)	E_l (K)	g_l	A_{ij} (s^{-1})	v_{LSR} (km s^{-1})	Δv (km s^{-1})	τ_0	N_l ($\times 10^{14}$ cm^{-2})
^{12}CO ν = 1–2	P1	4.7327	3088.6	3	68.2	-37.5 ± 0.3	4.5 ± 0.3	0.14 ± 0.005	16.1 ± 0.8
	P2	4.7413	3099.5	5	45.2	-37.5 ± 0.5	4.5 ± 0.5	0.166 ± 0.004	15.7 ± 1.4
	P3	4.75	3116	7	40.5	-37.5 ± 0.2	4.5 ± 0.2	0.177 ± 0.006	15.8 ± 0.6
	P4	4.7589	3137.9	9	38.3	-37.6 ± 0.5	4.5 ± 0.5	0.198 ± 0.005	16.8 ± 1.5
	R4	4.6832	3137.9	9	32	-37.7 ± 0.3	4.5 ± 0.3	0.259 ± 0.007	17.5 ± 0.9
	P6	4.7769	3198.2	13	36.1	-38.5 ± 0.6	4.5 ± 0.6	0.273 ± 0.008	22.2 ± 2.4
	R6	4.6675	3198.2	13	33.2	-37.5 ± 0.2	4.5 ± 0.2	0.27 ± 0.006	18.8 ± 0.5
	R7	4.6598	3236.5	15	33.7	-37.5 ± 0.1	4.5 ± 0.1	0.253 ± 0.004	17.8 ± 0.4
	P8	4.7954	3280.4	17	34.9	-37.5 ± 0.4	4.5 ± 0.4	0.308 ± 0.005	24.5 ± 1.5
	R8	4.6523	3280.4	17	34.1	-37.5 ± 0.2	4.5 ± 0.2	0.25 ± 0.004	17.6 ± 0.5
	R9	4.6448	3329.7	19	34.4	-37.5 ± 0.1	4.5 ± 0.1	0.295 ± 0.004	20.9 ± 0.5
	P11	4.824	3444.7	23	33.7	-37.6 ± 0.1	4.5 ± 0.1	0.253 ± 0.005	19.9 ± 0.4
	R11	4.6302	3444.7	23	35	-37.5 ± 0.2	4.5 ± 0.2	0.285 ± 0.006	20.4 ± 0.6
	R12	4.623	3510.4	25	35.3	-37.7 ± 0.2	4.5 ± 0.1	0.245 ± 0.007	17.7 ± 0.5
	R13	4.616	3581.6	27	35.6	-37.5 ± 0.2	4.5 ± 0.2	0.276 ± 0.004	19.9 ± 0.5
	P15	4.8637	3740.3	31	32.5	-37.5 ± 0.3	4.5 ± 0.3	0.238 ± 0.006	18.5 ± 1
	R17	4.5887	3920.8	35	36.6	-37.5 ± 0.3	4.5 ± 0.3	0.318 ± 0.011	22.9 ± 1.3
	P18	4.8948	4019.3	37	31.7	-37.5 ± 0.1	4.5 ± 0.2	0.178 ± 0.007	13.9 ± 0.4
	P19	4.9054	4123.2	39	31.4	-37.5 ± 0.2	4.5 ± 0.3	0.189 ± 0.004	14.7 ± 0.7
	R19	4.5757	4123.2	39	37	-38.5 ± 0.4	4.5 ± 0.4	0.22 ± 0.009	16.2 ± 1.1
	P20	4.9161	4232.5	41	31.2	-37.5 ± 0.3	4.5 ± 0.3	0.166 ± 0.004	13 ± 0.7
	R20	4.5694	4232.5	41	37.2	-37.5 ± 0.2	4.5 ± 0.2	0.205 ± 0.006	15.1 ± 0.5
	P21	4.9269	4347.3	43	31	-38.5 ± 0.8	4.5 ± 0.8	0.134 ± 0.004	10.5 ± 1.6
	R21	4.5631	4347.3	43	37.4	-37.5 ± 0.3	4.5 ± 0.3	0.173 ± 0.006	12.8 ± 0.7
	P22	4.9379	4467.5	45	30.7	-37.5 ± 0.5	4.5 ± 0.5	0.152 ± 0.005	11.9 ± 1.1
	P25	4.9716	4860.6	51	30.1	-37.5 ± 0.3	4.5 ± 0.3	0.101 ± 0.003	8 ± 0.5
	P26	4.9831	5002.5	53	29.8	-37.5 ± 0.2	4.5 ± 0.2	0.127 ± 0.006	10 ± 0.4
…									

Table C.25: MIR2: ^{12}CO ν= 1–2 Line Parameters of $v = -38$ km s^{-1} (2 of 2)

Species	tr.s.	λ (μm)	E_l (K)	g_l	A_{ij} (s^{-1})	v_{LSR} (km s^{-1})	Δv (km s^{-1})	τ_0	N_l ($\times 10^{14}$ cm^{-2})
^{12}CO ν = 1–2	R27	4.5275	5149.8	55	38.6	-38.1 $\pm$ 0.3	4 $\pm$ 0.3	0.089 $\pm$ 0.016	5.9 $\pm$ 0.4
	P28	5.0065	5302.5	57	29.4	-37.5 $\pm$ 0.4	4.5 $\pm$ 0.4	0.072 $\pm$ 0.004	5.7 $\pm$ 0.4
	P32	5.0548	5967.1	65	28.5	-38.5 $\pm$ 0.3	4.2 $\pm$ 0.3	0.048 $\pm$ 0.003	3.6 $\pm$ 0.2
	P33	5.0673	6146.8	67	28.3	-38.1 $\pm$ 0.4	3.9 $\pm$ 0.4	0.033 $\pm$ 0.003	2.2 $\pm$ 0.2
	P34	5.0798	6331.7	69	28.1	-38.5 $\pm$ 0.9	2.8 $\pm$ 0.9	0.032 $\pm$ 0.007	1.5 $\pm$ 0.4

Table C.26: MIR1: ^{13}CO Line Parameters of $v = -38\ \mathrm{km\,s^{-1}}$

Species	tr.s.	λ (μm)	E_l (K)	g_l	A_{ij} (s^{-1})	v_{LSR} ($\mathrm{km\,s^{-1}}$)	Δv ($\mathrm{km\,s^{-1}}$)	τ_0	N_l ($\times 10^{14}$ $\mathrm{cm^{-2}}$)	W_v ($\mathrm{km\,s^{-1}}$)
^{13}CO ν = 0–1	R0	4.7626	0	2	10.9	-38.7 ± 0.3	2 ± 0.1	1.203 ± 0.016	36.4 ± 4.6	3.209 ± 0.642
	P1	4.7792	5.3	6	32.4	-38.4 ± 0.9	2 ± 0.4	1.098 ± 0.007	104.3 ± 45.2	2.98 ± 2.124
	P2	4.7877	15.9	10	21.5	-38.5 ± 0.3	2 ± 0.1	1.277 ± 0.009	101.4 ± 11.6	3.21 ± 0.651
	P3	4.7963	31.7	14	19.2	-39 ± 0.4	2 ± 0.1	1.375 ± 0.017	102.8 ± 17.8	3.107 ± 1.073
	R3	4.7383	31.7	14	14.8	-38.6 ± 0.5	2 ± 0.2	1.551 ± 0.01	90.6 ± 16.5	3.392 ± 1.327
	P4	4.805	52.9	18	18.2	-38.8 ± 0.3	1.7 ± 0.2	1.368 ± 0.017	83.3 ± 16.1	2.623 ± 1.01
	P7	4.8317	148	30	16.9	-39 ± 0.5	2 ± 0.2	1.004 ± 0.008	72.5 ± 14.5	2.742 ± 0.951
	P8	4.8408	190.3	34	16.6	-39 ± 2.4	2 ± 1.8	0.697 ± 0.022	51.4 ± 42.3	2.411 ± 2.801
	P9	4.8501	237.9	38	16.4	-39 ± 1.7	2 ± 1	0.426 ± 0.006	31.6 ± 20.3	1.563 ± 1.355
	R10	4.6853	290.7	42	16.5	-39 ± 1.5	2 ± 0.8	0.275 ± 0.004	19.4 ± 11.5	1.003 ± 0.85
	P11	4.8689	348.9	46	16.1	-39 ± 3.6	2 ± 1.9	0.144 ± 0.003	11.2 ± 15.1	0.54 ± 1.013
	P12	4.8784	412.3	50	15.9	-38.7 ± 5.4	2 ± 2.6	0.113 ± 0.003	8.3 ± 17.1	0.377 ± 1.154
	R12	4.6711	412.3	50	16.8	-37 ± 1.2	2 ± 0.8	0.12 ± 0.005	8.3 ± 4	0.483 ± 0.297
	P13	4.8881	480.9	54	15.8	-37.9 ± 2.7	2 ± 1.5	0.074 ± 0.005	4.9 ± 5.6	0.229 ± 0.377
	R13	4.6641	480.9	54	16.9	-37.9 ± 3.5	2 ± 2	0.107 ± 0.003	7.1 ± 10.6	0.397 ± 0.781

Appendix D: Appendices for Chapter 4

D.1 Telluric Molecular Lines from 5.36 to 7.92 μm

We present in Figure D.1 the important telluric lines from 5.36 to 7.92 μm produced by the PSG models under representative observational parameters (see Table D.1). Eight molecular species, H_2O, O_3, CH_4, NO_2, N_2O, CO_2, HNO_3, and O_2 are among the most important ones. For the 15 observational settings, the input surface pressure and scaling factors are tuned to visually match the telluric features in observed spectra, and therefore, may not represent the actual values.

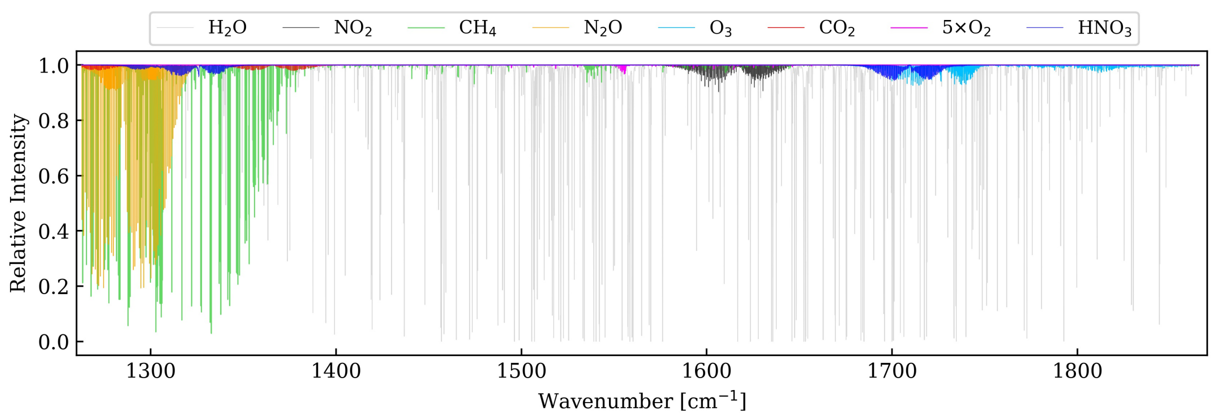

Figure D.1: Important atmospheric telluric lines from 5.36 to 7.92 μm.

Table D.1: Inputs for the PSG Models

Source	λ (μm)	P (bar)	H_2O	O_3	CH_4	NO_2	N_2O	CO_2	HNO_3	O_2
(1)	(2)	(3)	(4)	(5)	(6)	(7)	(8)	(9)	(10)	(11)
W3 IRS 5	5.36–5.51	0.75	1	1	–	–	–	–	–	–
	5.48–5.67	0.7	1	1	–	–	–	–	–	–
	5.65–5.84	0.85	0.7	1	–	–	–	–	–	–
	5.83–6.02	0.92	0.5	1.5	–	–	–	–	2	–
	6.01–6.20	0.83	1	–	1	1	–	–	–	–
	6.01–6.20	0.75	1	–	1	1.5	–	–	–	–
	6.18–6.37	0.83	0.8	–	1	1.3	–	–	–	–
	6.19–6.37	0.85	0.6	–	1	0.8	–	–	–	–
	6.35–6.61	0.75	0.8	–	2	–	–	–	–	1
	6.35–6.61	0.83	0.9	–	1.5	–	–	–	–	–
	6.59–6.85	0.77	1	–	2	–	–	–	–	–
	6.59–6.85	0.85	1	–	1	–	–	–	–	–
	6.79–7.06	0.75	1.5	–	1.8	–	–	–	–	–
	7.19–7.45	0.8	1	–	1.5	–	–	1	–	–
	7.67–7.92	0.7	1	–	2	–	2.5	1	1	–
Sirius	7.18–7.46	0.7	1.4	–	1.7	–	–	1	–	–

Column (1): Sirius is the standard star for the observation session on 2022-02-24 at 7.19–7.45 μm. Column (3): the input surface pressure (Earth at 4084 m) in the PSG models. Column (4)–(11): the input scaling factors of different atmospheric molecular species in the PSG models. See Figure D.1 for an illustration of the contribution of different molecular species at different wavelengths.

D.2 Data Reduction: Sirius vs. PSG models

The standard star, Sirius, was observed only in one setting from 7.28–7.46 μm. While the Sirius spectrum has advantages in reflecting the actual baseline, we compare the qualities of the results derived by using the Sirius spectrum as well as using the PSG models. The data reduction with Sirius is straightforward, as the median filtering processes or the modeling of telluric lines are not needed.

As a result, we present in Figure D.2 the equivalent widths of each individually identified line derived from the two data reduction methods. We conclude that the results are in good

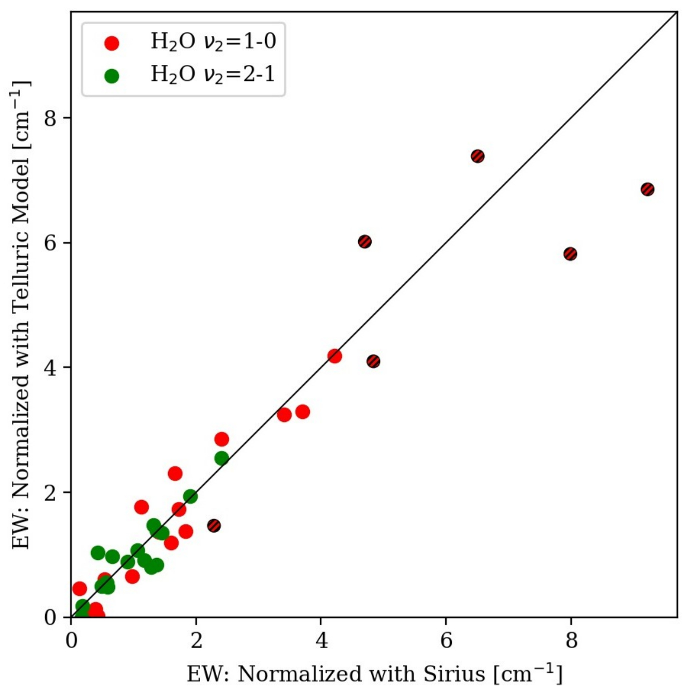

Figure D.2: Comparison between the equivalent width estimated by taking the standard Sirius spectra vs. by adopting the PSG models.

agreement with each other by $\sim 10\%$.

D.3 The Hidden Component at -38 km s^{-1}

As presented in § 4.4 and § 4.5, data analyses in this paper are based on the decomposition of the absorption profiles into the three components at -54.5, -45, and -39.5 km s^{-1} in low-energy levels, while the -39.5 km s^{-1} component is hot. However, we realize that one cold component of ∼50 K may exist at -38 km s^{-1} because of the detection of the cold CO component (Li et al., 2022).

We argue that a cold component is possibly hidden in Figure D.3, in which a list of accumulative average spectra is presented. We note that the absorption feature at -35 km s^{-1} is possibly related to the cold component because it disappears as the energy levels increase. We

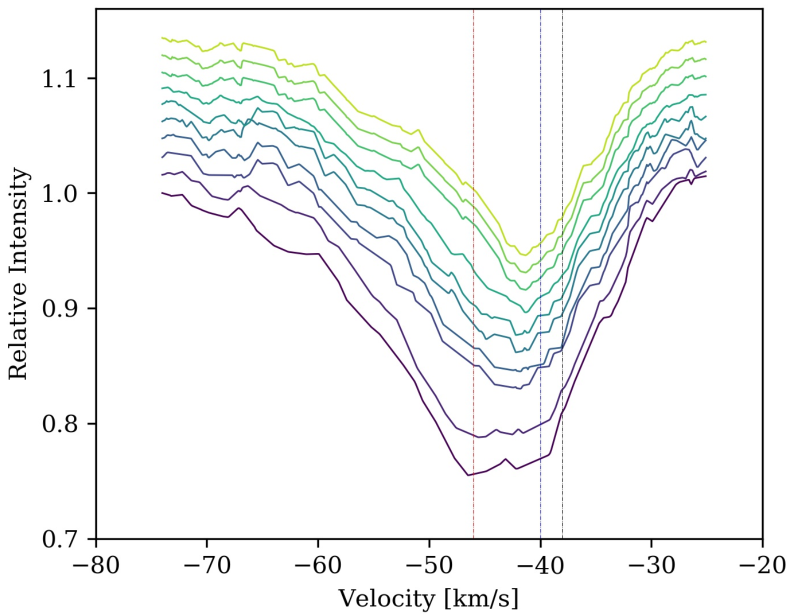

Figure D.3: Accumulative average spectra from 100 to 1000 K. Each spectrum represents the median of spectra in energy levels between 0 to 100 K, 0 to 200 K, ..., 0 to 1000 K. The dashed vertical lines represent -46, -40, and $-38\ \mathrm{km\,s^{-1}}$.

also present two different Gaussian fitting methods for the average spectrum below 200 K in Figure D.4, while in one we fix the right wing with a component at $-38\ \mathrm{km\,s^{-1}}$ and in the other at $-40\ \mathrm{km\,s^{-1}}$. We conclude that the previous one provides a better fit, suggesting that at this energy level the cold $-38\ \mathrm{km\,s^{-1}}$ component possibly indeed dominates the line profile.

Even if the cold $-38\ \mathrm{km\,s^{-1}}$ component does exist, we conclude that the water-to-CO abundance is still low at this temperature. Otherwise, very saturated water absorption lines will dominate the line profiles. We estimate an upper limit of such a water-to-CO ratio of 0.4% by Figure D.5.

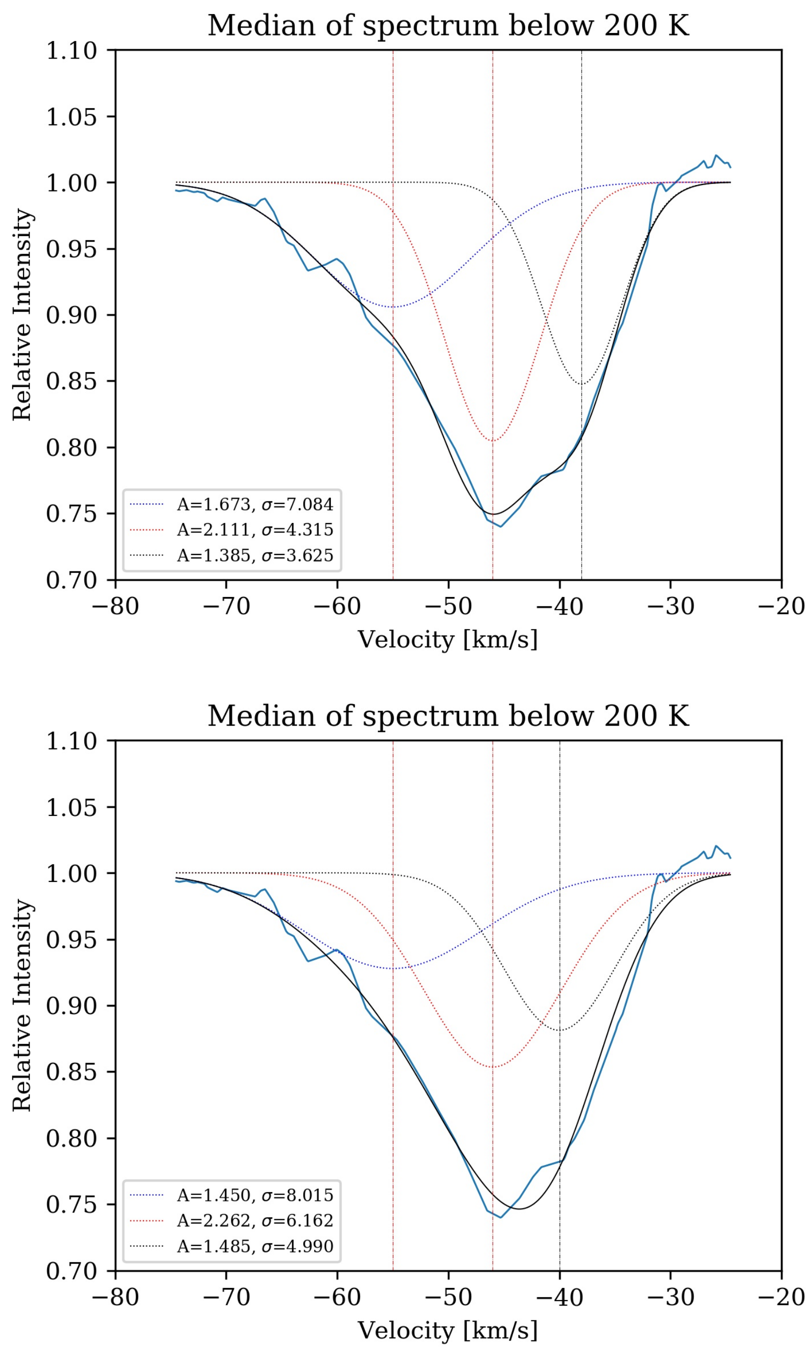

Figure D.4: Two different Gaussian fitting results for the spectrum averaged below 200 K. In the upper panel, the central velocities are -55, -46, and -38 $\mathrm{km\,s^{-1}}$. In the lower panel, the central velocities are -55, -46, and -40 $\mathrm{km\,s^{-1}}$.

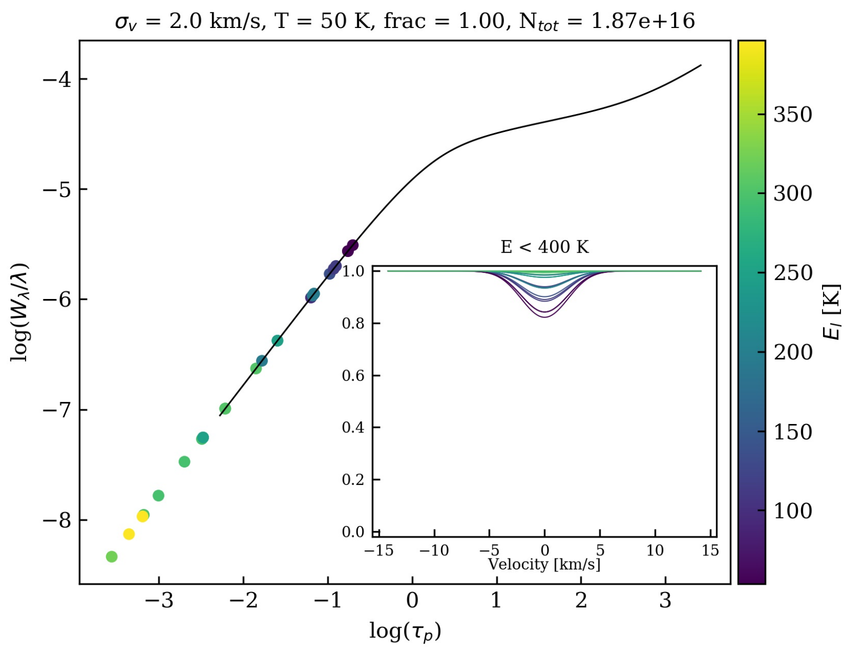

Figure D.5: Expected cold line profiles of water and the correspondent curve-of-growth based on parameters constrained in CO observations.

D.4 Additional Figures

We present in Figure D.6 the two grid-search results and the best-fitted curve-of-growth for the 'H2' component.

D.5 List of the Water Lines

We present from Table D.2 to D.15 the properties of decomposed water lines, H_2O ν_2=1–0 and ν_2=2–1, of W3 IRS 5 from 5.36 to 7.92 μm in this study.

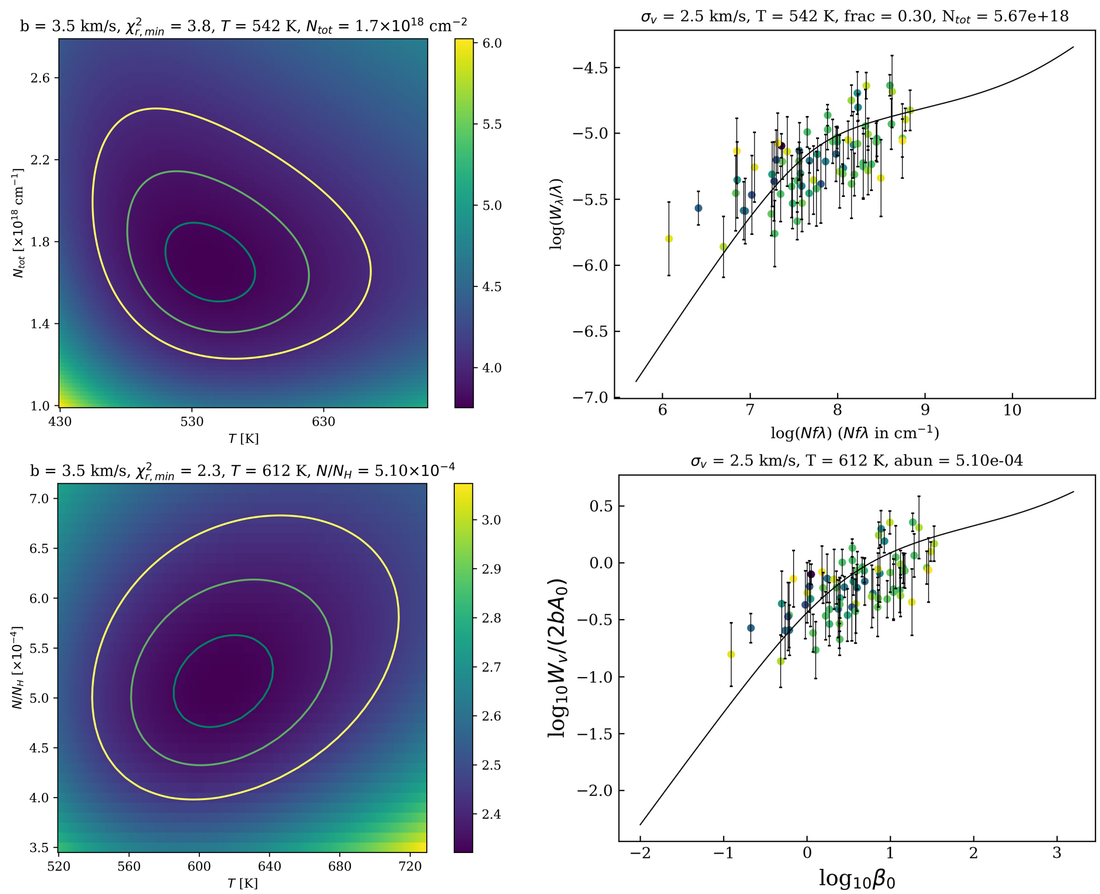

Figure D.6: *Left panels:* Grid-search results of 'H2' for both the slab and the disk model illustrating the best-fitting results. The contours represent the 1σ, 2σ, and 3σ uncertainty levels. *Right panels*: the curves of growth for the slab and the disk model.

Table D.2: Line Parameters of the -39.5 km s^{-1} Component in the ν_2=1–0 Transition (1 of 6)

Transition	λ (μm)	E_l (K)	g_l	g_u	A_{ul} (s^{-1})	v_{LSR} (km s^{-1})	σ_v (km s^{-1})	W_v (km s^{-1})	$\log_{10}(\tau_{p,\mathrm{thin}})$	$\log_{10}(\tau_{p,\mathrm{slab}})$	$\log_{10}(\beta_0)$
$12_{1,11}$-$11_{2,10}$	5.3737	2193.9	23	25	10.9	-39.2 ± 1.3	6.0 ± 1.0	1.835 ± 0.401	-0.55	0.35	0.58
$11_{3,8}$-$10_{4,7}$	5.3772	2274.8	63	69	3.3	-40.7 ± 1.4	5.2 ± 1.0	1.186 ± 0.350	-0.68	0.20	0.43
$7_{6,1}$-$7_{5,2}$	5.4183	1524.6	45	45	1.3	-40.5 ± 0.8	4.2 ± 0.8	0.952 ± 0.263	-0.70	0.30	0.50
$11_{2,10}$-$10_{1,9}$	5.4248	1860.0	21	23	10.2	-41.4 ± 0.6	6.0 ± 0.5	2.490 ± 0.265	-0.39	0.61	0.82
$11_{6,5}$-$11_{5,6}$	5.4521	2875.6	69	69	2.4	-39.0 ± 1.2	4.0 ± 1.2	0.300 ± 0.090	-1.21	-0.48	-0.23
$10_{1,9}$-$9_{2,8}$	5.4862	1554.1	19	21	9.5	-41.0 ± 0.8	6.0 ± 0.8	2.255 ± 0.362	-0.44	0.84	1.04
$10_{1,9}$-$9_{2,8}$	5.4862	1554.1	19	21	9.5	-38.2 ± 0.8	5.6 ± 0.9	1.883 ± 0.296	-0.50	0.84	1.04
$10_{3,7}$-$9_{4,6}$	5.4904	1928.9	19	21	2.6	-42.0 ± 4.0	6.0 ± 2.4	0.925 ± 0.622	-0.87	-0.07	0.14
$11_{4,7}$-$10_{5,6}$	5.5031	2472.4	63	69	1.7	-39.1 ± 3.2	6.0 ± 3.1	1.208 ± 0.678	-0.75	-0.23	0.00
$9_{2,7}$-$8_{3,6}$	5.5179	1447.3	51	57	4.6	-39.0 ± 0.6	5.3 ± 0.6	2.013 ± 0.244	-0.44	1.06	1.25
$5_{3,3}$-$4_{2,2}$	5.5229	454.3	9	11	3.9	-37.5 ± 1.5	5.5 ± 1.2	1.954 ± 0.557	-0.42	1.19	1.35
$11_{1,10}$-$11_{0,11}$	5.5290	1909.1	69	69	0.8	-39.1 ± 1.1	4.0 ± 0.9	0.448 ± 0.134	-1.03	-0.04	0.17
$12_{4,9}$-$12_{3,10}$	5.5298	2823.1	75	75	2.2	-36.0 ± 3.5	6.0 ± 3.3	0.596 ± 0.376	-1.08	-0.41	-0.16
$9_{2,8}$-$8_{1,7}$	5.5319	1270.0	17	19	8.7	-39.1 ± 1.4	5.4 ± 0.8	1.940 ± 0.560	-0.45	1.03	1.22
$9_{1,8}$-$8_{2,7}$	5.5479	1273.9	51	57	8.7	-39.5 ± 0.6	5.5 ± 0.6	2.406 ± 0.303	-0.37	1.50	1.69
$10_{5,6}$-$10_{4,7}$	5.5496	2274.8	63	63	2.7	-40.2 ± 1.0	4.0 ± 1.0	0.523 ± 0.134	-0.95	0.12	0.35
$5_{5,0}$-$5_{4,1}$	5.5685	878.0	33	33	1.1	-39.6 ± 2.4	4.0 ± 2.2	1.094 ± 0.753	-0.61	0.74	0.92
$6_{5,1}$-$6_{4,2}$	5.5707	1090.1	13	13	1.8	-40.4 ± 1.3	5.5 ± 1.2	1.348 ± 0.322	-0.66	0.35	0.53
$7_{5,2}$-$7_{4,3}$	5.5775	1339.6	45	45	2.2	-40.3 ± 0.8	4.2 ± 0.8	1.199 ± 0.227	-0.59	0.76	0.95
$8_{2,7}$-$7_{1,6}$	5.5836	1013.0	45	51	7.9	-40.5 ± 1.7	6.0 ± 1.1	3.093 ± 1.013	-0.25	1.66	1.84
$9_{3,6}$-$8_{4,5}$	5.6118	1615.0	51	57	2.0	-39.7 ± 3.4	6.0 ± 2.0	1.514 ± 0.899	-0.63	0.57	0.77
$7_{2,6}$-$6_{1,5}$	5.6318	781.0	13	15	6.9	-39.3 ± 3.3	5.0 ± 1.9	1.695 ± 1.107	-0.40	1.30	1.47
$9_{2,8}$-$9_{1,9}$	5.6485	1323.7	19	19	1.1	-42.9 ± 1.1	6.0 ± 1.0	1.823 ± 0.326	-0.55	0.12	0.32
$9_{1,9}$-$8_{0,8}$	5.6551	1070.3	17	19	13.1	-39.7 ± 0.9	5.6 ± 1.0	1.874 ± 0.400	-0.51	1.42	1.60
$9_{1,9}$-$8_{0,8}$	5.6551	1070.3	17	19	13.1	-41.8 ± 1.2	5.1 ± 0.9	1.749 ± 0.460	-0.48	1.42	1.60
$9_{4,6}$-$9_{3,7}$	5.6590	1749.6	19	19	3.0	-38.2 ± 3.0	5.4 ± 2.1	0.937 ± 0.574	-0.82	0.15	0.36
$9_{4,6}$-$9_{3,7}$	5.6590	1749.6	19	19	3.0	-39.5 ± 2.5	5.2 ± 1.8	0.892 ± 0.466	-0.81	0.15	0.36

Table D.3: Line Parameters of the -39.5 km s^{-1} Component in the ν_2=1–0 Transition (2 of 6)

Transition	λ (μm)	E_l (K)	g_l	g_u	A_{ul} (s^{-1})	v_{LSR} (km s^{-1})	σ_v (km s^{-1})	W_v (km s^{-1})	$\log_{10}(\tau_{p,\text{thin}})$	$\log_{10}(\tau_{p,\text{slab}})$	$\log_{10}(\beta_0)$
$10_{2,8}$-$10_{1,9}$	5.6645	1860.0	21	21	2.1	-37.3 ± 1.0	5.2 ± 1.1	0.620 ± 0.130	-1.00	-0.06	0.15
$9_{3,7}$-$9_{2,8}$	5.6784	1554.1	19	19	2.3	-40.8 ± 1.4	4.4 ± 1.5	0.483 ± 0.159	-1.04	0.23	0.43
$11_{5,6}$-$11_{4,7}$	5.6789	2731.7	69	69	4.0	-38.9 ± 2.0	4.0 ± 1.8	0.366 ± 0.212	-1.12	-0.07	0.18
$8_{4,5}$-$8_{3,6}$	5.6864	1447.3	51	51	3.1	-38.6 ± 1.0	6.0 ± 0.8	2.084 ± 0.345	-0.48	0.89	1.08
$7_{1,6}$-$6_{2,5}$	5.6921	795.4	39	45	6.6	-37.5 ± 0.9	5.4 ± 0.7	2.616 ± 0.416	-0.25	1.75	1.93
$7_{4,4}$-$7_{3,5}$	5.7051	1174.8	15	15	3.1	-38.4 ± 1.5	5.7 ± 1.0	1.526 ± 0.441	-0.60	0.61	0.79
$11_{3,8}$-$11_{2,9}$	5.7131	2432.0	69	69	3.2	-37.5 ± 1.1	4.4 ± 0.9	0.615 ± 0.178	-0.92	0.12	0.35
$6_{4,3}$-$6_{3,4}$	5.7162	933.6	39	39	2.9	-39.2 ± 0.8	6.0 ± 0.6	2.791 ± 0.508	-0.32	1.21	1.39
$5_{2,4}$-$4_{1,3}$	5.7187	396.3	9	11	5.2	-38.2 ± 1.2	5.0 ± 1.2	2.132 ± 0.565	-0.30	1.41	1.57
$5_{4,2}$-$5_{3,3}$	5.7217	725.0	11	11	2.4	-37.8 ± 1.3	5.0 ± 1.2	1.811 ± 0.447	-0.41	0.78	0.95
$4_{4,0}$-$4_{3,1}$	5.7281	552.2	9	9	1.6	-38.2 ± 1.4	5.0 ± 1.1	1.484 ± 0.365	-0.50	0.68	0.84
$8_{3,6}$-$8_{2,7}$	5.7320	1273.9	51	51	2.7	-39.0 ± 0.4	5.2 ± 0.4	2.063 ± 0.178	-0.42	0.99	1.18
$3_{2,1}$-$2_{1,2}$	5.7477	114.4	15	21	2.7	-38.4 ± 1.5	5.0 ± 1.4	2.256 ± 0.836	-0.21	1.68	1.83
$6_{4,2}$-$6_{3,3}$	5.7550	951.6	13	13	3.2	-39.6 ± 1.3	5.7 ± 0.9	1.759 ± 0.430	-0.54	0.77	0.94
$7_{2,6}$-$7_{1,7}$	5.7735	843.7	15	15	1.7	-39.2 ± 1.4	6.0 ± 1.3	1.999 ± 0.478	-0.51	0.66	0.84
$7_{3,5}$-$7_{2,6}$	5.7792	1020.8	15	15	3.1	-40.3 ± 2.2	6.0 ± 1.3	1.604 ± 0.698	-0.61	0.76	0.94
$10_{3,7}$-$10_{2,8}$	5.7995	2068.5	21	21	4.1	-37.9 ± 1.1	4.7 ± 0.9	0.958 ± 0.297	-0.72	0.07	0.29
$7_{1,6}$-$7_{0,7}$	5.8022	843.3	45	45	1.8	-39.8 ± 0.7	5.2 ± 0.7	2.588 ± 0.367	-0.29	1.16	1.34
$11_{4,7}$-$11_{3,8}$	5.8050	2608.3	69	69	5.3	-37.5 ± 2.5	6.0 ± 2.4	1.151 ± 0.515	-0.78	0.20	0.44
$8_{4,4}$-$8_{3,5}$	5.8088	1510.7	17	17	4.5	-36.1 ± 2.0	6.0 ± 1.9	1.277 ± 0.454	-0.72	0.54	0.74
$9_{4,5}$-$9_{3,6}$	5.8280	1845.5	57	57	5.2	-38.8 ± 0.8	5.0 ± 0.8	1.582 ± 0.265	-0.53	0.82	1.03
$6_{0,6}$-$5_{1,5}$	5.8304	469.9	11	13	10.8	-38.3 ± 1.5	5.0 ± 1.2	2.308 ± 0.650	-0.20	1.76	1.92
$6_{2,5}$-$6_{1,6}$	5.8342	643.4	39	39	2.1	-37.9 ± 1.1	5.3 ± 0.9	2.367 ± 0.470	-0.29	1.36	1.53
$8_{2,6}$-$8_{1,7}$	5.8380	1270.0	17	17	3.3	-38.1 ± 1.8	6.0 ± 1.3	1.979 ± 0.770	-0.50	0.63	0.82
$5_{3,3}$-$5_{2,4}$	5.8473	598.7	11	11	3.5	-37.8 ± 2.5	5.7 ± 1.8	2.719 ± 1.236	-0.31	1.08	1.25
$4_{3,2}$-$4_{2,3}$	5.8670	432.1	27	27	3.2	-37.1 ± 0.8	5.1 ± 1.1	2.256 ± 0.557	-0.26	1.60	1.76
$9_{3,6}$-$9_{2,7}$	5.8729	1729.0	57	57	5.2	-41.1 ± 1.7	6.0 ± 1.2	2.083 ± 0.576	-0.48	0.93	1.14

Table D.4: Line Parameters of the -39.5 km s^{-1} Component in the ν_2=1–0 Transition (3 of 6)

Transition	λ (μm)	E_l (K)	g_l	g_u	A_{ul} (s^{-1})	v_{LSR} (km s^{-1})	σ_v (km s^{-1})	W_v (km s^{-1})	$\log_{10}(\tau_{p,\text{thin}})$	$\log_{10}(\tau_{p,\text{slab}})$	$\log_{10}(\beta_0)$
$3_{3,1}$-$3_{2,2}$	5.8784	296.8	7	7	2.3	-38.8 ± 2.6	5.8 ± 1.4	3.092 ± 1.374	-0.24	1.00	1.15
$8_{3,6}$-$7_{4,3}$	5.8860	1339.6	45	51	1.0	-37.8 ± 1.9	6.0 ± 1.1	2.121 ± 0.778	-0.46	0.54	0.73
$5_{2,4}$-$5_{1,5}$	5.8909	469.9	11	11	2.5	-38.5 ± 1.0	5.0 ± 0.7	1.699 ± 0.272	-0.39	1.07	1.23
$7_{2,5}$-$7_{1,6}$	5.9228	1013.0	45	45	4.4	-38.6 ± 2.0	6.0 ± 1.2	2.978 ± 1.161	-0.28	1.43	1.61
$8_{3,5}$-$8_{2,6}$	5.9246	1413.9	17	17	6.1	-39.0 ± 0.5	4.4 ± 0.5	1.501 ± 0.160	-0.50	0.78	0.98
$7_{3,4}$-$7_{2,5}$	5.9507	1125.5	45	45	6.5	-40.7 ± 1.1	6.0 ± 0.8	3.299 ± 0.593	-0.23	1.50	1.69
$6_{3,3}$-$6_{2,4}$	5.9530	867.1	13	13	6.0	-40.1 ± 1.4	6.0 ± 0.9	3.423 ± 0.873	-0.20	1.17	1.34
$6_{3,3}$-$5_{4,2}$	5.9792	877.7	11	13	0.7	-40.5 ± 1.1	4.8 ± 1.1	1.182 ± 0.279	-0.66	0.26	0.44
$6_{2,4}$-$6_{1,5}$	5.9942	781.0	13	13	5.8	-39.0 ± 3.5	5.0 ± 2.2	1.930 ± 1.324	-0.33	1.24	1.41
$6_{3,4}$-$5_{4,1}$	6.0191	878.0	33	39	0.7	-41.4 ± 1.3	4.5 ± 1.3	1.267 ± 0.376	-0.60	0.71	0.89
$5_{2,3}$-$5_{1,4}$	6.0441	574.6	33	33	7.2	-36.0 ± 3.0	6.0 ± 2.6	3.984 ± 2.146	-0.07	1.94	2.10
$4_{2,2}$-$4_{1,3}$	6.0702	396.3	9	9	7.7	-38.1 ± 1.4	5.0 ± 1.2	2.426 ± 0.641	-0.20	1.57	1.73
$5_{3,2}$-$4_{4,1}$	6.0887	702.1	27	33	0.4	-39.0 ± 3.3	5.0 ± 2.1	1.295 ± 0.652	-0.63	0.52	0.69
$2_{0,2}$-$1_{1,1}$	6.1432	53.4	3	5	3.8	-36.8 ± 2.1	5.0 ± 2.2	1.248 ± 0.622	-0.47	1.34	1.49
$2_{0,2}$-$1_{1,1}$	6.1432	53.4	3	5	3.8	-36.9 ± 1.1	5.0 ± 1.4	1.573 ± 0.482	-0.39	1.34	1.49
$5_{4,1}$-$6_{3,4}$	6.2388	933.6	39	33	0.3	-41.1 ± 2.5	6.0 ± 1.4	1.248 ± 0.566	-0.72	0.33	0.51
$2_{0,2}$-$2_{1,1}$	6.3703	136.9	5	5	11.0	-37.7 ± 1.8	5.0 ± 1.6	3.427 ± 1.193	0.05	1.78	1.92
$3_{1,2}$-$3_{2,1}$	6.4092	305.2	21	21	10.0	-36.6 ± 1.9	5.0 ± 2.3	1.793 ± 1.085	-0.34	2.21	2.36
$6_{4,3}$-$7_{3,4}$	6.4266	1211.7	45	39	0.6	-38.7 ± 0.9	4.3 ± 0.8	0.828 ± 0.184	-0.77	0.43	0.61
$5_{1,4}$-$5_{2,3}$	6.4335	642.3	33	33	11.5	-36.3 ± 0.6	5.3 ± 0.5	2.886 ± 0.330	-0.19	2.16	2.33
$7_{2,5}$-$7_{3,4}$	6.4506	1211.7	45	45	12.5	-40.2 ± 1.0	5.7 ± 1.0	2.926 ± 0.513	-0.28	1.81	2.00
$6_{2,4}$-$6_{3,3}$	6.4531	951.6	13	13	11.3	-39.4 ± 1.0	5.3 ± 0.7	2.284 ± 0.499	-0.37	1.47	1.65
$10_{3,7}$-$10_{4,6}$	6.4691	2325.3	21	21	13.7	-40.4 ± 1.8	5.6 ± 1.5	1.769 ± 0.720	-0.51	0.50	0.73
$8_{2,6}$-$8_{3,5}$	6.4697	1510.7	17	17	12.7	-41.3 ± 2.6	4.9 ± 2.1	1.641 ± 1.004	-0.50	1.13	1.32
$5_{2,3}$-$5_{3,2}$	6.4718	731.9	33	33	9.4	-37.9 ± 1.4	5.0 ± 1.2	2.200 ± 0.667	-0.25	2.00	2.17
$9_{3,6}$-$9_{4,5}$	6.4749	1956.7	57	57	12.7	-39.4 ± 1.4	4.5 ± 1.3	0.814 ± 0.319	-0.81	1.24	1.45
$6_{1,5}$-$6_{2,4}$	6.4788	867.1	13	13	10.6	-40.2 ± 0.8	5.8 ± 0.9	3.028 ± 0.589	-0.27	1.53	1.70

Table D.5: Line Parameters of the $-39.5\ \mathrm{km\,s^{-1}}$ Component in the ν_2=1–0 Transition (4 of 6)

Transition	λ (μm)	E_l (K)	g_l	g_u	A_{ul} ($\mathrm{s^{-1}}$)	v_{LSR} ($\mathrm{km\,s^{-1}}$)	σ_v ($\mathrm{km\,s^{-1}}$)	W_v ($\mathrm{km\,s^{-1}}$)	$\log_{10}(\tau_{p,\mathrm{thin}})$	$\log_{10}(\tau_{p,\mathrm{slab}})$	$\log_{10}(\beta_0)$
$11_{4,7}$-$11_{5,6}$	6.5067	2875.6	69	69	12.5	-39.2 ± 2.9	6.0 ± 1.8	1.922 ± 0.984	-0.50	0.48	0.73
$11_{4,7}$-$11_{5,6}$	6.5067	2875.6	69	69	12.5	-39.2 ± 2.0	6.0 ± 1.9	1.888 ± 0.640	-0.54	0.48	0.73
$9_{2,7}$-$9_{3,6}$	6.5126	1845.5	57	57	12.2	-38.4 ± 0.9	4.9 ± 0.7	1.952 ± 0.397	-0.42	1.33	1.54
$7_{3,4}$-$7_{4,3}$	6.5290	1339.6	45	45	9.5	-39.7 ± 1.0	4.6 ± 1.0	1.805 ± 0.392	-0.42	1.59	1.78
$13_{5,8}$-$13_{6,7}$	6.5392	3965.1	81	81	12.5	-38.2 ± 1.6	5.0 ± 1.7	0.932 ± 0.304	-0.79	-0.45	-0.16
$10_{4,6}$-$10_{5,5}$	6.5401	2481.0	21	21	11.1	-39.2 ± 2.6	6.0 ± 1.7	1.604 ± 0.756	-0.61	0.28	0.51
$3_{2,2}$-$3_{3,1}$	6.5421	410.3	7	7	4.5	-37.2 ± 3.6	6.0 ± 2.9	2.486 ± 1.602	-0.35	1.32	1.48
$3_{2,2}$-$3_{3,1}$	6.5421	410.3	7	7	4.5	-37.9 ± 2.8	5.2 ± 2.5	1.860 ± 1.163	-0.47	1.32	1.48
$7_{1,6}$-$7_{2,5}$	6.5474	1125.5	45	45	9.5	-39.4 ± 1.4	5.3 ± 0.9	2.440 ± 0.684	-0.33	1.79	1.97
$5_{3,3}$-$6_{2,4}$	6.5633	867.1	13	11	1.3	-37.4 ± 2.9	6.0 ± 1.8	2.429 ± 1.262	-0.39	0.56	0.74
$5_{3,3}$-$6_{2,4}$	6.5633	867.1	13	11	1.3	-39.0 ± 0.9	4.5 ± 0.9	1.735 ± 0.332	-0.43	0.56	0.74
$2_{0,2}$-$3_{1,3}$	6.5673	204.7	7	5	9.4	-36.3 ± 3.5	6.0 ± 3.1	1.409 ± 0.911	-0.53	1.69	1.84
$13_{3,10}$-$13_{4,9}$	6.5832	3644.9	81	81	13.2	-40.8 ± 2.5	4.0 ± 2.5	0.409 ± 0.256	-1.07	-0.13	0.15
$6_{3,4}$-$6_{4,3}$	6.6007	1088.6	39	39	7.5	-41.1 ± 1.0	5.5 ± 0.9	2.994 ± 0.539	-0.24	1.67	1.86
$6_{3,4}$-$6_{4,3}$	6.6007	1088.6	39	39	7.5	-39.6 ± 1.4	5.4 ± 0.9	2.727 ± 0.784	-0.27	1.67	1.86
$6_{3,4}$-$6_{4,3}$	6.6007	1088.6	39	39	7.5	-38.7 ± 1.2	5.4 ± 1.1	2.426 ± 0.551	-0.35	1.67	1.86
$10_{4,7}$-$10_{5,6}$	6.6409	2472.4	63	63	10.0	-40.3 ± 1.9	4.0 ± 2.0	0.845 ± 0.410	-0.73	0.74	0.97
$13_{5,9}$-$13_{6,8}$	6.6474	3953.2	27	27	11.4	-39.2 ± 2.3	4.0 ± 2.4	0.179 ± 0.106	-1.44	-0.94	-0.65
$4_{1,4}$-$5_{0,5}$	6.6834	468.0	33	27	8.4	-38.5 ± 3.8	5.0 ± 2.6	1.607 ± 1.016	-0.35	2.15	2.31
$12_{4,9}$-$12_{5,8}$	6.6867	3273.1	75	75	10.9	-43.0 ± 3.2	5.8 ± 3.1	0.646 ± 0.358	-1.03	0.12	0.39
$10_{3,8}$-$10_{4,7}$	6.7052	2274.8	63	63	9.6	-38.9 ± 1.6	5.0 ± 1.3	1.225 ± 0.399	-0.66	0.91	1.14
$10_{3,8}$-$10_{4,7}$	6.7052	2274.8	63	63	9.6	-40.0 ± 0.8	4.2 ± 0.9	1.379 ± 0.275	-0.52	0.91	1.14
$6_{1,6}$-$6_{2,5}$	6.7121	795.4	39	39	4.9	-38.4 ± 3.1	5.0 ± 2.3	1.889 ± 1.056	-0.33	1.78	1.95
$6_{3,4}$-$7_{2,5}$	6.7146	1125.5	45	39	1.9	-39.1 ± 1.1	4.9 ± 1.1	1.191 ± 0.276	-0.66	1.07	1.26
$6_{3,4}$-$7_{2,5}$	6.7146	1125.5	45	39	1.9	-37.9 ± 0.8	4.2 ± 0.7	1.777 ± 0.364	-0.37	1.07	1.26
$8_{2,7}$-$8_{3,6}$	6.7157	1447.3	51	51	7.7	-37.8 ± 1.6	4.0 ± 1.7	1.295 ± 0.529	-0.52	1.49	1.69
$7_{0,7}$-$7_{1,6}$	6.7731	1013.0	45	45	4.7	-40.7 ± 0.8	5.1 ± 0.8	2.620 ± 0.396	-0.28	1.64	1.82

Table D.6: Line Parameters of the $-39.5\ \mathrm{km\,s^{-1}}$ Component in the ν_2=1−0 Transition (5 of 6)

Transition	λ (μm)	E_l (K)	g_l	g_u	A_{ul} ($\mathrm{s^{-1}}$)	v_{LSR} ($\mathrm{km\,s^{-1}}$)	σ_v ($\mathrm{km\,s^{-1}}$)	W_v ($\mathrm{km\,s^{-1}}$)	$\log_{10}(\tau_{p,\mathrm{thin}})$	$\log_{10}(\tau_{p,\mathrm{slab}})$	$\log_{10}(\beta_0)$
$7_{0,7}$-$7_{1,6}$	6.7731	1013.0	45	45	4.7	-40.1 ± 0.9	6.0 ± 0.9	3.302 ± 0.493	-0.23	1.64	1.82
$9_{2,8}$-$9_{3,7}$	6.7826	1749.6	19	19	7.5	-40.1 ± 1.8	4.3 ± 1.8	1.294 ± 0.536	-0.56	0.79	1.00
$5_{0,5}$-$6_{1,6}$	6.7865	643.4	39	33	8.4	-36.2 ± 2.1	6.0 ± 1.7	2.260 ± 0.881	-0.38	2.09	2.26
$7_{1,7}$-$7_{2,6}$	6.7959	1020.8	15	15	4.6	-40.9 ± 1.3	5.6 ± 1.1	2.204 ± 0.480	-0.43	1.15	1.33
$7_{1,7}$-$7_{2,6}$	6.7959	1020.8	15	15	4.6	-39.2 ± 1.0	5.5 ± 0.9	2.330 ± 0.444	-0.38	1.15	1.33
$10_{1,9}$-$10_{2,8}$	6.8251	2068.5	21	21	7.5	-39.4 ± 2.4	6.0 ± 1.4	2.328 ± 0.961	-0.41	0.55	0.77
$10_{1,9}$-$10_{2,8}$	6.8251	2068.5	21	21	7.5	-38.3 ± 1.5	4.0 ± 1.3	1.047 ± 0.496	-0.61	0.55	0.77
$6_{0,6}$-$7_{1,7}$	6.8714	843.7	15	13	8.1	-39.7 ± 1.6	5.6 ± 1.0	2.741 ± 0.915	-0.29	1.51	1.68
$8_{0,8}$-$8_{1,7}$	6.8749	1270.0	17	17	4.4	-38.9 ± 0.9	5.2 ± 0.7	2.034 ± 0.393	-0.41	0.97	1.16
$8_{1,8}$-$8_{2,7}$	6.8867	1273.9	51	51	4.4	-40.2 ± 0.7	6.0 ± 0.6	2.769 ± 0.325	-0.33	1.44	1.63
$5_{1,4}$-$6_{2,5}$	6.9063	795.4	39	33	5.8	-38.0 ± 0.7	5.1 ± 0.6	2.258 ± 0.286	-0.24	1.82	1.99
$7_{1,7}$-$8_{0,8}$	6.9588	1070.3	17	15	7.8	-40.7 ± 0.9	4.9 ± 0.9	1.896 ± 0.356	-0.43	1.36	1.54
$7_{2,6}$-$8_{1,7}$	6.9655	1270.0	17	15	5.7	-39.5 ± 2.4	5.3 ± 2.1	1.423 ± 0.853	-0.61	1.04	1.23
$9_{0,9}$-$9_{1,8}$	6.9774	1552.3	57	57	4.2	-40.9 ± 2.1	5.2 ± 2.0	2.161 ± 0.852	-0.40	1.23	1.43
$9_{1,9}$-$9_{2,8}$	6.9833	1554.1	19	19	4.2	-38.8 ± 1.0	6.0 ± 1.0	1.823 ± 0.325	-0.55	0.75	0.95
$8_{3,6}$-$9_{2,7}$	7.0015	1729.0	57	51	3.4	-39.9 ± 0.7	5.1 ± 0.7	1.720 ± 0.246	-0.50	0.93	1.14
$12_{1,11}$-$12_{2,10}$	7.0134	2819.8	25	25	7.1	-39.0 ± 1.1	4.2 ± 0.9	0.744 ± 0.231	-0.82	-0.06	0.19
$7_{1,6}$-$8_{2,7}$	7.0218	1273.9	51	45	5.9	-39.9 ± 0.8	6.0 ± 0.6	3.742 ± 0.511	-0.15	1.54	1.73
$8_{1,8}$-$9_{0,9}$	7.0547	1323.7	57	51	7.4	-39.9 ± 0.6	5.2 ± 0.5	2.654 ± 0.456	-0.25	1.65	1.85
$8_{1,8}$-$9_{0,9}$	7.0547	1323.7	57	51	7.4	-39.9 ± 0.7	6.0 ± 1.0	2.725 ± 0.580	-0.34	1.65	1.85
$8_{2,7}$-$9_{1,8}$	7.0617	1552.3	57	51	5.8	-39.9 ± 0.3	4.6 ± 0.3	1.718 ± 0.135	-0.44	1.34	1.54
$10_{0,10}$-$10_{1,9}$	7.0818	1860.0	21	21	4.1	-40.4 ± 0.6	6.0 ± 0.8	1.151 ± 0.198	-0.78	0.52	0.73
$10_{1,10}$-$10_{2,9}$	7.0846	1860.9	63	63	4.1	-40.6 ± 1.3	5.9 ± 1.2	1.807 ± 0.485	-0.55	1.00	1.21
$8_{1,7}$-$9_{2,8}$	7.0924	1554.1	19	17	5.9	-40.7 ± 0.8	5.3 ± 0.8	1.525 ± 0.294	-0.58	0.87	1.07
$13_{1,12}$-$13_{2,11}$	7.1065	3232.2	81	81	7.0	-41.1 ± 1.1	5.6 ± 1.0	0.770 ± 0.153	-0.94	0.08	0.34
$5_{2,3}$-$6_{3,4}$	7.1175	933.6	39	33	5.5	-41.5 ± 1.2	5.4 ± 0.9	1.909 ± 0.587	-0.46	1.70	1.88

Table D.7: Line Parameters of the -39.5 km s^{-1} Component in the ν_2=1−0 Transition (6 of 6)

Transition	λ (μm)	E_l (K)	g_l	g_u	A_{ul} (s^{-1})	v_{LSR} (km s^{-1})	σ_v (km s^{-1})	W_v (km s^{-1})	$\log_{10}(\tau_{p,\mathrm{thin}})$	$\log_{10}(\tau_{p,\mathrm{slab}})$	$\log_{10}(\beta_0)$
$9_{3,7}$-$10_{2,8}$	7.1252	2068.5	21	19	4.0	-39.2 ± 1.5	4.3 ± 1.1	0.584 ± 0.260	-0.92	0.28	0.50
$4_{3,1}$-$5_{4,2}$	7.1643	877.7	11	9	10.4	-41.7 ± 0.6	4.0 ± 0.5	1.268 ± 0.272	-0.50	1.48	1.65
$11_{0,11}$-$11_{1,10}$	7.1889	2193.5	69	69	4.0	-40.5 ± 0.3	4.9 ± 0.3	1.310 ± 0.111	-0.62	0.74	0.96
$11_{0,11}$-$11_{1,10}$	7.1889	2193.5	69	69	4.0	-40.3 ± 1.0	6.0 ± 0.6	1.585 ± 0.278	-0.61	0.74	0.96
$11_{1,11}$-$11_{2,10}$	7.1903	2193.9	23	23	4.0	-40.3 ± 2.3	6.0 ± 1.4	0.972 ± 0.410	-0.84	0.26	0.49
$11_{1,11}$-$11_{2,10}$	7.1903	2193.9	23	23	4.0	-41.1 ± 1.1	6.0 ± 1.0	0.919 ± 0.163	-0.88	0.26	0.49
$14_{2,13}$-$14_{3,12}$	7.2028	3670.3	87	87	6.9	-37.1 ± 1.4	4.0 ± 1.4	0.250 ± 0.091	-1.29	-0.28	0.00
$10_{3,8}$-$11_{2,9}$	7.2356	2432.0	69	63	4.3	-38.5 ± 0.8	4.5 ± 0.6	0.725 ± 0.160	-0.84	0.52	0.75
$12_{0,12}$-$12_{1,11}$	7.2995	2552.8	25	25	3.9	-39.3 ± 0.8	4.0 ± 0.9	0.322 ± 0.068	-1.18	-0.02	0.22
$11_{2,10}$-$12_{1,11}$	7.3432	2552.8	25	23	5.6	-41.5 ± 2.9	5.4 ± 2.2	0.429 ± 0.272	-1.18	0.10	0.34
$11_{2,9}$-$12_{3,10}$	7.3945	2823.1	75	69	4.6	-42.4 ± 3.8	6.0 ± 2.0	0.924 ± 0.623	-0.88	0.25	0.50
$3_{0,3}$-$4_{3,2}$	7.4108	550.3	27	21	0.2	-38.7 ± 2.0	5.0 ± 1.9	0.964 ± 0.403	-0.77	0.40	0.56
$12_{3,10}$-$13_{2,11}$	7.4320	3232.2	81	75	4.5	-40.3 ± 1.6	6.0 ± 1.2	1.300 ± 0.355	-0.71	-0.09	0.18
$12_{2,11}$-$13_{1,12}$	7.4401	2937.9	81	75	5.4	-39.0 ± 2.9	6.0 ± 2.7	0.798 ± 0.398	-0.94	0.26	0.51
$8_{3,5}$-$9_{4,6}$	7.5193	1928.9	19	17	4.4	-39.5 ± 0.7	4.0 ± 0.8	0.622 ± 0.138	-0.88	0.47	0.69
$7_{4,3}$-$8_{5,4}$	7.5932	1805.6	51	45	7.5	-39.9 ± 0.2	4.0 ± 0.3	0.798 ± 0.072	-0.76	1.25	1.47
$9_{5,4}$-$10_{6,5}$	7.8984	2697.2	63	57	7.1	-36.0 ± 3.4	6.0 ± 2.6	1.093 ± 0.674	-0.78	0.56	0.81

Table D.8: Line Parameters of the -54.5 km s^{-1} Component in the ν_2=1–0 Transition (1 of 3)

Transition	λ (μm)	E_l (K)	g_l	g_u	A_{ul} (s^{-1})	v_{LSR} (km s^{-1})	σ_v (km s^{-1})	W_v (km s^{-1})	$\log_{10}(\tau_{p,\mathrm{thin}})$	$\log_{10}(\tau_{p,\mathrm{slab}})$	$\log_{10}(\beta_0)$
$11_{2,10}$-$10_{1,9}$	5.4248	1860.0	21	23	10.2	-55.9 ± 1.0	5.4 ± 1.2	0.915 ± 0.284	-0.78	0.00	0.19
$11_{6,5}$-$11_{5,6}$	5.4521	2875.6	69	69	2.4	-54.2 ± 1.7	5.0 ± 1.4	0.406 ± 0.120	-1.17	-0.97	-0.68
$10_{1,9}$-$9_{2,8}$	5.4862	1554.1	19	21	9.5	-53.7 ± 1.3	5.0 ± 1.5	0.920 ± 0.305	-0.78	0.19	0.36
$9_{2,7}$-$8_{3,6}$	5.5179	1447.3	51	57	4.6	-54.2 ± 1.1	5.0 ± 1.2	1.040 ± 0.290	-0.73	0.40	0.55
$9_{1,8}$-$8_{2,7}$	5.5479	1273.9	51	57	8.7	-54.0 ± 1.4	5.0 ± 1.5	0.729 ± 0.272	-0.87	0.82	0.96
$10_{5,6}$-$10_{4,7}$	5.5496	2274.8	63	63	2.7	-54.7 ± 2.0	5.0 ± 2.4	0.389 ± 0.197	-1.19	-0.44	-0.20
$6_{5,1}$-$6_{4,2}$	5.5707	1090.1	13	13	1.8	-54.9 ± 2.4	5.0 ± 2.8	0.511 ± 0.351	-1.04	-0.36	-0.23
$8_{2,7}$-$7_{1,6}$	5.5836	1013.0	45	51	7.9	-55.4 ± 3.2	7.0 ± 3.1	1.700 ± 1.081	-0.62	0.95	1.07
$3_{3,1}$-$2_{2,0}$	5.6456	195.9	5	7	5.8	-54.5	7.5 ± 1.7	1.391 ± 0.270	-0.74	0.62	0.67
$6_{2,5}$-$5_{1,4}$	5.6759	574.6	33	39	5.9	-54.5	9.0 ± 2.5	1.366 ± 0.419	-0.85	1.08	1.16
$9_{3,7}$-$9_{2,8}$	5.6784	1554.1	19	19	2.3	-56.3 ± 2.4	5.0 ± 2.6	0.386 ± 0.220	-1.20	-0.42	-0.25
$8_{4,5}$-$8_{3,6}$	5.6864	1447.3	51	51	3.1	-53.1 ± 2.2	5.4 ± 2.2	0.597 ± 0.348	-0.96	0.22	0.38
$7_{1,6}$-$6_{2,5}$	5.6921	795.4	39	45	6.6	-54.5	7.0 ± 3.0	0.872 ± 0.393	-0.89	1.01	1.11
$6_{4,3}$-$6_{3,4}$	5.7162	933.6	39	39	2.9	-54.3 ± 3.0	7.0 ± 2.4	0.916 ± 0.431	-0.89	0.49	0.60
$5_{2,4}$-$4_{1,3}$	5.7187	396.3	9	11	5.2	-54.5	8.4 ± 2.0	1.295 ± 0.313	-0.83	0.62	0.69
$4_{4,0}$-$4_{3,1}$	5.7281	552.2	9	9	1.6	-54.5	7.0 ± 4.5	0.649 ± 0.447	-1.04	-0.09	-0.01
$8_{3,6}$-$8_{2,7}$	5.7320	1273.9	51	51	2.7	-54.1 ± 0.9	5.6 ± 1.1	0.928 ± 0.195	-0.83	0.31	0.45
$3_{2,1}$-$2_{1,2}$	5.7477	114.4	15	21	2.7	-54.5	8.3 ± 2.3	3.022 ± 1.125	-0.44	0.86	0.90
$7_{2,6}$-$7_{1,7}$	5.7735	843.7	15	15	1.7	-53.8 ± 1.9	5.0 ± 1.9	0.942 ± 0.491	-0.75	-0.07	0.03
$10_{3,7}$-$10_{2,8}$	5.7995	2068.5	21	21	4.1	-52.4 ± 2.8	7.0 ± 3.9	0.664 ± 0.440	-1.10	-0.52	-0.30
$7_{1,6}$-$7_{0,7}$	5.8022	843.3	45	45	1.8	-54.3 ± 2.5	5.0 ± 2.9	0.619 ± 0.421	-0.95	0.43	0.53
$8_{4,4}$-$8_{3,5}$	5.8088	1510.7	17	17	4.5	-50.6 ± 2.4	5.1 ± 2.1	0.732 ± 0.411	-0.88	-0.12	0.05
$6_{3,4}$-$6_{2,5}$	5.8180	795.4	39	39	3.4	-54.5	7.0 ± 3.9	0.817 ± 0.401	-0.99	0.69	0.79
$6_{1,6}$-$5_{0,5}$	5.8227	468.0	33	39	10.8	-54.5	7.0 ± 2.3	2.237 ± 0.790	-0.45	1.46	1.53
$9_{4,5}$-$9_{3,6}$	5.8280	1845.5	57	57	5.2	-53.3 ± 1.6	5.3 ± 1.9	0.744 ± 0.302	-0.91	0.21	0.40
$6_{2,5}$-$6_{1,6}$	5.8342	643.4	39	39	2.1	-54.5	7.0 ± 3.1	1.043 ± 0.498	-0.83	0.60	0.69
$2_{2,0}$-$1_{1,1}$	5.8605	53.4	3	5	5.0	-54.5	7.0 ± 2.5	1.300 ± 0.496	-0.65	0.57	0.60

Table D.9: Line Parameters of the -54.5 $\mathrm{km\,s^{-1}}$ Component in the ν_2=1−0 Transition (2 of 3)

Transition	λ (μm)	E_l (K)	g_l	g_u	A_{ul} ($\mathrm{s^{-1}}$)	v_{LSR} ($\mathrm{km\,s^{-1}}$)	σ_v ($\mathrm{km\,s^{-1}}$)	W_v ($\mathrm{km\,s^{-1}}$)	$\log_{10}(\tau_{p,\mathrm{thin}})$	$\log_{10}(\tau_{p,\mathrm{slab}})$	$\log_{10}(\beta_0)$
$4_{3,2}$-$4_{2,3}$	5.8670	432.1	27	27	3.2	-54.5	9.0 ± 4.7	1.226 ± 0.710	-0.82	0.81	0.88
$3_{3,1}$-$3_{2,2}$	5.8784	296.8	7	7	2.3	-54.5	7.0 ± 3.1	1.106 ± 0.542	-0.83	0.20	0.25
$8_{3,5}$-$8_{2,6}$	5.9246	1413.9	17	17	6.1	-53.5 ± 1.7	5.0 ± 2.1	0.440 ± 0.192	-1.13	0.12	0.27
$5_{1,4}$-$5_{0,5}$	5.9683	468.0	33	33	3.0	-54.5	9.0 ± 1.9	2.356 ± 0.547	-0.61	0.87	0.94
$4_{2,2}$-$4_{1,3}$	6.0702	396.3	9	9	7.7	-54.5	7.0 ± 4.6	0.620 ± 0.371	-0.95	0.79	0.85
$3_{1,2}$-$3_{0,3}$	6.1138	196.7	21	21	6.4	-54.5	8.0 ± 4.2	1.761 ± 0.773	-0.62	1.24	1.29
$2_{0,2}$-$1_{1,1}$	6.1432	53.4	3	5	3.8	-54.5	7.0 ± 2.7	1.598 ± 0.562	-0.57	0.51	0.54
$2_{0,2}$-$1_{1,1}$	6.1432	53.4	3	5	3.8	-54.5	7.6 ± 1.4	2.053 ± 0.374	-0.53	0.51	0.54
$4_{2,3}$-$3_{3,0}$	6.1630	410.6	21	27	0.4	-54.5	7.0 ± 1.5	1.204 ± 0.250	-0.80	0.04	0.10
$2_{0,2}$-$2_{1,1}$	6.3703	136.9	5	5	11.0	-54.5	7.2 ± 1.9	3.438 ± 0.785	-0.24	0.96	1.00
$5_{1,4}$-$5_{2,3}$	6.4335	642.3	33	33	11.5	-54.5	7.0 ± 1.2	1.904 ± 0.374	-0.57	1.41	1.49
$7_{2,5}$-$7_{3,4}$	6.4506	1211.7	45	45	12.5	-55.2 ± 2.9	5.0 ± 2.9	0.686 ± 0.460	-0.88	1.12	1.26
$10_{3,7}$-$10_{4,6}$	6.4691	2325.3	21	21	13.7	-55.9 ± 3.1	7.0 ± 3.1	1.263 ± 0.660	-0.79	-0.06	0.18
$5_{2,3}$-$5_{3,2}$	6.4718	731.9	33	33	9.4	-54.5	9.0 ± 4.0	3.102 ± 1.955	-0.47	1.25	1.35
$2_{1,2}$-$3_{0,3}$	6.4922	196.7	21	15	7.2	-54.5	7.0 ± 1.5	3.454 ± 0.637	-0.21	1.23	1.27
$13_{3,10}$-$13_{4,9}$	6.5832	3644.9	81	81	13.2	-50.5 ± 6.1	5.0 ± 2.6	1.100 ± 0.626	-0.71	-0.52	-0.16
$13_{5,9}$-$13_{6,8}$	6.6474	3953.2	27	27	11.4	-54.7 ± 3.5	5.0 ± 3.0	0.238 ± 0.153	-1.41	-1.30	-0.91
$4_{1,4}$-$5_{0,5}$	6.6834	468.0	33	27	8.4	-54.5	7.0 ± 2.6	1.375 ± 0.456	-0.67	1.37	1.44
$12_{4,9}$-$12_{5,8}$	6.6867	3273.1	75	75	10.9	-58.5 ± 4.0	5.0 ± 2.3	0.828 ± 0.504	-0.84	-0.32	0.01
$10_{3,8}$-$10_{4,7}$	6.7052	2274.8	63	63	9.6	-53.4 ± 2.9	5.7 ± 3.1	0.662 ± 0.395	-1.00	0.35	0.59
$7_{0,7}$-$7_{1,6}$	6.7731	1013.0	45	45	4.7	-55.4 ± 2.0	5.0 ± 2.5	0.840 ± 0.477	-0.82	0.92	1.04
$7_{0,7}$-$7_{1,6}$	6.7731	1013.0	45	45	4.7	-55.6 ± 2.0	5.0 ± 2.5	0.891 ± 0.542	-0.77	0.92	1.04
$8_{0,8}$-$8_{1,7}$	6.8749	1270.0	17	17	4.4	-54.4 ± 1.6	7.0 ± 1.7	1.532 ± 0.405	-0.71	0.29	0.43
$5_{1,4}$-$6_{2,5}$	6.9063	795.4	39	33	5.8	-54.5	7.9 ± 2.3	1.294 ± 0.458	-0.75	1.08	1.17
$7_{1,7}$-$8_{0,8}$	6.9588	1070.3	17	15	7.8	-55.5 ± 2.1	5.0 ± 2.8	0.769 ± 0.487	-0.87	0.65	0.77
$9_{1,9}$-$9_{2,8}$	6.9833	1554.1	19	19	4.2	-53.8 ± 1.9	5.0 ± 2.1	0.592 ± 0.320	-0.95	0.11	0.27
$3_{2,2}$-$4_{3,1}$	6.9933	552.2	9	7	8.6	-54.5	9.0 ± 2.2	2.657 ± 0.710	-0.56	0.78	0.86
$8_{3,6}$-$9_{2,7}$	7.0015	1729.0	57	51	3.4	-54.4 ± 2.0	5.0 ± 2.4	0.526 ± 0.279	-1.03	0.31	0.49

Table D.10: Line Parameters of the -54.5 km s^{-1} Component in the ν_2=1–0 Transition (3 of 3)

Transition	λ (μm)	E_l (K)	g_l	g_u	A_{ul} (s^{-1})	v_{LSR} (km s^{-1})	σ_v (km s^{-1})	W_v (km s^{-1})	$\log_{10}(\tau_{p,\mathrm{thin}})$	$\log_{10}(\tau_{p,\mathrm{slab}})$	$\log_{10}(\beta_0)$
$7_{1,6}$-$8_{2,7}$	7.0218	1273.9	51	45	5.9	-54.4 $\pm$ 1.6	5.6 $\pm$ 1.6	1.247 $\pm$ 0.494	-0.64	0.86	1.00
$3_{3,0}$-$4_{4,1}$	7.0447	702.1	27	21	14.2	-54.5	7.0 $\pm$ 4.1	1.312 $\pm$ 0.851	-0.75	1.37	1.46
$4_{2,3}$-$5_{3,2}$	7.1469	731.9	33	27	5.6	-54.5	7.0 $\pm$ 2.3	1.287 $\pm$ 0.424	-0.72	1.07	1.17
$11_{0,11}$-$11_{1,10}$	7.1889	2193.5	69	69	4.0	-54.8 $\pm$ 2.1	6.5 $\pm$ 2.4	0.656 $\pm$ 0.358	-1.02	0.17	0.39
$14_{2,13}$-$14_{3,12}$	7.2028	3670.3	87	87	6.9	-51.6 $\pm$ 2.5	5.0 $\pm$ 2.7	0.207 $\pm$ 0.110	-1.47	-0.67	-0.31
$10_{3,8}$-$11_{2,9}$	7.2356	2432.0	69	63	4.3	-53.0 $\pm$ 2.0	7.0 $\pm$ 2.9	0.519 $\pm$ 0.251	-1.21	-0.02	0.23
$12_{3,10}$-$13_{2,11}$	7.4320	3232.2	81	75	4.5	-54.8 $\pm$ 2.9	5.8 $\pm$ 2.7	0.527 $\pm$ 0.347	-1.07	-0.53	-0.21
$9_{5,4}$-$10_{6,5}$	7.8984	2697.2	63	57	7.1	-50.5 $\pm$ 3.6	5.9 $\pm$ 2.5	1.088 $\pm$ 0.658	-0.78	0.05	0.33

Table D.11: Line Parameters of the -45 km s^{-1} Component in the ν_2=1–0 Transition

Transition	λ (μm)	E_l (K)	g_l	g_u	A_{ul} (s^{-1})	v_{LSR} (km s^{-1})	σ_v (km s^{-1})	W_v (km s^{-1})	$\log_{10}(\tau_{p,\mathrm{thin}})$
$7_{1,6}$-$6_{2,5}$	5.6921	795.4	39	45	6.6	-45	5.0 ± 2.5	0.717 ± 0.419	-0.25
$6_{0,6}$-$5_{1,5}$	5.8304	469.9	11	13	10.8	-45	4.7 ± 1.8	1.244 ± 0.661	-0.20
$4_{3,2}$-$4_{2,3}$	5.8670	432.1	27	27	3.2	-45	5.0 ± 1.8	1.165 ± 0.434	-0.26
$5_{2,4}$-$5_{1,5}$	5.8909	469.9	11	11	2.5	-45	5.0 ± 1.5	0.893 ± 0.263	-0.39
$4_{2,2}$-$4_{1,3}$	6.0702	396.3	9	9	7.7	-45	5.0 ± 2.4	1.297 ± 0.618	-0.20
$2_{0,2}$-$1_{1,1}$	6.1432	53.4	3	5	3.8	-45	5.0 ± 1.9	2.000 ± 0.786	-0.47
$2_{0,2}$-$1_{1,1}$	6.1432	53.4	3	5	3.8	-45	4.6 ± 0.8	2.000 ± 0.428	-0.39
$2_{0,2}$-$2_{1,1}$	6.3703	136.9	5	5	11.0	-45	5.0 ± 3.3	1.948 ± 1.328	0.05
$3_{1,2}$-$3_{2,1}$	6.4092	305.2	21	21	10.0	-45	4.3 ± 1.6	1.667 ± 0.824	-0.34
$5_{1,4}$-$5_{2,3}$	6.4335	642.3	33	33	11.5	-45	4.0 ± 0.5	1.665 ± 0.331	-0.19
$2_{0,2}$-$3_{1,3}$	6.5673	204.7	7	5	9.4	-45	5.0 ± 1.5	1.940 ± 0.927	-0.53
$5_{0,5}$-$6_{1,6}$	6.7865	643.4	39	33	8.4	-45	4.7 ± 1.5	1.394 ± 0.809	-0.38
$5_{1,4}$-$6_{2,5}$	6.9063	795.4	39	33	5.8	-45	4.9 ± 0.9	1.218 ± 0.283	-0.24

Table D.12: Line Parameters of the -39.5 km s^{-1} Component in the ν_2=2−1 Transition (1 of 3)

Transition	λ (μm)	E_l (K)	g_l	g_u	A_{ul} (s^{-1})	v_{LSR} (km s^{-1})	σ_v (km s^{-1})	W_v (km s^{-1})	$\log_{10}(\tau_{p,\rm thin})$	$\log_{10}(\tau_{p,\rm slab})$	$\log_{10}(\beta_0)$
$4_{4,1}$-$3_{3,0}$	5.4373	2744.1	21	27	9.8	-38.7 ± 1.5	4.8 ± 1.2	0.798 ± 0.453	-0.85	-1.62	-1.15
$5_{3,2}$-$4_{2,3}$	5.5105	2744.7	27	33	6.1	-37.6 ± 4.8	6.0 ± 2.8	0.834 ± 0.769	-0.92	-1.72	-1.25
$4_{3,2}$-$3_{2,1}$	5.6226	2617.1	21	27	8.6	-41.3 ± 2.7	4.4 ± 2.7	0.522 ± 0.758	-1.00	-1.54	-1.08
$9_{2,8}$-$8_{1,7}$	5.6247	3582.4	17	19	16.1	-38.2 ± 3.5	4.0 ± 3.8	0.245 ± 0.419	-1.30	-2.07	-1.57
$11_{0,11}$-$10_{1,10}$	5.6670	3891.4	63	69	27.6	-36.0 ± 2.2	5.5 ± 1.6	0.917 ± 0.415	-0.82	-1.47	-0.96
$11_{0,11}$-$10_{1,10}$	5.6670	3891.4	63	69	27.6	-40.2 ± 3.1	5.2 ± 2.0	0.964 ± 0.624	-0.77	-1.47	-0.96
$6_{2,5}$-$5_{1,4}$	5.7627	2878.3	33	39	10.9	-38.5 ± 3.8	6.0 ± 2.2	1.074 ± 0.789	-0.78	-1.43	-0.96
$9_{1,9}$-$8_{0,8}$	5.7754	3362.5	17	19	25.2	-37.4 ± 1.5	4.6 ± 1.2	0.773 ± 0.325	-0.81	-1.69	-1.20
$9_{0,9}$-$8_{1,8}$	5.7769	3362.7	51	57	25.2	-39.9 ± 2.8	5.0 ± 2.7	0.799 ± 1.265	-0.87	-1.22	-0.73
$8_{3,6}$-$8_{2,7}$	5.7823	3589.3	51	51	5.3	-40.2 ± 10.6	6.0 ± 5.9	1.069 ± 2.074	-0.79	-2.09	-1.60
$7_{4,3}$-$7_{3,4}$	5.7954	3542.9	45	45	6.4	-40.5 ± 2.2	4.2 ± 1.9	0.607 ± 0.413	-0.91	-2.03	-1.53
$8_{1,8}$-$7_{0,7}$	5.8322	3136.9	45	51	23.9	-38.5 ± 2.2	4.9 ± 1.5	0.731 ± 0.330	-0.87	-1.12	-0.65
$4_{2,3}$-$3_{1,2}$	5.8491	2549.6	21	27	9.1	-40.0 ± 1.4	4.1 ± 1.2	0.928 ± 0.518	-0.68	-1.42	-0.97
$4_{2,3}$-$3_{1,2}$	5.8491	2549.6	21	27	9.1	-40.0 ± 1.4	4.1 ± 1.2	0.928 ± 0.518	-0.68	-1.42	-0.97
$3_{2,2}$-$2_{1,1}$	5.9031	2436.3	5	7	9.5	-36.0 ± 3.5	6.0 ± 2.5	0.734 ± 0.704	-0.96	-1.91	-1.45
$6_{2,5}$-$6_{1,6}$	5.9052	2938.5	39	39	4.2	-37.8 ± 2.1	4.0 ± 1.9	0.378 ± 0.233	-1.09	-1.85	-1.38
$6_{1,6}$-$5_{0,5}$	5.9485	2763.0	33	39	20.7	-36.9 ± 1.1	4.8 ± 0.9	1.196 ± 0.357	-0.63	-1.03	-0.56
$6_{0,6}$-$5_{1,5}$	5.9622	2766.0	11	13	20.6	-39.2 ± 3.2	5.1 ± 2.2	0.755 ± 0.575	-0.90	-1.51	-1.04
$6_{0,6}$-$5_{1,5}$	5.9622	2766.0	11	13	20.6	-39.2 ± 3.2	5.1 ± 2.2	0.755 ± 0.575	-0.90	-1.51	-1.04
$5_{3,2}$-$5_{2,3}$	5.9925	2954.6	33	33	8.7	-38.3 ± 1.8	4.1 ± 1.9	1.071 ± 1.109	-0.63	-1.60	-1.12
$5_{1,5}$-$4_{0,4}$	6.0059	2614.4	9	11	18.8	-39.2 ± 1.5	4.0 ± 1.7	0.561 ± 0.514	-0.84	-1.51	-1.05
$4_{2,3}$-$4_{1,4}$	6.0224	2620.4	27	27	5.9	-36.0 ± 13.3	6.0 ± 7.7	0.836 ± 2.400	-0.86	-1.62	-1.16
$4_{2,3}$-$4_{1,4}$	6.0224	2620.4	27	27	5.9	-39.8 ± 5.2	6.0 ± 2.8	1.412 ± 1.355	-0.65	-1.62	-1.16
$7_{3,4}$-$7_{2,5}$	6.0232	3441.8	45	45	11.7	-36.0 ± 2.5	4.0 ± 2.6	0.420 ± 0.590	-1.06	-1.65	-1.16
$4_{1,4}$-$3_{0,3}$	6.0613	2491.3	21	27	16.6	-39.4 ± 0.9	4.5 ± 0.6	1.029 ± 0.240	-0.66	-1.08	-0.62
$5_{1,4}$-$5_{0,5}$	6.0802	2763.0	33	33	6.4	-37.0 ± 2.6	5.6 ± 1.8	1.155 ± 1.166	-0.72	-1.58	-1.11
$2_{2,1}$-$2_{1,2}$	6.1010	2412.5	15	15	5.9	-37.8 ± 1.8	4.4 ± 1.4	0.453 ± 0.198	-1.05	-1.72	-1.27
$5_{2,3}$-$5_{1,4}$	6.1498	2878.3	33	33	14.1	-39.6 ± 9.1	4.9 ± 6.3	0.848 ± 1.920	-0.83	-1.30	-0.83

Table D.13: Line Parameters of the -39.5 km s^{-1} Component in the ν_2=2−1 Transition (2 of 3)

Transition	λ (μm)	E_l (K)	g_l	g_u	A_{ul} (s^{-1})	v_{LSR} (km s^{-1})	σ_v (km s^{-1})	W_v (km s^{-1})	$\log_{10}(\tau_{p,\mathrm{thin}})$	$\log_{10}(\tau_{p,\mathrm{slab}})$	$\log_{10}(\beta_0)$
$4_{1,3}$-$4_{0,4}$	6.1686	2614.4	9	9	9.2	-38.0 ± 3.4	4.0 ± 4.0	0.283 ± 0.574	-1.22	-1.87	-1.41
$3_{2,1}$-$3_{1,2}$	6.1716	2549.6	21	21	12.5	-38.3 ± 2.3	4.0 ± 2.8	0.707 ± 1.232	-0.82	-1.33	-0.87
$2_{1,2}$-$1_{0,1}$	6.1753	2328.3	9	15	13.9	-40.9 ± 1.4	4.8 ± 1.0	1.201 ± 0.445	-0.65	-1.28	-0.83
$2_{1,2}$-$1_{0,1}$	6.1753	2328.3	9	15	13.9	-39.2 ± 1.7	5.3 ± 1.3	1.330 ± 0.846	-0.61	-1.28	-0.83
$3_{0,3}$-$2_{1,2}$	6.2028	2412.5	15	21	11.8	-39.0 ± 4.4	6.0 ± 2.5	2.244 ± 3.339	-0.40	-1.25	-0.80
$3_{1,2}$-$3_{0,3}$	6.2394	2491.3	21	21	13.2	-38.6 ± 1.6	4.2 ± 1.9	0.752 ± 0.762	-0.78	-1.25	-0.79
$2_{1,1}$-$2_{0,2}$	6.2878	2395.1	5	5	17.7	-40.2 ± 4.9	6.0 ± 3.3	1.391 ± 1.488	-0.67	-1.67	-1.22
$2_{1,1}$-$2_{0,2}$	6.2878	2395.1	5	5	17.7	-40.5 ± 1.4	4.0 ± 1.2	0.951 ± 0.389	-0.68	-1.67	-1.22
$1_{1,0}$-$1_{0,1}$	6.3157	2328.3	9	9	21.3	-39.4 ± 2.6	4.0 ± 2.4	0.401 ± 0.304	-1.07	-1.29	-0.84
$1_{1,0}$-$1_{0,1}$	6.3157	2328.3	9	9	21.3	-39.2 ± 2.7	5.6 ± 1.9	1.466 ± 0.783	-0.61	-1.29	-0.84
$1_{0,1}$-$1_{1,0}$	6.5149	2359.9	9	9	24.9	-38.5 ± 3.3	4.0 ± 4.0	0.492 ± 1.091	-0.97	-1.20	-0.75
$3_{1,2}$-$3_{2,1}$	6.5994	2617.1	21	21	19.1	-39.5 ± 5.3	6.0 ± 3.2	1.620 ± 1.494	-0.56	-1.10	-0.64
$3_{1,2}$-$3_{2,1}$	6.5994	2617.1	21	21	19.1	-38.1 ± 3.1	4.0 ± 2.7	0.700 ± 0.612	-0.77	-1.10	-0.64
$5_{1,4}$-$5_{2,3}$	6.6160	2954.6	33	33	23.3	-38.5 ± 1.2	4.2 ± 1.0	1.106 ± 0.410	-0.60	-1.04	-0.57
$2_{1,2}$-$3_{0,3}$	6.6400	2491.3	21	15	13.5	-37.5 ± 2.7	4.2 ± 3.1	0.772 ± 1.195	-0.79	-1.31	-0.85
$7_{2,5}$-$7_{3,4}$	6.6462	3542.9	45	45	24.3	-37.5 ± 6.2	6.0 ± 5.3	0.816 ± 1.350	-0.92	-1.27	-0.78
$7_{2,5}$-$7_{3,4}$	6.6462	3542.9	45	45	24.3	-36.0 ± 6.6	6.0 ± 4.0	0.944 ± 1.256	-0.86	-1.27	-0.78
$6_{2,4}$-$6_{3,3}$	6.6574	3283.5	13	13	21.5	-40.0 ± 15.1	6.0 ± 12.7	0.777 ± 3.196	-0.95	-1.69	-1.20
$4_{0,4}$-$4_{1,3}$	6.6674	2697.9	9	9	15.1	-38.4 ± 6.1	5.6 ± 4.2	1.314 ± 2.654	-0.68	-1.61	-1.15
$4_{2,2}$-$4_{3,1}$	6.7113	2885.5	9	9	13.9	-42.1 ± 8.3	4.0 ± 8.1	0.184 ± 0.706	-1.42	-1.76	-1.29
$7_{1,6}$-$7_{2,5}$	6.7261	3441.8	45	45	20.3	-38.9 ± 2.6	4.0 ± 2.7	0.735 ± 0.963	-0.80	-1.27	-0.78
$3_{2,1}$-$3_{3,0}$	6.7334	2744.1	21	21	9.1	-38.6 ± 2.6	4.5 ± 2.4	0.664 ± 0.747	-0.85	-1.48	-1.01
$2_{0,2}$-$3_{1,3}$	6.7455	2502.3	7	5	18.4	-37.7 ± 2.5	4.0 ± 2.2	0.804 ± 0.686	-0.72	-1.63	-1.18
$7_{3,4}$-$7_{4,3}$	6.7536	3700.0	45	45	18.0	-36.0 ± 4.0	4.0 ± 3.8	0.242 ± 0.294	-1.26	-1.49	-0.99
$5_{0,5}$-$5_{1,4}$	6.7653	2878.3	33	33	12.5	-38.5 ± 5.0	6.0 ± 2.9	1.328 ± 2.289	-0.71	-1.23	-0.76
$4_{2,3}$-$4_{3,2}$	6.7693	2883.9	27	27	12.6	-38.7 ± 7.1	6.0 ± 4.0	0.807 ± 1.654	-0.94	-1.32	-0.84
$6_{3,3}$-$6_{4,2}$	6.7814	3451.2	13	13	15.2	-36.0 ± 2.3	4.0 ± 2.2	0.371 ± 0.259	-1.09	-1.93	-1.44
$4_{1,4}$-$4_{2,3}$	6.7857	2744.7	27	27	11.1	-37.0 ± 1.8	4.2 ± 1.8	0.706 ± 0.467	-0.82	-1.27	-0.81

Table D.14: Line Parameters of the -39.5 km s^{-1} Component in the ν_2=2−1 Transition (3 of 3)

Transition	λ (μm)	E_l (K)	g_l	g_u	A_{ul} (s^{-1})	v_{LSR} (km s^{-1})	σ_v (km s^{-1})	W_v (km s^{-1})	$\log_{10}(\tau_{p,\text{thin}})$	$\log_{10}(\tau_{p,\text{slab}})$	$\log_{10}(\beta_0)$
$5_{3,2}$-$5_{4,1}$	6.7987	3239.3	33	33	12.1	-37.6 $\pm$ 6.5	6.0 $\pm$ 3.8	0.631 $\pm$ 0.800	-1.05	-1.48	-1.00
$9_{4,5}$-$9_{5,4}$	6.7993	4518.4	57	57	18.6	-36.9 $\pm$ 6.5	4.0 $\pm$ 4.4	0.226 $\pm$ 0.472	-1.33	-1.90	-1.37
$3_{0,3}$-$4_{1,4}$	6.8136	2620.4	27	21	17.1	-39.9 $\pm$ 4.3	5.7 $\pm$ 3.3	1.212 $\pm$ 1.305	-0.73	-1.11	-0.65
$3_{0,3}$-$4_{1,4}$	6.8136	2620.4	27	21	17.1	-39.8 $\pm$ 2.7	5.1 $\pm$ 2.3	1.127 $\pm$ 1.512	-0.67	-1.11	-0.65
$3_{0,3}$-$4_{1,4}$	6.8136	2620.4	27	21	17.1	-38.9 $\pm$ 2.2	4.6 $\pm$ 2.0	0.752 $\pm$ 0.697	-0.85	-1.11	-0.65
$8_{1,7}$-$8_{2,6}$	6.8165	3734.1	17	17	18.4	-36.0 $\pm$ 11.6	6.0 $\pm$ 7.6	0.584 $\pm$ 2.375	-1.03	-1.91	-1.41
$6_{3,4}$-$6_{4,3}$	6.8186	3450.1	39	39	14.6	-37.8 $\pm$ 2.0	4.0 $\pm$ 2.2	0.557 $\pm$ 0.573	-0.93	-1.46	-0.97
$7_{4,3}$-$7_{5,2}$	6.8295	3918.7	45	45	14.0	-40.0 $\pm$ 8.2	6.0 $\pm$ 4.5	1.023 $\pm$ 1.577	-0.81	-1.73	-1.22
$9_{5,4}$-$9_{6,3}$	6.8322	4777.3	57	57	15.4	-36.0 $\pm$ 7.3	6.0 $\pm$ 4.4	0.778 $\pm$ 1.125	-0.91	-2.15	-1.61
$8_{4,5}$-$8_{5,4}$	6.8395	4199.9	51	51	16.1	-37.3 $\pm$ 6.7	6.0 $\pm$ 5.6	0.763 $\pm$ 1.414	-0.95	-1.79	-1.28
$4_{1,4}$-$5_{0,5}$	6.8449	2763.0	33	27	16.0	-39.3 $\pm$ 1.4	5.1 $\pm$ 1.0	1.416 $\pm$ 0.458	-0.58	-1.12	-0.65
$8_{3,6}$-$8_{4,5}$	6.8498	3977.0	51	51	17.9	-36.2 $\pm$ 3.3	4.0 $\pm$ 3.5	0.700 $\pm$ 1.130	-0.77	-1.60	-1.09
$1_{1,0}$-$2_{2,1}$	6.8512	2506.3	15	9	26.0	-43.0 $\pm$ 3.0	6.0 $\pm$ 2.1	1.328 $\pm$ 1.317	-0.62	-1.21	-0.76
$6_{0,6}$-$6_{1,5}$	6.8786	3087.4	13	13	10.9	-39.5 $\pm$ 7.4	5.7 $\pm$ 5.8	0.535 $\pm$ 1.451	-1.10	-1.81	-1.33
$1_{1,1}$-$2_{2,0}$	6.8842	2508.0	5	3	22.5	-41.0 $\pm$ 3.0	4.4 $\pm$ 2.7	0.565 $\pm$ 0.737	-0.91	-1.75	-1.29
$4_{0,4}$-$5_{1,5}$	6.8848	2766.0	11	9	16.6	-40.1 $\pm$ 3.0	5.1 $\pm$ 2.4	1.367 $\pm$ 1.654	-0.62	-1.57	-1.11
$3_{1,2}$-$4_{2,3}$	7.0096	2744.7	27	21	13.1	-38.2 $\pm$ 1.1	4.0 $\pm$ 1.3	0.857 $\pm$ 0.508	-0.66	-1.27	-0.80
$6_{1,6}$-$7_{0,7}$	7.0362	3136.9	45	39	15.6	-39.3 $\pm$ 3.4	6.0 $\pm$ 2.0	1.127 $\pm$ 1.117	-0.70	-1.18	-0.70
$3_{2,1}$-$4_{3,2}$	7.2050	2883.9	27	21	18.3	-39.0 $\pm$ 4.0	5.5 $\pm$ 2.9	0.642 $\pm$ 1.039	-1.01	-1.18	-0.71
$7_{1,6}$-$8_{2,7}$	7.2245	3589.3	51	45	11.1	-38.8 $\pm$ 1.7	5.1 $\pm$ 1.4	0.402 $\pm$ 0.307	-1.18	-1.53	-1.04
$8_{0,8}$-$9_{1,9}$	7.2337	3614.1	19	17	14.5	-39.0 $\pm$ 1.1	5.0 $\pm$ 0.8	0.387 $\pm$ 0.155	-1.11	-1.85	-1.36
$3_{2,2}$-$4_{3,1}$	7.2371	2885.5	9	7	17.5	-38.9 $\pm$ 1.1	6.0 $\pm$ 0.7	0.602 $\pm$ 0.121	-1.07	-1.67	-1.20
$3_{2,2}$-$4_{3,1}$	7.2371	2885.5	9	7	17.5	-38.9 $\pm$ 1.1	6.0 $\pm$ 0.7	0.602 $\pm$ 0.121	-1.07	-1.67	-1.20
$3_{3,0}$-$4_{4,1}$	7.2937	3063.4	27	21	28.4	-39.9 $\pm$ 1.5	5.8 $\pm$ 0.9	0.868 $\pm$ 0.262	-0.88	-1.09	-0.62
$4_{2,3}$-$5_{3,2}$	7.3988	3064.7	33	27	11.9	-40.8 $\pm$ 2.2	5.0 $\pm$ 2.7	0.782 $\pm$ 1.248	-0.87	-1.35	-0.87
$4_{3,2}$-$5_{4,1}$	7.4294	3239.3	33	27	20.8	-36.0 $\pm$ 2.3	6.0 $\pm$ 1.5	1.009 $\pm$ 0.834	-0.76	-1.21	-0.73
$10_{1,10}$-$11_{0,11}$	7.4372	4194.5	69	63	13.2	-38.1 $\pm$ 1.7	4.1 $\pm$ 1.7	0.258 $\pm$ 0.201	-1.29	-1.68	-1.16

Table D.15: Line Parameters of the -54.5 km s^{-1} Component in the ν_2=2–1 Transition (1 of 2)

Transition	λ (μm)	E_l (K)	g_l	g_u	A_{ul} (s^{-1})	v_{LSR} (km s^{-1})	σ_v (km s^{-1})	W_v (km s^{-1})	$\log_{10}(\tau_{p,\text{thin}})$
$11_{0,11}$-$10_{1,10}$	5.6670	3891.4	63	69	27.6	-51.5 ± 3.1	7.0 ± 4.0	0.791 ± 0.568	-1.01
$11_{0,11}$-$10_{1,10}$	5.6670	3891.4	63	69	27.6	-55.2 ± 7.2	7.0 ± 11.7	0.529 ± 1.193	-1.19
$6_{2,5}$-$5_{1,4}$	5.7627	2878.3	33	39	10.9	-53.0 ± 6.1	7.0 ± 6.7	0.676 ± 0.968	-1.05
$9_{1,9}$-$8_{0,8}$	5.7754	3362.5	17	19	25.2	-51.9 ± 2.9	7.0 ± 4.1	0.702 ± 0.482	-1.07
$8_{1,8}$-$7_{0,7}$	5.8322	3136.9	45	51	23.9	-54.0 ± 3.5	7.0 ± 5.7	0.735 ± 0.864	-1.05
$4_{2,3}$-$3_{1,2}$	5.8491	2549.6	21	27	9.1	-54.5 ± 7.9	8.0 ± 13.3	0.520 ± 1.106	-1.27
$4_{2,3}$-$3_{1,2}$	5.8491	2549.6	21	27	9.1	-54.5 ± 7.9	8.0 ± 13.3	0.520 ± 1.106	-1.27
$6_{2,5}$-$6_{1,6}$	5.9052	2938.5	39	39	4.2	-53.3 ± 5.5	7.0 ± 8.7	0.324 ± 0.478	-1.42
$6_{1,6}$-$5_{0,5}$	5.9485	2763.0	33	39	20.7	-51.4 ± 2.9	7.0 ± 3.6	0.769 ± 0.462	-1.03
$5_{1,5}$-$4_{0,4}$	6.0059	2614.4	9	11	18.8	-53.7 ± 4.2	9.0 ± 9.7	0.983 ± 1.508	-1.04
$4_{2,3}$-$4_{1,4}$	6.0224	2620.4	27	27	5.9	-50.5 ± 14.4	7.4 ± 13.0	1.061 ± 2.755	-0.89
$4_{2,3}$-$4_{1,4}$	6.0224	2620.4	27	27	5.9	-54.3 ± 7.5	7.0 ± 9.2	0.945 ± 1.883	-0.90
$4_{1,4}$-$3_{0,3}$	6.0613	2491.3	21	27	16.6	-53.9 ± 1.5	7.0 ± 2.3	1.058 ± 0.436	-0.89
$2_{2,1}$-$2_{1,2}$	6.1010	2412.5	15	15	5.9	-53.3 ± 4.3	7.0 ± 8.0	0.340 ± 0.529	-1.40
$2_{1,2}$-$1_{0,1}$	6.1753	2328.3	9	15	13.9	-54.7 ± 6.0	9.0 ± 12.7	0.938 ± 1.963	-1.05
$2_{1,1}$-$2_{0,2}$	6.2878	2395.1	5	5	17.7	-54.7 ± 11.8	7.0 ± 12.3	0.620 ± 1.648	-1.08
$1_{1,0}$-$1_{0,1}$	6.3157	2328.3	9	9	21.3	-54.7 ± 5.1	7.0 ± 6.1	0.874 ± 0.949	-0.96
$3_{1,2}$-$3_{2,1}$	6.5994	2617.1	21	21	19.1	-55.0 ± 5.9	7.0 ± 4.1	2.756 ± 2.254	-0.41
$3_{1,2}$-$3_{2,1}$	6.5994	2617.1	21	21	19.1	-53.6 ± 4.2	7.0 ± 4.7	1.632 ± 1.266	-0.69
$5_{1,4}$-$5_{2,3}$	6.6160	2954.6	33	33	23.3	-53.0 ± 2.9	7.0 ± 3.9	0.928 ± 0.555	-0.95
$7_{2,5}$-$7_{3,4}$	6.6462	3542.9	45	45	24.3	-52.0 ± 17.7	7.0 ± 13.5	0.354 ± 1.012	-1.32
$2_{0,2}$-$3_{1,3}$	6.7455	2502.3	7	5	18.4	-52.2 ± 6.4	7.3 ± 9.7	0.787 ± 1.187	-1.05
$7_{3,4}$-$7_{4,3}$	6.7536	3700.0	45	45	18.0	-51.5 ± 5.6	7.0 ± 5.9	0.528 ± 0.479	-1.21
$6_{3,3}$-$6_{4,2}$	6.7814	3451.2	13	13	15.2	-51.5 ± 4.6	7.0 ± 6.7	0.443 ± 0.483	-1.29
$4_{1,4}$-$4_{2,3}$	6.7857	2744.7	27	27	11.1	-51.5 ± 6.7	7.0 ± 9.1	0.405 ± 0.587	-1.32
$9_{5,4}$-$9_{6,3}$	6.8322	4777.3	57	57	15.4	-50.5 ± 7.6	7.0 ± 5.9	0.977 ± 1.227	-0.91
$4_{1,4}$-$5_{0,5}$	6.8449	2763.0	33	27	16.0	-54.3 ± 2.7	7.0 ± 3.8	1.008 ± 0.683	-0.90
$1_{1,0}$-$2_{2,1}$	6.8512	2506.3	15	9	26.0	-57.5 ± 6.8	9.0 ± 5.6	1.491 ± 1.381	-0.82

Table D.16: Line Parameters of the -54.5 km s^{-1} Component in the ν_2=2–1 Transition (2 of 2)

Transition	λ (μm)	E_l (K)	g_l	g_u	A_{ul} (s^{-1})	v_{LSR} (km s^{-1})	σ_v (km s^{-1})	W_v (km s^{-1})	$\log_{10}(\tau_{p,\mathrm{thin}})$
$3_{1,2}$-$4_{2,3}$	7.0096	2744.7	27	21	13.1	-52.7 ± 5.2	9.0 ± 5.8	1.001 ± 0.705	-1.03
$6_{1,6}$-$7_{0,7}$	7.0362	3136.9	45	39	15.6	-54.8 ± 4.7	9.0 ± 7.8	1.565 ± 2.010	-0.81
$8_{0,8}$-$9_{1,9}$	7.2337	3614.1	19	17	14.5	-54.5 ± 1.9	9.0 ± 3.8	0.643 ± 0.401	-1.23
$3_{2,2}$-$4_{3,1}$	7.2371	2885.5	9	7	17.5	-54.4 ± 5.3	7.0 ± 6.5	0.138 ± 0.181	-1.73
$3_{2,2}$-$4_{3,1}$	7.2371	2885.5	9	7	17.5	-54.4 ± 5.3	7.0 ± 6.5	0.138 ± 0.181	-1.73
$3_{3,0}$-$4_{4,1}$	7.2937	3063.4	27	21	28.4	-54.4 ± 4.7	7.0 ± 5.7	0.317 ± 0.380	-1.38
$4_{3,2}$-$5_{4,1}$	7.4294	3239.3	33	27	20.8	-50.5 ± 5.4	9.0 ± 6.1	1.072 ± 1.088	-0.97

Appendix E: Facilities and Software

E.1 Facilities

A summary of facilities used in this thesis is listed below:

- *Green Bank Telescope*

  Argus at the GBT was used to obtain the molecular cloud images of IC 342 (Chapter 2).

- *The Infrared Telescope Facility*

  iSHELL at the IRTF was utilized to obtain the M-band spectra of W3 IRS 5 (Chapter 3).

- *Stratospheric Observatory for Infrared Astronomy*

  EXES at the SOFIA was used to get the 5–8 μm spectra of W3 IRS 5 (Chapter 4).

E.2 Software

A summary of software used in this thesis is listed below:

- astropy (Astropy Collaboration et al., 2013, 2018)
- degas (https://github.com/GBTSpectroscopy/degas)
- gbtpipe (https://github.com/GBTSpectroscopy/gbtpipe)

- NumPy (Harris et al., 2020)
- Planetary Spectrum Generator (Villanueva et al., 2018)
- RADEX (Van der Tak et al., 2007)
- Redux (Clarke et al., 2015)
- SciPy (Virtanen et al., 2020)
- Spectral-Cube (Ginsburg et al., 2019)
- Spextool (Cushing et al., 2004)
- Xtellcor (Vacca et al., 2003)

Bibliography

Agúndez, M., Cernicharo, J., & Goicoechea, J. R. 2008, A&A, 483, 831. doi:10.1051/0004-6361:20077927

Agúndez, M., Roueff, E., Le Petit, F., et al. 2018, A&A, 616, A19. doi:10.1051/0004-6361/201732518

Andrews, S. M., Huang, J., Pérez, L. M., et al. 2018, ApJL, 869, L41. doi:10.3847/2041-8213/aaf741

Asplund, M., Grevesse, N., Sauval, A. J., et al. 2009, ARA&A, 47, 481. doi:10.1146/annurev.astro.46.060407.145222

Astropy Collaboration, Robitaille, T. P., Tollerud, E. J., et al. 2013, A&A, 558, A33. doi:10.1051/0004-6361/201322068

Astropy Collaboration, Price-Whelan, A. M., Sipőcz, B. M., et al. 2018, AJ, 156, 123. doi:10.3847/1538-3881/aabc4f

Bally, J. & Zinnecker, H. 2005, AJ, 129, 2281. doi:10.1086/429098

Banwell, C. N. & McCash, E. M. McGraw-Hill, 1994, 4th ed.

Barr, A. G., Boogert, A., DeWitt, C. N., et al. 2018, ApJL, 868, L2. doi:10.3847/2041-8213/aaeb23

Barr, A. G., Boogert, A., DeWitt, C. N., et al. 2020, ApJ, 900, 104. doi:10.3847/1538-4357/abab05

Barr, A. G., Boogert, A., Li, J., et al. 2022, ApJ, 935, 165. doi:10.3847/1538-4357/ac74b8

Barr, A. G., Li, J., Boogert, A., et al. 2022, A&A, 666, A26. doi:10.1051/0004-6361/202143003

Bast, J. E., Lahuis, F., van Dishoeck, E. F., et al. 2013, A&A, 551, A118. doi:10.1051/0004-6361/201219908

Beltrán, M. T. & de Wit, W. J. 2016, A&A Rv, 24, 6. doi:10.1007/s00159-015-0089-z

Bergin, E. A., Alves, J., Huard, T., et al. 2002, ApJL, 570, L101. doi:10.1086/340950

Bergin, E. A. & Tafalla, M. 2007, ARA&A, 45, 339. doi:10.1146/annurev.astro.45.071206.100404

Bernstein, M. P., Sandford, S. A., Allamandola, L. J., et al. 1995, ApJ, 454, 327

Bernstein, M. P., Allamandola, L. J., & Sandford, S. A. 1997, Advances in Space Research, 19, 991

Beuther, H., Churchwell, E. B., McKee, C. F., et al. 2007, Protostars and Planets V, 165

Bigiel, F., Leroy, A., Walter, F., et al. 2008, AJ, 136, 6

Bigiel, F., Leroy, A. K., Jiménez-Donaire, M. J., et al. 2016, ApJL, 822, L26. doi:10.3847/2041-8205/822/2/L26

Blake, G. A., Sutton, E. C., Masson, C. R., et al. 1987, ApJ, 315, 621. doi:10.1086/165165

Bohlin, R. C., Savage, B. D., & Drake, J. F. 1978, ApJ, 224, 132. doi:10.1086/156357

Bolatto, A. D., Wolfire, M., & Leroy, A. K. 2013, ARA&A, 51, 207. doi:10.1146/annurev-astro-082812-140944

Bonnell, I. A., Bate, M. R., & Zinnecker, H. 1998, MNRAS, 298, 93. doi:10.1046/j.1365-8711.1998.01590.x

Bonnell, I. A., Vine, S. G., & Bate, M. R. 2004, MNRAS, 349, 735. doi:10.1111/j.1365-2966.2004.07543.x

Bonnell, I. A. & Bate, M. R. 2006, MNRAS, 370, 488. doi:10.1111/j.1365-2966.2006.10495.x

Boonman, A. M. S. & van Dishoeck, E. F. 2003, A&A, 403, 1003. doi:10.1051/0004-6361:20030364

Boonman, A. M. S., Doty, S. D., van Dishoeck, E. F., et al. 2003, A&A, 406, 937. doi:10.1051/0004-6361:20030765

Boonman, A. M. S., van Dishoeck, E. F., Lahuis, F., et al. 2003, A&A, 399, 1063. doi:10.1051/0004-6361:20021868

Bottinelli, S., Ceccarelli, C., Lefloch, B., et al. 2004, ApJ, 615, 354. doi:10.1086/423952

Bottinelli, S., Ceccarelli, C., Williams, J. P., et al. 2007, A&A, 463, 601. doi:10.1051/0004-6361:20065139

Campbell, M. F., Butner, H. M., Harvey, P. M., et al. 1995, ApJ, 454, 831. doi:10.1086/176536

Caratti o Garatti, A., Stecklum, B., Garcia Lopez, R., et al. 2017, Nature Physics, 13, 276. doi:10.1038/nphys3942

Cardelli, J. A., Meyer, D. M., Jura, M., et al. 1996, ApJ, 467, 334. doi:10.1086/177608

Carr, J. S. & Najita, J. R. 2008, Science, 319, 1504. doi:10.1126/science.1153807

Cartledge, S. I. B., Lauroesch, J. T., Meyer, D. M., et al. 2004, ApJ, 613, 1037. doi:10.1086/423270

Caselli, P. & Ceccarelli, C. 2012, A&A Rv, 20, 56. doi:10.1007/s00159-012-0056-x

Cazaux, S., Tielens, A. G. G. M., Ceccarelli, C., et al. 2003, ApJL, 593, L51. doi:10.1086/378038

Cernicharo, J., Lim, T., Cox, P., et al. 1997, A&A, 323, L25

Cesaroni, R., Galli, D., Lodato, G., et al. 2007, Protostars and Planets V, 197

Charnley, S. B. & Rodgers, S. D. 2005, Astrochemistry: Recent Successes and Current Challenges, 231, 237. doi:10.1017/S174392130600723X

Chavarría, L., Herpin, F., Jacq, T., et al. 2010, A&A, 521, L37. doi:10.1051/0004-6361/201015113

Chyba, C. F., Thomas, P. J., Brookshaw, L., et al. 1990, Science, 249, 366. doi:10.1126/science.11538074

Clarke, M., Vacca, W. D., & Shuping, R. Y. 2015, Astronomical Data Analysis Software an Systems XXIV (ADASS XXIV), 495, 355

Crosthwaite, L. P., Turner, J. L., Hurt, R. L., et al. 2001, AJ, 122, 797

Cushing, M. C., Vacca, W. D., & Rayner, J. T. 2004, PASP, 116, 362

Dahmen, G., Huttemeister, S., Wilson, T. L., et al. 1998, A&A, 331, 959

de Wit, W. J., Hoare, M. G., Oudmaijer, R. D., et al. 2011, A&A, 526, L5. doi:10.1051/0004-6361/201016062

Downes, D., Radford, S. J. E., Guilloteau, S., et al. 1992, A&A, 262, 424

Draine, B. T., Roberge, W. G., & Dalgarno, A. 1983, ApJ, 264, 485. doi:10.1086/160617

Draine, B. T. & McKee, C. F. 1993, ARA&A, 31, 373. doi:10.1146/annurev.aa.31.090193.002105

Draine, B. T. 2011, Physics of the Interstellar and Intergalactic Medium by Bruce T. Draine. Princeton University Press, 2011. ISBN: 978-0-691-12214-4

Eckart, A., Downes, D., Genzel, R., et al. 1990, ApJ, 348, 434

Eddington, A. S. 1926, Proceedings of the Royal Society of London Series A, 111, 424. doi:10.1098/rspa.1926.0076

Egusa, F., Koda, J., & Scoville, N. 2011, ApJ, 726, 85

Elmegreen, B. G. 2002, ApJ, 577, 206. doi:10.1086/342177

Evans, N. J., Rawlings, J. M. C., Shirley, Y. L., et al. 2001, ApJ, 557, 193

Faure, A. & Josselin, E. 2008, A&A, 492, 257. doi:10.1051/0004-6361:200810717

Federrath, C. & Klessen, R. S. 2013, ApJ, 763, 51. doi:10.1088/0004-637X/763/1/5110.48550/arXiv.1211.6433

Frost, A. J., Oudmaijer, R. D., Lumsden, S. L., et al. 2021, ApJ, 920, 48. doi:10.3847/1538-4357/ac1741

Frayer, D. T., Maddalena, R. J., White, S., et al. 2019, arXiv e-prints, arXiv:1906.02307

Frost, A. J., Oudmaijer, R. D., de Wit, W. J., et al. 2021, A&A, 648, A62. doi:10.1051/0004-6361/202039748

Galametz, M., Kennicutt, R. C., Calzetti, D., et al. 2013, MNRAS, 431, 1956. doi:10.1093/mnras/stt313

Gao, Y., & Solomon, P. M. 2004, ApJ, 606, 271

Gao, Y. & Solomon, P. M. 2004, ApJS, 152, 63. doi:10.1086/383003

Garcia-Burillo, S., Guelin, M., & Cernicharo, J. 1993, A&A, 274, 123

Gibb, E. L., Whittet, D. C. B., Boogert, A. C. A., et al. 2004, ApJS, 151, 35. doi:10.1086/381182

Ginsburg, A., Bally, J., Goddi, C., et al. 2018, ApJ, 860, 119

Ginsburg, A., Koch, E., Robitaille, T., et al. 2019, Zenodo

F. Ghigo: Azimuth and Parallactic Angle Tracking near the Zenith, `http://www.gb.nrao.edu/ rcreager/GBTMetrology/140ft/l0058/gbtmemo52/`

Goldsmith, P. F., Melnick, G. J., Bergin, E. A., et al. 2000, ApJL, 539, L123. doi:10.1086/312854

Goldsmith, P. F. 2001, ApJ, 557, 736

Graciá-Carpio, J., García-Burillo, S., Planesas, P., et al. 2006, ApJL, 640, L135. doi:10.1086/503361

Graciá-Carpio, J., García-Burillo, S., Planesas, P., et al. 2008, A&A, 479, 703

Gwinn, C. R. 1994, ApJ, 429, 241. doi:10.1086/174315

Halfen, D. T., Woolf, N. J., & Ziurys, L. M. 2017, ApJ, 845, 158. doi:10.3847/1538-4357/aa816b

Harris, C. R., Millman, K. J., van der Walt, S. J., et al. 2020, Nature, 585, 357. doi:10.1038/s41586-020-2649-2

Haslam, C. G. T. and Quigley, M. J. S. and Salter, C. J., MNRAS, 147, 405

Heiderman, A., Evans, N. J., Allen, L. E., et al. 2010, ApJ, 723, 1019. doi:10.1088/0004-637X/723/2/1019

Helfer, T. T., Thornley, M. D., Regan, M. W., et al. 2003, ApJS, 145, 259. doi:10.1086/346076

Herbst, E. & van Dishoeck, E. F. 2009, ARA&A, 47, 427. doi:10.1146/annurev-astro-082708-101654

Herzberg, G. 1950, New York: Van Nostrand Reinhold, 1950, 2nd ed.

Heyer, M. & Dame, T. M. 2015, ARA&A, 53, 583. doi:10.1146/annurev-astro-082214-122324

Hirota, A., Kuno, N., Sato, N., et al. 2010, PASJ, 62, 1261. doi:10.1093/pasj/62.5.1261

Hollenbach, D., Kaufman, M. J., Bergin, E. A., et al. 2009, ApJ, 690, 1497. doi:10.1088/0004-637X/690/2/1497

Hollenbach, D., Elitzur, M., & McKee, C. F. 2013, ApJ, 773, 70. doi:10.1088/0004-637X/773/1/70

Hosokawa, T., Yorke, H. W., & Omukai, K. 2010, ApJ, 721, 478. doi:10.1088/0004-637X/721/1/478

Hsieh, T.-H., Takami, M., Connelley, M. S., et al. 2021, ApJ, 912, 108. doi:10.3847/1538-4357/abee88

Indriolo, N., Neufeld, D. A., Barr, A. G., et al. 2020, ApJ, 894, 107. doi:10.3847/1538-4357/ab88a1

Iglesias, E. R. & Silk, J. 1978, ApJ, 226, 851. doi:10.1086/156665

Ilee, J. D., Cyganowski, C. J., Nazari, P., et al. 2016, MNRAS, 462, 4386. doi:10.1093/mnras/stw191210.48550/arXiv.1608.05561

Imai, H., Kameya, O., Sasao, T., et al. 2000, ApJ, 538, 751. doi:10.1086/309165

Imai, H., Deguchi, S., & Sasao, T. 2002, ApJ, 567, 971. doi:10.1086/338582

Imanishi, M., Nakanishi, K., & Kohno, K. 2006, AJ, 131, 2888. doi:10.1086/503527

Imanishi, M., Nakanishi, K., Tamura, Y., et al. 2007, AJ, 134, 2366. doi:10.1086/523598

Imanishi, M., Nakanishi, K., Tamura, Y., et al. 2009, AJ, 137, 3581. doi:10.1088/0004-6256/137/3/3581

Indebetouw, R., Mathis, J. S., Babler, B. L., et al. 2005, ApJ, 619, 931. doi:10.1086/426679

Jacob, A. M., Menten, K. M., Wiesemeyer, H., et al. 2019, A&A, 632, A60. doi:10.1051/0004-6361/201936037

Jacob, A. M., Neufeld, D. A., Schilke, P., et al. 2022, ApJ, 930, 141. doi:10.3847/1538-4357/ac5409

Jenkins, E. B. 2009, ApJ, 700, 1299. doi:10.1088/0004-637X/700/2/1299

Jensen, A. G., Snow, T. P., Sonneborn, G., et al. 2010, ApJ, 711, 1236. doi:10.1088/0004-637X/711/2/1236

Jiménez-Donaire, M. J., Bigiel, F., Leroy, A. K., et al. 2017, MNRAS, 466, 49. doi:10.1093/mnras/stw2996

Jiménez-Donaire, M. J., Bigiel, F., Leroy, A. K., et al. 2019, ApJ, 880, 127. doi:10.3847/1538-4357/ab2b95

Johansen, A., Blum, J., Tanaka, H., et al. 2014, Protostars and Planets VI, 547. doi:10.2458/azu_uapress_9780816531240-ch024

Johnston, K. G., Robitaille, T. P., Beuther, H., et al. 2015, ApJL, 813, L19. doi:10.1088/2041-8205/813/1/L1910.48550/arXiv.1509.08469

Johnston, K. G., Hoare, M. G., Beuther, H., et al. 2020, A&A, 634, L11. doi:10.1051/0004-6361/20193715410.48550/arXiv.1911.09692

Jørgensen, J. K., Belloche, A., & Garrod, R. T. 2020, ARA&A, 58, 727. doi:10.1146/annurev-astro-032620-021927

Karska, A., Herpin, F., Bruderer, S., et al. 2014, A&A, 562, A45. doi:10.1051/0004-6361/201321954

Kauffmann, J., Bertoldi, F., Bourke, T. L., et al. 2008, A&A, 487, 993. doi:10.1051/0004-6361:200809481

Kauffmann, J., Goldsmith, P. F., Melnick, G., et al. 2017, A&A, 605, L5. doi:10.1051/0004-6361/201731123

Kaufman, M. J. & Neufeld, D. A. 1996, ApJ, 456, 250. doi:10.1086/176645

Kaufman, M. J. & Neufeld, D. A. 1996, ApJ, 456, 611. doi:10.1086/176683

Kaźmierczak-Barthel, M., van der Tak, F. F. S., Helmich, F. P., et al. 2014, A&A, 567, A53. doi:10.1051/0004-6361/201322819

Kennicutt, R. C. 1998, ApJ, 498, 541. doi:10.1086/305588

Kennicutt, R. C. 2005, Massive Star Birth: A Crossroads of Astrophysics, 227, 3. doi:10.1017/S1743921305004308

Kennicutt, R. C., Calzetti, D., Aniano, G., et al. 2011, PASP, 123, 1347. doi:10.1086/663818

Kennicutt, R. C., & Evans, N. J. 2012, ARA&A, 50, 531

Keady, J. J., Hall, D. N. B., & Ridgway, S. T. 1988, ApJ, 326, 832. doi:10.1086/166141

Klessen, R. S. 2011, EAS Publications Series, 51, 133. doi:10.1051/eas/115100910.48550/arXiv.1109.0467

Knudsen, K. K., Walter, F., Weiss, A., et al. 2007, ApJ, 666, 156

Kochanov, R. V., Gordon, I. E., Rothman, L. S., et al. 2016, JQSRT, 177, 15. doi:10.1016/j.jqsrt.2016.03.005

Koda, J., Scoville, N., Sawada, T., et al. 2009, ApJL, 700, L132

Kreckel, K., Faesi, C., Kruijssen, J. M. D., et al. 2018, ApJL, 863, L21. doi:10.3847/2041-8213/aad77d

Krips, M., Neri, R., García-Burillo, S., et al. 2008, ApJ, 677, 262

Krips, M., Crocker, A. F., Bureau, M., et al. 2010, MNRAS, 407, 2261

Kruijssen, J. M. D. & Longmore, S. N. 2014, MNRAS, 439, 3239. doi:10.1093/mnras/stu098

Krumholz, M. R., McKee, C. F., & Klein, R. I. 2005, ApJL, 618, L33. doi:10.1086/427555

Krumholz, M. R. & McKee, C. F. 2005, ApJ, 630, 250. doi:10.1086/43173410.48550/arXiv.astro-ph/0505177

Krumholz, M. R., Klein, R. I., McKee, C. F., et al. 2009, Science, 323, 754. doi:10.1126/science.1165857

Kuiper, R., Klahr, H., Beuther, H., et al. 2010, ApJ, 722, 1556. doi:10.1088/0004-637X/722/2/1556

Kuiper, R., Klahr, H., Beuther, H., et al. 2011, ApJ, 732, 20. doi:10.1088/0004-637X/732/1/20

Kuno, N., Sato, N., Nakanishi, H., et al. 2007, PASJ, 59, 117

Kutner, M. L., & Ulich, B. L. 1981, ApJ, 250, 341

Lacy, J. H., Richter, M. J., Greathouse, T. K., et al. 2003, Proc. SPIE, 4841, 1572. doi:10.1117/12.461194

Lacy, J. H. 2013, ApJ, 765, 130. doi:10.1088/0004-637X/765/2/130

Lada, C. J. & Lada, E. A. 2003, ARA&A, 41, 57. doi:10.1146/annurev.astro.41.011802.094844

Lada, C. J., Lombardi, M., & Alves, J. F. 2010, ApJ, 724, 687. doi:10.1088/0004-637X/724/1/687

Lada, C. J., Forbrich, J., Lombardi, M., et al. 2012, ApJ, 745, 190. doi:10.1088/0004-637X/745/2/19010.48550/arXiv.1112.4466

Lahuis, F. & van Dishoeck, E. F. 2000, A&A, 355, 699

Lambrechts, M. & Johansen, A. 2012, A&A, 544, A32. doi:10.1051/0004-6361/201219127

Laux, C. O., Spence, T. G., Kruger, C. H., et al. 2003, Plasma Sources Science Technology, 12, 125. doi:10.1088/0963-0252/12/2/301

Leroy, A. K., Walter, F., Brinks, E., et al. 2008, AJ, 136, 2782. doi:10.1088/0004-6256/136/6/2782

Leroy, A. K., Usero, A., Schruba, A., et al. 2017, ApJ, 835, 217. doi:10.3847/1538-4357/835/2/217

Leroy, A. K., Schinnerer, E., Hughes, A., et al. 2021, ApJS, 257, 43. doi:10.3847/1538-4365/ac17f3

Li, J., Boogert, A., Barr, A. G., et al. 2022, ApJ, 935, 161. doi:10.3847/1538-4357/ac7ce7

Loison, J.-C., Wakelam, V., Hickson, K. M., et al. 2014, MNRAS, 437, 930. doi:10.1093/mnras/stt1956

Luhman, K. L. 2012, ARA&A, 50, 65. doi:10.1146/annurev-astro-081811-125528

Mangum, J. G., Emerson, D. T., & Greisen, E. W. 2007, A&A, 474, 679

Maud, L. T., Cesaroni, R., Kumar, M. S. N., et al. 2019, A&A, 627, L6. doi:10.1051/0004-6361/201935633

McKee, C. F. & Tan, J. C. 2003, ApJ, 585, 850. doi:10.1086/346149

McKee, C. F. & Ostriker, E. C. 2007, ARA&A, 45, 565. doi:10.1146/annurev.astro.45.051806.110602

Megeath, S. T., Herter, T., Beichman, C., et al. 1996, A&A, 307, 775

Megeath, S. T., Wilson, T. L., & Corbin, M. R. 2005, ApJL, 622, L141. doi:10.1086/429720

Meier, D. S., Turner, J. L., & Hurt, R. L. 2000, ApJ, 531, 200

Meier, D. S., & Turner, J. L. 2001, ApJ, 551, 687

Meier, D. S., & Turner, J. L. 2005, ApJ, 618, 259

Meier, D. S., Turner, J. L., & Schinnerer, E. 2011, AJ, 142, 32

Meijerink, R., Spaans, M., & Israel, F. P. 2007, A&A, 461, 793. doi:10.1051/0004-6361:20066130

Menten, K. M., Melnick, G. J., & Phillips, T. G. 1990, Liege International Astrophysical Colloquia, 29, 243

Mihalas, D. 1978, San Francisco: W.H. Freeman, 1978

Milam, S. N., Savage, C., Brewster, M. A., et al. 2005, ApJ, 634, 1126. doi:10.1086/497123

Mitchell, G. F., Maillard, J.-P., Allen, M., et al. 1990, ApJ, 363, 554. doi:10.1086/169365

Mitchell, G. F., Maillard, J.-P., & Hasegawa, T. I. 1991, ApJ, 371, 342. doi:10.1086/169896

Monnier, J. D., Tuthill, P. G., Ireland, M., et al. 2009, ApJ, 700, 491. doi:10.1088/0004-637X/700/1/491

Moscadelli, L. & Goddi, C. 2014, A&A, 566, A150

Moscadelli, L., Sanna, A., Cesaroni, R., et al. 2019, A&A, 622, A206

Murphy, E. J., Dong, D., Leroy, A. K., et al. 2015, ApJ, 813, 118. doi:10.1088/0004-637X/813/2/118

Nakano, T. 1989, ApJ, 345, 464. doi:10.1086/167919

Navarete, F., Galli, P. A. B., & Damineli, A. 2019, MNRAS, 487, 2771. doi:10.1093/mnras/stz1442

Nazari, P., Tabone, B., & Rosotti, G. P. 2022, arXiv:2211.00126. doi:10.48550/arXiv.2211.00126

Neufeld, D. A. & Hollenbach, D. J. 1994, ApJ, 428, 170. doi:10.1086/174230

Nguyen, Q.-R., Jackson, J. M., Henkel, C., et al. 1992, ApJ, 399, 521

Nguyen-Rieu, Viallefond, F., Combes, F., et al. 1994, IAU Colloq. 140: Astronomy with Millimeter and Submillimeter Wave Interferometry, 336

Nieva, M.-F. & Przybilla, N. 2012, A&A, 539, A143. doi:10.1051/0004-6361/201118158

Öberg, K. I., van der Marel, N., Kristensen, L. E., et al. 2011, ApJ, 740, 14. doi:10.1088/0004-637X/740/1/14

Olguin, F. A., Hoare, M. G., Johnston, K. G., et al. 2020, MNRAS, 498, 4721. doi:10.1093/mnras/staa2406

Ormel, C. W. & Klahr, H. H. 2010, A&A, 520, A43. doi:10.1051/0004-6361/201014903

Ormel, C. W., Min, M., Tielens, A. G. G. M., et al. 2011, A&A, 532, A43. doi:10.1051/0004-6361/201117058

Pan, H.-A., Schinnerer, E., Hughes, A., et al. 2022, ApJ, 927, 9. doi:10.3847/1538-4357/ac474f

Papadopoulos, P. P. 2007, ApJ, 656, 792. doi:10.1086/510186

Pascucci, I., Apai, D., Luhman, K., et al. 2009, ApJ, 696, 143. doi:10.1088/0004-637X/696/1/143

Pascucci, I., Herczeg, G., Carr, J. S., et al. 2013, ApJ, 779, 178. doi:10.1088/0004-637X/779/2/178

Pontoppidan, K. M., Fraser, H. J., Dartois, E., et al. 2003, A&A, 408, 981. doi:10.1051/0004-6361:20031030

Privon, G. C., Herrero-Illana, R., Evans, A. S., et al. 2015, ApJ, 814, 39

Privon, G. C., Ricci, C., Aalto, S., et al. 2020, ApJ, 893, 149. doi:10.3847/1538-4357/ab8015

Purser, S. J. D., Lumsden, S. L., Hoare, M. G., et al. 2021, MNRAS. doi:10.1093/mnras/stab747

Raymond, S. N., Kokubo, E., Morbidelli, A., et al. 2014, Protostars and Planets VI, 595. doi:10.2458/azu_uapress_9780816531240-ch026

Rayner, J. T., Toomey, D. W., Onaka, P. M., et al. 2003, PASP, 115, 362. doi:10.1086/367745

Rayner, J., Tokunaga, A., Jaffe, D., et al. 2022, PASP, 134, 015002. doi:10.1088/1538-3873/ac3cb4

Richter, M. J., Dewitt, C. N., McKelvey, M., et al. 2018, Journal of Astronomical Instrumentation, 7, 1840013. doi:10.1142/S2251171718400135

Roche, P. F. & Aitken, D. K. 1984, MNRAS, 208, 481. doi:10.1093/mnras/208.3.481

Rodgers, C. D. & Williams, A. P. 1974, JQSRT, 14, 319. doi:10.1016/0022-4073(74)90113-7

Rodón, J. A., Beuther, H., Megeath, S. T., et al. 2008, A&A, 490, 213. doi:10.1051/0004-6361:200810158

Rosen, A. L. & Krumholz, M. R. 2020, AJ, 160, 78. doi:10.3847/1538-3881/ab9abf

Rothman, L. S., Gordon, I. E., Babikov, Y., et al. 2013, JQSRT, 130, 4. doi:10.1016/j.jqsrt.2013.07.002

Ruze, J. 1966, IEEE Proceedings, 54, 633

Saha, A., Claver, J., & Hoessel, J. G. 2002, AJ, 124, 839. doi:10.1086/341649

Salyk, C., Pontoppidan, K. M., Blake, G. A., et al. 2011, ApJ, 731, 130. doi:10.1088/0004-637X/731/2/130

Schinnerer, E., Böker, T., Meier, D. S., et al. 2008, ApJL, 684, L21. doi:10.1086/592109

Schruba, A., Leroy, A. K., Walter, F., et al. 2010, ApJ, 722, 1699. doi:10.1088/0004-637X/722/2/1699

Schulz, A., Güsten, R., Köster, B., et al. 2001, A&A, 371, 25

Sheffer, Y., Rogers, M., Federman, S. R., et al. 2008, ApJ, 687, 1075. doi:10.1086/591484

Sheth, K., Vogel, S. N., Regan, M. W., et al. 2002, AJ, 124, 2581

Shirley, Y. L. 2015, PASP, 127, 299. doi:10.1086/680342

Shu, F. H. 1977, ApJ, 214, 488. doi:10.1086/155274

Shu, F. H., Adams, F. C., & Lizano, S. 1987, ARA&A, 25, 23. doi:10.1146/annurev.aa.25.090187.000323

Sieth, M., Devaraj, K., Voll, P., et al. 2014, Proc. SPIE, 91530P

Silk, J. 1997, ApJ, 481, 703. doi:10.1086/304073

Smith, R. L., Pontoppidan, K. M., Young, E. D., et al. 2009, ApJ, 701, 163. doi:10.1088/0004-637X/701/1/163

Snell, R. L., Howe, J. E., Ashby, M. L. N., et al. 2000, ApJL, 539, L101. doi:10.1086/312848

Sofia, U. J., Cardelli, J. A., Guerin, K. P., et al. 1997, ApJL, 482, L105. doi:10.1086/310681

Suri, S., Beuther, H., Gieser, C., et al. 2021, A&A, 655, A84. doi:10.1051/0004-6361/202140963

Takahashi, T., Silk, J., & Hollenbach, D. J. 1983, ApJ, 275, 145. doi:10.1086/161521

Tan, Q.-H., Gao, Y., Zhang, Z.-Y., et al. 2018, ApJ, 860, 165

Tennyson, J., Zobov, N. F., Williamson, R., et al. 2001, Journal of Physical and Chemical Reference Data, 30, 735. doi:10.1063/1.1364517

Tielens, A. G. G. M. & Hollenbach, D. 1985, ApJ, 291, 722. doi:10.1086/163111

Tielens, A. G. G. M. & Allamandola, L. J. 1987, Interstellar Processes, 134, 397. doi:10.1007/978-94-009-3861-8_16

Tielens, A. G. G. M. 2005, The Physics and Chemistry of the Interstellar Medium, by A. G. G. M. Tielens, pp. . ISBN 0521826349. Cambridge, UK: Cambridge University Press, 2005.

Tielens, A. G. G. M. 2021, Molecular Astrophysics. Cambridge: Cambridge University Press. doi:10.1017/9781316718490

Turner, J. L. & Ho, P. T. P. 1983, ApJL, 268, L79. doi:10.1086/184033

Turner, J. L., & Hurt, R. L. 1992, ApJ, 384, 72

Vacca, W. D., Cushing, M. C., & Rayner, J. T. 2003, PASP, 115, 389. doi:10.1086/346193

van der Tak, F. F. S., van Dishoeck, E. F., Evans, N. J., et al. 2000, ApJ, 537, 283. doi:10.1086/309011 van der Tak, F. F. S., Boonman, A. M. S., Braakman, R., et al. 2003, A&A, 412, 133. doi:10.1051/0004-6361:20031409

van der Tak, F. F. S., Tuthill, P. G., & Danchi, W. C. 2005, A&A, 431, 993. doi:10.1051/0004-6361:20041595

Van der Tak, F.F.S., Black, J.H., Schöier, F.L., Jansen, D.J., van Dishoeck, E.F., 2007, A&A, 468, 627

van Dishoeck, E. F. 1988, Rate Coefficients in Astrochemistry, 146, 49. doi:10.1007/978-94-009-3007-0_4

van Dishoeck, E. F. & Helmich, F. P. 1996, A&A, 315, L177

van Dishoeck, E. F. & Blake, G. A. 1998, ARA&A, 36, 317. doi:10.1146/annurev.astro.36.1.317

van Dishoeck, E. F., Herbst, E., & Neufeld, D. A. 2013, Chemical Reviews, 113, 9043. doi:10.1021/cr4003177

van Dishoeck, E. F. 2018, IAU Symposium, 332, 3. doi:10.1017/S1743921317011528

van Dishoeck, E. F., Kristensen, L. E., Mottram, J. C., et al. 2021, A&A, 648, A24. doi:10.1051/0004-6361/202039084

Villanueva, G. L., Smith, M. D., Protopapa, S., et al. 2018, JQSRT, 217, 86. doi:10.1016/j.jqsrt.2018.05.023

Vinogradoff, V., Fray, N., Duvernay, F., et al. 2013, A&A, 551, A128

Virtanen, P., Gommers, R., Oliphant, T. E., et al. 2020, Nature Methods, 17, 261. doi:10.1038/s41592-019-0686-2

Viti, S. 2017, A&A, 607, A118. doi:10.1051/0004-6361/201628877

Wang, Y., Beuther, H., Zhang, Q., et al. 2012, ApJ, 754, 87. doi:10.1088/0004-637X/754/2/87

Wang, K.-S., Bourke, T. L., Hogerheijde, M. R., et al. 2013, A&A, 558, A69. doi:10.1051/0004-6361/201322087

Whittet, D. C. B. 2010, ApJ, 710, 1009. doi:10.1088/0004-637X/710/2/1009

Williams, J. P. & Cieza, L. A. 2011, ARA&A, 49, 67. doi:10.1146/annurev-astro-081710-102548

Wilson, T. L. & Rood, R. 1994, ARA&A, 32, 191. doi:10.1146/annurev.aa.32.090194.001203

Wilson, T. L. 1999, Reports on Progress in Physics, 62, 143. doi:10.1088/0034-4885/62/2/002

Wilson, T. L., Boboltz, D. A., Gaume, R. A., et al. 2003, ApJ, 597, 434. doi:10.1086/378233

Wolfire, M. G. & Cassinelli, J. P. 1987, ApJ, 319, 850. doi:10.1086/165503

Wouterloot, J. G. A., Henkel, C., Brand, J., et al. 2008, A&A, 487, 237. doi:10.1051/0004-6361:20078156

Young, E. T., Becklin, E. E., Marcum, P. M., et al. 2012, ApJL, 749, L17. doi:10.1088/2041-8205/749/2/L17

Yorke, H. W. & Bodenheimer, P. 1999, ApJ, 525, 330. doi:10.1086/307867

Zapata, L. A., Garay, G., Palau, A., et al. 2019, ApJ, 872, 176

Zinnecker, H. & Yorke, H. W. 2007, ARA&A, 45, 481. doi:10.1146/annurev.astro.44.051905.092549